UNIVERSITY OF CALGARY

Inversion of azimuthal velocity and amplitude variations for seismic anisotropy

by

Khaled Al Dulaijan

A THESIS

SUBMITTED TO THE FACULTY OF GRADUATE STUDIES

IN PARTIAL FULFILMENT OF THE REQUIREMENTS FOR THE

DEGREE OF DOCTOR OF PHILOSOPHY

GRADUATE PROGRAM IN GEOLOGY AND GEOPHYSICS

CALGARY, ALBERTA

DECEMBER, 2017

Abstract

Natural fractures can play a key role in production of hydrocarbon in the form of increased porosity and permeability for efficient fluid flow especially for unconventional reservoirs of low matrix permeability. Thus, knowledge related to fracture orientation and intensity is vital for the development of unconventional hydrocarbon reservoirs, such as tight sand oil and shale gas reservoirs. The most productive horizontal wells are those crossing the most vertical fractures. A pattern of vertical fractures causes the seismic wavefield to exhibit azimuthal anisotropy. The best way known to detect fractures, at large scales, is by recognizing the effect of them on seismic data in attempt of inversing it. The Altamont-Bluebell play is within the Uinta Basin in northeast Utah, and is considered an unconventional play in the sense that natural fractures act as fluid storage and conduits in mostly the tight sandstones and partially in the tight carbonates. Consequently, analyzing the azimuthal variation in the observed amplitudes and velocities of the 3D seismic data acquired over the Altamont-Bluebell field is of great value in ascertaining important and relevant reservoir conditions in terms of porosity and permeability. In the Altamont-Bluebell field, azimuthal anisotropy was analysed using two types of data (3D surface seismic and VSP) and using three different methods (inversion of azimuthal amplitude, inversion of azimuthal travel times, and S-wave splitting). To use the VSP data, several types of VSPs were processed from field files to final products (P and S wavefield images and velocities). All results of different methods and data types were correlated to each other where similarities were pointed out and differences were explained.

Numerical seismic modeling provides a valuable tool for geophysicists to test and validate their methodologies. Fractures make numerical modeling more complicated and introduce complexities that might even require geophysicists to validate their numerical models before using them to assess their methods. Scaled-down physical modeling of seismic surveys provides a unique opportunity to test, validate, and develop methods for characterizing fractured reservoirs, because it can produce experimental data from known physical properties and geometries that can be comparable with both numerical and field seismic data. Therefore, physical modeling is utilized to determine stiffness coefficients associated with the anisotropic material and validate techniques used for anisotropy, such as S-wave splitting.

Keywords: azimuthal, seismic anisotropy, HTI, fractures, inversion, AVAZ, VVAZ, physical modeling, 3D seismic, and VSP.

Acknowledgements

First and foremost, I am deeply grateful to my lord, Allah, for countless blessings. May God make this work of use for others.

My heartfelt gratitude is to my lovely wife, Sara. She was there for our family when I was not. She continues providing us with love, peace, and strength. I am also grateful to my daughters, Dana and Tala. They are our source of inspiration and joy. I genuinely acknowledge my parents and siblings for their nonstop love and support.

My sincere appreciation is to my supervisor, Dr. Gary Margrave, for his support, guidance, and leadership. He sets an example to follow through his dedication and hard work. I also thank Dr. Joe Wong for acquiring the physical modeling datasets and proofreading parts of this research. I am also grateful to Khalid Almuteri, Dr. Jon Downton, David Henley, Dr. Mohammed Kanfar, Dr. Hassan Khaniani, Kevin Hall, Nassir Saeed, Dr. Haitham Hamid, Dr. Farank Mahmoudian, and Dr. Marcelo Guardio for their inputs to this research. My appreciation is extended to CREWES sponsors, directors, staff, and students.

The 3D seismic and VSP data were provided by Devon Energy. The well logs were provided by Linn Energy. Therefore, I acknowledge Devon Energy and Linn Energy for providing field data and allowing to publish the results. From Saudi Aramco, I thank Dr. Saleh Al-Saleh, my specialist development program mentor and former chief geophysicist, and Dr. Aiman Bakhorji, my current chief geophysicist, for their encouragement and support. My gratitude is extended to Dr. Mohammed Alfaraj, Dr. John Owusu, and all my colleagues who have contributed to my technical and personal growth. Lastly by not least, I am grateful to Saudi Aramco for sponsoring my Ph.D. study.

Table of Contents

List of Tables

List of Figures and Illustrations

List of Symbols, Abbreviations and Nomenclature

Symbol	Definition
′	Feet
º	Degree
α	Compressional-wave vertical velocity
β	Shear-wave vertical velocity polarized in plane of propagation
δ, ε, γ	Thomsen's parameters for VTI media
δ^V, ε^V, γ	Thomsen's-style parameters for HTI media
η	Alkhalifa and Tsvankin parameter for VTI media
ρ	Bulk density
3C	3-Component
3D	3-Dimensional
4C	4-Component
AGC	Automatic Gain Control
A_{ij}	Density-normalized stiffness coefficients
A_{ani}	Anisotropic intercept
A_{iso}	Isotropic intercept
AVA	Amplitude Variation with Angle
AVAZ	Amplitude Variation with Azimuth
B_{ani}	Anisotropic Gradient
B_{iso}	Isotropic Gradient
C_{ij}	Stiffness coefficients
CDP	Common-Depth Point
CMP	Common Mid-Point
COV	Common-Offset Vector
ft	Feet
HTI	Horizontal Transverse Isotropy
KB	Kelly Bushing
m	Meter
ms	Millisecond
MD	Measured Depth
NMO	Normal Moveout
PSTM	Pre-stack time migration
P wave	Compressional body wave
Q	Quality factor
QC	Quality Control
qP	Quasi compressional body wave
qS_v	Quasi Shear body wave polarized in plane of propagation
qS_H	Quasi Shear body wave polarized orthogonal to plane of propagation
RMS	Root-Mean Square

s	Second
SRD	Seismic Reference Datum
S wave	Shear body wave
TD	Total Depth of borehole
TVD	True-Vertical Depth
VOT	Vector-Offset Tile
V_{fast}	Fast RMS velocity for HTI media
V_p	P-wave velocity (isotropic)
V_s	S-wave velocity (isotropic)
V_{slow}	Slow RMS velocity for HTI media
VSP	Vertical Seismic Profile
VTI	Vertical Transverse Isotropy
VVAZ	Velocity Variation with Azimuth

Epigraph

"There is a crack in everything, that's how the light gets in."

Leonard Cohen (1934-2016).

Chapter 1 Introduction

Information related to fracture orientation and intensity is vital for the development of unconventional hydrocarbons, such as tight sand oil and shale gas. A pattern of vertical fractures causes the seismic wavefield to exhibit azimuthal anisotropy. The best way known to detect fractures at large scales is by recognizing the effect of them on seismic data in an attempt of inverting it. Numerical seismic modeling provides a valuable tool for geophysicists to test and validate their methodologies. Fractures make numerical modeling more complicated and introduce complexities that might even require geophysicists to validate their numerical models before using them to assess their methods. Scaled-down physical modeling of seismic surveys provides a unique opportunity to test, validate, and develop methods for characterizing fractured reservoirs, because it can produce experimental data from known physical properties and geometries that can be compared with both numerical and field seismic data. Therefore, physical modeling is utilized to investigate azimuthal anisotropy and to validate its estimation techniques before these techniques are applied to unconventional reservoirs.

The Altamont-Bluebell play is within the Uinta Basin in northeast Utah, and is considered an unconventional play in the sense that natural fractures act as fluid storage and conduits in mostly the tight sandstones and partially in the carbonates. Consequently, analyzing the azimuthal variation in the observed amplitudes and velocities of the 3D seismic data acquired over the Altamont-Bluebell field is of great value in ascertaining important and relevant reservoir conditions in terms of porosity and permeability. Along with S-wave splitting analysis, these techniques are applied to VSP data within the same field.

1.1 Thesis objective

The overall objective of this thesis is to investigate and assess methods of utilizing azimuthal variations of amplitude and travel times observed in seismic data to characterize seismic anisotropy and then to deduce from such observations important properties of the underlying fracture system. One specific objective is to acquire physically-modeled seismic data through material exhibiting azimuthal anisotropy, and then use the relevant observations to determine stiffness coefficients associated with the anisotropic material and validate techniques used for anisotropy, such as S-wave splitting.

A main objective is to analyze 3-D seismic data to identify the density and direction of fractures are really needed. The objective of acquiring the Altamont-Bluebell survey (3-D surface seismic and VSP data) is to identify density and direction of fractures to help in determining well spacing to existing wells needed to effectively drain the remaining hydrocarbon reserves, and to identify new drilling opportunities (Adams et al., 2015). To this end, azimuthal variations of amplitude and travel times were extracted from the 3-D seismic data to create maps of estimated seismic anisotropy intensity and orientation for the main reservoirs within the survey. Beside inversion of amplitude variations with azimuth and S-wave splitting for VSP data, a new technique was developed for azimuthal travel time analysis of offset VSP data that can be applied to 3-D VSP, multi walkaway VSPs, and walkaround VSP data.

1.2 Data used in thesis

3-D seismic data and different types of VSP data in Altamont-Bluebell field along some well-log information were used. Also, different sets of physical modeling datasets were acquired for this research as outline below.

1.2.1 Physical modeling datasets

Several different physical modelling datasets were acquired for different objectives at the CREWES physical modeling laboratory. These datasets are used for anisotropy analysis and testing of anisotropy methods. The first dataset is used to test variations of azimuthal travel time. Travel times of P waves traveling through layers that simulate a pattern of vertical fractures are elliptical as function of azimuth (Al Dulaijan et al., 2012). Therefore, fitting of an ellipse by least square inversion identifies the presence of seismic anisotropy, its orientation, and intensity. The second dataset is used to measure the stiffness coefficient of phenolic which is mainly HTI and partially orthorhombic. Both datasets are described and used in **Chapter 3**.

The third dataset is a complete 3D survey over three-layer model. In **Chapter 5**, it is completely processed and used to test the inversion of azimuthal travel time variations code. It can be used also to test azimuthal amplitude variations. However, AVAZ is tested here only using numerical synthetic data created by deconvolution, and Mahmoudian (2013) is referenced for AVAZ physical modeling test. The fourth dataset is four-component gathers that are used for S-wave splitting analysis in **Chapter 6**.

1.2.2 Altamont-Bluebell seismic data

3D seismic data were acquired over an area of 35 square miles within the Bluebell field in 2010. 3D pre-stack seismic data are analyzed for azimuthal amplitude variations in **Chapter 4** and for azimuthal travel time variations in **Chapter 5**. Figure 1.1 shows a basemap of 3D seismic data, with color indicating fold. Two vibrators were used for each shot and an array of six geophones over a 6′ circle was used for each channel. The receiver and source intervals were 220′. The receiver lines were oriented E-W and spaced 1100′, while source lines were oriented N-S and spaced 660′. Bin size is 110′x110′, and the nominal fold is 240.

A set of zero-offset, four-component, offset VSPs were acquired in the borehole indicated by the black dot in Figure 1.1, and they are described and fully processed in **Chapter 6**. The source-receiver azimuth and offset distribution across the survey is shown by Figure 1.2, where the color indicates number of traces falling in an offset-azimuth bin. Good azimuthal coverage (0^o-360^o) can been seen for offsets up to 14000′. 3-D data acquisition meet the requirements discussed in the azimuthal analysis data requirements section.

1.3 Software used in thesis

Most of software for this research was written in MATLAB. I developed software packages for the calculation of stiffness coefficients, least-squares elliptical fitting of azimuthal travel times, linear inversion of azimuthal travel times, 4-component rotations, and nonlinear iterative inversion of azimuthal amplitudes. The development of the inversion of azimuthal velocity and amplitude for 3D pre-stack seismic data software packages was quite challenging because of the memory requirements of 3D pre-stack data. Therefore, the codes were made efficient by utilizing disk and releasing memory. That required writing hundreds of thousands of files into disk. The MATALB software packages were written to handle not only surface seismic geometry but also VSP geometry. Moreover, Geoview® by Hampson-Russell is used for well to seismic calibration, horizon picking, and pre-stack seismic elastic inversion. Finally, VISTA® by Schlumberger is used to process all VSP datasets and ProMAX® by Halliburton is used to process 3D physical modeling datasets.

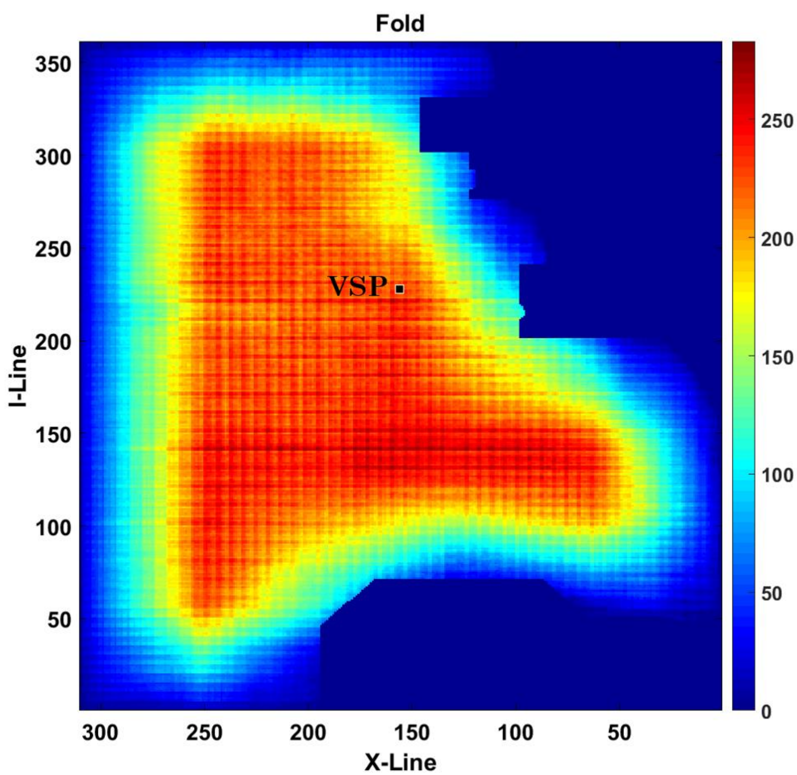

Figure 1.1 Fold base map with VSP borehole location indicated by black dot.

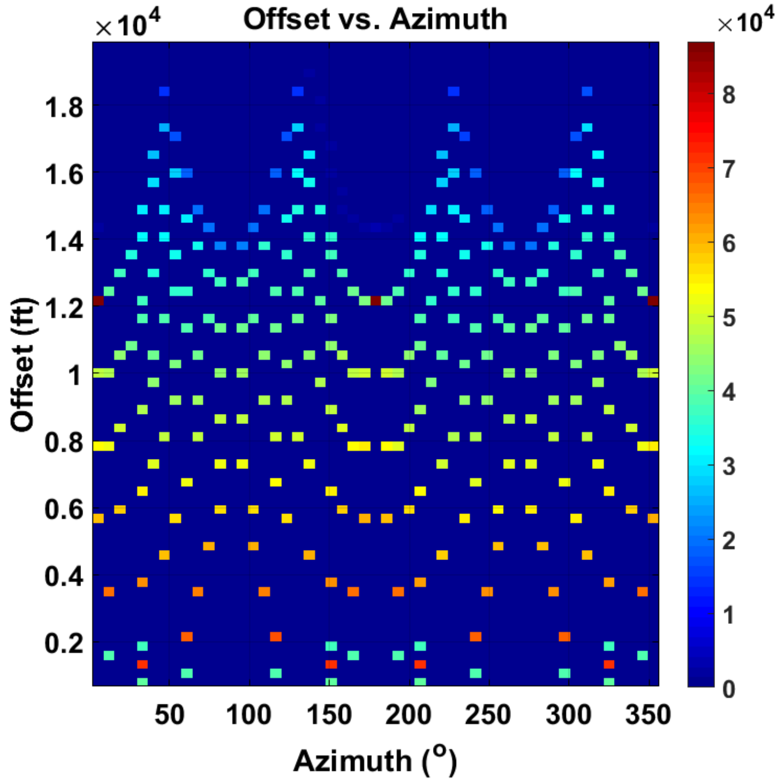

Figure 1.2 Offset vs Azimuth distribution for the whole survey. Color indicates fold distribution.

1.4 Thesis organization

Chapter 1 briefly introduces the thesis. Its objectives and contributions, along with the data and software used are discussed. **Chapter 2** provides a background of seismic anisotropy, fractures, travel time and amplitude azimuthal methods, and the geology of Altamont-Bluebell field. **Chapter 3** investigates seismic anisotropy through physical modeling datasets, where the first dataset is used to test variations of azimuthal travel time, and the second dataset is used to measure the stiffness coefficient of Phenolic which is mainly HTI and partially orthorhombic. **Chapter 4** uses 3-D pre-stack seismic data from Altamont-Bluebell field for elastic inversion and for AVAZ nonlinear iterative inversion that is based on Rüger (1997). **Chapter 5** utilizes elliptical NMO equation by Grechka and Tsvankin (1998) for VVAZ on 3D physical model dataset and on 3-D pre-stack seismic data from Altamont-Bluebell field. Also, Dix (1955)-type interval properties are estimated. **Chapter 6** uses multiple VSP datasets. Offset VSPs are used for inversion of azimuthal travel time and amplitude variations. The four-component VSP is used for S-wave splitting analysis.

1.5 Contributions made in this thesis

One contribution made in this thesis is the invention of a new technique for offset, walkaway, walkaround, and 3D VSPs inversion of azimuthal variations of travel times. This technique is usually used only for 3-D surface seismic NMO velocities. Another contribution is software development of an iterative nonlinear inversion of azimuthal amplitudes and linear inversion of azimuthal velocities. Both can handle 3-D pre-stack surface seismic and VSP geometry. In fact, in one survey at the Altamont-Bluebell field, azimuthal anisotropy was analysed using two types of data (3-D surface seismic and VSP) and using three different methods (inversion of azimuthal amplitude, inversion of azimuthal travel times, and S-wave splitting). In order to use VSP data, several types of VSPs were processed from field files to final products (P and S wavefield images and velocities). All results of different methods and data types were correlated to each other where similarities were pointed out and differences were explained. Last but not least, the inversion of azimuthal travel times technique was tested using a full 3-D physical modeling dataset over a physical model that its anisotropy is fully estimated here by measuring stiffness coefficients. I fully processed the 3-D physical modeling dataset in order to be used here.

Chapter 2 Background

This chapter provides a brief background about seismic anisotropy and fractures. It also explains the stiffness tensor in terms of elasticity and in terms of wave propagation. Reviews of amplitude-based methods of azimuthal anisotropy, along with those based on travel times and how they can be implemented to proper azimuthal seismic data, are provided.

2.1 Seismic anisotropy

Suppose that we throw a stone into a swimming pool. A wave will originate when and where the stone hits the water surface. The wave will travel along all directions at the same speed, resulting in a circular wavefront. This property (velocity being same in all directions) of the wave is called isotropy. On the other hand, the dependence of velocity on direction is called anisotropy. When anisotropy exists, i.e., when velocity depends on direction, as shown in Figure 1. The group velocity ($\vec{g}$) of the wave, at point A, is equal to the ratio of distance between the origin and the time that took the wave to travel that distance. The group velocity is not normal to the wavefront, as shown by Figure 2.1. The phase velocity ($\vec{v}$) is normal to the wavefront and it measures the velocity of a single frequency (Vestrum, 1994).

Stiffness coefficients are used to describe anisotropy. Stiffness relates stress to the strain by Hooke's law:

$$\sigma_{ij} = c_{ijkl}\epsilon_{kl} \ , \tag{2.1}$$

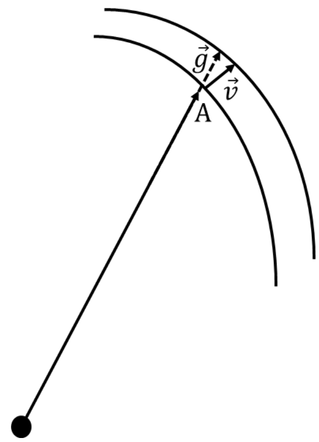

Figure 2.1. Non-circular seismic wavefronts in an anisotropic medium at two different times. The vector $\vec{g}$ shows the group velocity direction, while the vector $\vec{v}$ shows the direction of the phase velocity (perpendicular to the wavefronts). The magnitude of the group velocity vector $\vec{g}$ is equal to the distance between the two wavefronts divided by their difference in time (modified after Vestrum 1994).

where *i, j, k,* and *l* are 1, 2, and 3. σ_{ij} is the second-order stress tensor, c_{ijkl} is the fourth order stiffness tensor, and ϵ_{kl} is the second order strain tensor. The stress and strain tensors have 9 (3x3) elements each, while the stiffness tensor has 81 elements. In the unit cube, shown in Figure 2.2, σ_{ij} defines the stress exerted on the i^{th} face along the j^{th} direction. Similarly, ϵ_{kl} defines the stress exerted on the k^{th} face along the l^{th} direction. Because of symmetry, stress elements σ_{ij} and σ_{ji} are equal (i.e. $\sigma_{32} = \sigma_{23}$). The symmetry of σ_{ij} is due to the fact that there are no net torques on the body. Therefore, the stress tensor is reduced to 6 independent elements. Similarly, the strain tensor is reduced to 6 elements. From the symmetry of the stress and strain,

$$c_{ijkl} = c_{jikl}, \tag{2.2}$$

and

$$c_{ijkl} = c_{ijlk}. \tag{2.3}$$

Therefore, the stiffness tensor is reduced to 36 elements. The fact the 6x6 stiffness tensor is c_{ij} is symmetric means that there are 21 independent elastic constants. For simplicity, the stiffness tensor is represented in the Voigt notation, such that 11 is 1, 22 is 2, 33 is 3, 32 and 23 are 4, 31 and 13 are 5, 21 and 12 are 6. The fourth order tensor c_{ijkl} is represented by a second order tensor C_{ij}, where i and j are 1, 2, …, 6 (Thomsen, 1986).

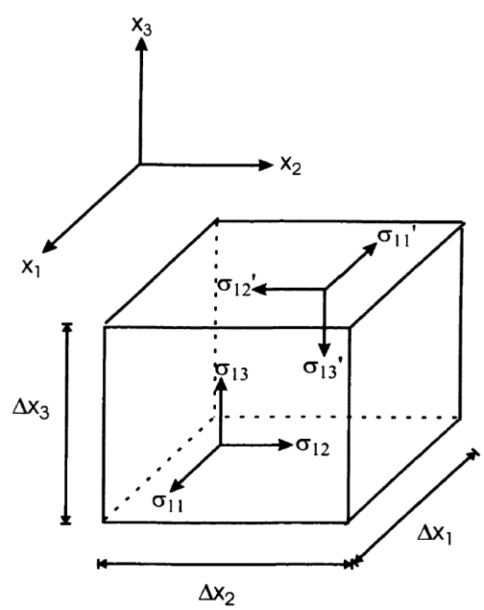

Figure 2.2 Components of stress tensor. σ_{ij} defines the stress exerted on the i face along the j direction (after Mah 1999)

To understand wave propagation in anisotropic media, consider how the wave equation is expressed using the stress-strain relation (Equation 2 .1). The wave equation is written in terms of displacement vector (**u**), force vector (**f**), density (ρ), and time (t).

Because the medium of propagation is anisotropic, the Laplace operator will be insufficient; instead, we use the Christoffel differential operator (Γ) is used (Auld, 1973)

$$\rho \frac{\partial^2 \mathbf{u}}{\partial t^2} = \quad \Gamma\, \mathbf{u} + \mathbf{f}, \tag{2.4}$$

where

$$\Gamma_{11} = C_{11}\frac{\partial^2}{\partial x_1^2} + C_{66}\frac{\partial^2}{\partial x_2^2} + C_{55}\frac{\partial^2}{\partial x_3^2} + C_{56}\frac{\partial^2}{\partial x_2 \partial x_3} + C_{15}\frac{\partial^2}{\partial x_1 \partial x_3} + C_{16}\frac{\partial^2}{\partial x_1 \partial x_2}, \tag{2.5}$$

$$\Gamma_{22} = C_{66}\frac{\partial^2}{\partial x_1^2} + C_{22}\frac{\partial^2}{\partial x_2^2} + C_{44}\frac{\partial^2}{\partial x_3^2} + C_{24}\frac{\partial^2}{\partial x_2 \partial x_3} + C_{46}\frac{\partial^2}{\partial x_1 \partial x_3} + C_{26}\frac{\partial^2}{\partial x_1 \partial x_2}, \tag{2.6}$$

$$\Gamma_{33} = C_{55}\frac{\partial^2}{\partial x_1^2} + C_{44}\frac{\partial^2}{\partial x_2^2} + C_{33}\frac{\partial^2}{\partial x_3^2} + C_{34}\frac{\partial^2}{\partial x_2 \partial x_3} + C_{35}\frac{\partial^2}{\partial x_1 \partial x_3} + C_{45}\frac{\partial^2}{\partial x_1 \partial x_2}, \tag{2.7}$$

$$\Gamma_{23} = C_{56}\frac{\partial^2}{\partial x_1^2} + C_{24}\frac{\partial^2}{\partial x_2^2} + C_{34}\frac{\partial^2}{\partial x_3^2} + (C_{44} + C_{23})\frac{\partial^2}{\partial x_2 \partial x_3} + (C_{36} + C_{45})\frac{\partial^2}{\partial x_1 \partial x_3} + (C_{25} + C_{46})\frac{\partial^2}{\partial x_1 \partial x_2}, \tag{2 .8}$$

$$\Gamma_{13} = C_{15}\frac{\partial^2}{\partial x_1^2} + C_{46}\frac{\partial^2}{\partial x_2^2} + C_{35}\frac{\partial^2}{\partial x_3^2} + (C_{45} + C_{36})\frac{\partial^2}{\partial x_2 \partial x_3} + (C_{13} + C_{55})\frac{\partial^2}{\partial x_1 \partial x_3} + (C_{14} + C_{56})\frac{\partial^2}{\partial x_1 \partial x_2}, \tag{2.9}$$

$$\Gamma_{12} = C_{16}\frac{\partial^2}{\partial x_1^2} + C_{26}\frac{\partial^2}{\partial x_2^2} + C_{45}\frac{\partial^2}{\partial x_3^2} + (C_{46} + C_{25})\frac{\partial^2}{\partial x_2 \partial x_3} + (C_{14} + C_{56})\frac{\partial^2}{\partial x_1 \partial x_3} + (C_{12} + C_{66})\frac{\partial^2}{\partial x_1 \partial x_2}. \tag{2.10}$$

For simplified classes of anisotropy, some of the terms in Christoffel differential operator in Equations (2.5)-(2.10) vanish because corresponding stiffness coefficients become zero. In the simplest case (isotropy), there are only two independent elements in the tensor (C_{ij}), so that stiffness coefficient tensor can be written in matrix form using only the Lamé parameters λ and μ (Musgrave 1970):

$$C_{ij} = \begin{bmatrix} \lambda+2\mu & \lambda & \lambda & 0 & 0 & 0 \\ \lambda & \lambda+2\mu & \lambda & 0 & 0 & 0 \\ \lambda & \lambda & \lambda+2\mu & 0 & 0 & 0 \\ 0 & 0 & 0 & \mu & 0 & 0 \\ 0 & 0 & 0 & 0 & \mu & 0 \\ 0 & 0 & 0 & 0 & 0 & \mu \end{bmatrix} \qquad (2.11)$$

Anisotropy can be classified according to symmetry. Transverse isotropy (TI) is the simplest and most commonly used by geophysicists type of anisotropy. Transverse isotropy, has only one axis of symmetry, and the stiffness coefficient tensor has only five independent elements. Transverse isotropy is classified into: Vertically-Transverse Isotropy (VTI), Horizontally-Transverse Isotropy (HTI), and Tilted-Transverse Isotropy (TTI). Figure 2.3 (top) shows the two types of TI symmetry: HTI and VTI. Required stiffness coefficients for such type of symmetry are discussed in **Chapter 4**.

Another classification of anisotropy, which is often used by geophysicists, is orthorhombic symmetry. Orthorhombic media have two orthogonal planes of symmetry, as shown by Figure 2.3 (bottom). The density-normalized stiffness coefficient tensor ($A_{ij} = C_{ij} / \rho$; where ρ is density) for an orthorhombic media has nine independent elements;

$$A_{ij} = \begin{bmatrix} A_{11} & A_{12} & A_{13} & 0 & 0 & 0 \\ A_{12} & A_{22} & A_{23} & 0 & 0 & 0 \\ A_{13} & A_{23} & A_{33} & 0 & 0 & 0 \\ 0 & 0 & 0 & A_{44} & 0 & 0 \\ 0 & 0 & 0 & 0 & A_{55} & 0 \\ 0 & 0 & 0 & 0 & 0 & A_{66} \end{bmatrix} \qquad (2.12)$$

(Vestrum, 1994). Other types of symmetry, such as cubic or monoclinic, are rarely used by geophysicists due to their complexity.

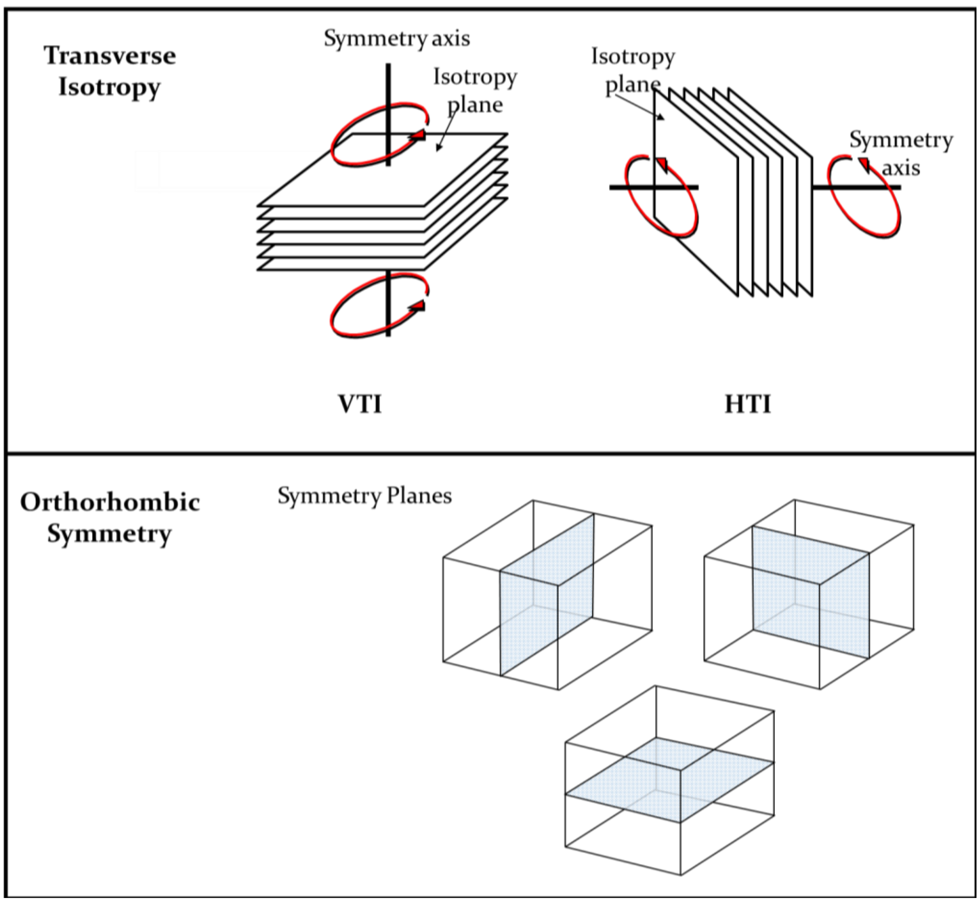

Figure 2.3 Common classes of symmetry used for seismic anisotropy. Transverse Isotropy (top): two types of transverse isotropy are displayed. VTI has vertical symmetry axis and HTI has horizontal symmetry axis. Orthorhombic Symmetry (bottom): two orthogonal planes of symmetry.

2.2 Fractures

Fractures in rocks cause seismic anisotropy by slowing down seismic waves traveling perpendicular to them and therefore changing the reflectivity along different directions of propagation. The next two sections discuss the methods used in this thesis to invert the effect of fractures on seismic for possible fracture properties. The effect of vertical fractures on pre-stack seismic data can be seen only by azimuthally variant data. The data requirement is discussed later in this Chapter, but first different models of fractures are reviewed:

- Schoenberg Linear Slip Theory: In this model, fractures are described as surfaces inside an isotropic background (Figure 2.4). Fractured rocks are parametrized in terms of compliances, where compliance is simply the inverse of stiffness (C_{ij}). Using compliances instead of stiffness coefficients enables representing the compliance of the fractured rock by adding the compliance of the isotropic background to the compliance of the fractures (Schoenberg, 1980).
- Hudson (Penny-Shaped Cracks) Model: In this model, fractures are considered as a single set of penny-shaped cracks, as shown in Figure 2.5. Fractured rocks are parametrized using three terms: crack density and aspect ratio (crack shape), and fluid term ($\boldsymbol{k}$) that represents the stiffening effect of the fluid content (Hudson, 1988).
- Thomsen-style model: This model is a rotated version of Thomsen (1986) model of VTI media (top left of Figure 2.3). This extension to HTI was preformed by Rüger (1996). Using this model, a fractured medium can be described using vertical P-wave velocity,

vertical S-wave velocity, and two Thomsen parameters, as described later in **Chapter 4**.

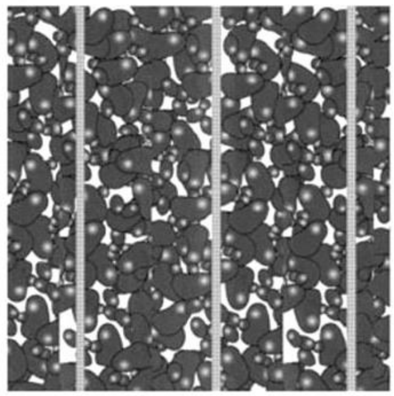

Figure 2.4 Schoenberg Linear Slip model (after Gurevich et al, 2009).

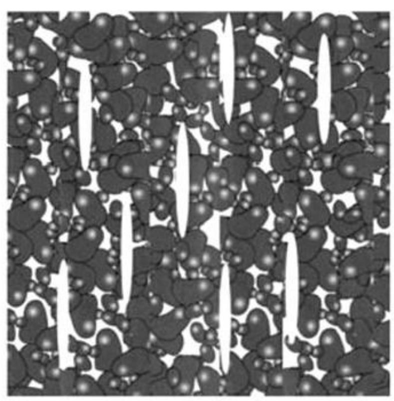

Figure 2.5 Hudson (Penny-Shaped Cracks) model (after Gurevich et al, 2009).

2.3 Amplitude variation with azimuth methods

The presence of fractures affects the P-wave and S-wave velocities by different magnitudes resulting in different reflection coefficients for different azimuths. Let's consider the case of an HTI reservoir overlain by an isotropic overburden. If the impedance of the reservoir is lower than above layer, the P wave traveling parallel to isotropy planes will have a lower reflectivity compared to waves traveling perpendicular to fractures because of the impedance contrast. For different offsets or angles, the gradient or rate of change varies azimuthally. Assuming Hudson's model, the magnitude of the anisotropic gradient is interpreted as direct indicator of fracture density. The most widely used method for AVAZ is the inversion of near-offset Rüger (1998) reflections as function of offset and azimuth for anisotropy parameters. For the case of isotropy, this method will reduce to Amplitude Variation with Angle (AVA) This method is discussed and used in **Chapter 4**, where a code is written and implemented to calculate theoretical amplitude variations using Rüger (1998) from an initial model and compare them to actual azimuthal variations. Then, an iterative nonlinear inversion is used to minimize the objective function. In **Chapter 6**, the code is modified to handle VSP geometry and used for offset VSPs.

There are other amplitude-based methods, such as Azimuthal Fourier Coefficients that rewrite the Rüger (1998) equation in the form of Fourier series (Downton et al., 2015). AVAZ has some shortcomings, such as the assumption of axis of symmetry being almost constant, and ambiguity in the estimated orientation of symmetry that is discussed later. Also, it measures the properties of interface rather than layers. On the other hand, it has its own advantage of higher resolution.

2.4 Travel time variation with azimuth methods

A key advantage of travel-time based methods is that they measure layer properties rather than interface or boundary properties. Compared to amplitude based methods, they have a higher accuracy but lower resolution as will be discussed in

Chapter 7. S-wave splitting is a travel-time and polarization based method that depends on a special phenomenon called S-wave birefringence (Delbecq et al., 2013), in which S-waves in anisotropic media split into two quasi-S types that propagate with different velocities. Detection of S-wave splitting requires multicomponent acquisition and processing, but can provide arguably the most accurate results among all travel time and amplitude methods. In Chapter 6, a four-component analysis is preformed to four-component VSP and S-wave fast and slow velocities along their directions are estimated.

Velocity variations with azimuth (VVAZ) use an elliptical NMO equation for azimuthal data rather than conventional NMO to invert for fast and slow RMS velocities. The fast direction most likely will indicate the fracture direction, while the ratio of the fast and slow velocities indicates the HTI anisotropy magnitude. In such a way, the cumulative influence up to target including overburden is estimated. Then, Dix (1955)-type interval properties can be estimated for single layers. In **Chapter 4**, this code was validated using physically modeled data, and then used on VVAZ effects observed on real seismic data to create maps of anisotropic intensity and orientation. Subsequently, the VVAZ code was modified and used put in offset VSPs workflow to produce the VVAZ results in **Chapter 6**.

2.5 Azimuthal analysis data requirements

In order to analyze VVAZ and AVAZ properly, 3D data with sufficient azimuthal and offset coverage must be available. In **Chapter 5**, its shown how the resolution matrix (Lay, 1996) in an inversion algorithm for travel times can be used to test for adequate geometry. Maximum usable offset in a real dataset may or may not conform with the requirements of the method. Also, fold is also an important factor. A fold of 9 may sound sufficient to fit an ellipsoid, but low signal-to-noise ratios (SNR) of real data and processing shortcomings would suggest VVAZ and AVAZ analysis is more robust if a much higher fold is used. The high spatial sampling of the land 3D datasets analyzed in this thesis enabled the use of 160 fold and higher.

Migration must be in the workflow for VVAZ and AVAZ analysis of real 3D data. It collapses the Fresnel zone and diffractions (Mosher et al.,1996), and it must be used to remove dip dependency from elliptical NMO velocity analysis (Grechka and Tsvankin, 1999). Pre-stack time migration (PSTM) generally is adequate for handling land data. However, the migration needs to preserve azimuthal variations.

There are two common ways for azimuthal preservations. The first is to sector the data prior to migration. Then, migration is applied to each azimuthal sector. Usually there will be variations between different azimuths and offsets, especially in the near offset. Walkarounds for this issue is trace borrowing and interpolation. The second method is Common Offset Vector binning prior to migration (Cary, 1999). For orthogonally acquired seismic data (source lines are perpendicular to receiver lines), the data can be binned into x-offset and y-offset directions, generating a series of single fold sub-volumes that contain almost same offset and azimuth. Each sub-volume is called Offset Vector Tile (OVT) gather. Migration is applied to each of these one-fold sub-volumes. COV binning can be confusing for seismic data processors and needs special quality control (QC). The number of input traces should be equal to the number of output traces (Downton, 2016).

2.6 The Altamont-Bluebell field

Altamont- Bluebell field is located in northeastern Utah in the Uinta basin. The Uinta basin is an asymmetric east-west trending basin with a south flank that slopes gently. The north flank is bounded by east-west trending Uinta Mountains. The Altamont-Bluebell field is located in the northern-central part of the basin, as can be seen by Figure 2.6 and Figure 2.6. The Altamont-bluebell field is unconventional in the sense that natural fractures act as storage and conduits in the tight sandstones and carbonates. The Bluebell field is the eastern portion of the Altamont-bluebell field. Its cumulative production is 336 MMBO, 588 BCFG, and 701 MMBW. The objective of the seismic survey is to identify density and direction of fractures to help in determining well spacing to existing wells needed to effectively drain the remaining hydrocarbon reserves in the Bluebell field, and to identify new drilling opportunities (Adams et. al, 2015).

The Altamont-Bluebell field extends to an area of 450 square miles, and the 3D seismic data covers an area of 36 square miles within the field. Most of the field is produced at one well per square mile, and more than a quarter of the wells are abandoned because of depletion of hydrocarbons and increasing production of water. Petrophysical properties, facies changes, and fluid pressure influence the quality of reservoir, but their influence can not be quantified, while fractures and clay content affect the permeability of reservoirs the most. Hydrocarbon production is mostly from sandstone beds, and partially from shale and carbonate beds. The Paleocene- and Eocene-age Upper Green River, Lower Green River, and Wasatch (Colton) formations are the main hydrocarbon producers in the field (Lynn et al., 1995; Morgan et al., 2003). Figure 2.8 shows the main targets within the Uinta basin and the Altamont-Bluebell field, while the stratigraphic column is shown in Figure 2.9.

The strata were deposited in lacustrine and alluvial environments. The Upper Green River formation was deposited in open-lacustrine and most of the kerogen is immature. Gas may be migrated from deeper formations. The Lower Green River formation was deposited in marginal and open lacustrine. Open and marginal lacustrine corresponds respectively to center and margin of lake deposition. The kerogen-rich shale and marlstone are the sources of oil. Lastly, the Wasatch formation is alluvial and its source of oil is the Kerogen-rich shale. It is a highly overpressured reservoir because of hydrocarbon generation. The hydrocarbon generation in the deep Wasatch/Colton formation is the main cause for natural fractures. Natural fractures in the shallower Green River reservoirs are tectonically induced (Morgan et al., 2003).

The local and regional stress at the Altamont-Bluebell field were estimated using different sources. The borehole breakout data indicates Northwest-Southeast orientation of maximum horizontal direction (Lynn et al., 1999). Regional stress studies by Zoback and Zoback (1990) indicates that the northern Colorado Plateu, Uinta basin, has North-South/Northwest-Southeast trends of maximum horizontal stress directions. Gilsonite veins, interpreted as occurring in the direction of pales stress in Cenozoic time, the age of the targets, occur in long veins that trends Northwest-Southeast in outcrops near the field (Fouchet et al., 1992). In summary, the geological and stress observations suggest that there are two major trends of fractures, within the target formations. They are Northwest-Southeast and Northeast-Southwest trends (Bates et al., 1997). Of those two, the Northwest-Southeast is more dominant as summarized by Table 2.1. Those observations were found to be in agreement with our results from the seismic azimuthal analysis discussed later in this thesis.

Information Type	Azimuth of Dominant Fracture Direction	Location (Depth of Information)	Azimuth of Other Fracture Directions	Location or Depth of Information
Field exposure mapping of near vertical fractures	N20–40W	0 m (surface)	N60-70E	Surface
Well log, FMS*	N20–30W	2000–3320 m	East-west	>3320 m
Well log, borehole breakout	Northeast, minimum horizontal stress N45–30W	2030–2140 m	N30W-N10E	>3320 m
Regional stress, Gilsonite veins		0 m (surface)		
Regional stress (Zobak and Zobak, 1991)	N30W, maximum horizontal compression	0 m (surface)		
Regional stress; earthquake focus 35 mi west	N10–20W, maximum horizontal compression	20,000 ft focus		

*FMS = Formation Microscanner™.

Table 2.1 Fracture azimuth observations from geological and stress observations (Bates et al., 1997)

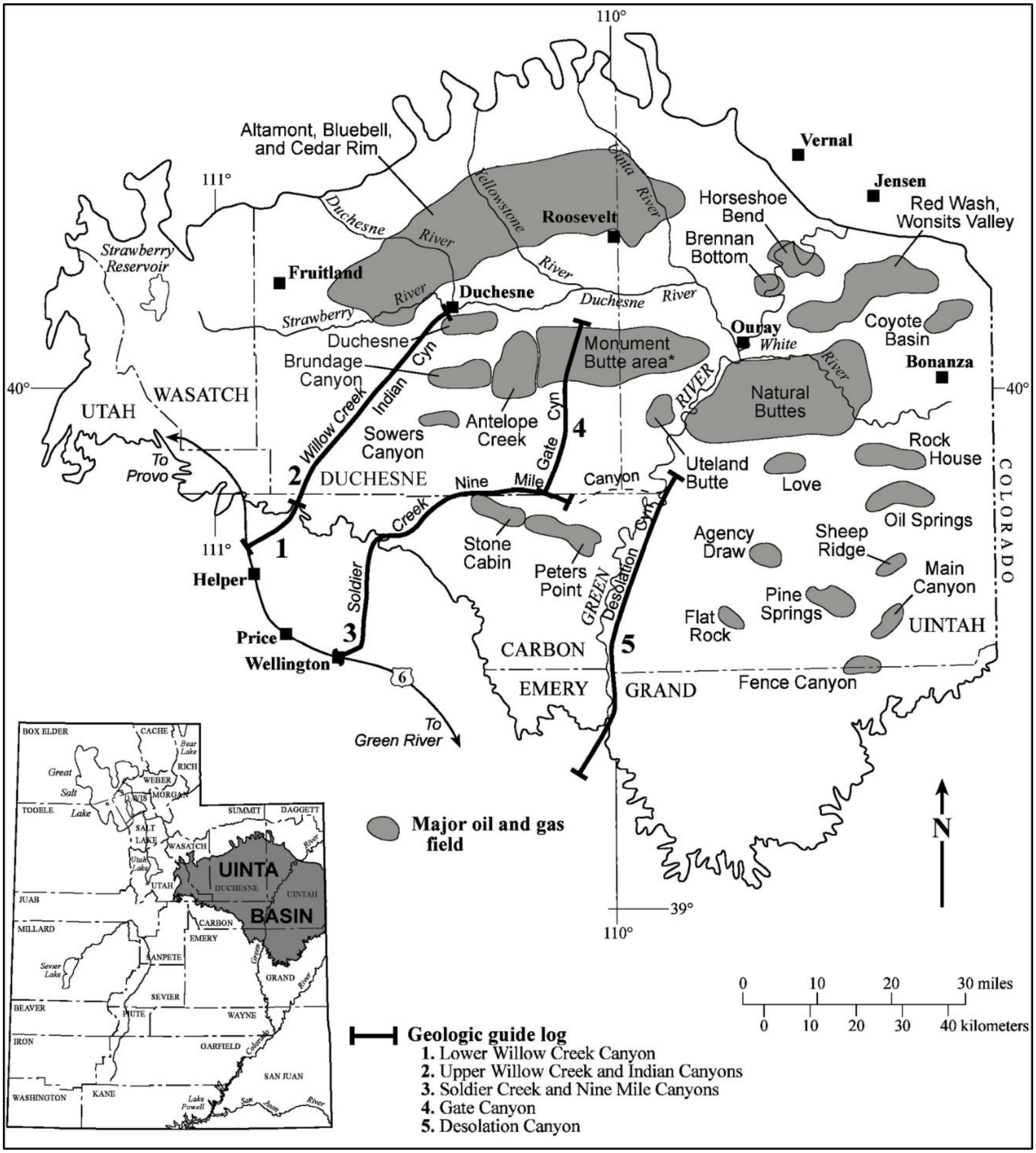

Figure 2.6 Location of Uinta basin, Utah (bottom left) and major oil and gas fields within Uinta basin (after Morgan, 2003).

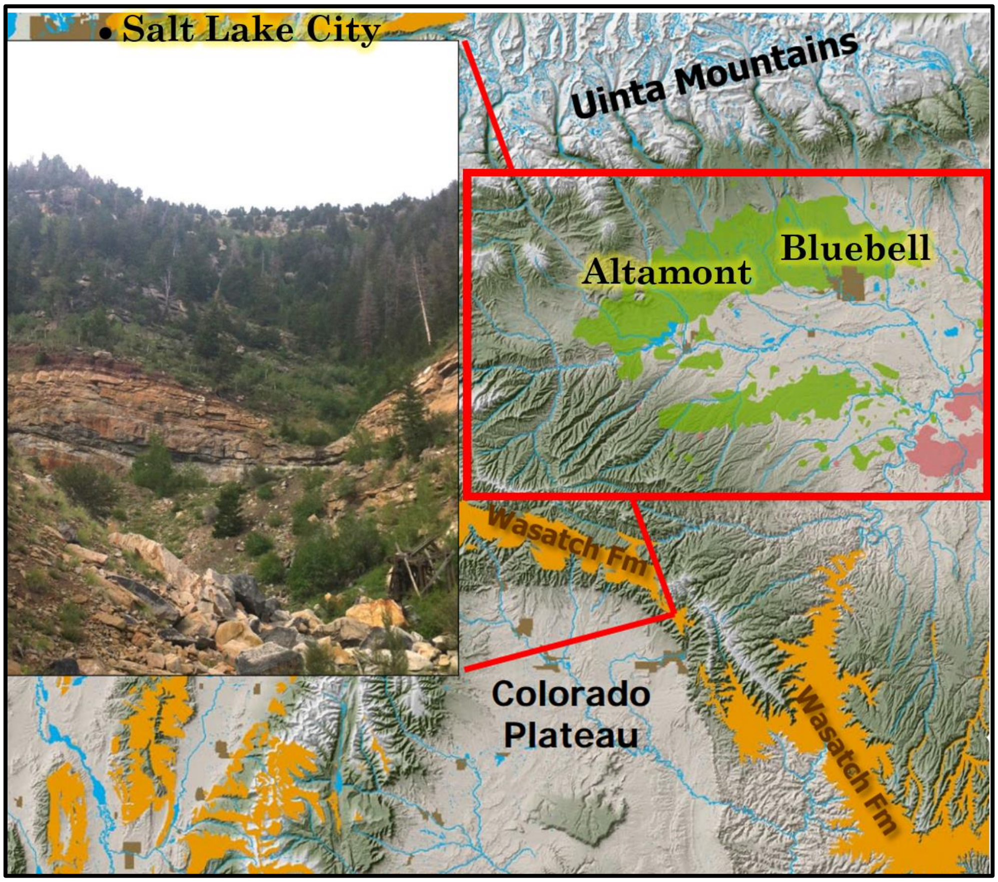

Figure 2.7 Altamont-Bluebell field to the south east of Salt Lake City, Utah. The Bluebell field is the eastern portion of the field. An outcrop photo of Wasatch formation is shown to the left (after Roseink and Anderson, 2013).

In this research, we will focus on two targets. First is the most prolific oil reservoir which a section Wasatch called **Wasatch-180**. Second is the shallowest reservoir, which is the gas reservoir from the top of **Upper Green River** Formation to the Mahogany Bench marker. Mahogany Bench is the strongest seismic reflector in the data. Most of the hydrocarbon production is in sandstone. 1613′ of core were analysed for lithology, clay content, permeability, and fractures by Wenger (1996) and Wenger and Morris (1996) within Altamont-Bluebell field. Sandstone was found to be highly fractured (Morgan et al., 2003), as shown by Figure 2.10.

2.7 Summary

This chapter sets this research by providing a brief background about seismic anisotropy and fractures by explaining the theory behind stiffness tensor in terms of elasticity and propagation and also introduces the amplitude- and travel time- based methods that can be useful in detecting azimuthal anisotropy. It also reviews the geology and targets of the Altamont-Bluebell field in order to be used in this research for azimuthal analysis techniques.

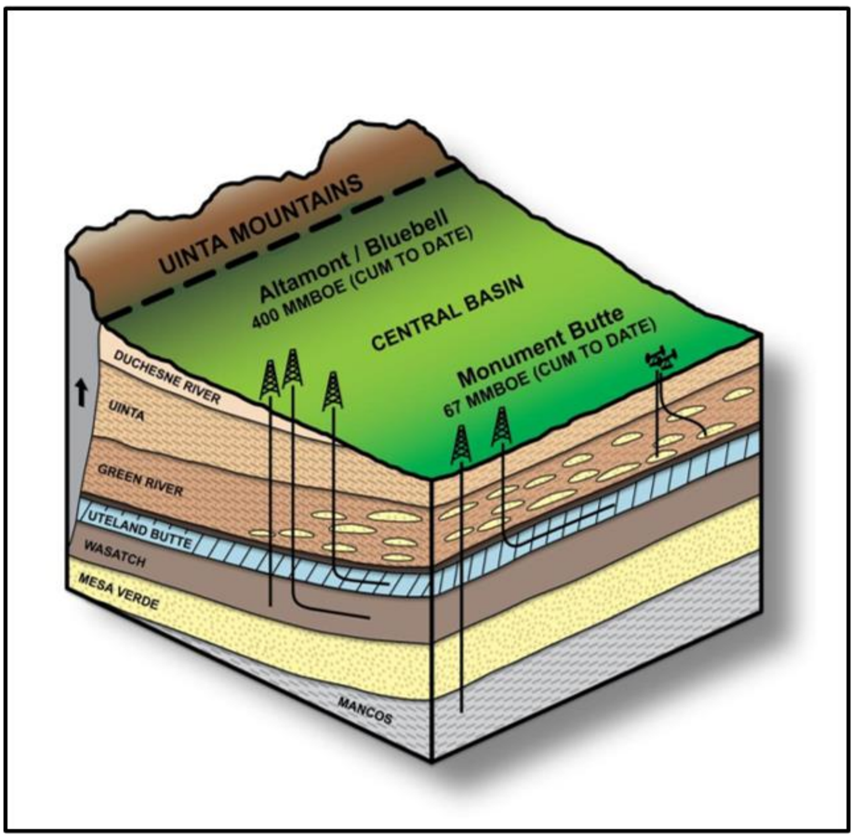

Figure 2.8 Uinta Basin, Utah. Altamont-Bluebell field is the northern central part of the basin, and the Bluebell field is the eastern part of Altamont-Bluebell Field. Three main targets are: Upper Green River, Lower Green River (Uteland Butte and Castle Peak), and Wastach formations. Courtesy of: Newfield Exploration Company.

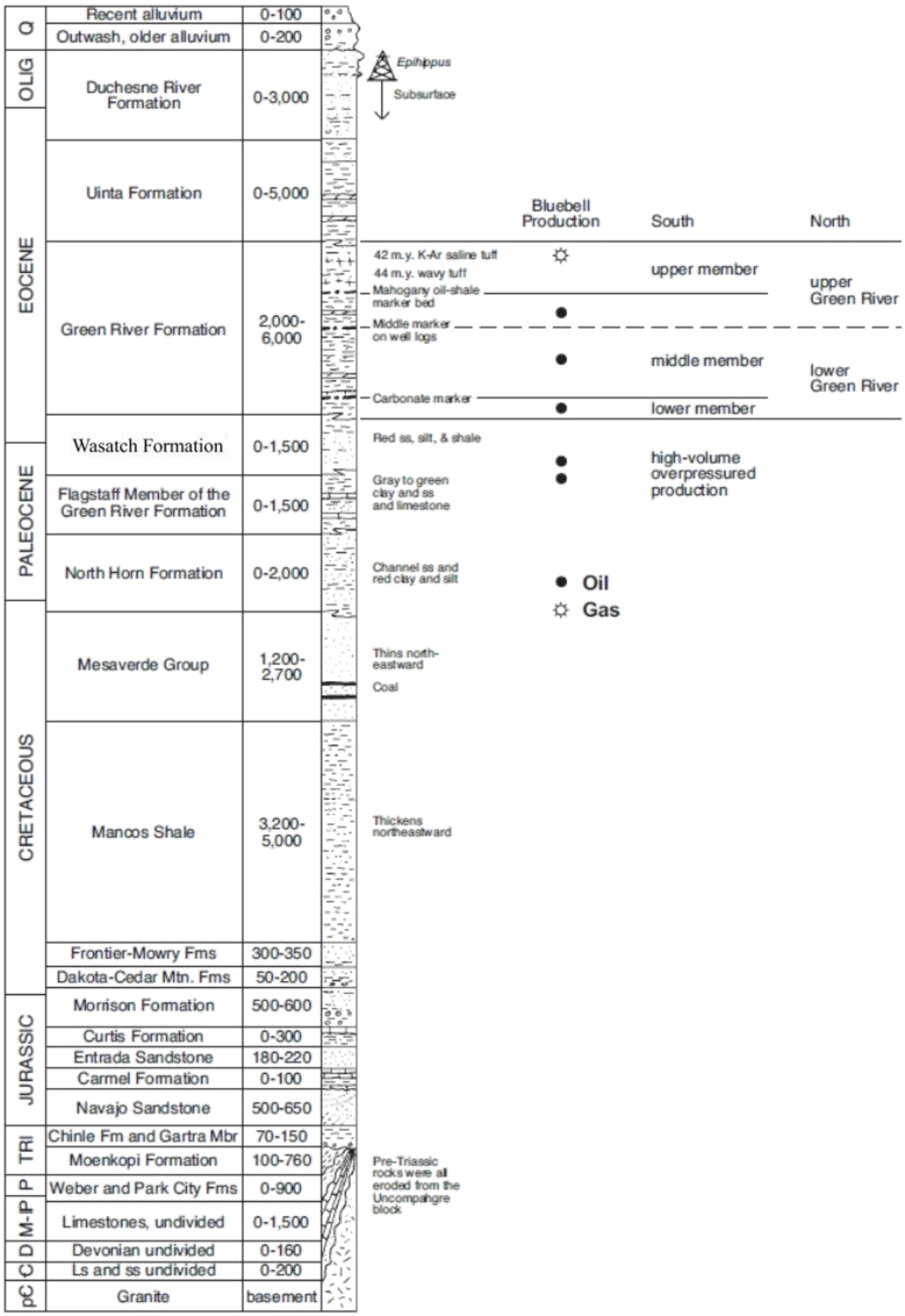

Figure 2.9 Stratigraphic column of the Uinta Basin (modified from Hintze, 1988).

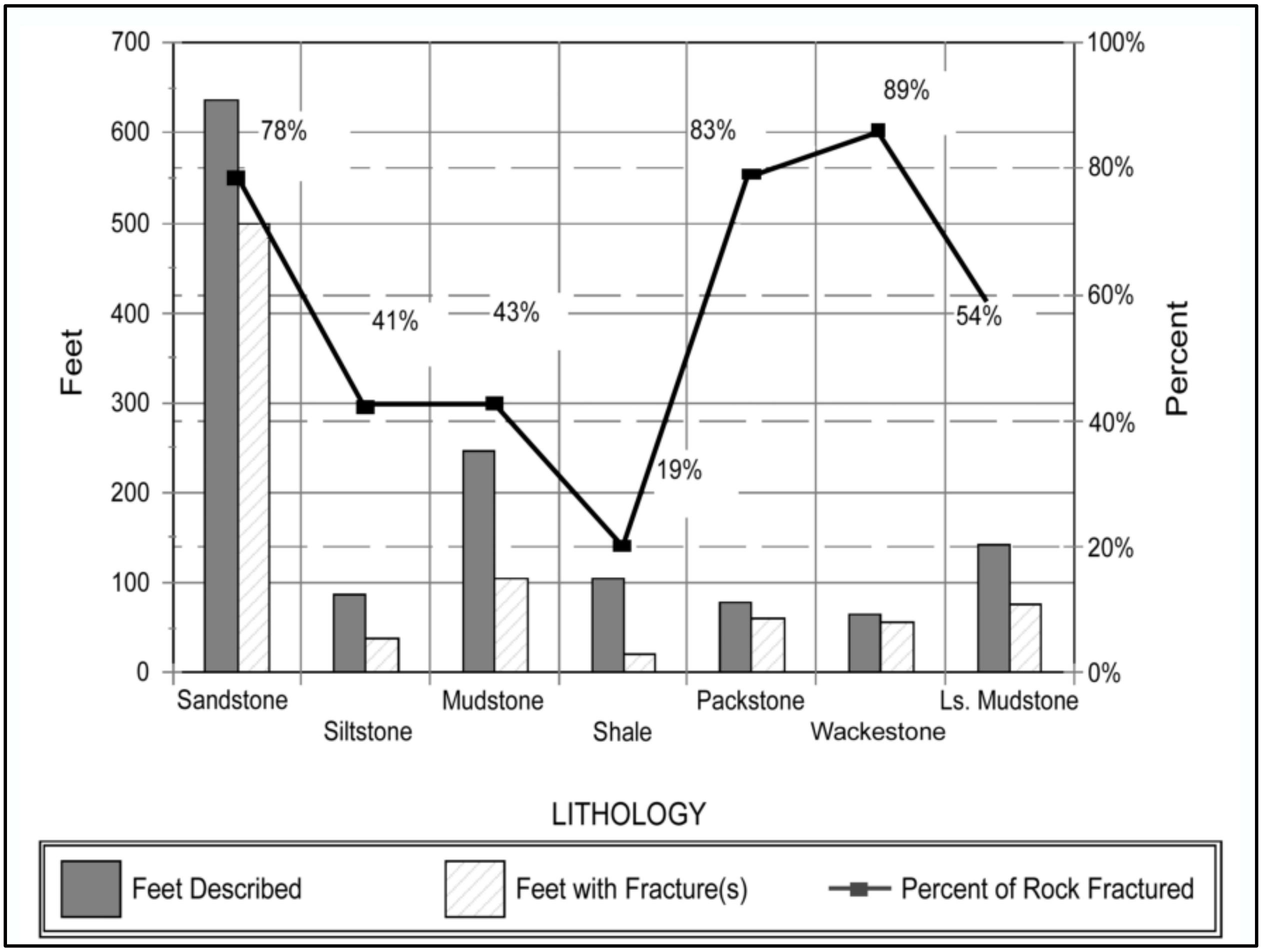

Figure 2.10 Fracture percentage per lithology based on 1613′ of core in the Altamont-Bluebell field (after Morgan et. al., 2003).

Chapter 3 A Physical Modelling Experiment for Azimuthal Anisotropy Investigations

In the physical modeling laboratory, a fractured reservoir overlain by isotropic overburden can be represented by two layers: an anisotropic material (Phenolic) lying under an isotropic material (acrylic-Plexiglas). The two layers are coupled by glue that may influence the results. Because azimuthal anisotropy is of interest to us, we want to acquire gathers of common offset and varying azimuthal angles. In such a way, fracture orientation can be predicted from azimuthal analysis of P-wave first arrival times. Also, it can be predicted by S-wave splitting because the polarization direction of fast S wave indicates directly the orientation of fractures (Winterstein, 1992). Regularly, a four-component horizontal rotation (i.e. Alford rotation) is needed to separate the fast S wave from the slow S wave. Azimuthal common-offset receiver gathers have a wide range of azimuth angles but a limited range of angles of incidence. Shots are distributed along a circle covering 360^{o} azimuth. Therefore, they are ideal for Horizontally-Transverse Isotropy (HTI) media. In this study, common azimuth shot gathers were also collected and analyzed. Such gathers are ideal for Vertically-Transverse Isotropy (VTI) media. Two datasets were acquired over different models for this thesis:

1. Three circular common-receiver gathers with scaled radii equal to 250 m, 500 m and 1000 m were acquired over a 2-layer model. In that dataset, a 3-C receiver and a 3-C source yield produce 9-C receiver gathers.

2. One circular gather, which has a 700-m scaled radius, and two linear gathers with 0^{o} and 90^{o} azimuths respectively were acquired over the anisotropic

medium. In that dataset, a 3-component receiver and a 2-component horizontal source resulted in 6-component shot gathers.

3.1 Physical modeling

A physical model was constructed to represent a vertically fractured reservoir overlain by an isotropic overburden, as shown in Figure 4. Laminated phenolic material with laminations oriented vertically to simulate fractures was used to represent the reservoir with vertical fractures. The Phenolic layer representing the vertically-fractured reservoir exhibits HTI anisotropy, or more precisely, mainly HTI and slightly orthorhombic anisotropy (Cheadle et al., 1991; Mahmoudian, 2013). For VTI or HTI anisotropy, Phenolic material can be used. Vertically laminated sheets of linen fabric bonded with Phenolic resin compose the Phenolic HTI medium (Figure 3.1) with the laminations simulating fractures.

Figure 3.1 A physical model consisting of a Phenolic layer under a Plexiglas layer, and representing a fractured reservoir overlain by isotropic overburden. Laboratory to field scale is 1:10,000 in both length and time. Scaled thicknesses of Plexiglas and Phenolic layers are 480 m and 450 m respectively.

In the Phenolic medium, the P wave is fastest (3570 m/s) along the vertical laminations, slowest (2900 m/s) perpendicular to the vertical lamination, and somewhere in between along other directions. On the other hand, the S wave is fastest (1700 m/s) along the vertical laminations when particle motion is vertical. and slower (1520 m/s) perpendicular to the vertical lamination when particle motion is vertical, and undergoes S-wave splitting in other directions. Plexiglas, an isotropic plastic material, was used to represent an isotropic overburden. P-wave and S-wave velocities in the isotropic medium are 2745 m/s and 1520 m/s respectively. Properties of Phenolic and Plexiglas are summarized in Table 3.1 (Mahmoudian, 2013).

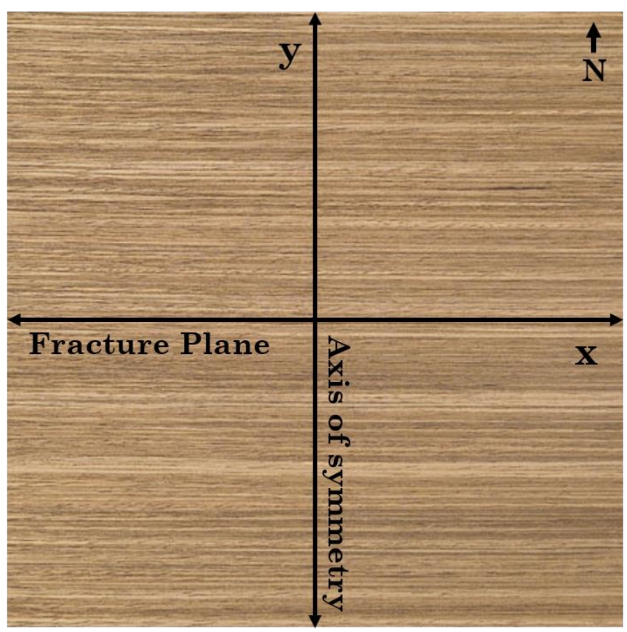

Figure 3.2 An expanded view of laminated Phenolic layer. Lamination direction is along the x-axis and represents the reservoir fracture plane. Axis of symmetry is along the y-axis.

	P-wave velocity (m/s)	S-wave velocity (m/s)	Density (g/cc)
Plexiglas	2745	1380	1.19
Phenolic	3570/2900	1700/1520	1.39

Table 3.1 Velocities and densities of Plexiglas and Phenolic.

As previously mentioned, the laboratory to field scale is 1: 10,000 in both length and time. Scaled thicknesses of Plexiglas and Phenolic layers are 480 m and 450 m respectively. These physically-modeled data are used later for VVAZ analysis in **Chapter 5**. The acquisition layout for the first dataset is illustrated in Figure 3.3. A single receiver transducer was placed at the center of the bottom surface of the Phenolic layer. This receiver location projected to the top surface served as the center of concentric circles on the top surface. For each circle of radius (r), 90 source locations were distributed on the circumference at 4^{o} intervals. Three receiver gathers were acquired with $\boldsymbol{r}$ = 250 m, 500 m and 1000 m. 3-C receiver and 3-C source yield into 9-component receiver gathers.

For the second dataset, one circular gather which has 700 m radius and two linear gathers with 0^{o} and 90^{o} azimuths were acquired over the Phenolic medium. 3-component receiver and 2-component horizontal source produced 6-component shot gathers. The acquisition layout of the second dataset is described in Figure 3.4.

Contact transducers were used as P-wave and S-wave sources and receivers. P-wave transducers have a central frequency at 2.38 MHz, while S-wave transducers have central frequency at 5.82 MHz. At each station (source/receiver), three transducers were used; one for the vertical component and two for the horizontal components along x- and y-axes. Source and receiver transducers were positioned with a robotic system that has an error of less than 0.1 mm in laboratory scale, which is equivalent to 1 m in field scale

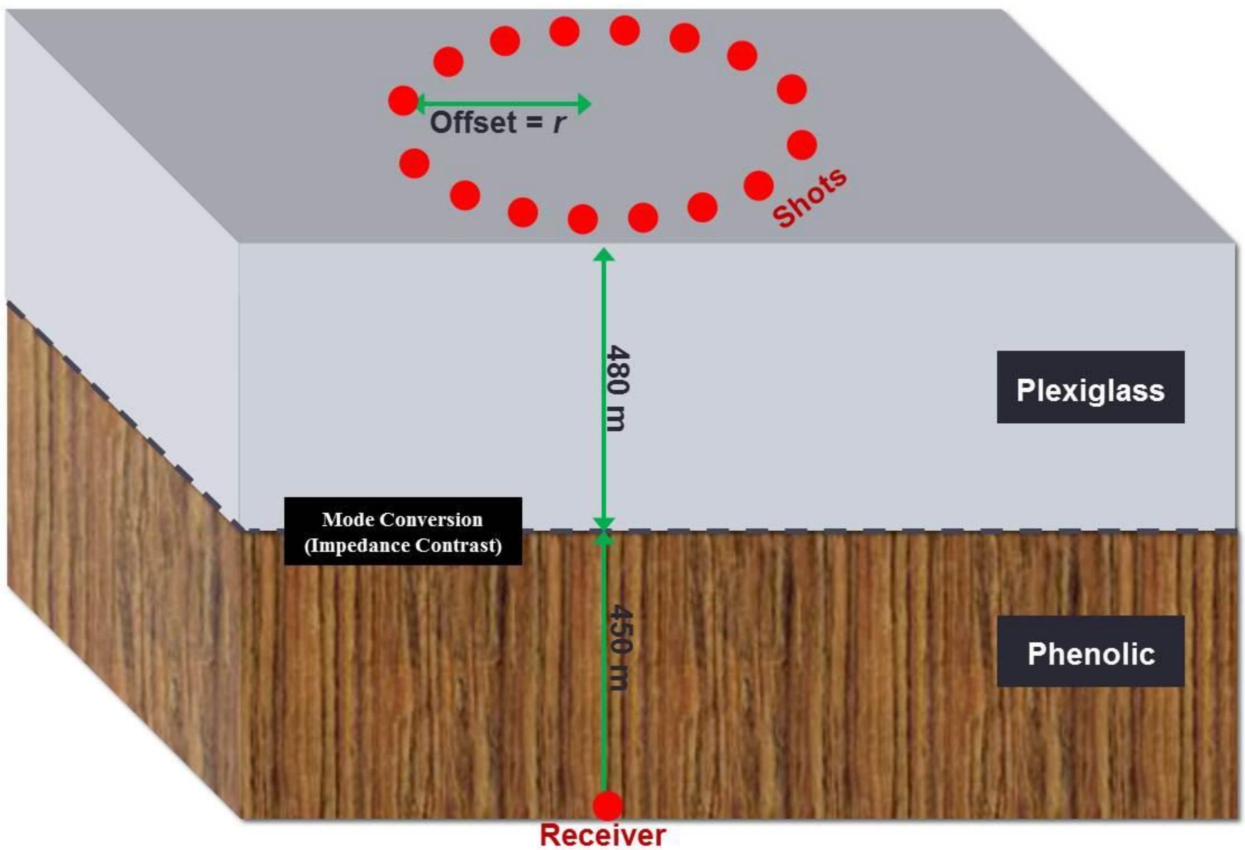

Figure 3.3 Acquisition layout for first dataset. One receiver is located at the bottom of the Phenolic layer and centered at the middle of its surface. 90 shot locations are distributed along a circle of radius (***r***) and separated by 4^{o}. Three receiver gathers are acquired with r = 250 m, 500 m and 1000 m. 3-C receiver and 3-C source yield 9-C receiver gathers.

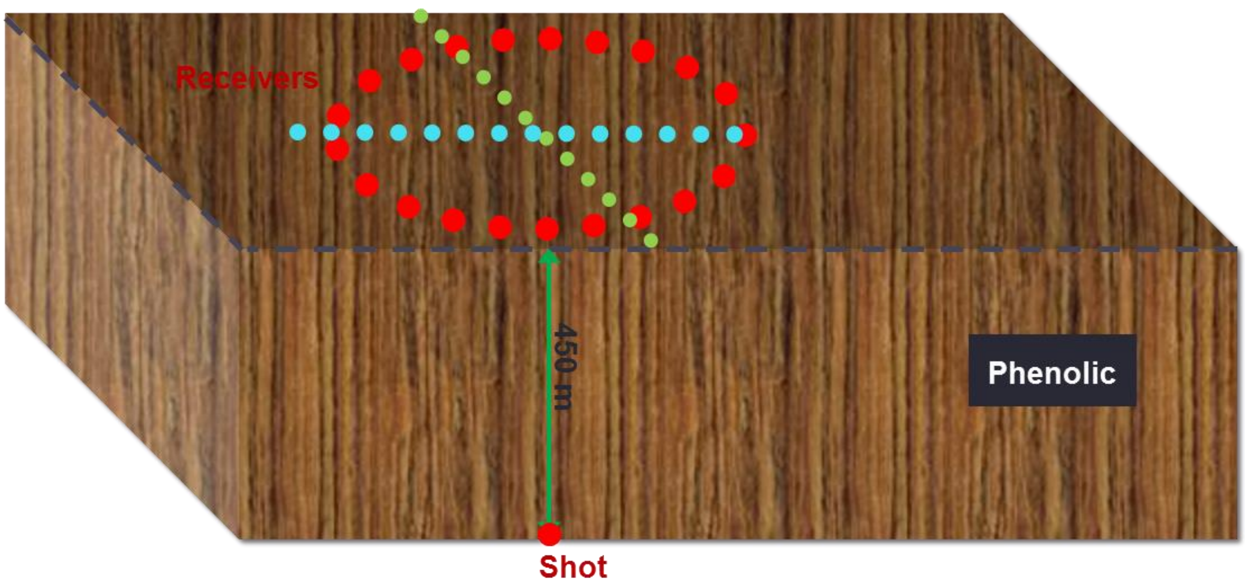

Figure 3.4 Acquisition layout for second dataset. One shot is located at the bottom of the Phenolic layer and centered at the middle of its surface. For the first common-shot gather, 90 receiver locations are distributed along a circle of radius equal to 700 m (field scale) and separated by 4^{o}. Receivers are distributed along a line with azimuth equal to 0^{o} (indicated by blue circles) and 90^{o} (indicated by green circles) for the second and third common-shot gathers respectively. 3-C receiver and 2-C horizontal source yield 6-C shot gathers.

3.2 P-wave first-arrival times analysis using first dataset

Three common-receiver gathers at r = 250 m, 500 m and 1000 m are shown in Figure 3.5, Figure 3.6, and Figure 3.7. Each gather (V_{ij}) is composed of 9 components. The first subscript of V denotes the receiver component, while the second subscript denotes the source component. The x-, y-, and z-components are labeled by the numbers 1, 2, and 3 respectively. For example, V_{31} was acquired with a vertical receiver due to a source along the x-axis.

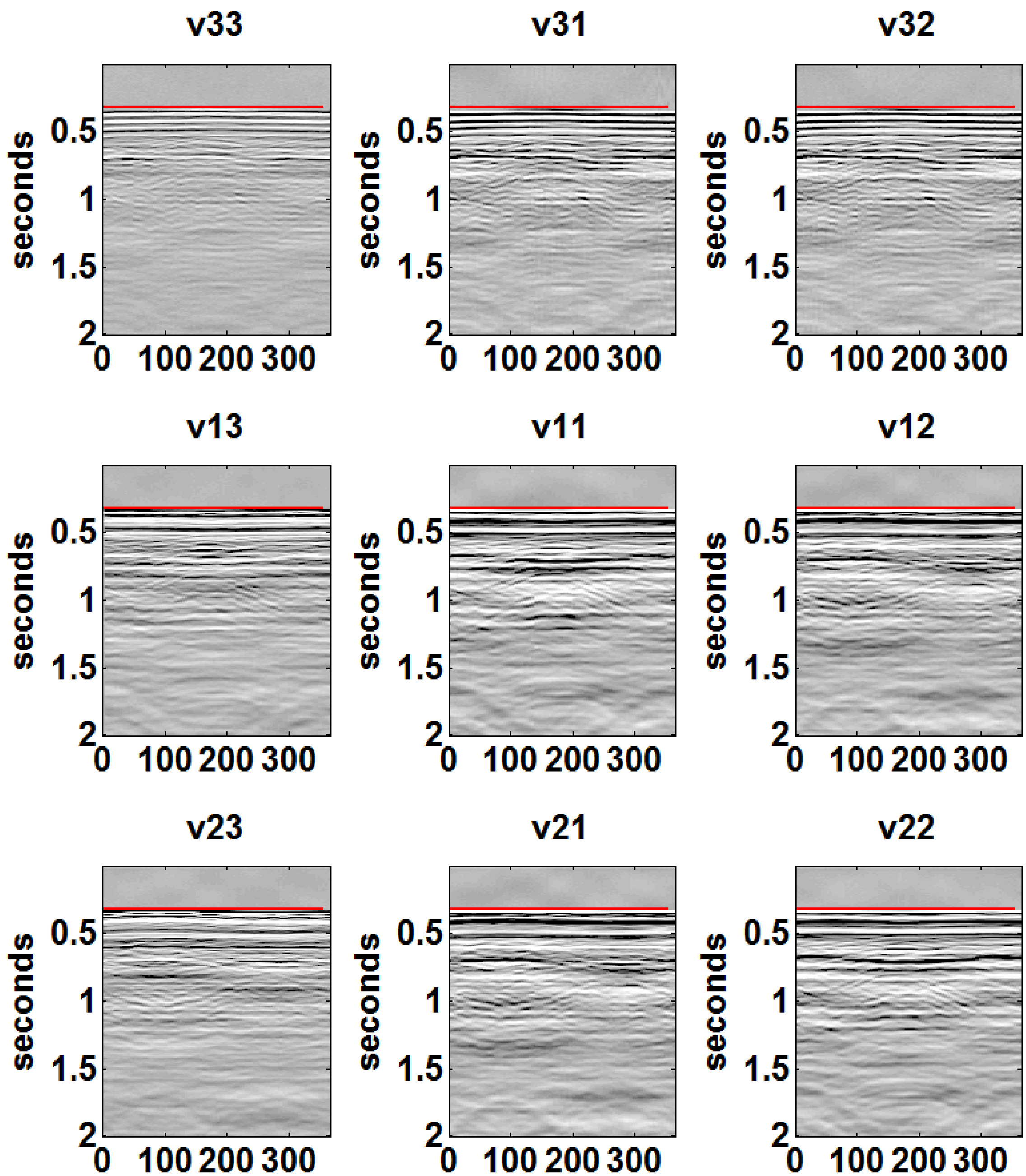

Figure 3.5 9-C receiver gather with $\boldsymbol{r}$ = 250 m. P-wave first arrival times are indicated by red. The horizontal axis is the azimuth angles which go from 0^{o} to 360^{o} with a 4^{o} increment. Frist P-wave arrival times are indicated by red.

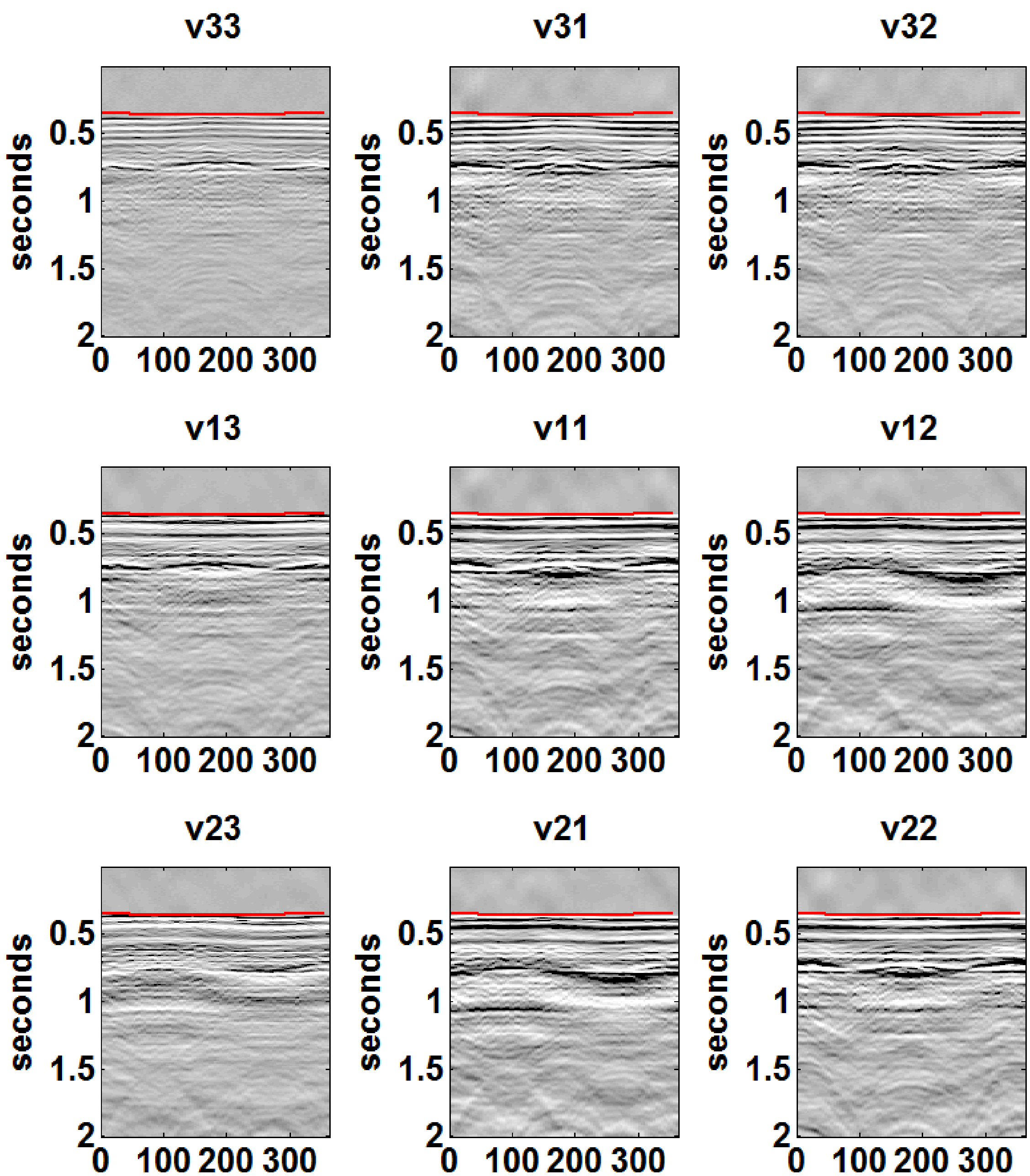

Figure 3.6 9-C receiver gather with $\boldsymbol{r}$ = 500 m. P-wave first arrival times are indicated by red. The horizontal axis is the azimuth angles which go from 0o to 360o with a 4o increment. Frist P-wave arrival times are indicated by red.

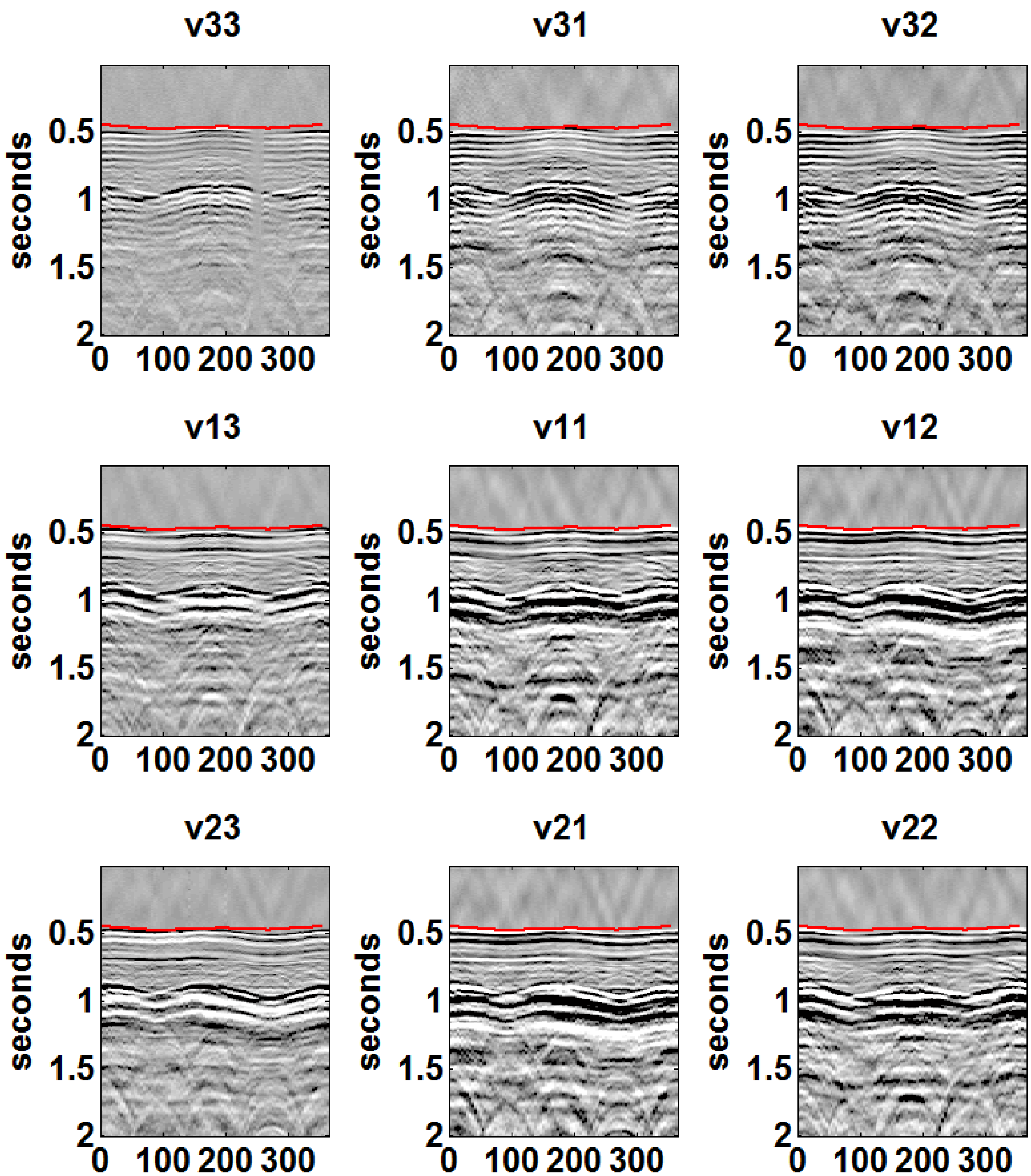

Figure 3.7 9-C receiver gather with $\boldsymbol{r}$ = 1000 m. P-wave first arrival times are indicated by red. The horizontal axis is the azimuth angles which go from 0^o to 360^o with a 4^o increment. Frist P-wave arrival times are indicated by red.

The three common-receiver gathers in Figure 3.5, Figure 3.6, Figure 3.7 and are plotted with the same amplitude range. Azimuth varies from 0^o to 360^o with an increment of 4^o for the 1^{st} to the 90th trace. First arrival times were picked on first onset and indicated by red. The 250-m and 500-m common-receiver gathers show nearly constant first-arrival times with increasing azimuth angle. The 1000-m common-receiver gather shows a sinusoidal variation of first arrival times with increasing azimuth angle. Even more obvious is the S-wave event at about 1 second. Both P-wave and S-wave fast directions are along the Phenolic lamination planes. The acquisition layout suggests that components v_{11} of the three gathers in Figure 3.5, Figure 3.6, and Figure 3.7 are acquired with horizontal receivers and sources whose polarization directions are along the x-axis (or parallel to fracture plane). Similarly, v_{22} components have transducer polarization perpendicular to fracture plane.

In isotropic media, P-wave first-arrival times are constant for the same offset and different azimuths. Each common-receiver gather in Figure 3.5, Figure 3.6, and Figure 3.7 has a constant offset. Figure 3.7 shows first-arrival times that vary with azimuth angle and look like a sinusoidal function. Early first arrivals are at 0^o, 180^o, and 360^o. Those angles define the fast P-wave direction which is parallel to the fracture plane. This result is in agreement with the physical model where fracture plane within the Phenolic is along x-axis, as can be seen by Figure 3.2. In Figure 3.5 and Figure 3.6Figure 3.9, it is hard to see sinusoidal first-arrival times.

If plotted azimuthally in a polar view, sinusoidal first-arrival times appear as an ellipse. The minor axis of the ellipse indicates early first-arrival times, while the major axis indicates late first-arrival times. Therefore, the minor axis indicates the fracture plane (Al Dulaijan et al., 2012). For each common-receiver gather, first-arrival times are plotted azimuthally in a polar view. Then by least-squares fitting, an ellipse is fitted. Figure 3.8, Figure 3.9, and Figure 3.10 show elliptical fitting of first-arrival times for each gather. The minor axis for the first and second gather (Figure 3.8 and Figure 3.9) is at 5°. The minor axis for the third gather is 1° (Figure 3.10). The minor axes indicate the fracture plane which is supposed to be 0° (along x-axis) according to the physical model (Figure 3.2). The first and second common-receiver gathers have a smaller offset than the third gather, and therefore are more sensitive to acquisition inaccuracies.

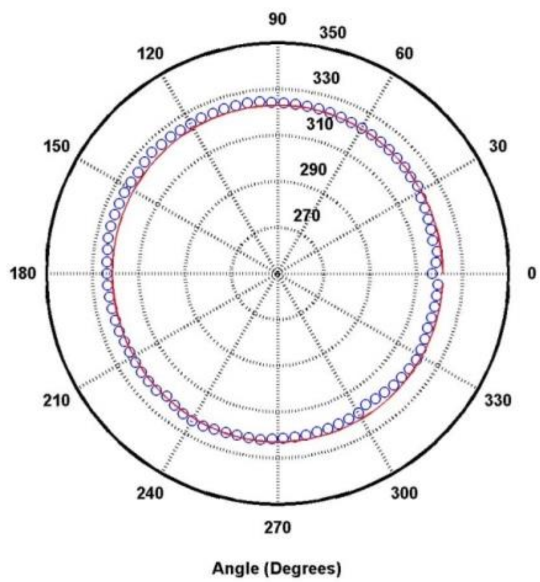

Figure 3.8 Elliptical fitting of first-arrival times for the 1st receiver gather ($\boldsymbol{r}$ = 250 m). The minor axis is at 5^0. Small blue circles are observed times; red lines are fitted ellipses.

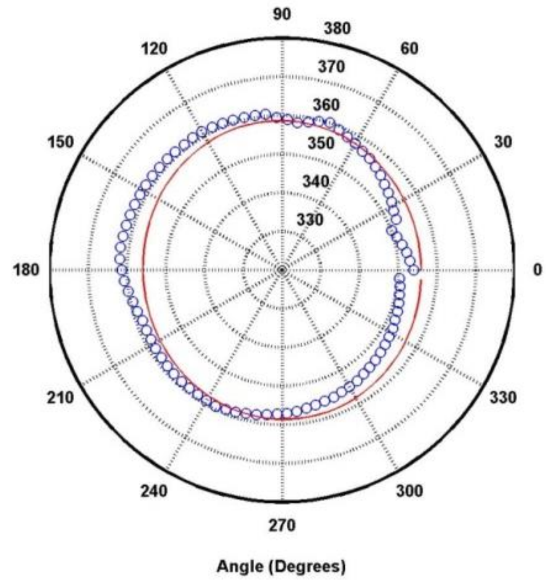

Figure 3.9 Elliptical fitting of first-arrival times for the 2nd receiver gather (r = 500 m). The minor axis is at 5^0. Small blue circles are observed times; red lines are fitted ellipses.

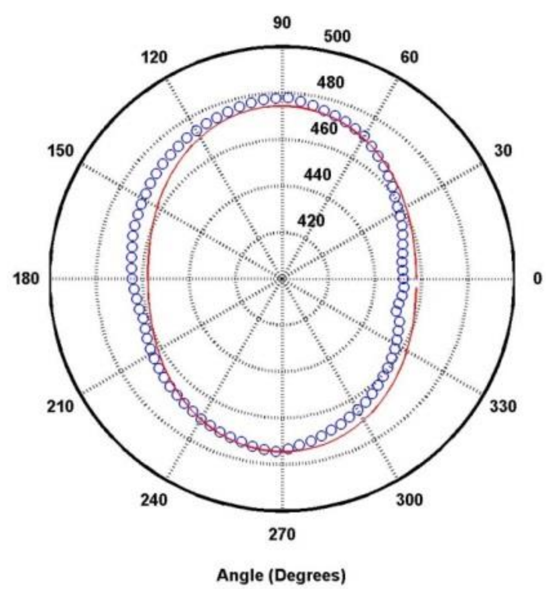

Figure 3.10 Elliptical fitting of first-arrival times for the 3rd receiver gather (r = 1,000 m). The minor axis is at 1^0. Small blue circles are observed times; red lines are fitted ellipses.

3.3 Estimation of elastic stiffness coefficients using second dataset

In anisotropic media, phase and group velocities are not generally equal, except along the directions of symmetry axes and symmetry planes. Group velocities at different angles of incidence (θ) and azimuthal angles (Φ) can be easily measured in laboratory, as well in field. For orthorhombic media, Daley and Krebes (2006) have derived a relation between the P group velocity (V) and the density-normalized stiffness coefficients (A_{ij}):

$$\frac{1}{V^2(\vec{N})} \approx \frac{N_1^2}{A_{11}} + \frac{N_2^2}{A_{22}} + \frac{N_3^2}{A_{33}} - \frac{E_{23}N_2^2N_3^2}{A_{22}A_{33}} - \frac{E_{13}N_1^2N_3^2}{A_{11}A_{33}} - \frac{E_{12}N_1^2N_2^2}{A_{11}A_{22}} \tag{3.1}$$

where

$$\vec{N} = (N_1, N_2, N_3) \tag{3.2}$$

$$N_1 = \sin(\theta)\cos(\phi) \tag{3.3}$$

$$N_2 = \sin(\theta)\sin(\phi) \tag{3.4}$$

$$N_3 = \cos(\phi) \tag{3.5}$$

$$E_{23} = 2(A_{23} + 2A_{44}) - (A_{22} + A_{33}) \tag{3.6}$$

$$E_{13} = 2(A_{13} + 2A_{55}) - (A_{11} + A_{33}) \tag{3.7}$$

and

$$E_{12} = 2(A_{12} + 2A_{66}) - (A_{11} + A_{22}) \tag{3.8}$$

In the Phenolic medium, A_{11}, A_{22}, A_{33}, A_{44}, A_{55}, and A_{66} can be measured by estimating body wave (P and S) group velocities (V_{ij}) propagating along the x_j-axis and polarized along the x_i-axis as follows:

$$A_{11} = V_{11}^2 \tag{3.9}$$

$$A_{22} = V_{22}^2 \tag{3.10}$$

$$A_{33} = V_{33}^2 \tag{3.11}$$

$$A_{44} = V_{23}^2 = V_{32}^2 \tag{3.12}$$

$$A_{55} = V_{13}^2 = V_{31}^2 \tag{3.13}$$

$$A_{66} = V_{12}^2 = V_{21}^2 \tag{3.14}$$

In the laboratory, $\sqrt{A_{44}}$, $\sqrt{A_{55}}$, and $\sqrt{A_{66}}$ were measured. $\sqrt{A_{33}}$ was measured too, but was assumed unknown in the inversion in order to use it to validate the results. Five stiffness coefficients (A_{11}, A_{22}, A_{33}, A_{12}, A_{13}, and A_{23}) are determined from the inversion. For the inversion the second dataset was chosen, which has the acquisition explained by Figure 3.4 and Figure 3.11. That dataset consists of 3 common-shot gathers: one circular that has 700 m radius; and two linear at 0° and 90° azimuths. First P-wave arrival times (indicated by red on Figure 3.12) are picked and used to calculate P group velocities by dividing distance between source and receiver over the time. Angles of incidence (θ) and azimuthal angles (Φ) are calculated by trigonometric functions and shown in Figure 3.13. The circular gather has a wide range of azimuthal angles and a single angle of incidence that is approximately 24°. The line gathers have a single azimuthal angle 0° or 90° and a wide range of incidence angles.

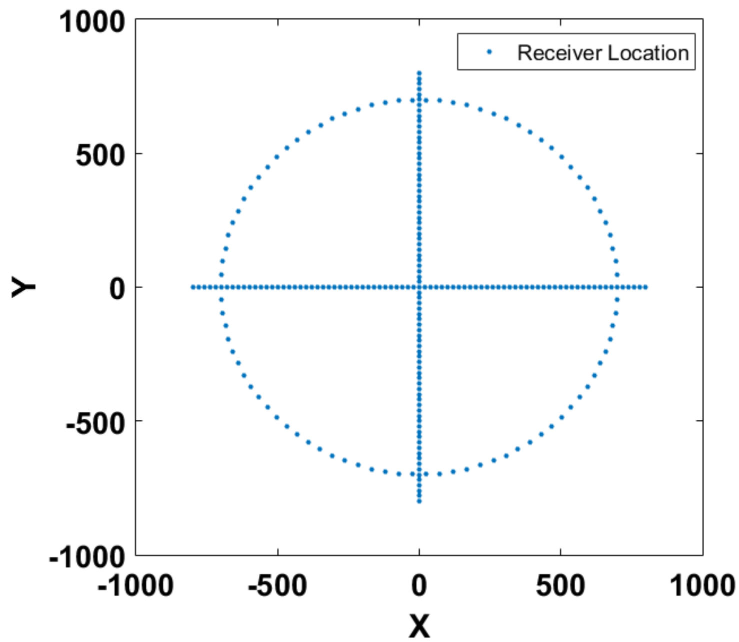

Figure 3.11 Surface view of the receiver locations at the top of the HTI layer. One source is fixed at the bottom of the HTI layer and positioned at the center.

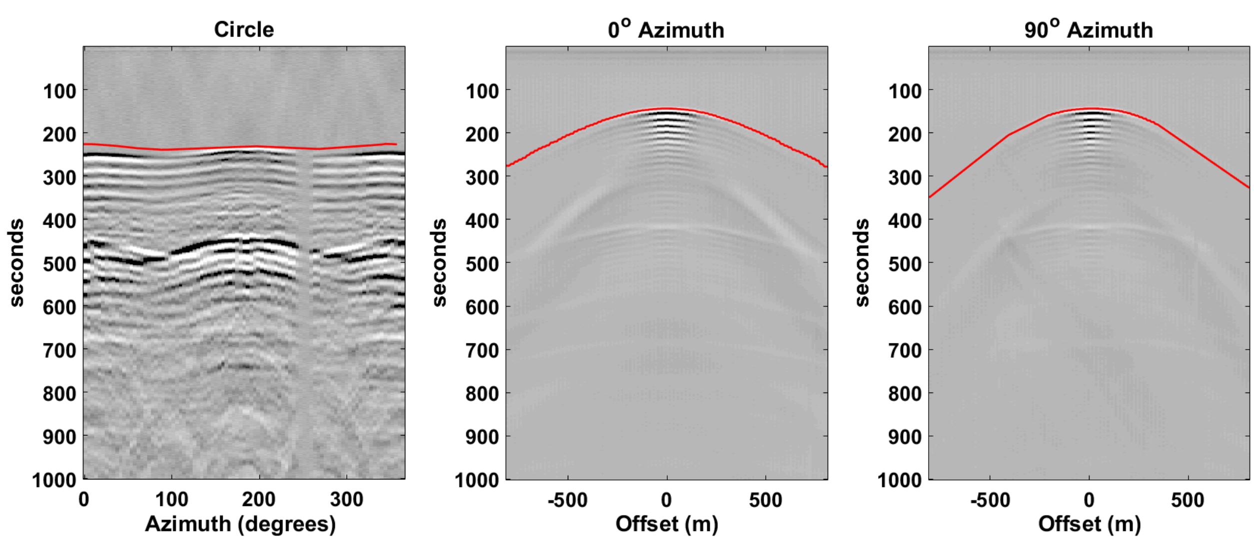

Figure 3.12 Second dataset: one circular gather (left) that has 200 m radius; and two linear with 0° (middle) and 90° (right) azimuths. First P-wave arrival times are indicated by red.

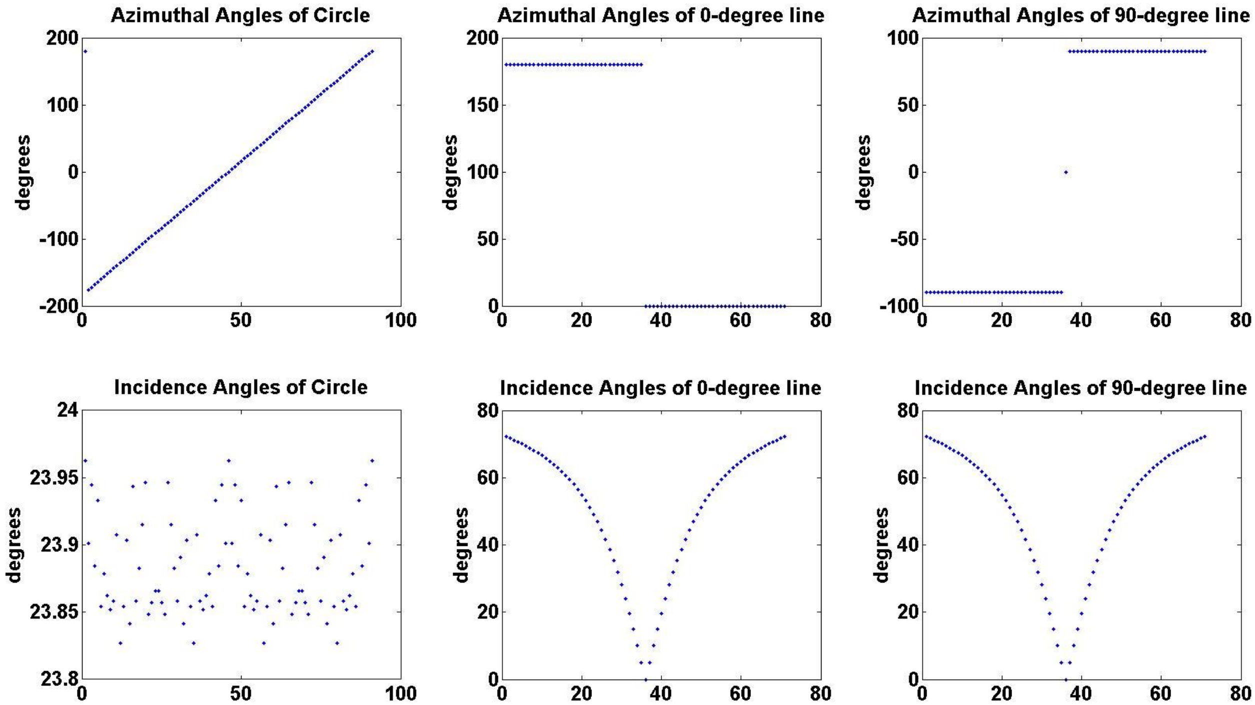

Figure 3.13 Azimuthal and incidence angles of the three common-shot gathers. The circular gather has a wide range of azimuthal angles and a single angle of incidence that is approximately 24°. The linear gathers have a single azimuthal angle 0° or 90° and a wide range of incidence angles.

The P group velocity and stiffness coefficients relation, given by equation (3.1), can be rewritten in the form of

$$d = Gm \, , \tag{3.15}$$

where d is n-dimensional data vector, m is the 6-dimension model parameter vector, and G is the n-by-6 data kernel as:

$$\begin{bmatrix} \frac{1}{V_1^2} \\ \frac{1}{V_2^2} \\ \frac{1}{V_3^2} \\ \vdots \\ \frac{1}{V_n^2} \end{bmatrix} = \begin{bmatrix} N_{11}^2 & N_{21}^2 & N_{31}^2 & N_{21}^2 N_{31}^2 & N_{11}^2 N_{31}^2 & N_{11}^2 N_{21}^2 \\ N_{12}^2 & N_{22}^2 & N_{32}^2 & N_{22}^2 N_{32}^2 & N_{12}^2 N_{32}^2 & N_{11}^2 N_{22}^2 \\ N_{13}^2 & N_{23}^2 & N_{33}^2 & N_{23}^2 N_{33}^2 & N_{13}^2 N_{33}^2 & N_{11}^2 N_{23}^2 \\ \vdots & \vdots & \vdots & \vdots & \vdots & \vdots \\ N_{1n}^2 & N_{2n}^2 & N_{3n}^2 & N_{2n}^2 N_{3n}^2 & N_{1n}^2 N_{3n}^2 & N_{1n}^2 N_{2n}^2 \end{bmatrix} \begin{bmatrix} \frac{1}{A_{11}^2} \\ \frac{1}{A_{22}^2} \\ \frac{1}{A_{33}^2} \\ -\frac{E_{23}}{A_{22}A_{33}} \\ -\frac{E_{13}}{A_{11}A_{33}} \\ -\frac{E_{13}}{A_{11}A_{22}} \end{bmatrix} \quad (3.16)$$

The linear problem is solved by inverting Equation (3.16) to get the model parameter vector on the right-hand side. The first three elements of the model parameter vector can provide us with A_{11}, A_{22}, and A_{33}. In the laboratory, V_{13} is estimated by measuring the group velocity of S wave that propagates along the x_3-axis and is polarized along the x_1-axis. It was found to be 1562.5 m/s. Similarly, V_{21} and V_{23} were measured and found to be 1785.7 m/s and 1451.6 m/s. A_{44}, A_{55}, and A_{66} can then be calculated using Equations (3.12), (3.13), and (3.14) respectively. Hence, the last three elements of the model parameter vector can provide us with A_{23}, A_{13}, and A_{12}. Three measured coefficients and six inverted coefficients from the density-normalized stiffness coefficients of the Phenolic layer in (m^2/s^2) are as follows:

$$A_{ij} = \begin{bmatrix} 6.193x10^6 & 2.698x10^6 & 3.202x10^6 & & & \\ & 11.791x10^6 & 6.617x10^6 & & & \\ & & 9.810x10^6 & & & \\ & & & 2.107x10^6 & & \\ & & & & 2.441x10^6 & \\ & & & & & 3.189x10^6 \end{bmatrix} \quad (3.17)$$

From equation (3.11), V_{33} can also be calculated from the inverted A_{33}. It is equal to 3132.0 m/s. In the laboratory, V_{33} was measured too by measuring the group velocity of P wave that propagates along the x_3-axis and polarized along the x_3-axis and found to be 3129.7m/s. The error between measured and calculated V_{33} is very small and equal to 0.073%. Table 3.2 summarizes body wave group velocities (V_{ij}) in the Phenolic. The resolution matrix (N) measures how well the data kernel resolves the model parameter (Lay, 1996). It is calculated by

$$N = GG^{-1} \tag{3.18}$$

and is shown in Figure 3.14. for the three common-shot gathers together. The resolution matrix for each gather is shown by Figure 3.15. The ideal resolution matrix is diagonal, any off diagonal indicates trade-off between model parameters. The resolution matrix of all gathers and the one of the circular gather resolve the model parameter well. On the other hand, the resolution matrix of each azimuthal line does not resolve the model parameter well, but the combination of both lines does.

V_{11}	V_{22}	V_{33}	V_{23}	V_{13}	V_{12}
2488.7	3433.8	3132.0	1785.7	1451.6	1562.5

Table 3.2 Three Body wave velocities (V_{ij}) that propagates along x_i-axis and polarized along x_j-axis in (m/s).

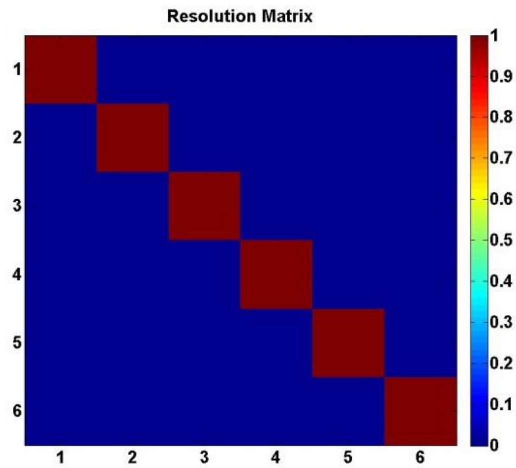

Figure 3.14 The resolution matrix of all gathers: one circle and two lines.

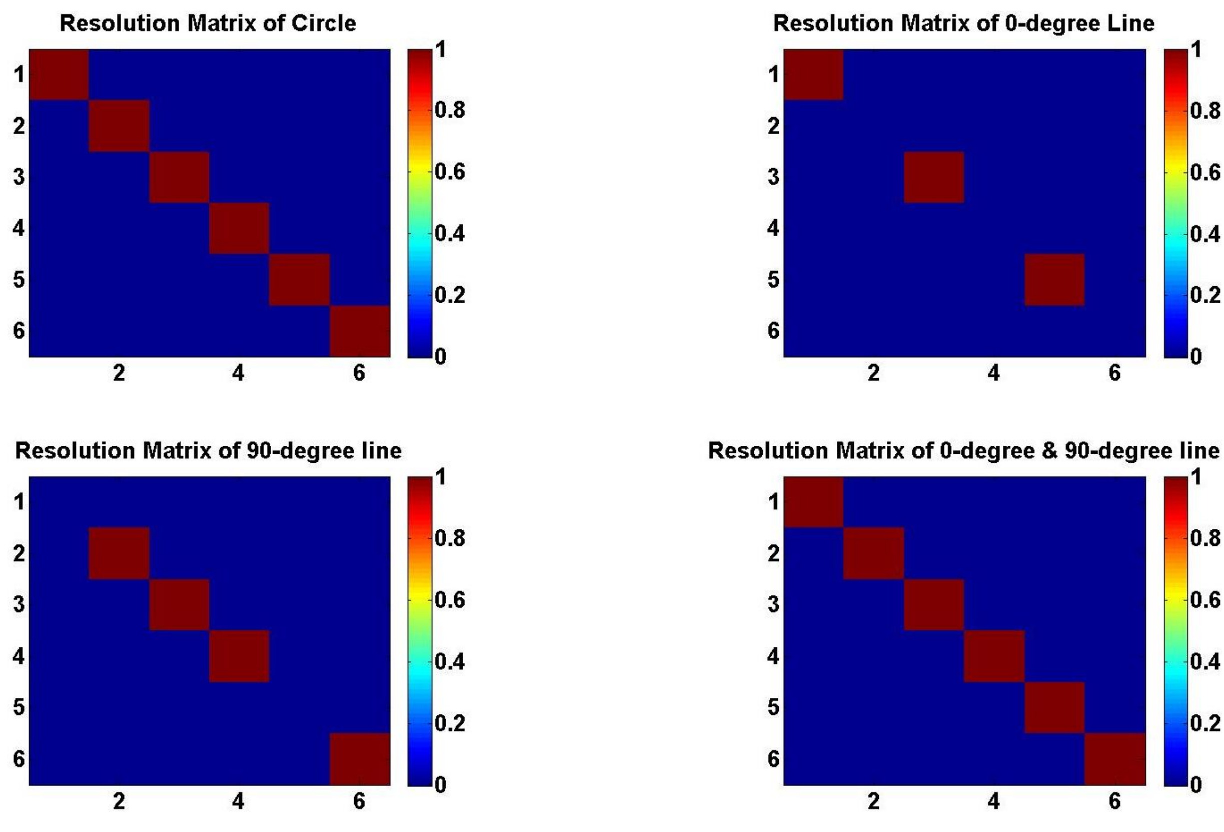

Figure 3.15 The resolution matrix of: one circle (top left), 0^{o} line (top right), 90^{o} line (bottom left), and both lines (bottom right).

3.4 Summary

Physical modeling is a valuable tool that can assist in the evaluation and development of practices for fracture characterization. This part of thesis has utilized physical modeling, and in summary:

- A two-layer physical model consisting of an anisotropic phenolic layer lying under an isotropic plexiglas layer was constructed to represent a vertically-fractured reservoir overlain by an isotropic overburden.
- The first dataset analysed in this chapter was acquired over the two-layer model using a fixed receiver on the bottom of the phenolic layer, and sources moving on the top of the Plexiglass layer. Source locations were on the circumferences of three concentric circles with radii of r = 250 m, 500 m and 1000 m, respectively. On each circle, the source locations covered azimuths of 0^{o}-360^{o} at 4^{o} intervals.
- Fracture plane orientation was easily identified from the third common-receiver gather (***r*** = 1000 m) by P-wave first-arrival times. Elliptical fitting of P-wave first-arrival times was employed to identify the fracture plane orientation from the three common-receiver gather.
- The second dataset was used to invert for the elastic stiffness coefficients of the anisotropic Phenolic medium using the approximations derived by Daley and Krebes (2006). The approximations are validated by the good agreement between various inverted and measured stiffness values for phenolic.
- The second dataset was used to invert for the elastic stiffness coefficients of the anisotropic Phenolic medium using the approximations derived by Daley and

Krebes (2006). The approximations are validated by the good agreement between various inverted and measured stiffness values for Phenolic.

The first dataset can be repeated in the field using walkaround VSP dataset to estimate anisotropy orientation at different depth levels and its intensity which is the ratio between fast and slow velocity or the ratio between major and minor axis. The second dataset also can be repeated in the field to estimate stiffness coefficient of s specific reservoir. The data needed would be 9-component crosswell seismic involving 3 wells, ideally located at the corners of an equilateral right triangle with well-to-well separations suitable for identifying the following fast and slow direct arrivals: qP events, qS_v events, and qS_h.

Chapter 4 AVA & AVAZ of 3D Pre-stack Seismic Data

In this chapter, the Altamont-Bluebell 3D pre-stack seismic data is analyzed using AVA to identify sweet spots and using AVAZ to identify azimuthal seismic anisotropy zones and correlate them to sweet spots. In AVA analysis, the reflection coefficient is a function of incident angle and the three elastic parameters or P-wave velocity, S-wave velocity, and density. Therefore, those parameters are inverted for. In AVAZ analysis, four additional quantities (the symmetry angle and the three TI symmetry parameters) need to be obtained by inversion of the azimuth/angle-dependent reflection coefficient. Since the reflection coefficient in the AVAZ case is a higher-order function of seven parameters, we may require include information from larger incident angles as compared to AVA analysis. This will be discussed later in this chapter. The geology of the field, and seismic data acquisition were described earlier in **Chapter 2**. As mentioned earlier, our focus will be on the main two targets. The first target is the most prolific oil interval within the overpressured Wasatch. This interval is about 500′ thick, and called Wasatch-180. Most horizontal wells are drilled within this target. The second target is shallower thick gas reservoir at the Upper Green River (UGR) formation.

4.1 **Seismic data processing for AVA & AVAZ**

A conventional 3D processing workflow was applied to the Altamont-Bluebell data. After geometry assignment, an amplitude recovery function of velocity was applied. Refraction statics were applied too with a replacement velocity of 8000 ft/sec and two-layer model. The offsets used were about 250 to 2000 feet for the first layer, and about

2100 to 7000 feet for the second layer. Figure 4.1, Figure 4.2, and Figure 4.3 show the elevation, elevation statics, and refraction statics of sources and receivers. For definitions of those statics and more about refraction statics, please refer to Al Dulaijan (2008). Significant noise was observed and suppressed in multiple domains (i.e., shot, CDP, inline-azimuth-shot line). Also, spherical divergence correction, surface-consistent amplitude corrections, and deconvolution were applied. The zero-offset VSP data were used to calculate Q corrections for the 3D seismic data, and also to determine phase corrections for bringing the surface seismic data to zero phase. Isotropic velocity analysis at one-mile intervals, NMO corrections, and residual statics corrections (for common-azimuth varying-offset gathers) were done in sequence. A second pass of velocity analysis at half-mile intervals was done, followed by another pass of residual statics corrections and by a second pass of surface-consistent amplitude processing.

In standard industry practice, azimuthal variations are usually preserved either by sectoring pre-stack data into azimuthal sectors, or by COV binning. The latter has the advantage of preserving more azimuthal variations. COV sorting is described by Cary (1999); Li (2008) gives a detailed explanation of the method. COV binning of the data prior to migration was chosen here.

Then, isotropic migration velocity analysis was preformed, and followed by anisotropic VTI migration velocity analysis. VTI COV Kirchhoff pre-stack time migration (PSTM) was carried on for at last. PSTM gather is shown by Figure 4.4. Trim statics processing was applied to flatten target horizons for both AVA and AVAZ data. For AVA inversion, a super gather was created from 9 gathers. For AVAZ inversion, 9 non-stacked gathers were used for each CDP location.

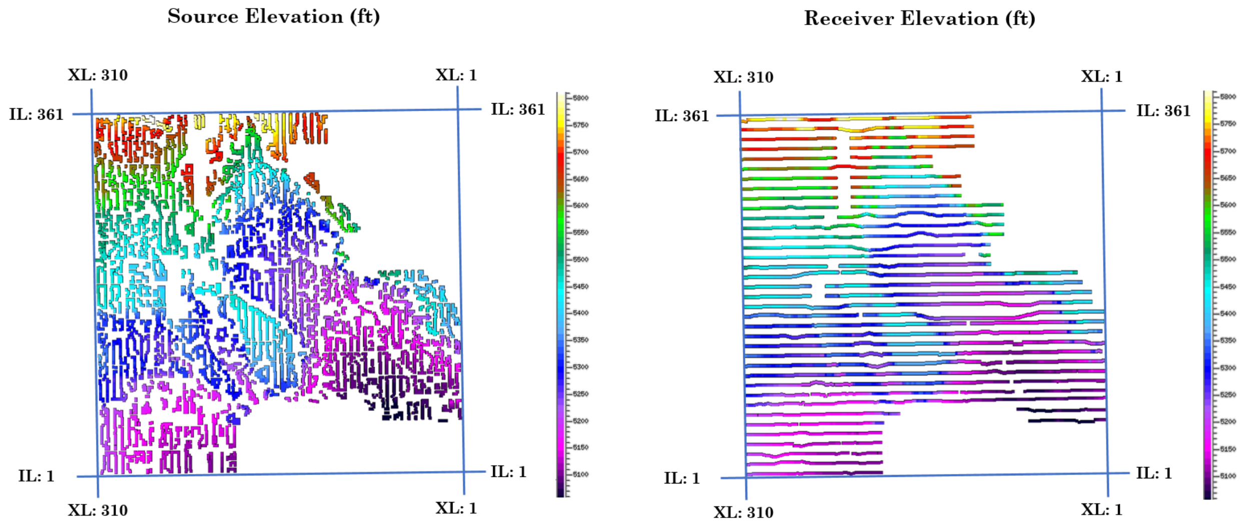

Figure 4.1 Elevation basemap (ft) of sources (left) and receivers (right). Elevation increases toward north and has about 800-ft range.

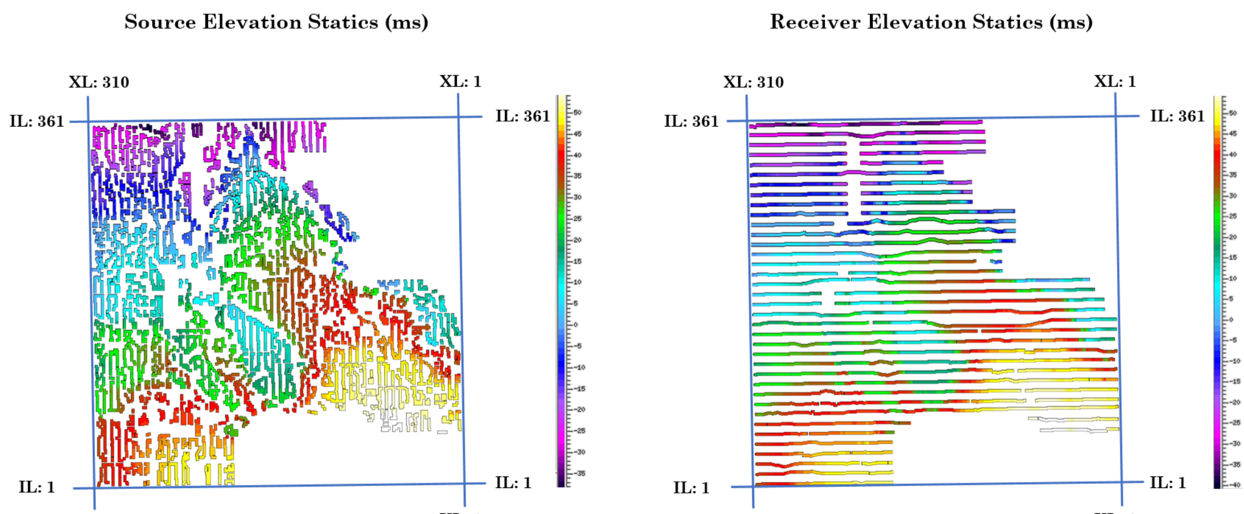

Figure 4.2 Elevation statics (ms) basemap of sources (left) and receivers (right).

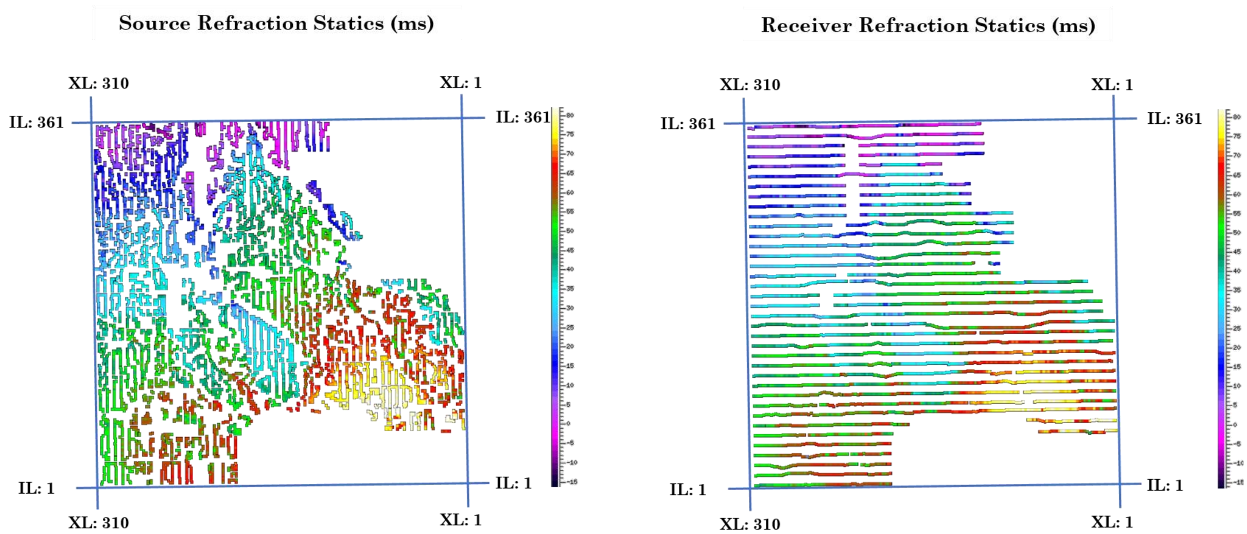

Figure 4.3 Refraction statics (ms) basemap of sources (left) and receivers (right).

PSTM gathers were stacked. Stacked data were correlated to well logs and used to pick horizons. Figure 4.5 shows inline and crossline stack sections with a well in the middle and two picked horizons, Upper Green River Formation and Mahogany Bench which are the top and base of the shallow target. An example logs for one of the available wells are shown by Figure 4.7. The original logs are shown indicated by grey curves. Those logs were temporally filtered to 100 Hz. Filtered logs are indicated by black curves. The base of Lower Green River is the marker for Wasatch that starts at depth of 12380′. The first target which the most prolific zone of Wasatch starts at 13750′ and is about 500′ thick. Even though Wasatch is overpressured as indicated by low P-wave velocities, the productive zone (Wastach-180) is not, according to high P-wave velocity logs for this well and other available well. The reason may be due to the fact that the reservoir has been producing for long and is in depleting stage now. Hydrocarbon generation in the low-permeability and low-porosity Flagstaff is the reason for the overpressure in Wasatch (Morgan et. al, 2003). For the shallower target, Upper Green River Formation, the only available log here is P-wave sonic. The porosity of Wasatch-180 is low. For all wells, Lower Green River formation showed the highest porosity. However, high porosity at Lower Green River in Altamont- Bluebell field do not translate into high oil production (Morgan et al., 2003). Well logs are correlated to seismic and used to pick the top and base of those two targets. The time picks for Upper Green River formation and Mahoney Bench are displayed in Figure 4.8. Isochrone or time thickness of this Upper Green River is displayed in Figure 4.9. Thickness of this reservoir does not vary significantly. Figure 4.10 shows time picks of Wasatch-180 and its base, and Figure 4.11 shows an isochrone of the reservoir. Wasatch-180 thins toward the North.

Angles of incidence were calculated from the ray parameter (p) (CGGVeritas, 2014):

$$p = \frac{\sin\theta}{Vint}, \tag{4.1}$$

where V_{int} is the isotropic interval P-wave velocity. The ray parameter (p) can also be calculated by taking the derivative of V_{rms} (i.e., RMS velocity from the NMO equation) with respect to the offset coordinate (x):

$$t_x^2 = t_0^2 + \frac{x^2}{Vrms^2}, \tag{4.2}$$

$$p = \frac{dt}{dx}, \tag{4.3}$$

$$\frac{dt}{dx} = \frac{x}{t_x Vrms^2}. \tag{4.4}$$

Rewriting Equation (4.1) yields

$$\sin\theta = \frac{x\,Vint}{t_x Vrms^2}. \tag{4.5}$$

From the geometry of source-receiver pair in a single constant velocity layer shown in Figure 4.6:

$$t_x = \frac{t_0}{cos\theta}. \tag{4.6}$$

For, a single layer $Vint$ and $Vrms$ are equal, therefore substituting t_x from Equation (4.6) into Equation (4.5) yields:

$$\tan\theta = \frac{x}{t_0 Vint}. \tag{4.7}$$

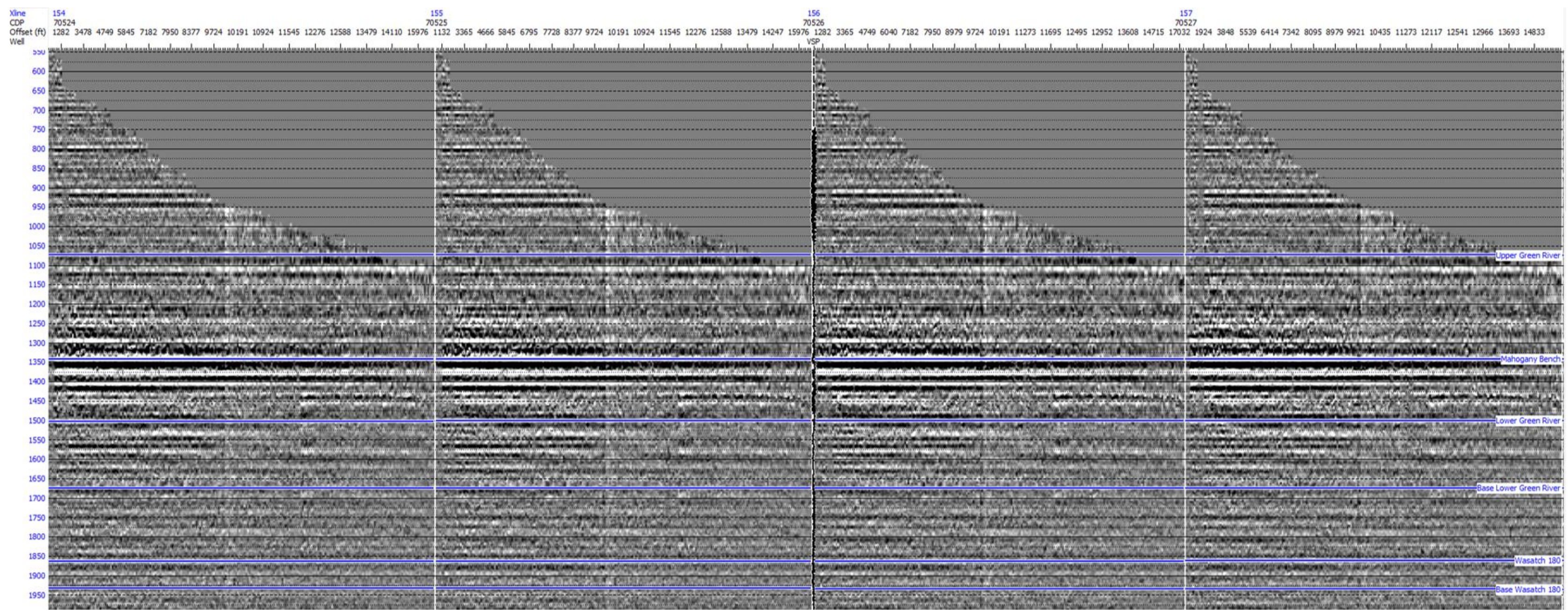

Figure 4.4 PSTM Gathers close to the VSP borehole. Five horizons are picked and shown by blue.

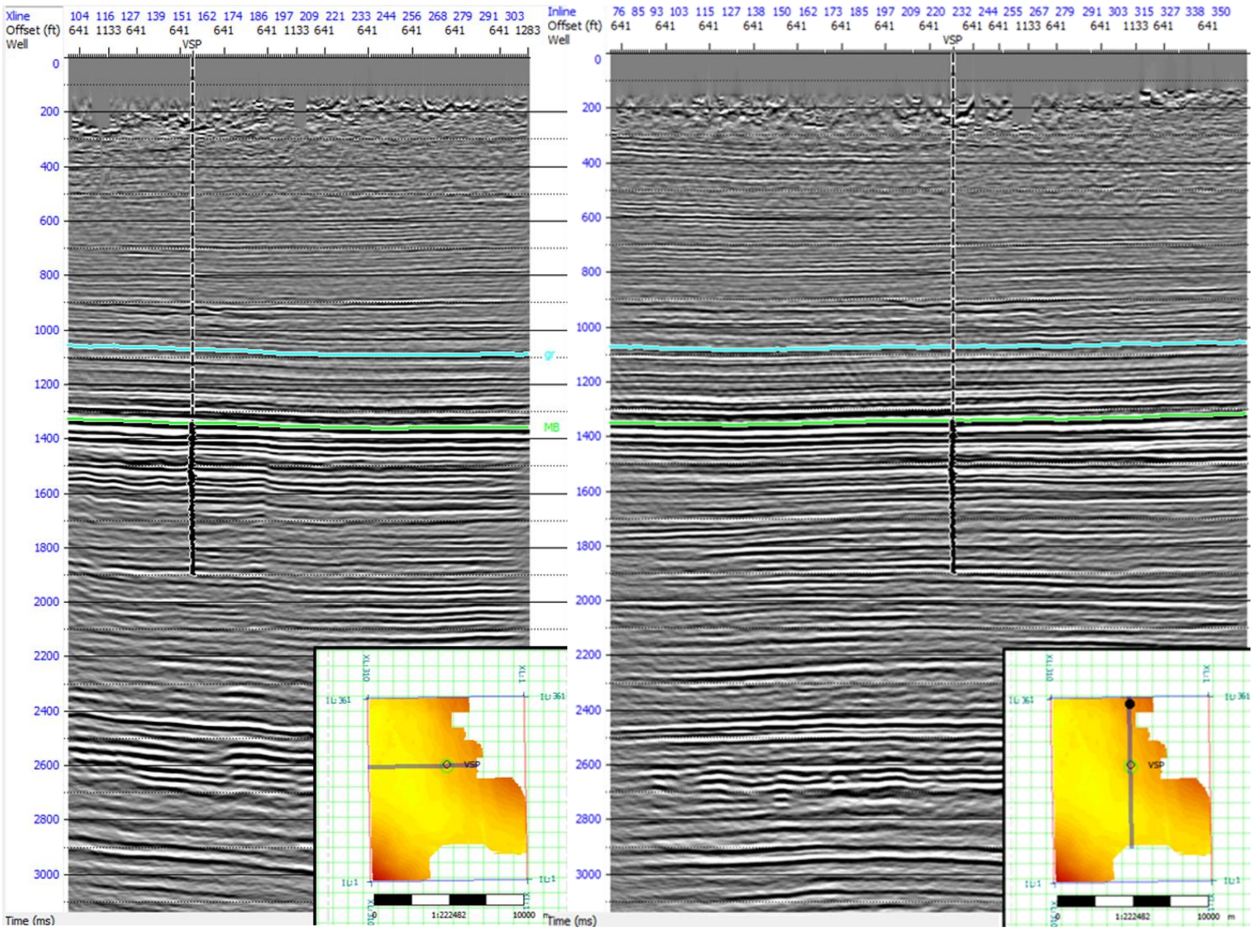

Figure 4.5 PSTM stacked inline (left) and crossline (right) with basemaps and relative stacked section location on bottom rights.

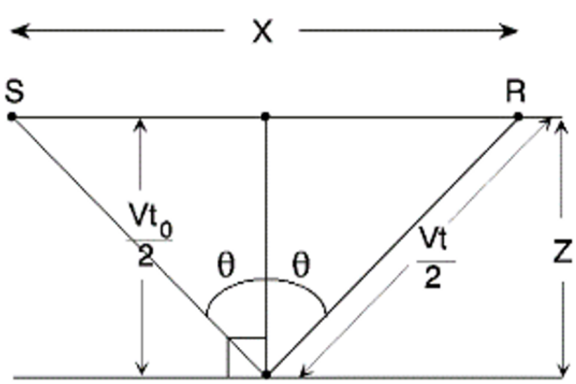

Figure 4.6 Raypath of a source-receiver pair in a single constant velocity layer.

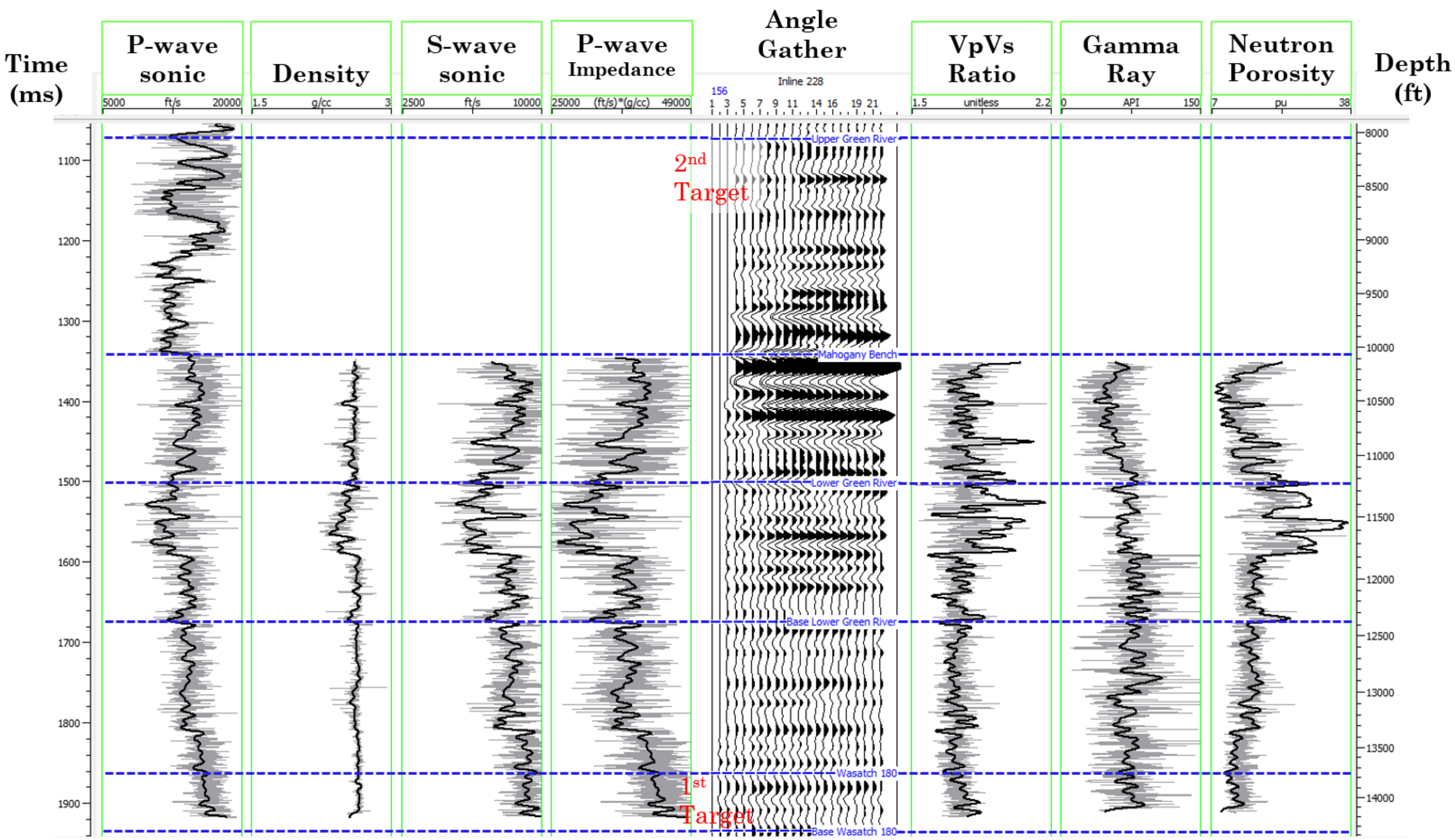

Figure 4.7 Available well log: grey indicates original logs, and black indicates filtered logs. Used filter is 100 Hz.

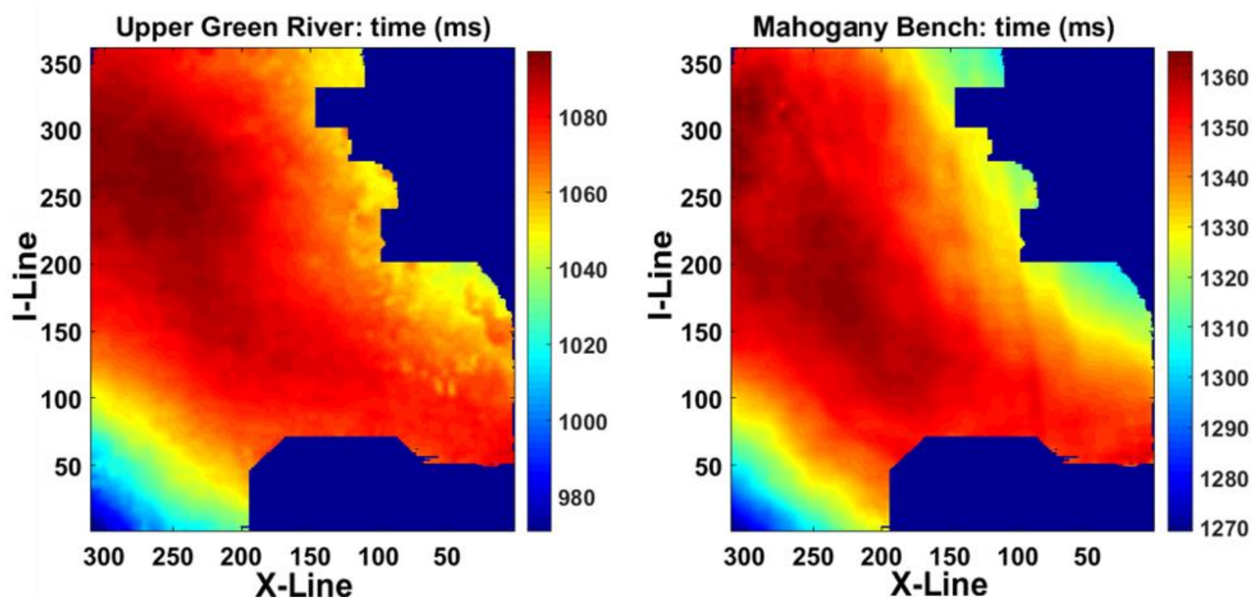

Figure 4.8 Two-way times in ms of Upper Green River formation.

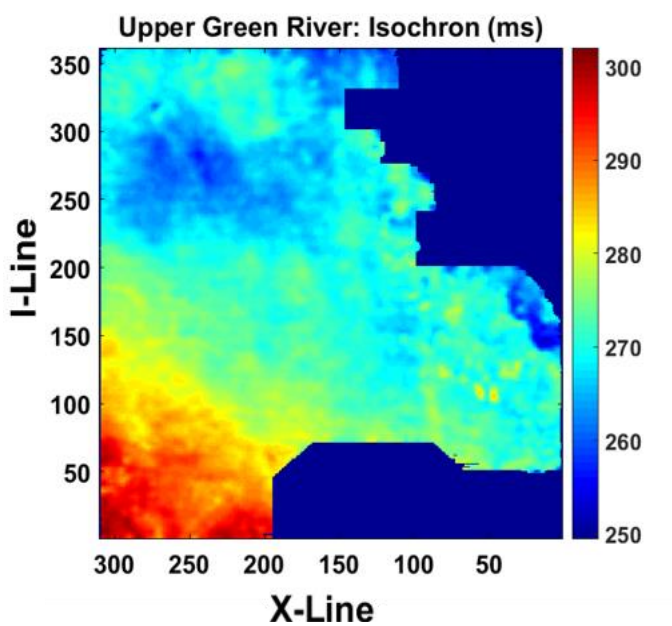

Figure 4.9 Isochrone of Upper Green River formation.

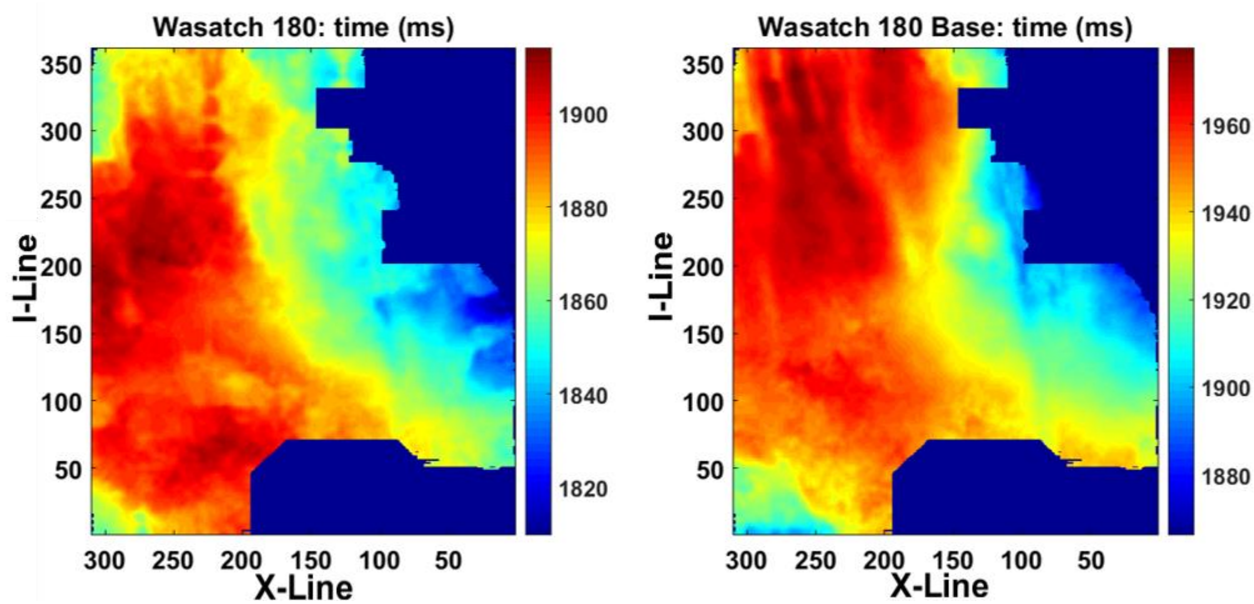

Figure 4.10 Two-way times in ms of Wasatch-180.

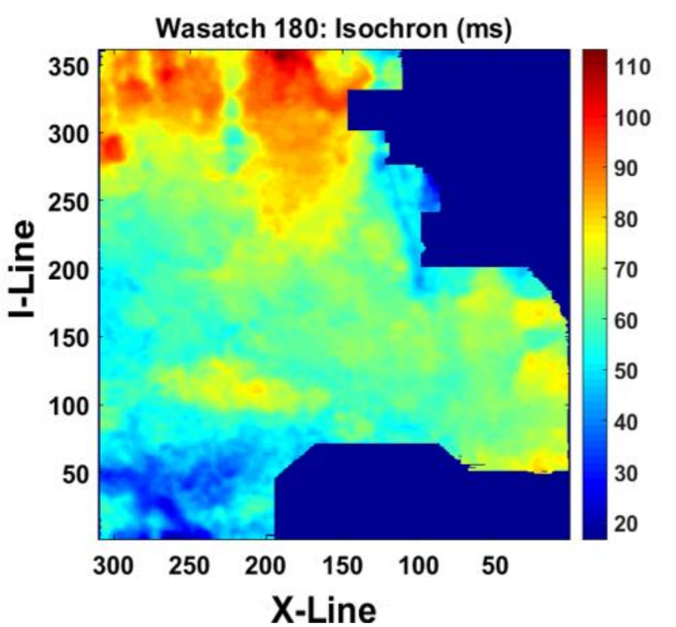

Figure 4.11 Isochrone of Wasatch-180. Unlike shallower target at Upper Green River formation, it thins out significantly towards the south part of the map.

4.2 **Amplitude Variations with Angle (AVA) analysis**

Zoeppritz (1919) derived equations that describe the conversion of an incident plane P wave at a velocity/density interface (Figure 4.12) with incident angle (θ) into four components: P-wave reflection (R_p), S-wave reflection (R_s), P-wave transmission (T_P), and S-wave transmission (T_s). His derivation is valid for incident angles up to the critical angle under two assumptions. First, the displacement amplitudes are continuous at the interface between media that are in welded contacts (i.e., the media on both sides of the interface cannot ripped apart). This condition can be called the kinematic boundary condition. Second, the stress tensor across the interface is continuous. This condition can be called the dynamic boundary condition. Note that these assumptions do not hold for vertical open fractures because the displacement is not contentious at the interface for such media.

A popular approximation of the Zoeppritz equation for the P-wave reflection that is often used for AVA is given by Aki and Richards (1980). It relates reflection amplitude to incident angle and the three elastic parameters; P-wave velocity (α), S-wave velocity (β), and density (ρ). Shuey (1985) writes it as:

$$R_P(\theta) = A_{iso} + B_{iso}\sin^2(\theta) + C_{iso}\sin^2(\theta)\tan^2(\theta) \tag{4.8}$$

where

$$A_{iso} = \frac{1}{2}\left[\frac{\Delta\alpha}{\bar{\alpha}} + \frac{\Delta\rho}{\bar{\rho}}\right] \tag{4.9}$$

$$B_{iso} = \frac{1}{2}\frac{\Delta\alpha}{\bar{\alpha}} - 4\left[\frac{\bar{\beta}}{\bar{\alpha}}\right]^2\left[\frac{\Delta\beta}{\bar{\beta}} + \frac{\Delta\rho}{2\bar{\rho}}\right] \tag{4.10}$$

$$C_{iso} = \frac{1}{2}\frac{\Delta\alpha}{\alpha} \tag{4.11}$$

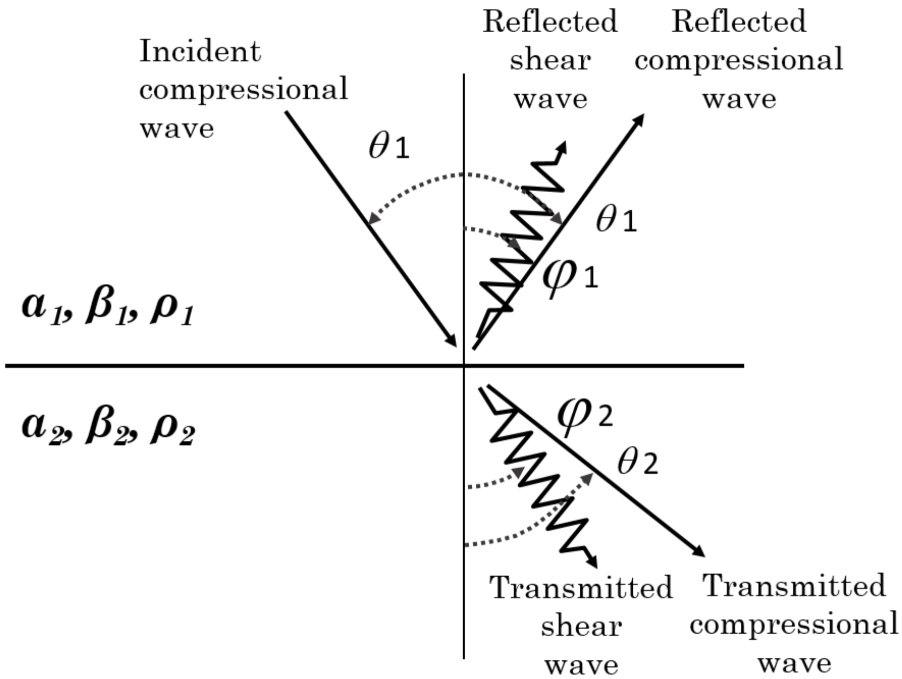

Figure 4.12 Incident P-wave energy partioning into P-wave reflection and transmission and S-wave reflection and transmission at a welded contact interface.

The overbar in Equations (4.9) to (4.11) represents the average value at the interface between the upper and lower layers, while the capital delta represents the difference between the values for the upper and the lower layer. The advantage of this representation is that the reflection coefficient as a function of incident angle can be represented by a curve that has an intercept ($\boldsymbol{A_{iso}}$) that is equivalent to normal-incidence reflection coefficient, a slope or first derivative of the curve ($\boldsymbol{B_{iso}}$), and a gradient or second derivative of the curve ($\boldsymbol{C_{iso}}$). This representation is called ***ABC*** method and very useful since it extract empirical information about the AVO. Such information can be plotted in cross plots as in the right of Figure 4.13. A positive impedance contrast means a positive normal-incidence reflection coefficient or a positive intercept. The slope is positive if the amplitude is increasing as incident angle increases and negative the amplitude is decreasing. The magnitude of the slope indicates the AVA strength. Shuey (1985) showed mathematically that contrast in Poisson's ratio is the parameter most directly related to AVA strength for incident angles up to 30°. Slope and gradient are the basis for AVA classifications. Figure 4.13 shows different classes of AVA based on intercept and slope. The third term, curvature, becomes important for incident angles larger than 20°.

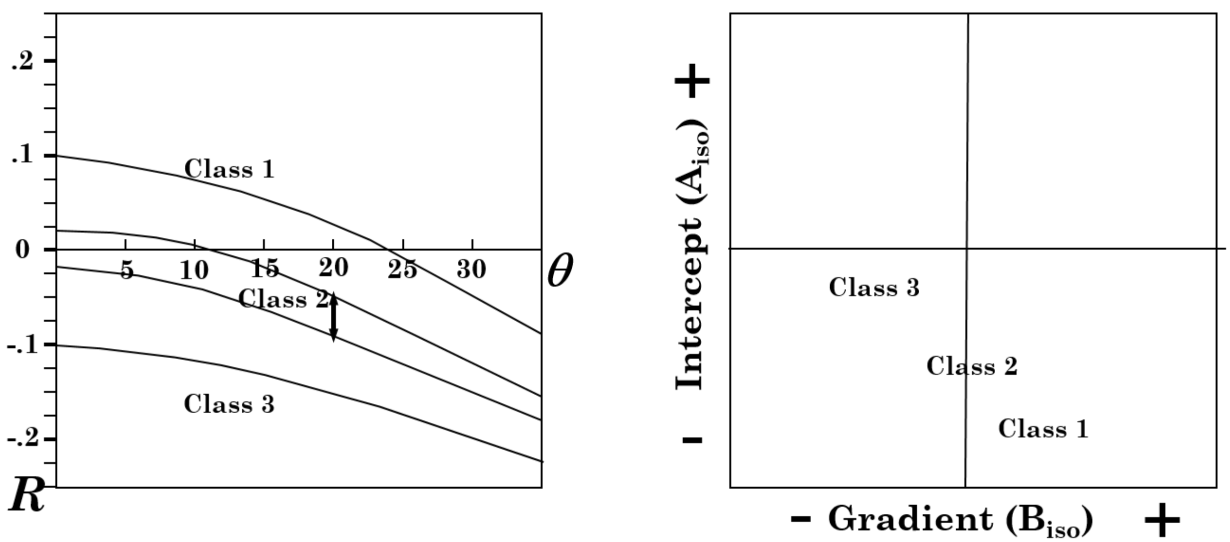

Figure 4.13 AVA 3 classes represented on reflectivity (R) vs. incident angle (θ) plot (left) and on intercept (A_{iso}) vs. gradient (B_{iso}) plot (right).

Another useful representation of Aki and Richards (1980) is Fatti et al. (1994):

$$R_P(\theta) = c_1 R_P + \ c_2 R_S + c_3 R_\rho \ , \tag{4.12}$$

where

$$c_1 = 1 + \tan^2\theta \tag{4.13}$$

$$c_2 = -8\left[\frac{\bar{\beta}}{\bar{\alpha}}\right]^2 \sin^2(\theta) \tag{4.14}$$

$$c_3 = -\frac{1}{2}\tan^2(\theta) + 2\left[\frac{\bar{\beta}}{\bar{\alpha}}\right]^2 \sin^2(\theta) \tag{4.15}$$

$$c_3 = -\frac{1}{2}\tan^2(\theta) + 2\left[\frac{\bar{\beta}}{\bar{\alpha}}\right]^2 \sin^2(\theta) \tag{4.16}$$

$$R_P = \frac{1}{2}\left[\frac{\Delta\alpha}{\bar{\alpha}} + \frac{\Delta\rho}{2\bar{\rho}}\right] \tag{4.17}$$

$$R_S = \frac{1}{2}\left[\frac{\Delta\beta}{\bar{\beta}} + \frac{\Delta\rho}{2\bar{\rho}}\right], \tag{4.18}$$

and

$$R_\rho = \frac{\Delta\rho}{2\bar{\rho}} \tag{4.19}$$

This representation separates the reflection coefficient for P-wave data into three terms. The first and the second terms are related to normal incidence reflection coefficients, while the third term is related to density contrast. In fact, we have used this representation to invert for the three elastic parameters (*α, β,* and *ρ*). In order to so, the small reflectivity approximation that relates P-wave reflectivity, R_P, to P-wave impedance, *Z*, is often used (Russell and Hampson, 2006):

$$R_P(i) = \frac{Z(i+1) - Z(i)}{Z(i+1) + Z(i)} \cong \frac{1}{2}[\mathrm{l_P}(i+1) - \mathrm{l}_P(i)], \tag{4.20}$$

where i denotes the interface between layers $i+1$ and i for a system of $n+1$ layers, and $l_P = \ln(Z_P)$. Equation (4.20) can be written into matrix form:

$$\begin{bmatrix} R_P(1) \\ R_P(2) \\ \vdots \\ R_P(n) \end{bmatrix} = \frac{1}{2} \begin{bmatrix} -1 & 1 & 0 & \cdots \\ 0 & -1 & 1 & \ldots \\ 0 & 0 & -1 & \ldots \\ \vdots & \vdots & \vdots & \ddots \end{bmatrix} \begin{bmatrix} l_P(1) \\ l_P(2) \\ \vdots \\ l_P(n) \end{bmatrix}, \tag{4.21}$$

where the second matrix represents the derivative matrix, *D*. Then, the seismic trace, $s(s_1,s_2, \ldots, s_n)$, can be expressed as matrix convolution of the wavelet $w(w_1,w_2, \ldots, w_k)$ with reflectivity:

$$\begin{bmatrix} s_1 \\ s_2 \\ \vdots \\ s_n \end{bmatrix} = \frac{1}{2} \begin{bmatrix} w_1 & 0 & 0 & \cdots \\ w_2 & w_1 & 0 & \ldots \\ 0 & w_2 & w_1 & \ldots \\ \vdots & \vdots & w_2 & \ddots \end{bmatrix} \begin{bmatrix} -1 & 1 & 0 & \cdots \\ 0 & -1 & 1 & \ldots \\ 0 & 0 & -1 & \ldots \\ \vdots & \vdots & \vdots & \ddots \end{bmatrix} \begin{bmatrix} \mathrm{l}_P(1) \\ l_P(2) \\ \vdots \\ l_P(n) \end{bmatrix} \tag{4.22}$$

Equation (4.22) can be used for post-stack P-wave impedance inversion using conjugate gradient method with a starting initial guess model. However, it needs to be extended for angle gathers to be used for pre-stack elastic inversion. For an angle gather, s(θ), Equation (4.22) and Equation (4.12) can be combined:

$$s(\theta) = \frac{1}{2}\, c_1\, w(\theta)\, D\, l_P + \frac{1}{2}\, c_2\, w(\theta)\, D\, l_s + \frac{1}{2}\, c_3\, w(\theta)\, D\, l_\rho \tag{4.23}$$

A relation between l_p and l_s and between l_p and l_ρ are derived from Gardner's rule assuming that $\frac{\bar{\beta}}{\bar{\alpha}}$ is constant for a wet trend. The relationships are:

$$l_s = k\, l_P + k_c + \Delta l_S \tag{4.24}$$

and

$$l_\rho = m\, l_P + m_c + \Delta l_\rho \tag{4.25}$$

where k, k_c, m, and m_c are constants.

The wavelet, *w,* is extended to varying wavelet for different angle of incidence, $w(\theta)$. Equations (4.23), (4.24), and (4.25) are combined into

$$T(\theta) = \widetilde{c_1}\, w(\theta)\, D\, l_P + \widetilde{c_2}\, w(\theta)\, D\, \Delta l_S + w(\theta)\, c_3\, D\, \Delta l_\rho \tag{4.26}$$

where

$$\widetilde{c_1} = \frac{1}{2} c_1 + \frac{1}{2}\, k\, c_2 + m\, c_3 \tag{4.27}$$

and

$$\widetilde{c_2} = \frac{1}{2} c_2 \tag{4.28}$$

Equation (4.23) can be rewritten into matrix form:

$$\begin{bmatrix} s(\theta_1) \\ s(\theta_2) \\ \vdots \\ s(\theta_n) \end{bmatrix} = \begin{bmatrix} \widetilde{c_1}(\theta_1)w(\theta_1)D & \widetilde{c_2}(\theta_1)w(\theta_1)D & \widetilde{c_3}(\theta_1)w(\theta_1)D \\ \widetilde{c_1}(\theta_2)w(\theta_2)D & \widetilde{c_2}(\theta_2)w(\theta_2)D & \widetilde{c_3}(\theta_2)w(\theta_2)D \\ \vdots & \vdots & \vdots \\ \widetilde{c_1}(\theta_n)w(\theta_n)D & \widetilde{c_2}(\theta_n)w(\theta_n)D & \widetilde{c_3}(\theta_n)w(\theta_n)D \end{bmatrix} \begin{bmatrix} l_P \\ \Delta l_S \\ \Delta l_\rho \end{bmatrix} \tag{4.29}$$

Similar to Equation (4.25), Equation (4.29) is solved using a conjugate gradient method with an initial guess model. Figure 4.14 shows a crossplot of l_P vs l_ρ and l_P vs l_S. The deviation between the best fit line and outliers, Δl_ρ and Δl_S, may be the hydrocarbon anomalies. The elastic parameters are first inverted and checked at the well locations. A synthetic gather is calculated using convolutional model. The model can be calculated using a convolutional model based on the Zoeppritz (1919) equations or on the linearized equations, i.e., Aki and Richards (1980).

The angles used for the inversion were limited to those less than or equal to 30° because the correlation between linearized Zoeppritz calculated data and measured data becomes poor when using larger angles, as shown by Figure 4.15 and Figure 4.16. Comparing the two figures, the slope when using larger angles seem to be flipped. Therefore, only small angles up to 30° were used. That restriction also avoids critical angles that violates the assumptions made for linearized AVO. A comparison of Figure 4.16 to Figure 4.13, indicates that the Upper Green River is likely AVA class 3.

The inversion results, the initial model, and original logs for one of the available wells are shown by Figure 4.17. The initial model is indicated by black, while original logs are indicated by blue. Also, the angle gather in red is compared to the synthetic gather in blue. The three elastic parameters, V_p, V_s, and ρ for isotropic medium are inverted for at the locations of the six available wells. The AVA inversion was carried for the pre-stack volume.

Two data slices were created across each reservoir from the inversion results. The first slice is for P-wave impedance and shown by Figure 4.18 for Upper Green River formation (left) and for Wasatch-180 (right). The second slice is for V_pV_s ratio and shown by Figure 4.19 for Upper Green River formation (left) and for Wasatch-180 (right).
These data slices show the six available wells used for parameter correlation and for the initial model. Accumulative production data for oil and gas were provided for different set of wells. Wells were drilled over a period of more than 40 years. Therefore, comparison of older well to newer ones would not be reasonable. In the Upper Green River, some correlation seems to exist between abnormally productive gas wells and low P-wave impedances. However, in general, abnormally productive oil wells do not correlate to either P-wave impedance or Vp/Vs ratio maps. Morgan et al. (2003) have concluded that neither structure nor stratigraphy help predict the largest oil production areas within the field.

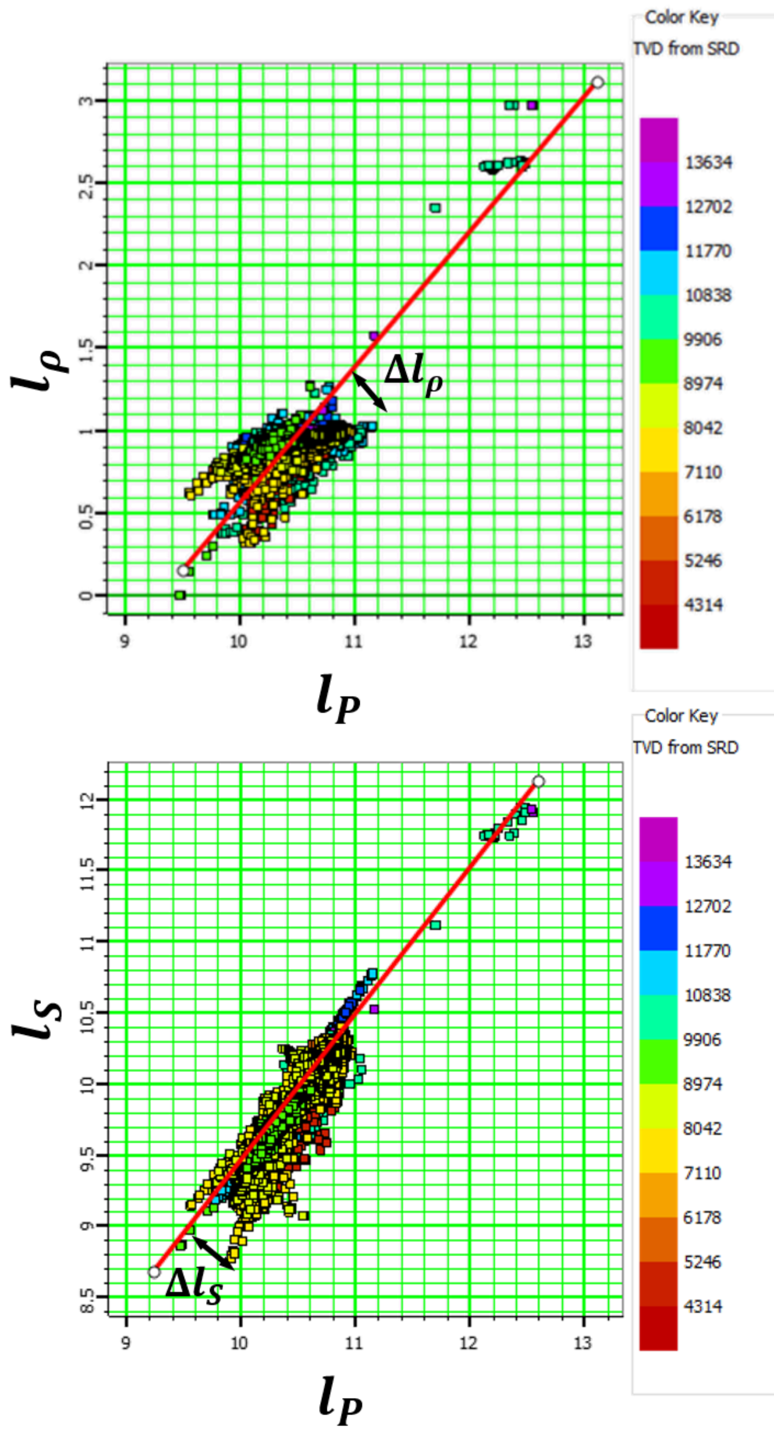

Figure 4.14 Crossplots of l_P vs $l\rho$ (upper) and l_P vs l_S (lower). The deviation between the best fit line and outliers, $\Delta l\rho$ and Δl_S, may be the hydrocarbon anomalies.

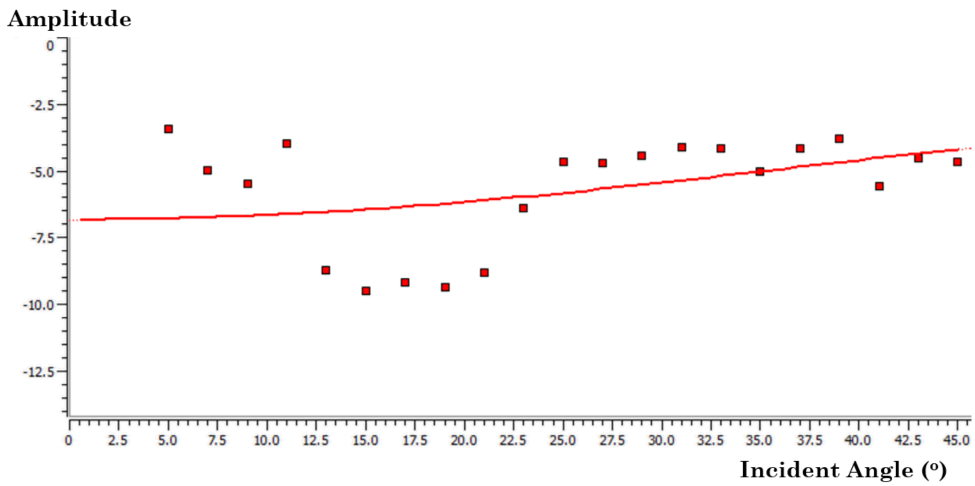

Figure 4.15 AVA: amplitude vs incident angle plot for one gather at Upper Green River. Incident angles ranges up to 45°. Correlation between theoretical and measured data is poor. Also, notice that the sign of the slope is flipped, and AVO class is not 3 anymore.

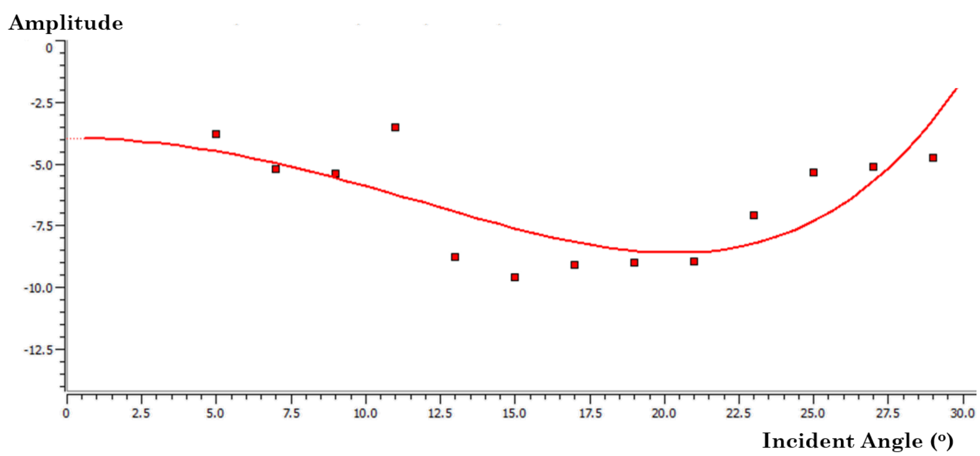

Figure 4.16 AVA: amplitude vs incident angle plot for one gather at Upper Green River. AVA class is 3. Incident angles ranges up to 30°. Correlation between theoretical and measured data is good.

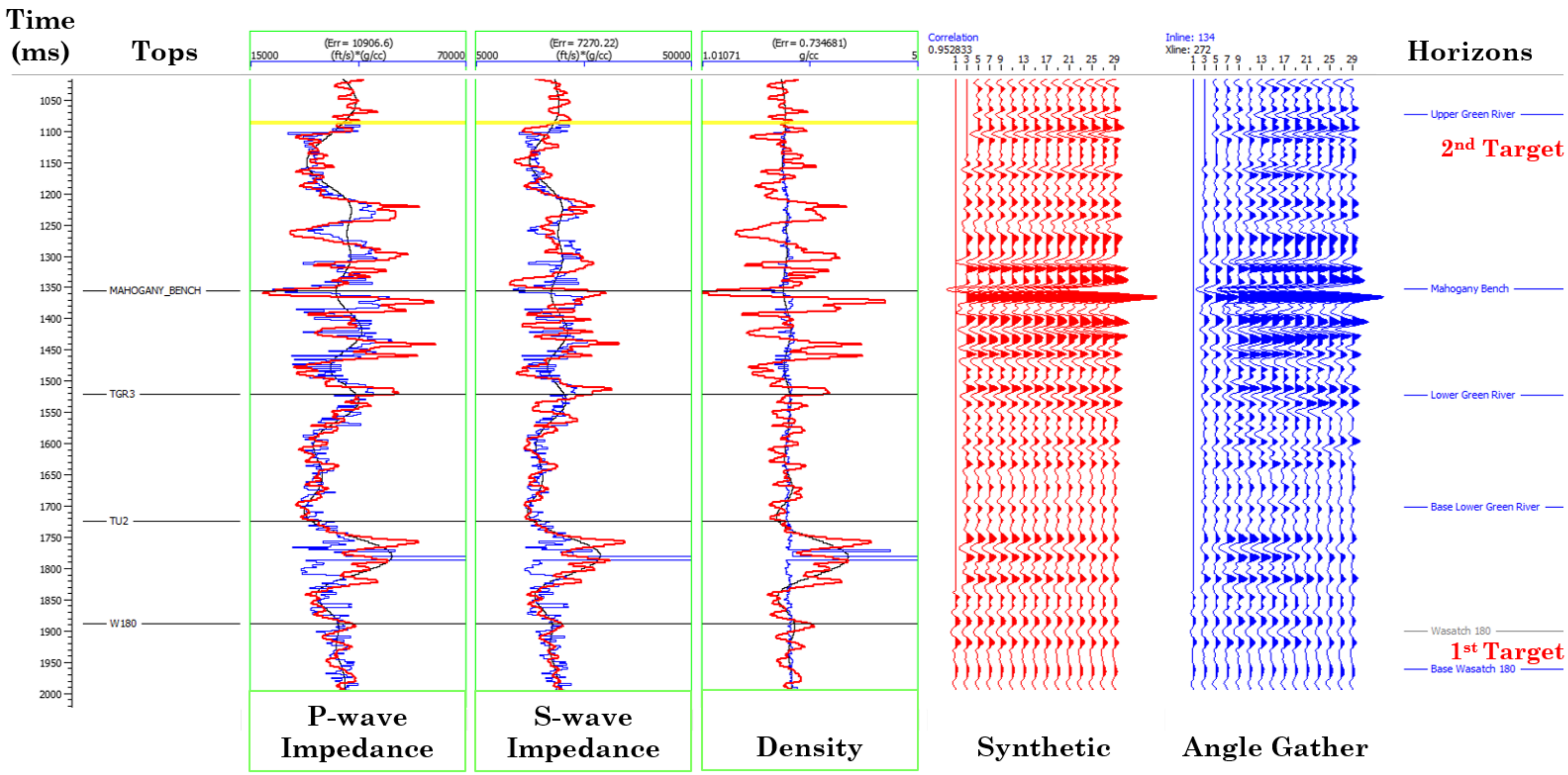

Figure 4.17 AVA inversion results indicated by red. Initial model is indicated by black, while original logs are indicated by blue.

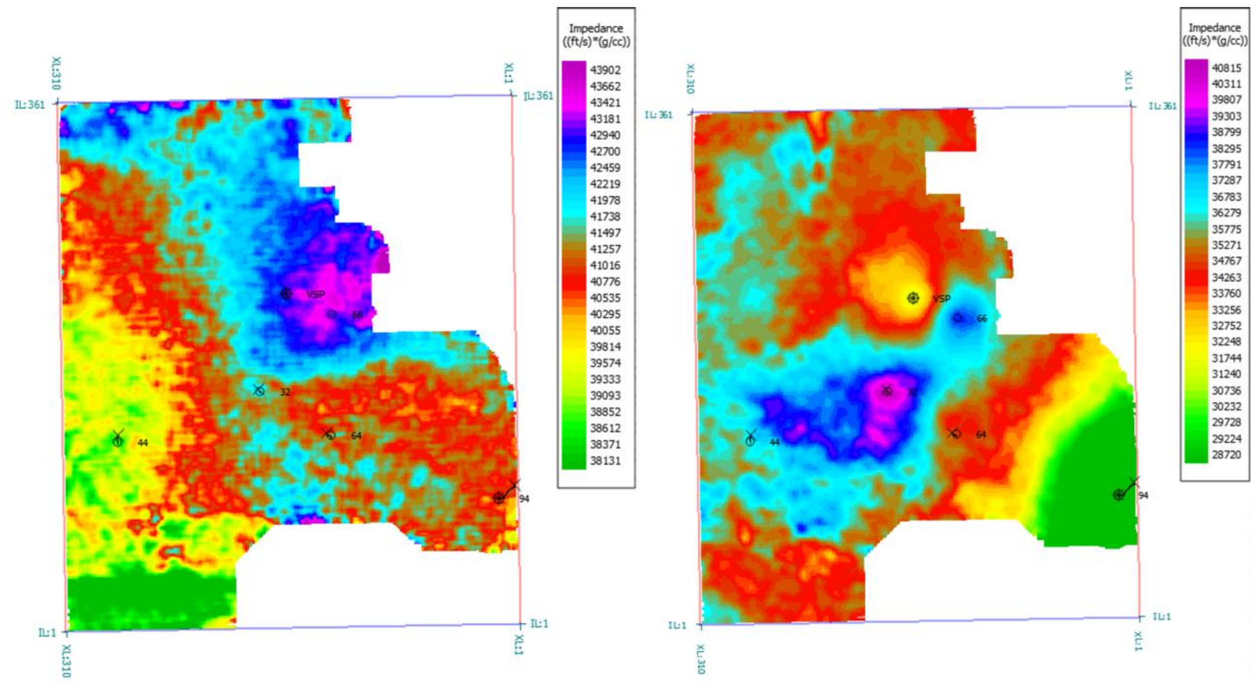

Figure 4.18 AVA inversion: horizon slice of inverted P-wave impedance of Upper Green River formation (left) and Wasatch-180 (right).

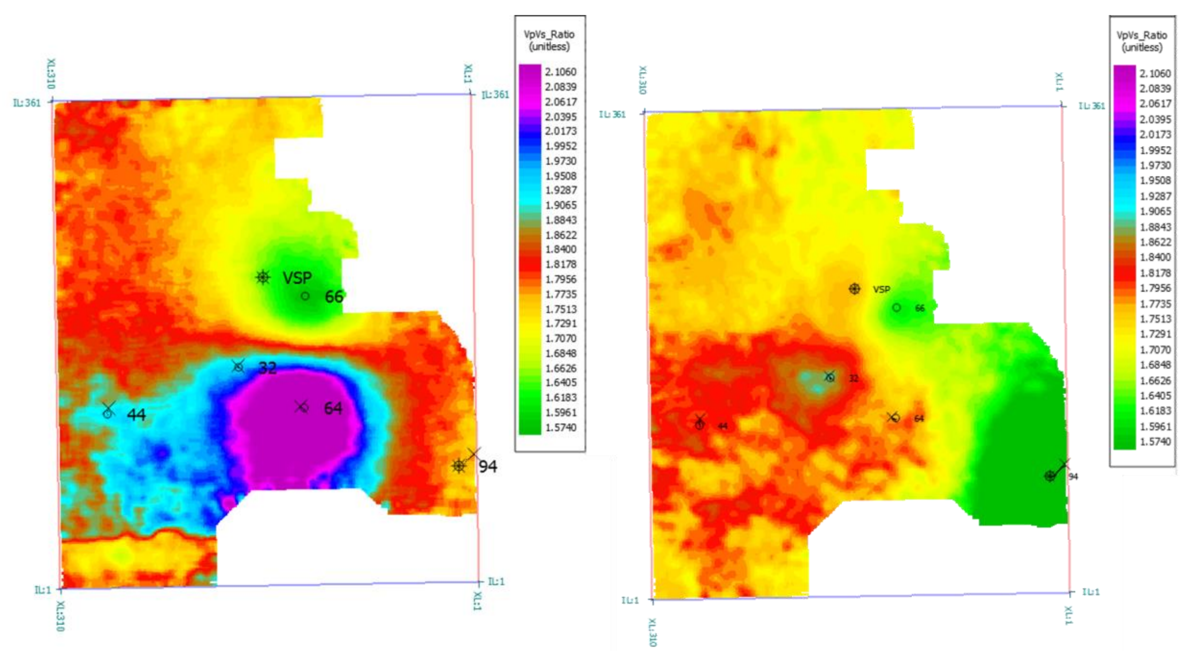

Figure 4.19 AVA inversion: horizon slice of inverted Vp/ Vs of Upper Green River formation (left) and Wasatch-180 (right).

4.3 Amplitude Variations with Azimuth (AVAZ) analysis

Rüger (1998) derived the reflection and transition function for different scenarios of transversely isotropic medium. His approximations include the PP, PS and SS waves for VTI and HTI cases. His approximation is valid for pre-critical incidence angles on an interface between two weakly anisotropic HTI media with the same direction of axis of symmetry and small jumps in the elastic properties across the boundary (Rüger, 1998). Vavryčuk and Pšenčík, (1998) derived the reflection and transmission coeffecients for interface separating two weak but arbitrary anisotropic media.

The stiffness tensors for HTI and VTI medium are different because of different directions of symmetry axes as defined by (Musgrave, 1970; Rüger,1996)

$$c^{HTI} = \begin{bmatrix} c_{11} & c_{13} & c_{13} & 0 & 0 & 0 \\ c_{13} & c_{33} & (c_{33} - 2c_{44}) & 0 & 0 & 0 \\ c_{13} & (c_{33} - 2c_{44}) & c_{33} & 0 & 0 & 0 \\ 0 & 0 & 0 & c_{44} & 0 & 0 \\ 0 & 0 & 0 & 0 & c_{55} & 0 \\ 0 & 0 & 0 & 0 & 0 & c_{55} \end{bmatrix} \tag{4.300}$$

and

$$c^{VTI} = \begin{bmatrix} c_{11} & (c_{11} - 2c_{66}) & c_{13} & 0 & 0 & 0 \\ (c_{11} - 2c_{66}) & c_{11} & c_{13} & 0 & 0 & 0 \\ c_{13} & c_{13} & c_{33} & 0 & 0 & 0 \\ 0 & 0 & 0 & c_{44} & 0 & 0 \\ 0 & 0 & 0 & 0 & c_{44} & 0 \\ 0 & 0 & 0 & 0 & 0 & c_{66} \end{bmatrix} \tag{4.31}$$

HTI and VTI media have five independent parameters. For VTI media, Thomsen (1986) defined three anisotropic parameters (δ, ε, and γ) together with two velocity parameters (α and β), where $\alpha = V_{P0}$ (the vertical P-wave velocity) and $\beta = V_{S0}$ (the vertical S-wave velocity). Those five parameters completely define VTI , and can be written in terms of the density r and the stiffness coefficients:

$$\alpha = \sqrt{\frac{c_{33}}{\rho}} \tag{4.32}$$

$$\beta = \sqrt{\frac{c_{44}}{\rho}} \tag{4.33}$$

$$\delta = \frac{(c_{13}+c_{44})^2-(c_{33}+c_{44})^2}{2c_{33}(c_{33}-c_{44})} \tag{4.34}$$

$$\epsilon = \frac{c_{11}-c_{33}}{2c_{33}} \tag{4.35}$$

$$\gamma = \frac{c_{66}-c_{44}}{2c_{44}} \tag{4.36}$$

The constant ε can be thought of as the fractional difference of the P-wave velocities in the horizontal direction and the vertical direction, while the constant γ measures the fractional difference of the S-wave velocity in the horizontal direction and the vertical direction. The reflectivity, in an HTI medium, depends on both incident angle and azimuth and is given by:

$$R_P(\theta,\phi) = \frac{1}{2}\frac{\Delta \mathrm{z}}{\bar{\mathrm{z}}} + \frac{1}{2}\left(\left[\frac{\Delta\alpha}{\bar{\alpha}} - 4\left[\frac{\bar{\beta}}{\bar{\alpha}}\right]^2\frac{\Delta G}{G}\right] + \left[\Delta\delta^{(v)} + 8\left[\frac{\bar{\beta}}{\bar{\alpha}}\right]^2\Delta\gamma\right]cos^2(\phi)\right)\sin^2(\theta) + \frac{1}{2}\left(\frac{\Delta\alpha}{\bar{\alpha}} + \Delta\epsilon^{(v)}\,cos^4(\phi) + \Delta\delta^{(v)}sin^2(\phi)\,cos^2(\phi)\right)\sin^2(\theta)\,tan^2(\theta) \tag{4.37}$$

Because of the presence of vertical factures, $\beta(=V_{S0})$ is defined in the HTI case as the velocity of the vertical S wave polarized parallel to the isotropy plane. $G = \rho\beta^s$ is S-wave modulus. The operator Δ is the differential operator on the bedding boundaries.

The angle between the symmetry axis measured from North, ϕ_s, and the source-receiver azimuth measured from North, ϕ_g, is given by $\phi = \phi_g - \phi_s$. The S-wave velocity (β) and the anisotropic parameters are defined in terms of stiffness coefficients with the following relationships:

$$\beta = \sqrt{\frac{c_{55}}{\rho}} \tag{4.38}$$

$$\delta^{(v)} = \frac{(c_{13}+c_{55})^2-(c_{33}+c_{55})^2}{2c_{33}(c_{33}-c_{55})} \tag{4.39}$$

$$\epsilon^{(v)} = \frac{c_{11}-c_{33}}{2c_{33}} \tag{4.40}$$

$$\gamma = \frac{c_{44}-c_{66}}{2c_{66}} \tag{4.41}$$

$\epsilon^{(v)}$ is negative to zero in the case of HTI because that horizontal P-wave velocity traveling perpendicular to fractures cannot be higher than vetrtical P-wave velocity. It can be negligibly small or zero (Thomsen, 1995) or small and negative (Tsvankin, 1997). Although HTI is useful to describe vertically fractured rocks, it is only true for penny-shaped cracks (Delbecq et al., 2013). Bakulin et al. (2000a) Bakulin et al. (2000b) described methods that are useful for lower symmetry than HTI. For AVAZ inversion, the HTI assumption may be sufficient because the deviation from HTI is small relative to signal-to-noise ratio and a form of Equation (4.37) that is similar to the Shuey (1985) form of AVA of Equation $RP(\theta) = A_{iso} + B_{iso}\sin^2(\theta) + C_{iso}\sin^2(\theta)\tan^2(\theta)$

(4.8) was used after ignoring the third term that relates to large incident angles:

$$R_P(\theta,\phi) = A_{iso} + (B_{iso} + B_{ani}\,cos^2(\phi))\sin^2(\theta) \tag{4.37}$$

where

$$B_{ani} = \frac{1}{2}\Delta\delta^{(v)} + 8\left(\frac{\bar{\beta}}{\bar{\alpha}}\right)^2 \Delta\gamma \tag{4.38}$$

The azimuthal angle ($\boldsymbol{\phi}$) is the difference between the source-receiver azimuth and one of the model parameters that is to be inverted for $\boldsymbol{\phi_s}$. The other model parameters are $\boldsymbol{A_{iso}}$, $\boldsymbol{B_{iso}}$, and $\boldsymbol{B_{ani}}$. The objective function is the sum of the square of the differences between the measured data and theoretical data, $\boldsymbol{R_P(\theta, \phi)}$, modeled using *Rüger* (1998). For the AVAZ done in this thesis, an iterative nonlinear optimization called the Barrier method (similar to Newton's method) was used to minimize the objective function. The optimization code calculates and employs full Jacobian and sparse Hessian matrices to search for the minimum of the objective function. The anisotropic gradient, B_{ani}, as function of azimuth forms an ellipse. Therefore, higher azimuthal coverage translates into more accurate fitting of ellipse. Due to the nonlinearity of Equation (4.42), the solution is not unique and yields two possible orientations of symmetry axis, ϕ_s, orthogonal to each other (Rüger, 1996).

To test the algorithm, a synthetic gather was created using the velocities and densities from well logs and assumed values for $\delta^{(v)}$ and γ. The synthetic gather is displayed on Figure 4.20. After 24 iterations of the optimization routine, the isotropy plane was obtained to be 35°; the intercept, isotropic gradient, and anisotropic gradient were estimated to be -0.057, 1.36, and 0.07, respectively (the intercept can be seen on Figure 4.20. The values for anisotropic gradient and isotropy plane obtained by inversion were identical to the values used for forward modeling of the synthetic data.

A single pre-stack reflection was picked on COV gathers for the measured data. $\boldsymbol{R_P(\theta, \phi)}$ is the theoretical data using Rüger (1998). For the stability of the inversion, only full fold (larger than 160) COV gathers were used. The full fold base map is shown in Figure 4.22. Also, the pre-stack amplitude values were borrowed from eight neighboring gathers for each gather. Therefore, pre-stack measured data were used nine times; once in its location and eight times by neighboring locations. The angles of incidence ($\boldsymbol{\theta}$) were calculated using Snell's Law as described above. The incidence angles that were used are up to 45° because of the dense azimuthal coverage from 30 to 40° angles of incidence. Figure 4.23 shows the azimuthal coverage of a single COV gather for different angles of incidence.

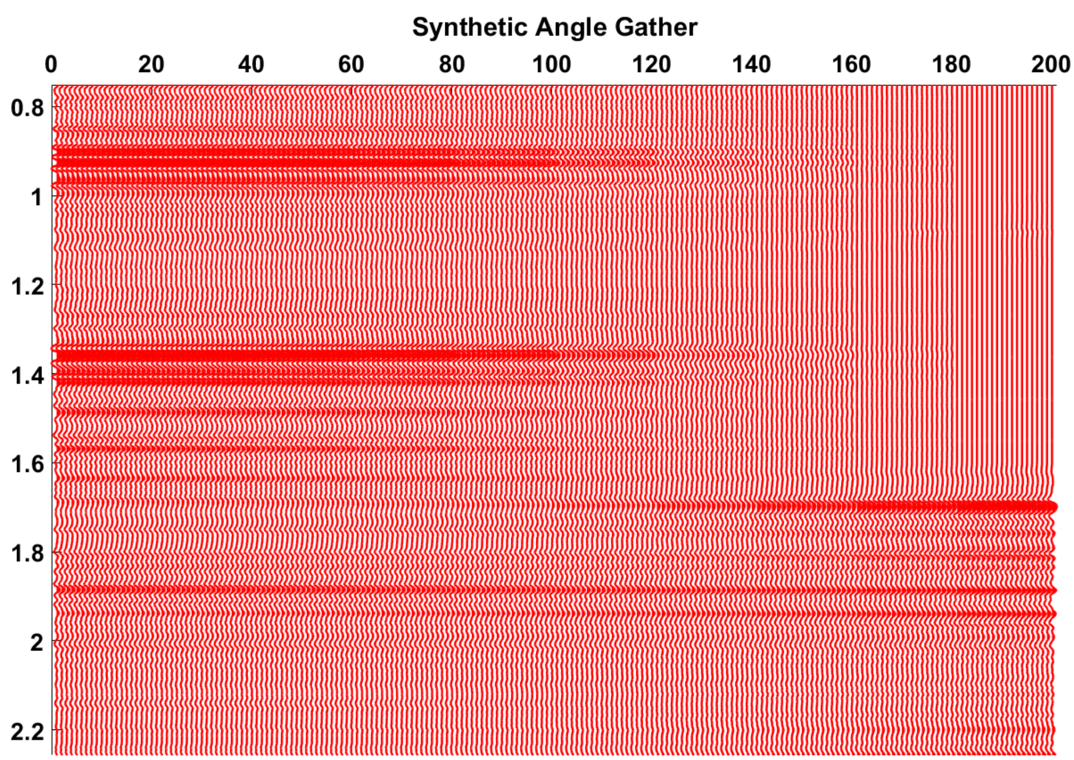

Figure 4.20: Synthetic angle gathers.

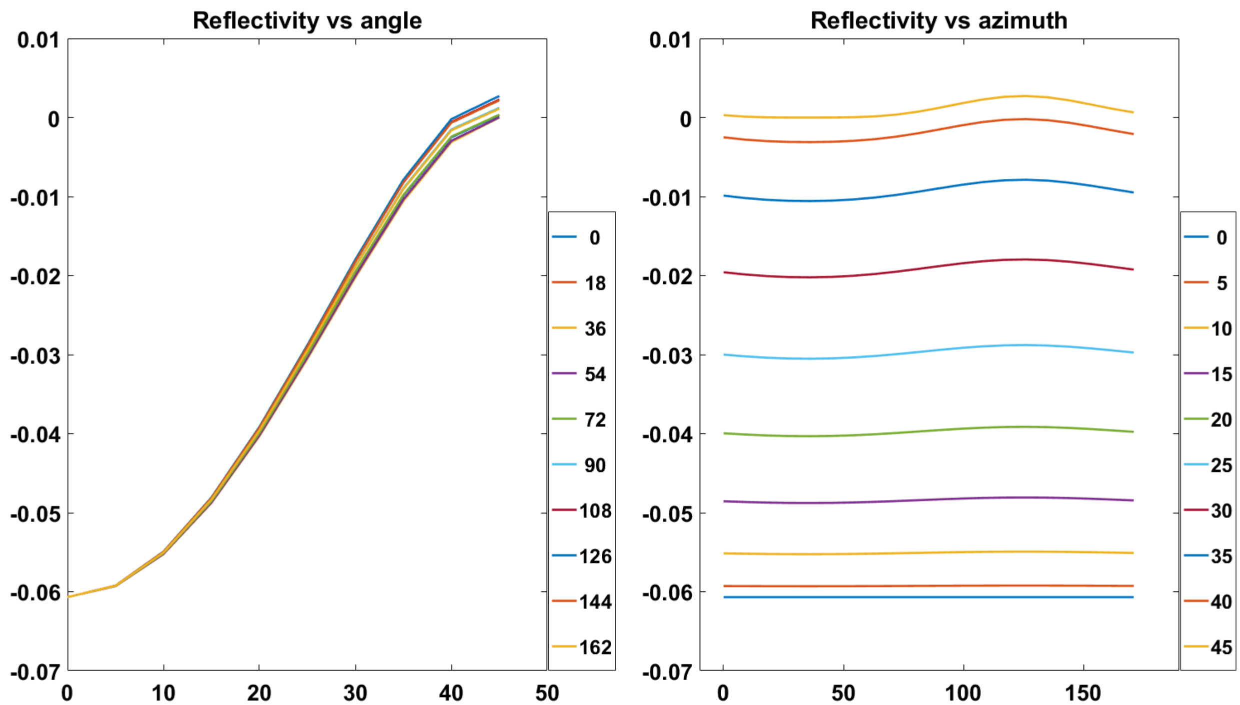

Figure 4.21 Amplitude vs incident angles for different azimuths indicated by curves of different colors (left) and Amplitude vs azimuth for different incident angles azimuths indicated by curves of different colors (right).

The amplitude of a single COV gathers as function of offset for different azimuths can be seen by Figure 4.24. An elliptical trend is found rather than circular which indicates the presence of azimuthal anisotropy. The initial model was set to ($\boldsymbol{\phi_s}, \boldsymbol{A_{iso}}, \boldsymbol{B_{iso}}, \boldsymbol{B_{ani}}$ = 0.1, 0.1, 0.1, 0.1). The model parameters were updated through many iterations of the Barrier optimization algorithm until the objective function was minimized to be less than a small fraction. On average, 25 iterations were required at each CDP location. The final Normalized-Root-Mean-Square (NRMS) error between the pre-stack theoretical and measured values at each CDP location is shown on Figure 4.25 for Upper Green River formation (left) and Wasatch-180 (right).

For penny-shaped cracks model (Hudson, 1981), B_{ani} can be proportional to the crack density, as shown by Figure 4.26. For simplicity, this rock physics model is often used by industry, and was used here. The ambiguity in inverted symmetry axis can be resolved by some priori information, such a rough estimate of $\boldsymbol{B_{ani}}$ or knowledge about symmetry axis directions (Rüger, 1996). For an external constraint, a correlation between AVAZ and VVAZ symmetry orientation can be calculated per horizon for positive and then negative $\boldsymbol{B_{ani}}$. The better correlation decides the sign of $\boldsymbol{B_{ani}}$ and 90^0 is added to $\boldsymbol{\phi_s}$ in the case of $\boldsymbol{B_{ani}}$ sign being altered. For the shallower gas reservoir (Upper Green River), the sign of $\boldsymbol{B_{ani}}$ was constrained to positive. According to Equation (4.43), the positive sign seems physical because it is the first fractured reservoir and the second term is positive and larger than the absolute value of the first negative term. The deeper oil reservoir (Wasatch-180) is overlain by several fractured reservoirs and it is hard to estimate a sign for $\boldsymbol{B_{ani}}$ physically, but a sign was estimated after correlation with VVAZ.

A second shortcoming of AVAZ inversion is that, unlike VVAZ inversion, the effect of overburden anisotropy and shallower layers cannot be removed for the reservoirs. Its main advantage is that, like other amplitude-based methods, it has a high resolution as will be discussed in **Chapter 7**.

AVAZ inversion results for the Upper Green River formation and Wasatch-180 horizons are shown in Figure 4.27 and Figure 4.28 respectively. On the left of those two figures is the B_{ani} that indicates the intensity of azimuthal anisotropy, and on the right is the orientation of the symmetry plane. The Upper Green River formation has two main directions of symmetry plane. The major trend is indicated by green and it is oriented Northwest-Southeast at -20° from North (or 20° from North counter clockwise). The minor trend is 40° from North clockwise. The major trend correlates well to high positive and high negative values of $\boldsymbol{B_{ani}}$. On the other hand, Wasatch-180 reservoir has symmetry plane oriented Northeast-Southwest at is 5° from North clockwise. The $\boldsymbol{B_{ani}}$ values of Wasatch-180 are greater than those of Upper Green River formation. According to the penny-shaped fracture model (Hudson, 1980), this means that the Wasatch-180 is more intensely fractured that the Upper Green River.

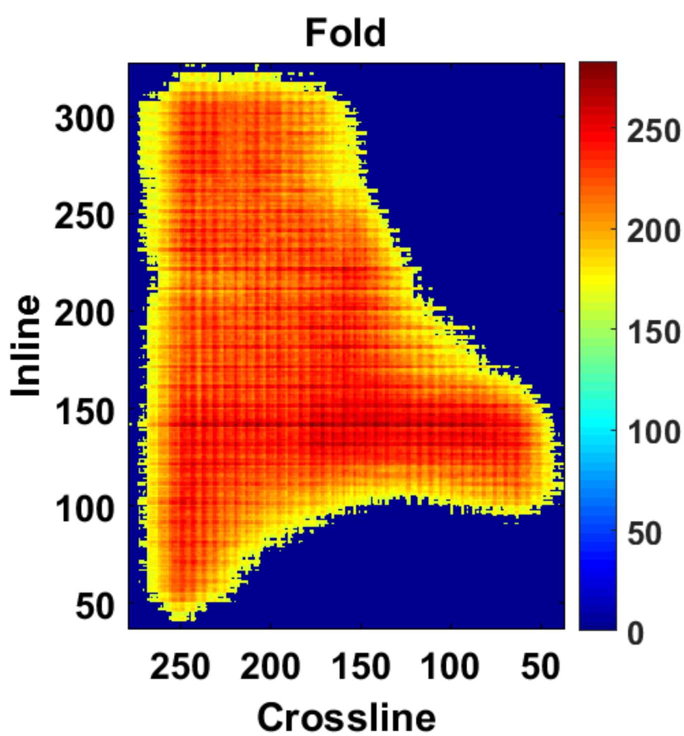

Figure 4.22 Base map of full fold (larger than 160) seismic used for AVAZ inversion.

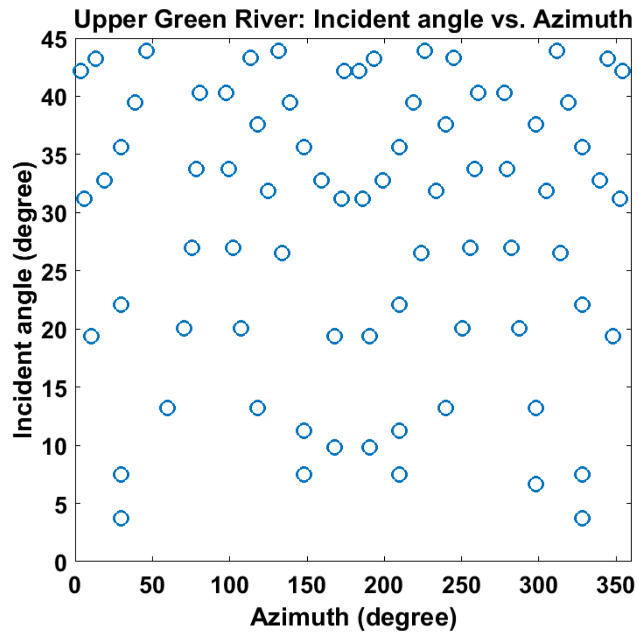

Figure 4.23 Azimuth vs incident angle distribution of a single gather at the Upper Green River horizon. Notice the dense coverage from 30º to 40º angles of incidence.

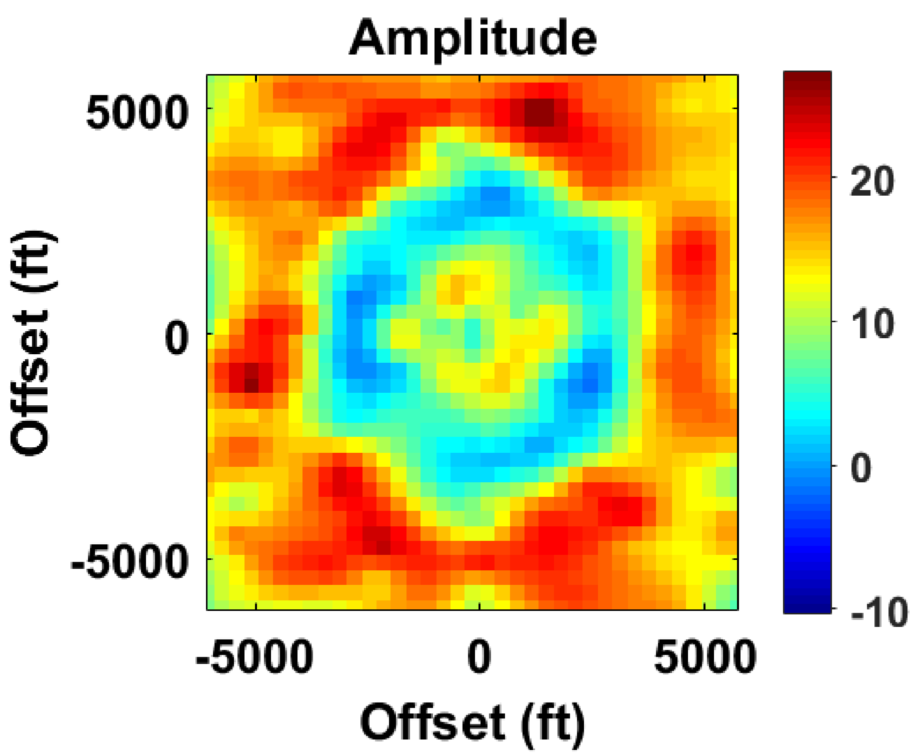

Figure 4.24 Amplitudes of a single pre-stack gather for different azimuths and offsets.

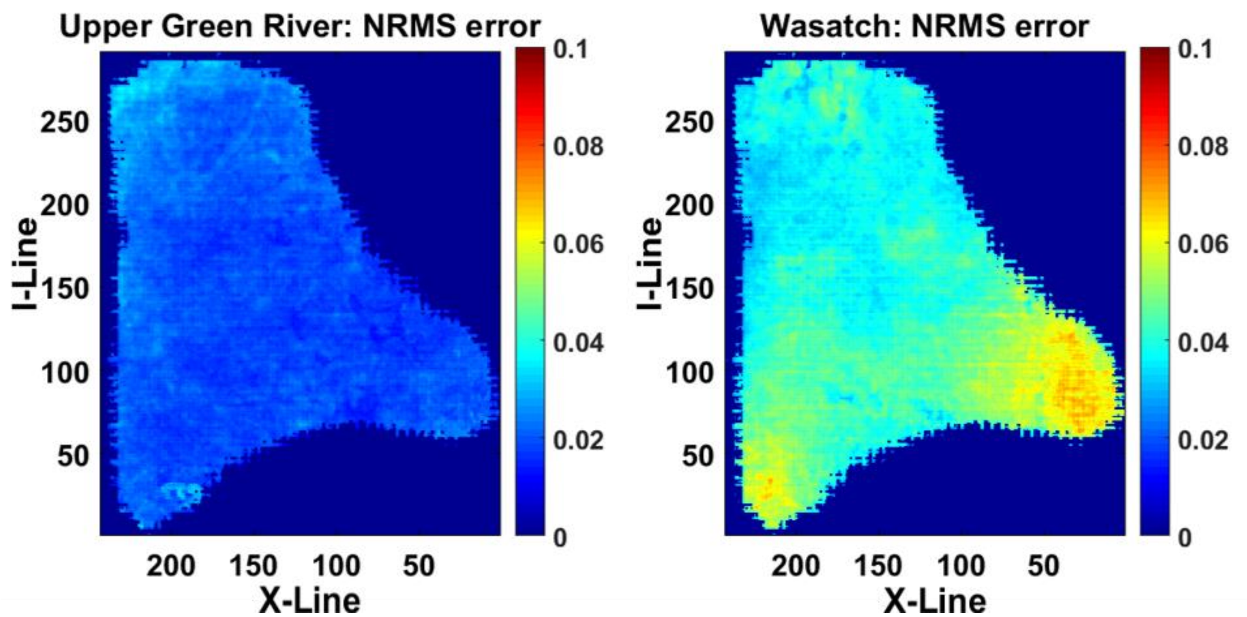

Figure 4.25 NRMS error between theoretical and measured data for Upper Green River formation (left) and Wasatch-180 (right)

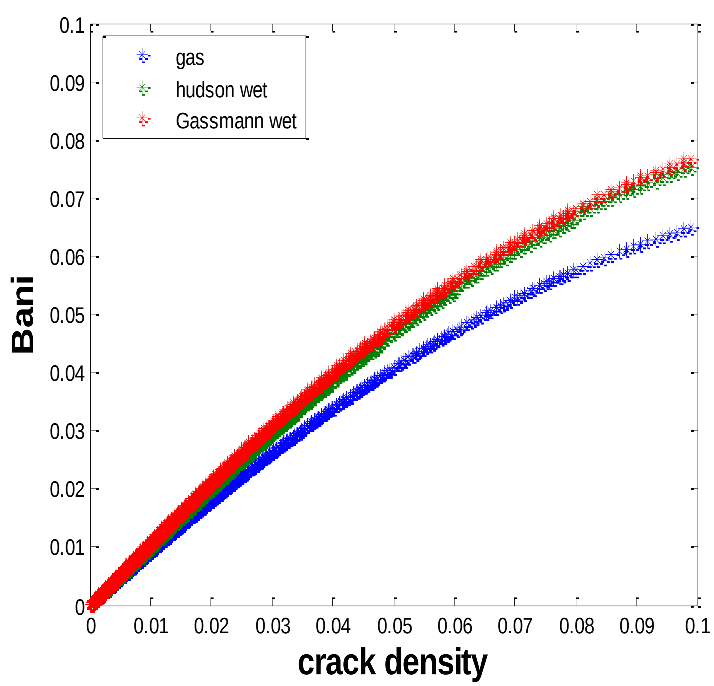

Figure 4.26 B_{ani} vs. crack density of penny-shaped fractures for gas (blue), Hudson wet (Green), and Gassmann wet (red). (after Downton, 2016)

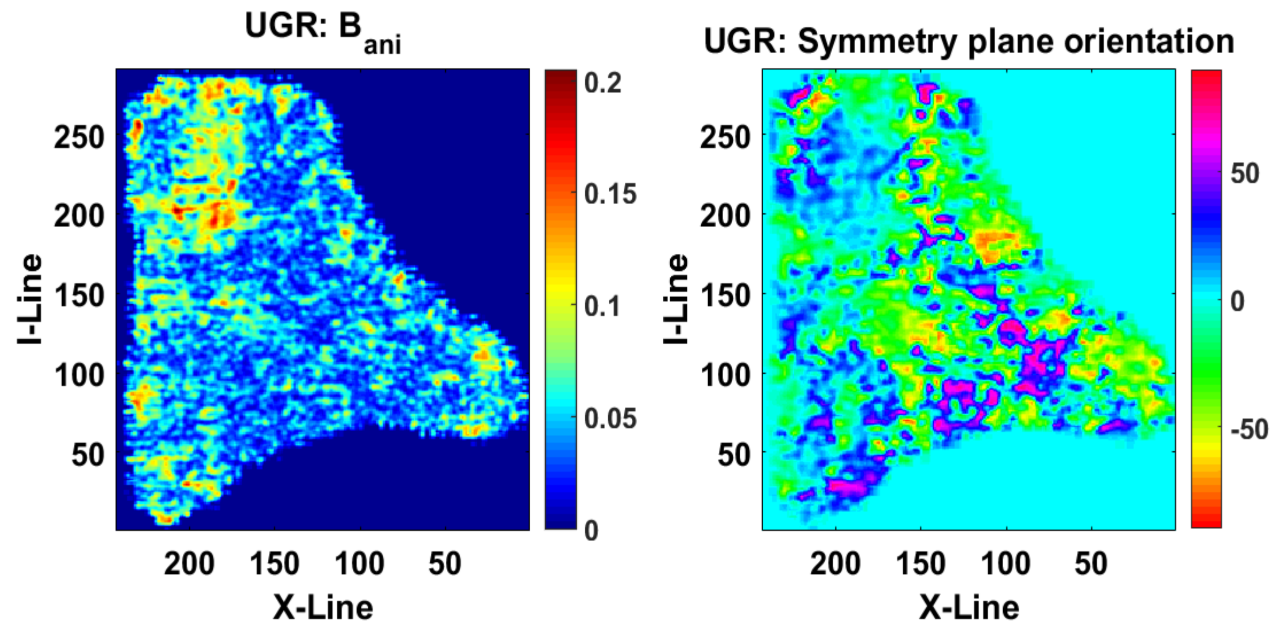

Figure 4.27 AVAZ inversion for Upper Green River: Bani horizon (left), symmetry plane orientation horizon (middle), and symmetry plane orientation circular histogram (right).

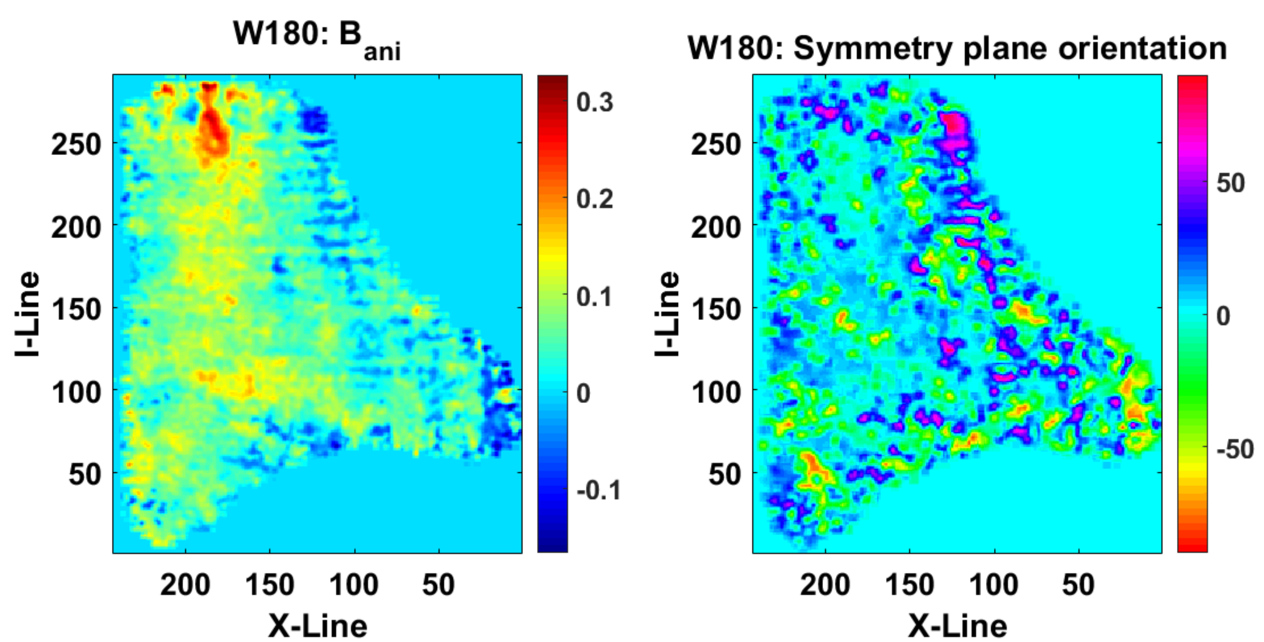

Figure 4.28 AVAZ inversion for Wasatch-180: Bani horizon (left), symmetry plane orientation horizon (right).

4.4 **Summary**

In this chapter, AVA inversion (based on a simplified Zoeppritz equation) was used to estimate elastic stiffness coefficients from 3D pre-stack data acquired at the Altamont-Bluebell field. These estimated isotropic elastic stiffness coefficients can be useful for identifying sweet spots, i.e., zones of high hydrocarbon potential.

In addition, AVAZ inversion (based on a simplified Rüger's equation describing reflections from HTI media) was used to estimate four anisotropic parameters from azimuthally varying reflection amplitudes and NMO velocities. These estimated anisotropic parameters can be useful for estimating fracture density and orientation in subsurface rock formations. An ambiguity exists in the estimated fracture plane orientation. This ambiguity can be resolved by using results of VVAZ inversion as a priori information for the AVAZ inversion.

Because, the reservoirs of Altamont-Bluebell are unconventional and fractures play a significant role in production, anisotropy intensity and orientation maps were calculated per reservoir top. The anisotropy plane orientation is found to have a major Northwest-Southeast trend for both reservoirs, while the anisotropy intensity is found to be greater for Wasatch-180 formation than Upper Green River formation. However, the interpretation of AVAZ inversion results in isolation is not recommended. Interpretation of the AVAZ results should be done in collaboration with the VVAZ inversion results. Joint interpretation is discussed in **Chapter 7**.

Chapter 5 VVAZ of 3D Pre-stack Seismic Data

A method for VVAZ inversion, based on the elliptical NMO equation for Transverse Isotropy (TI) media that was derived by Grechka and Tsvankin (1998), is applied. For Altamont-Bluebell field 3D seismic data, isotropic velocities are used along with azimuthally variant time residuals to estimate fast and slow NMO velocities and their directions. Along with fast and slow NMO velocity maps, maps of fracture-induced anisotropy orientation and intensity were created. Dix (1955)-type interval properties are calculated to estimate interval anisotropy for each reservoir interval.

Prior to applying the azimuthal velocity analysis technique, it was tested using a physical modeling dataset. In the laboratory, a three-layer model was built using vertically laminated Phenolic overlain by Plexiglas to represent a fractured reservoir overlain by an isotropic overburden. HTI planes of phenolic have an orientation in northern half of the model that is orthogonal to HTI planes in southern half. A third layer of water is added to the model. 3D seismic data are acquired in patches. The data are processed and deconvolved with surface-consistent true relative amplitudes so they can be used for amplitude analysis. The third reflector, in the CDP domain, is very weak due to attenuation of anisotropic phenolic and low fold of data. Consequently, data were azimuthally sectored, stacked and filtered. Then, orientation and intensity of anisotropy are estimated by VVAZ. The results of the anisotropy orientation analysis match the charachtristics of the physical model.

5.1 Velocity Variations with Azimuth (VVAZ)

Grechka and Tsvankin (1998) showed that azimuthal variations of NMO velocities can be estimated by fitting an ellipse in the horizontal plane to travel time variations under four assumptions. First, the medium is arbitrarily anisotropic and inhomogeneous, so the azimuthal variations in travel times are a smooth function of surface locations. Second, travel times exist at all azimuths. A case of salt domes creating a shadow zone at a specific azimuth violates the second assumption, for example. The third assumption is routinely made in seismic data processing steps, such as CMP binning and stacking. That is travel times can be described by a Taylor series expansion of $t^2 x_\phi^2$, where t and x_ϕ are travel times and source-receiver offset at specific azimuth. Lastly, travel times increase with offset at all azimuths. Those assumptions are non-restrictive in most cases. Grechka and Tsvankin (1998) derived an elliptical NMO equation for TI media where source-receiver offset does not exceed the depth of the reflector. Hyperbolic NMO can be approximated by:

$$T^2 = T_0^2 + \frac{x^2}{V_{NMO}^2(\phi)}, \qquad (5.1)$$

where

$$\frac{1}{V_{NMO}^2(\phi)} = \frac{1}{V_{slow}^2} cos^2(\phi - \beta_s) + \frac{1}{V_{fast}^2} sin^2(\phi - \beta_s), \qquad (5.2)$$

where T is the total two-way travel times, T_0 is the zero-offset two-way travel times. x is the offset, V_{fast} and V_{slow} are the fast and slow NMO velocities respectively. β_s is the azimuth of the slow NMO velocity, while $V_{NMO}(\phi)$ is the NMO velocity as function of the source-receiver azimuth (Figure 5.1).

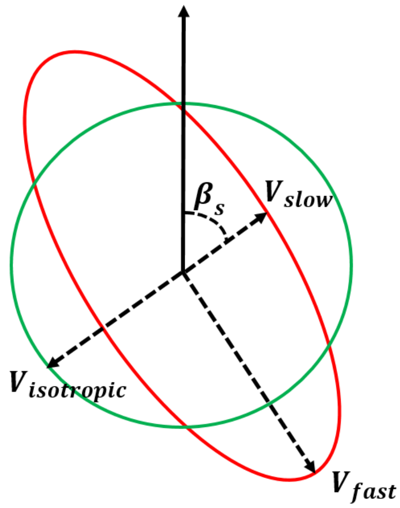

Figure 5.1. Isotropic RMS velocity vs azimuthally variant RMS velocity.

Equation (5.2) can be written as:

$$\frac{1}{V_{NMO}^2(\phi)} = W_{11}\cos^2(\phi) + 2W_{12}\cos(\phi)\sin(\phi) + W_{12}\sin^2(\phi), \tag{5.3}$$

where W_{11}, W_{12}, and W_{22} are the ellipse coefficients that are related to the slow and fast NMO velocities and to the azimuth of the slow NMO velocity by

$$\frac{1}{V_{fast}^2} = \frac{1}{2}[W_{11} + W_{22} - \sqrt{(W_{11} - W_{22})^2 + 4W_{12}^2}, \tag{5.4}$$

$$\frac{1}{V_{slow}^2} = \frac{1}{2}[W_{11} + W_{22} + \sqrt{(W_{11} - W_{22})^2 + 4W_{12}^2}, \tag{5.5}$$

$$\beta_s = \tan^{-1}\frac{W_{11}-W_{22}+\sqrt{(W_{11}-W_{22})^2+4W_{12}^2}}{2W_{12}}. \tag{5.6}$$

The azimuth of the fast velocity is oriented at 90° to the azimuth of the slow velocities as shown by Figure 5.1 (Jenner, 2001). The total travel can be written as:

$$T^2 = T_0^2 + x^2\cos^2(\phi)W_{11} + 2x\,cos(\phi)\sin(\phi)W_{12} + x^2\sin^2(\phi)W_{22}. \tag{5.7}$$

Equation (5.7) can be written as:

$$\boldsymbol{d} = \boldsymbol{Gm}\,, \tag{5.8}$$

where d is n-dimensional data vector, m is the 6-dimensionl model parameter vector, and G is the n-by-4 data kernel as:

$$\begin{pmatrix} T_1^2 \\ T_2^2 \\ \vdots \\ T_n^2 \end{pmatrix} = \begin{pmatrix} 1 & x_1^2\cos^2(\phi_1) & 2x_1\,cos(\phi_1)\sin(\phi_1) & x_1^2\sin^2(\phi_1) \\ 1 & x_1^2\cos^2(\phi_1) & 2x_1\,cos(\phi_1)\sin(\phi_1) & x_1^2\sin^2(\phi_1) \\ \vdots & \vdots & \vdots & \vdots \\ 1 & x_{n1}^2\cos^2(\phi_n) & 2x_1\,cos(\phi_1)\sin(\phi_1) & x_1^2\sin^2(\phi_1) \end{pmatrix} \begin{pmatrix} T_0^2 \\ W_{11} \\ W_{12} \\ W_{22} \end{pmatrix}. \tag{5.9}$$

Equation (5.9) can be used to solve for the model parameters and estimate anisotropic parameters:

$$\boldsymbol{m} = (\boldsymbol{G^T G})^{-1}\boldsymbol{G^T d}. \tag{5.10}$$

5.2 Physical modeling for VVAZ

A physical model was created in the laboratory and is shown in Figure 5.2. The physical model consists of three layers. The first layer is water and it is 300-m thick in field scale. The second layer is Plexiglas and its thickness is 510 m. The first two layers represent the isotropic overburden. The third layer is 650-m thick consisting of two phenolics joined at the linear boundary between north and south. Those two phenolics represent a fractured reservoir. In the northern half, the symmetry axis is orthogonal to the symmetry axis of the southern half as indicated by the surface view of the third layer shown in Figure 5.3. Notice that the two blocks of phenolic will not only affect travel times and amplitude, but also act as a fault in CDP time stacks as can be seen later.

To use the data for velocity and amplitude variations with azimuth, we implemented a standard 3D processing workflow. We faced and addressed three challenges to image the bottom of the Phenolic: 1. The fold was not large enough, 2. Phenolic generates very strong mode-converted PS waves, and 3. The Phenolic is attenuative.

In the Phenolic medium, the P wave is fastest (3570 m/s) along the vertical laminations, slowest (2900 m/s) perpendicular to the vertical lamination, and somewhere in between along other directions. On the other hand, the S wave is fastest (1700 m/s) along the vertical laminations, slowest (1520 m/s) perpendicular to the vertical lamination, and undergoes S-wave splitting in other directions.

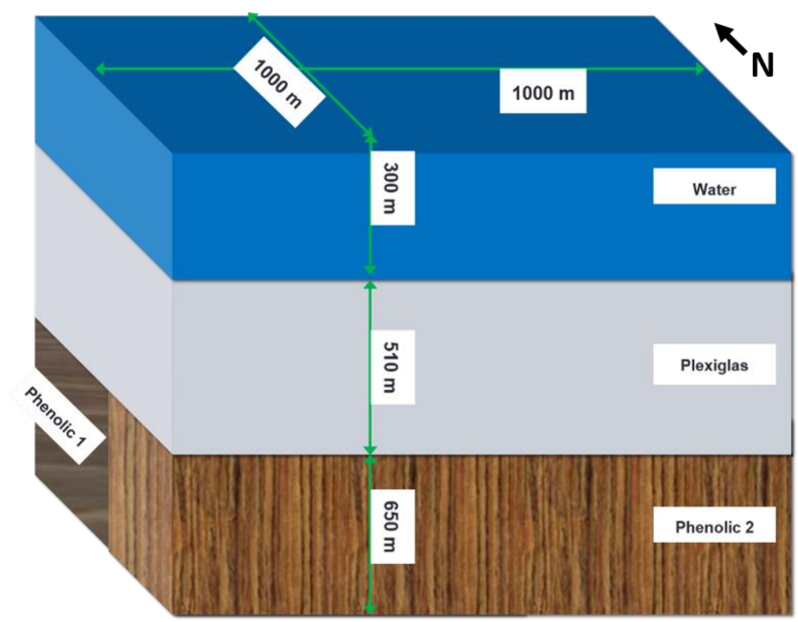

Figure 5.2. A three-layer physical model. The model is constructed using vertically laminated Phenolic overlain by Plexiglas to represent a fractured reservoir overlain by an isotropic overburden. HTI planes of phenolic have an orientation in northern half of the model that is orthogonal to HTI planes in southern half. A third layer of water is added to the model. Laboratory to field scale is 1:10,000 in both length and time. Scaled thicknesses of the three layers are: 300 m, 510 m, and 650 m.

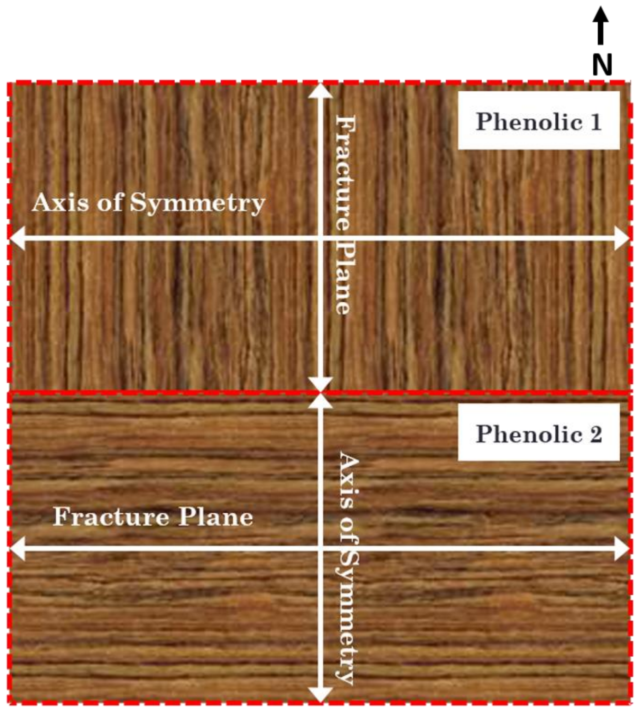

Figure 5.3. A surface-view of the third layer consisting of two Phenolic media with axis of symmetry in the northern half orthogonal to the axis of symmetry in the southern half. Acquisition inline direction is N-S, and crossline acquisition direction is E-W.

The 3D seismic data were acquired over the physical model shown in Figure 5.2. The laboratory to field scale is 1:10,000 in both length and time. Scaled thicknesses of the three layers are: 300 m, 510 m, and 650 m. 3D seismic data were acquired over a scaled area of 4,000 m^2. Piezopin transducers were used as P-wave sources and receivers, with a central frequency at 2.38 MHz. Source and receiver transducers were positioned with a robotic system that has an error of less than 0.1 mm in laboratory scale. Just as in conventional 3D seismic acquisition, data were acquired in patches. For each shot, 10 receivers were live with a specific maximum offset. Receiver lines are oriented east to west and have spacing of 50 m. Source lines are oriented north to south and have spacing of 100 m. Source and receiver spacings are 100 m and 50 m respectively.

Data specifications, described above, yield a fold and azimuth distribution that is shown by Figure 5.4. Color indicates fold of 50 m x 25 m bins. High fold zone is indicated by red where fold is 120. Lower histogram indicates the azimuth distribution from -90^o to 90^o with reference to the north (*y*-axis). Figure 5.16 shows a shot gather with 10 receiver lines, and three main reflectors indicated. These three reflectors are top of plexiglass, top of phenolic and base of phenolic. Notice that the third reflector can barely been seen. Our target is the anisotropic layer between the second and third reflector.

For Amplitude Variations with Azimuth (AVAZ) we are interested in the second reflector which is strong and there should not pose a problem. On the other hand, for Velocity Variations with Azimuth (VVAZ), we are interested in the third reflector which is very weak because P waves travel through the phenolic layer twice. The phenolic layer is observed to create very strong mode-converted waves. Also, it is P-wave attenuative. One solution to these issues is to increase the fold, which can be achieved only by acquisition. In this report, attempts to overcome the issues caused by inadequate spatial sampling are made by processing in time-domain and involve two main steps:

1. A common-offset stack for a complete half of the model where anisotropy orientation is known to be constant.
2. An FK filter designed to attenuate PS mode-converted waves.

A spherical divergence correction was applied. Then, surface-consistent amplitude scaling was calculated and applied. Four scalers (source, receiver, offset, and CDP) were specifically calculated and applied. A surface-consistent deconvolution (Cary and Lorentz, 1993) was applied, followed by another pass of surface-consistent amplitude scaling. Figure 5.6 shows a shot gather before and after the application of surface-consistent amplitude and deconvolution, while corresponding amplitude spectra are shown by Figure 5.7. From the gather and spectra, we can see that higher frequencies are boosted and the amplitude spectrum becomes flatter over the data frequency band.

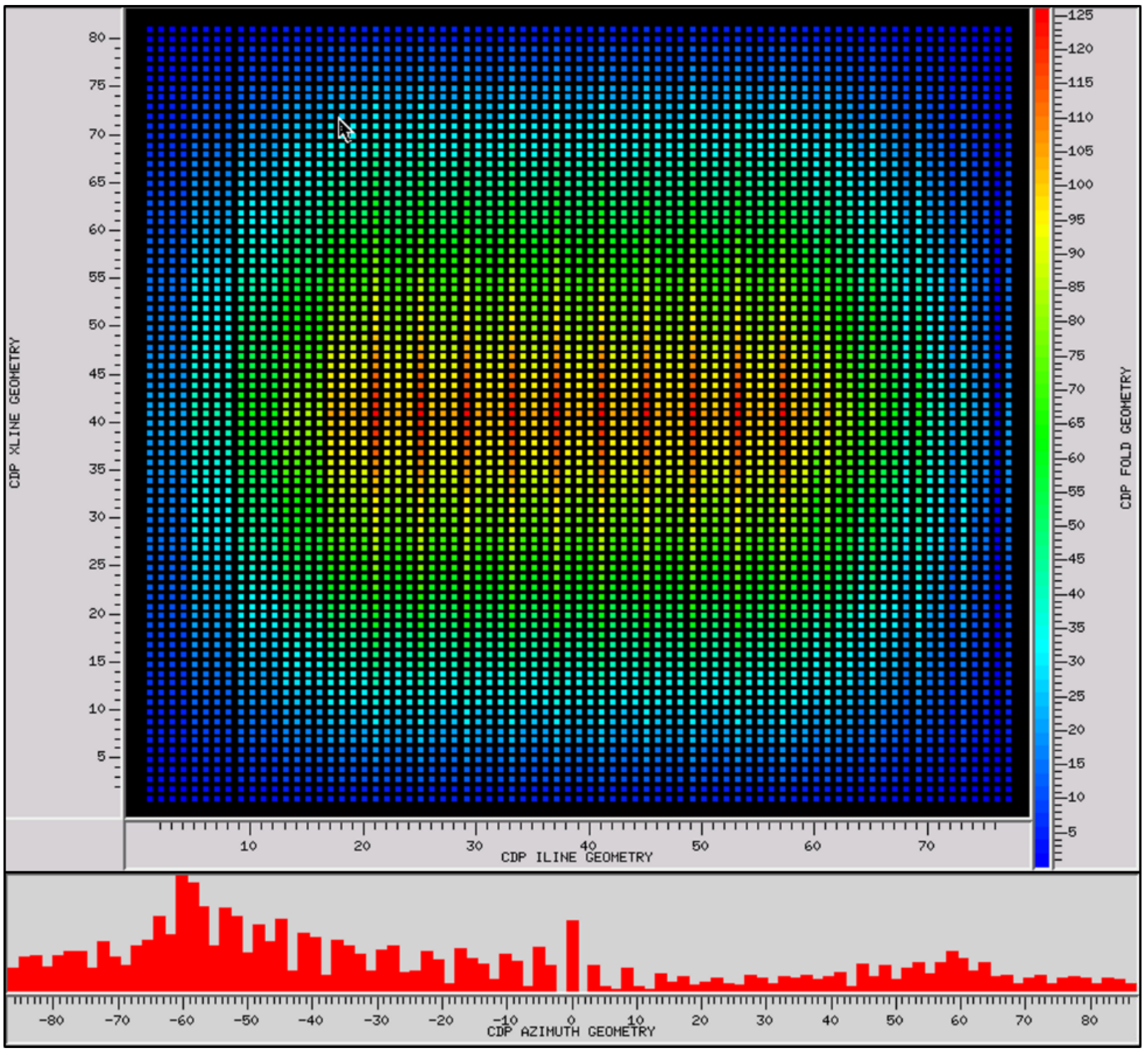

Figure 5.4. A basemap for the 3D seismic physical modeling dataset. Color indicates fold of 50mx25m bins. High fold zone is indicated by red where fold is 120. Lower histogram indicates the azimuth distribution from -90° to 90° with reference to the north (y-axis).

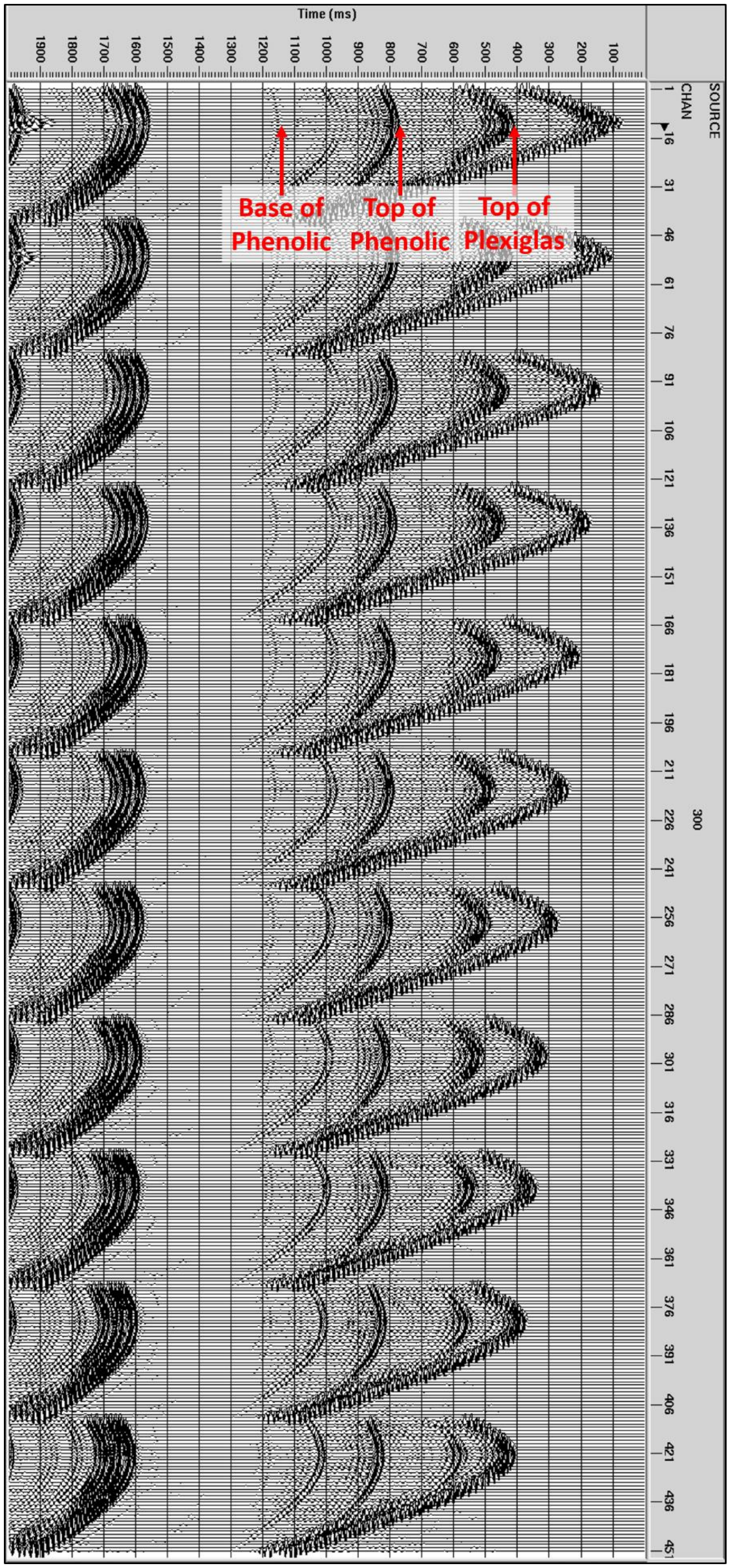

Figure 5.5 A shot gather: 10 receiver lines. Target is Phenolic, between 2nd and 3rd reflector.

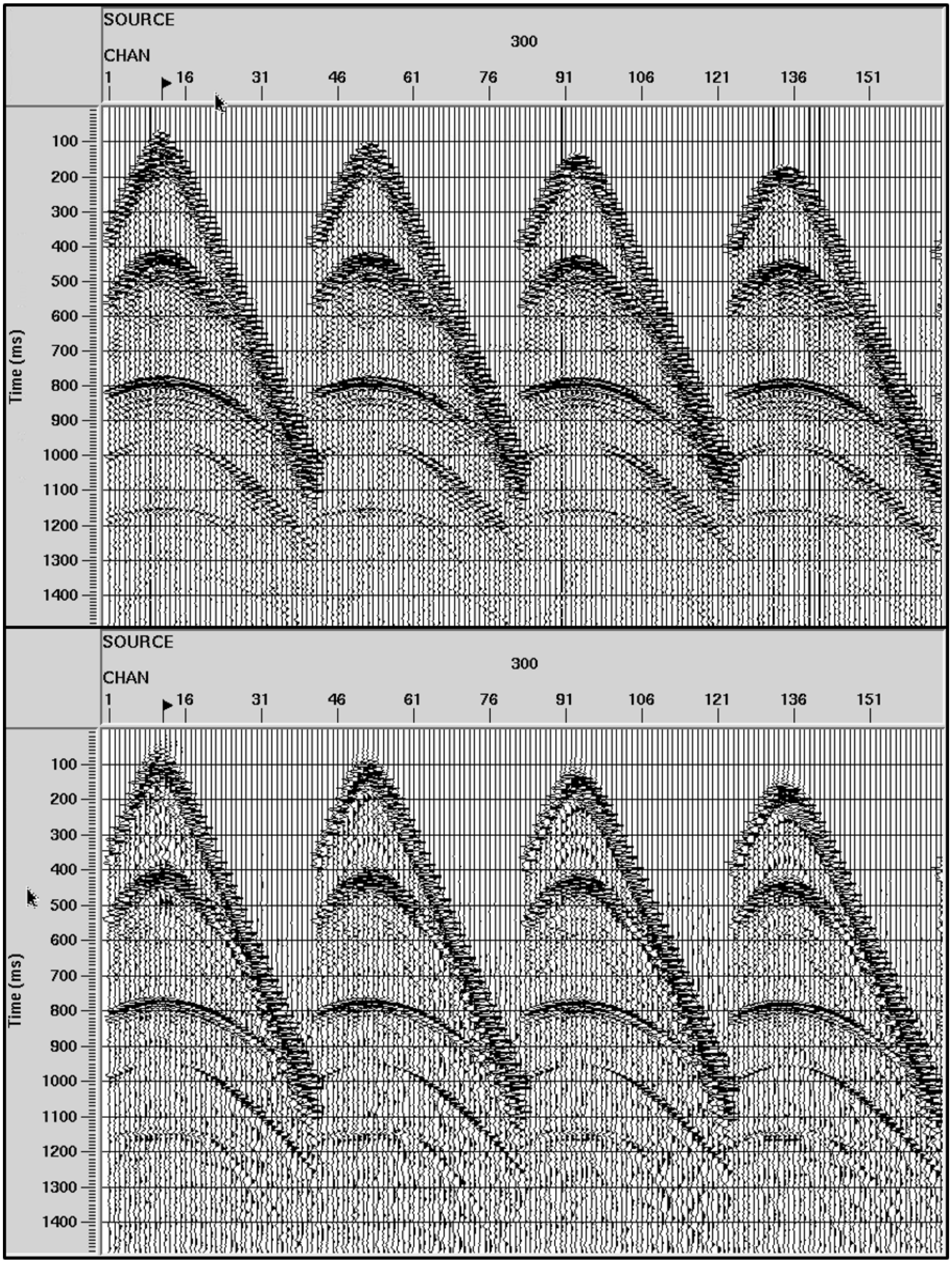

Figure 5.6 A shot gather: 4 out of 10 receiver lines are shown. Data are shown before applying surface-consistent amplitude scaling and deconvolution (top) and after applying surface-consistent amplitude scaling and deconvolution (bottom). Note the prominent PS arrivals with apexes at about 950 ms.

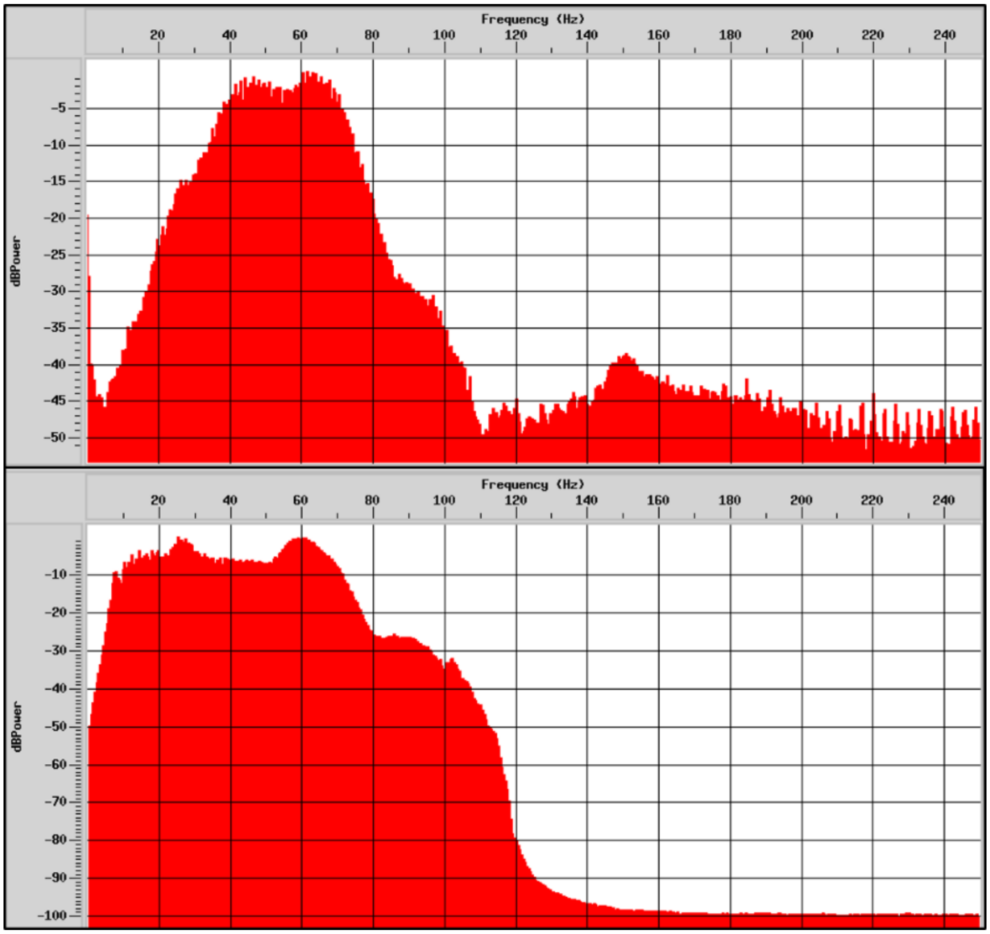

Figure 5.7 Amplitude spectra: before deconvolution (top) and after deconvolution (bottom).

Velocity analysis was done by creating semblance coherency of super gathers. The maximum semblance (stacking response) were picked manually as shown by Figure 5.8. Figure 5.8 also shows the super gather after applying the picked NMO velocities. NMO corrections were applied to all CDP sorted data and stacked. Figure 5.9 shows a N-S inline (top) and E-W crossline (bottom). The three strong reflectors are: the top of the plexiglas, the top of the phenolic and the bottom of the phenolic. HTI planes of phenolic have an orientation in the northern half of the model that is orthogonal to HTI planes in the southern half. CMP stacks are created using isotropic NMO velocities. From the geometry of the model, crosslines are always aligned either along the symmetry plane or the symmetry axis, while inlines are aligned along the symmetry planes in northern half of the model and along the symmetry axis in southern half (Figure 5.3). The boundary between the northern and southern halves can be considered as a fault, as well, in the CDP stack time domain. If non-hyperbolic NMO, or anisotropic time migration, had been applied, then this seam might be unnoticeable.

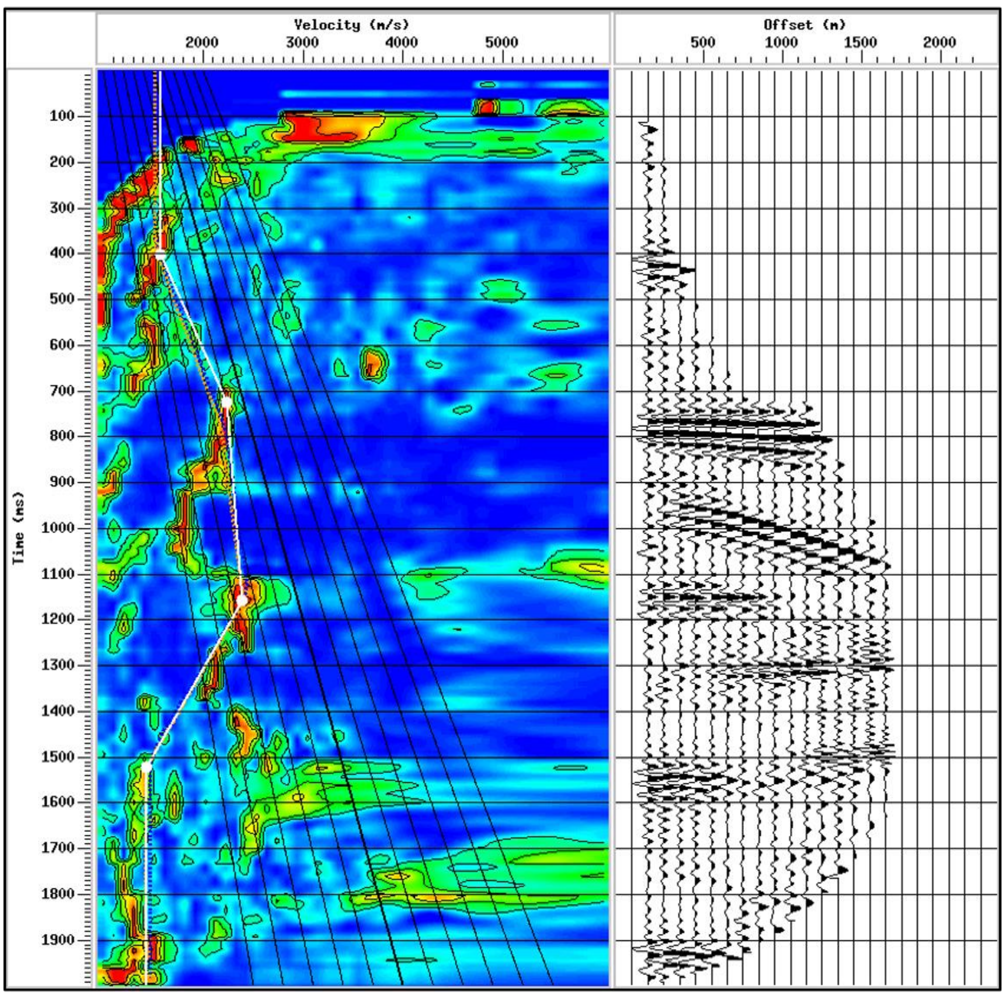

Figure 5.8 Velocity analysis: A semblance coherency with picks of maximum stacking indicated by white dots (left) and CDP gather with flat reflection events (right).

The resolution matrix (N) measures how well the data kernel, G, resolves the model parameter, m (Lay, 1996). The ideal resolution matrix is diagonal, any non-zero off-diagonal elements indicate trade-off between model parameters. The resolution matrix is calculated by Equation (3.18) and shown in Figure 5.10. Because the bottom of phenolic reflection is very weak, common-offset stacks were created for the two halves of the model where the anisotropy orientation of the phenolic is constant. To strengthen the energy of the third reflector, an FK filter was designed and applied in an attempt to attenuate the strong PS mode-converted waves. Figure 5.11 shows a common-offset stack of all azimuths: before (left) and after (right) application of FK filter for the attention of PS mode-converted wave at top of the phenolic. The reflector is significantly improved at time 1140 ms and near offset. Prior to stacking offset bins, the data were sectored every 30^o from -90^o to 90^o. Figure 5.12 shows two common-offset stacks: 0^o sector (left) and $\pm 90^o$ (right). Also, picks of the bottom of the phenolic are indicated by red. Those time picks at different azimuths form the data vector in Equation (5.8).

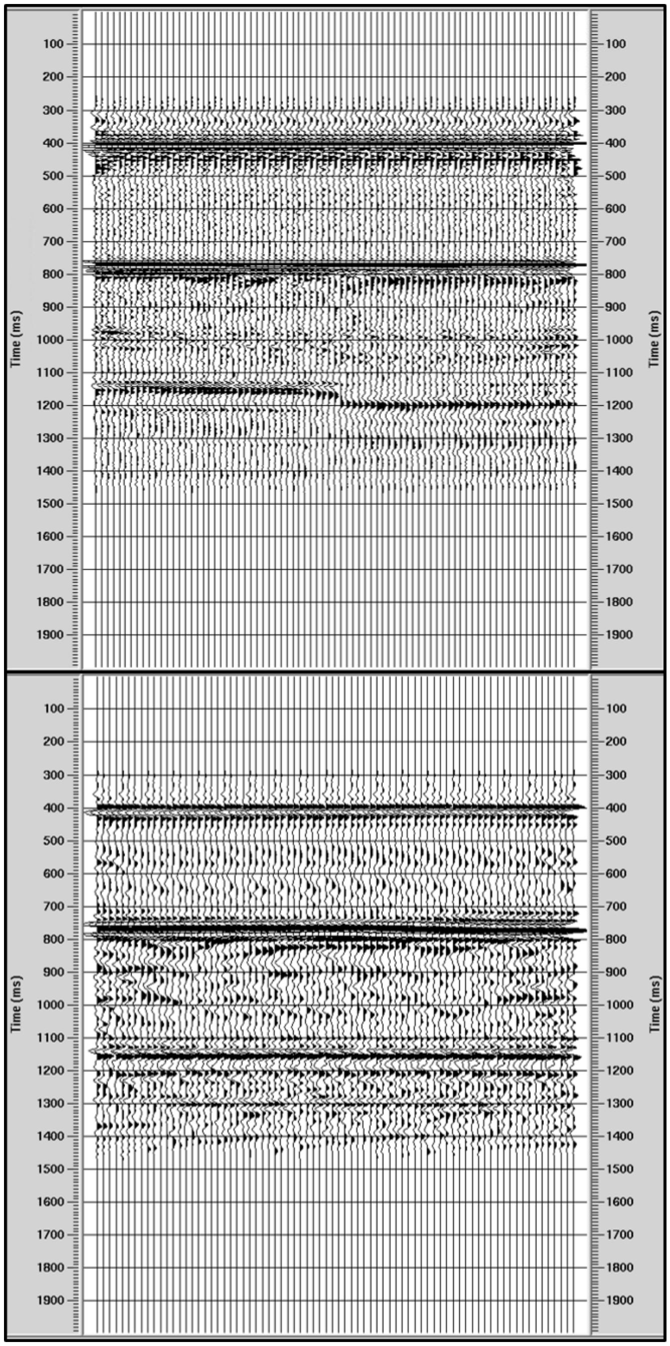

Figure 5.9 CDP Stacks: a N-S inline (top) and E-W crossline (bottom). The three strong reflectors are: top of plexiglas, top of phenolic and bottom of phenolic. HTI planes of phenolic have an orientation in northern half of the model that is orthogonal to HTI planes in southern half. CMP stacks are created using isotropic NMO velocities. From the geometry of the model, crosslines are always parallel to HTI planes in the northern half of the model. Crosslines are perpendicular to HTI planes in southern half of the model, as can be seen by the third reflector (bottom of phenolic). That seam can be interpreted as a fault.

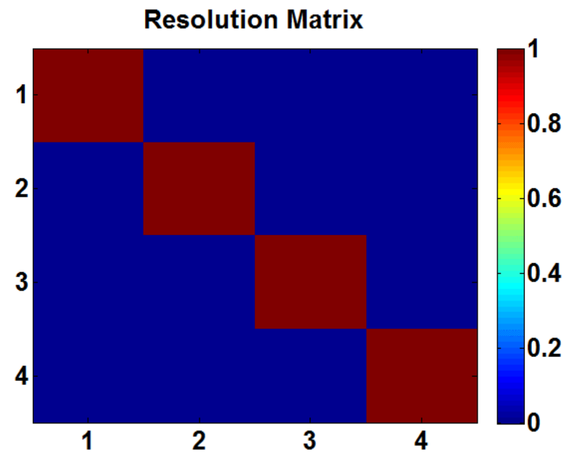

Figure 5.10 The resolution matrix of the geometry of all offset and azimuth used for VVAZ.

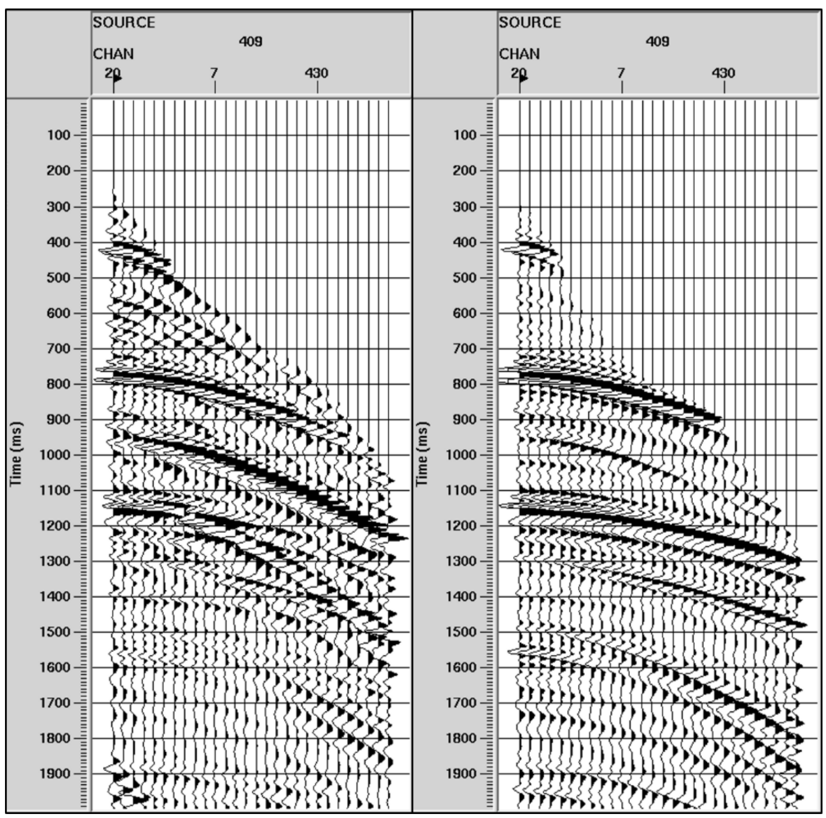

Figure 5.11 Common-offset stack of all azimuths: before (left) and after (right) application of FK filter for the attenuation of PS mode-converted wave at top of the phenolic.

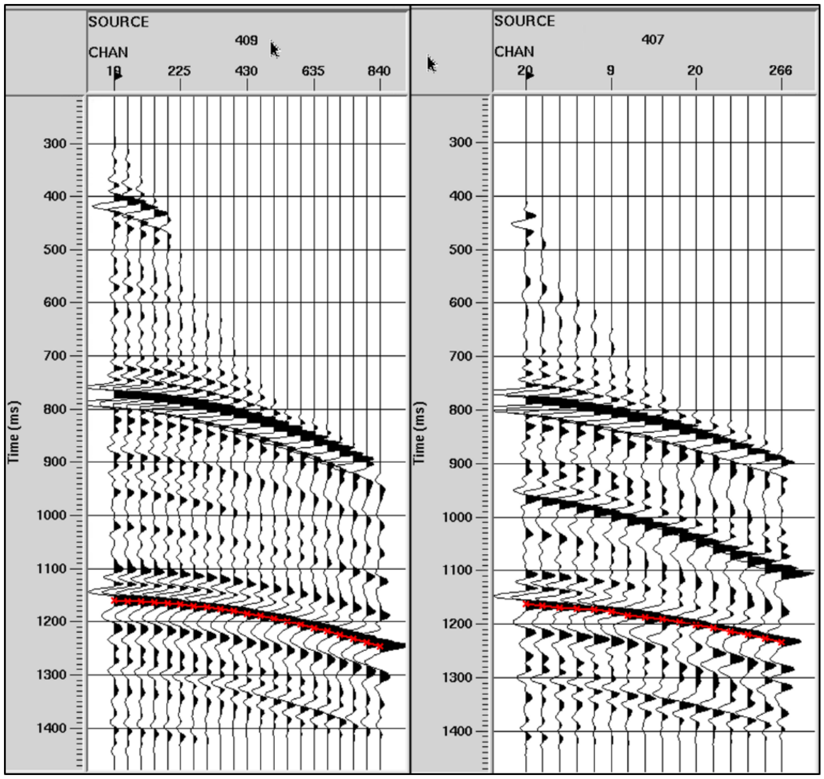

Figure 5.12 Common-offset stacks. Phenolic reflector picked in red: 0^o sector (left) and ± 90^o (right).

The VVAZ method described above is applied to sectored azimuthal common-offset gathers. Zero-offset two-way travel times (T_0) obtained by VVAZ are displayed for both halves of the model in the second column of Table. 1. T_0 was calculated using interval velocities (from **Chapter 3**). For the phenolic layer, V_{33} was used because it describes P-wave velocity at normal incidence. The T_0 values for the northern half of the model were very accurate. The azimuth of the slow RMS velocity, β_s, is accurate for both parts of the model. The slow and fast RMS velocities were obtained by VVAZ and calculated as well. To calculate them, we have used V_{11} and V_{22} that were measured in **Chapter 3**, for the fast and slow RMS velocities respectively and the interval to RMS velocity relation:

$$V_{RMS}^2 = \sum_{i=1}^{n} \frac{V_i^2 \Delta t_i}{\Delta t_i}, \tag{5.11}$$

where n is the number of layers and equal to 3. V is the interval velocity. Fast and slow RMS velocities obtained by VVAZ are more accurate for the north part of the model.

	T_0 from VVAZ	β_s from VVAZ	V_{slow} from VVAZ	V_{fast} from VVAZ	Anisotropy %	Actual β_s	Calc. T_0	Calc. V_{slow}	Calc. V_{fast}
North Half	1.1617	89.809	2454	2641.1	7.3	90	1.1616	2473.3	2764.7
South Half	1.1759	0.6368	2133.1	2623.2	20.6	0	1.1616	2473.3	2764.7

Table 5.1 Comparison between calculated and inversion results.

5.3 VVAZ of Altamont-Bluebell 3D pre-stack data

Data acquisition and processing of the Altamont-Bluebell 3D data were described earlier in **Chapter 2.** As described earlier in **Chapter 4**, well logs were correlated to the seismic data and horizons were picked. For example, the top of Upper Green River formation and Mahogany bench are shown by blue and green respectively in Figure 4.5. The two-way times in ms of the top and base of the two main targets (Upper Green River and Wasatch-180 formations) are shown by Figure 4.8 and Figure 4.10 respectively. Those zero-offset travel times, T_0 , along with isotropic NMO velocities, V_{NMO} , and azimuthally variant time residuals, dT_ϕ were used to estimate azimuthal travel times, T, as follows:

$$T = T_x + dT_\phi, \tag{5.12}$$

where

$$T_x = \sqrt{T_0^2 + \frac{x^2}{V_{NMO}^2}}. \tag{5.13}$$

Unlike Amplitude Variations with Azimuth methods, VVAZ methods use the base of the target rather than top of the target. The base of the target for the Upper Green River reservoir is the Mahogany Bench marker. The Mahogany bench travel times are displayed in the right of Figure 4.8 and are shallowest in the northeastern and southwestern part of the survey. The isochrone map indicating the thickness of the reservoir from top of Upper Green River to Mahogany Shale is shown in Figure 4.9. The reservoir thickens towards the southwest. At the Mahogany Bench reflection that can be analyzed, are up to 40^{o}, as shown by Figure 5.13 where at 1080 reflection extends up to 40^{o}.

The azimuthally-variant residuals were auto-picked and applied to the COV gathers. Figure 5.14 shows the gathers before applying the residual travel times (left) and after applying them (right). A sequence of white and yellow backgrounds indicates offset. Offset changes where background color changes. The Mahogany bench time picks from stacked data are indicated by light green on the pre-stack COV gather. The flatness of Mahogany bench is significantly improved after the application of residual travel times, especially at larger offsets. For a COV gather, azimuthally-variant travel time residuals are plotted as a function of increasing azimuth in Figure 5.15. Travel time residuals mostly indicate a fast velocity direction to the northwest around 22^{o} Northeast. Those residuals used to calculate travel times in Equation (5.12).

For the stability of the inversion, only full fold (larger than 160) COV gathers were used in a similar manner to AVAZ. The full fold base map is shown in Figure 4.22. Also, the pre-stack amplitude values were borrowed from eight neighboring gathers for each gather. Therefore, pre-stack measured data were used nine times; once in its location and eight times by neighboring locations. The angles of incidence ($\boldsymbol{\theta}$) are calculated using Snell's Law as described in **Chapter 4**. Please refer to Figure 4.23 for the azimuthal coverage of a single COV gather for different angles of incidence.

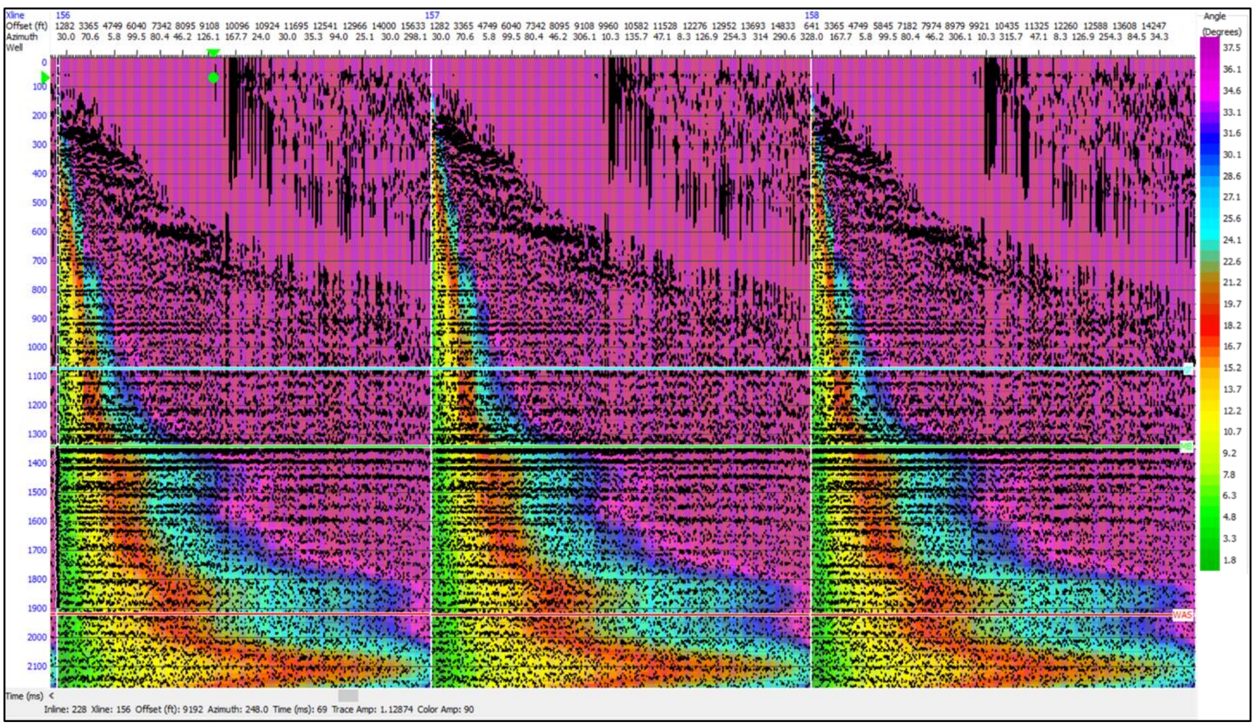

Figure 5.13 PSTM image Gather (COV). Color indicates angle of incidences. At Mahogany Bench (MB; light blue) level, maximum angles are 30° to 40°.

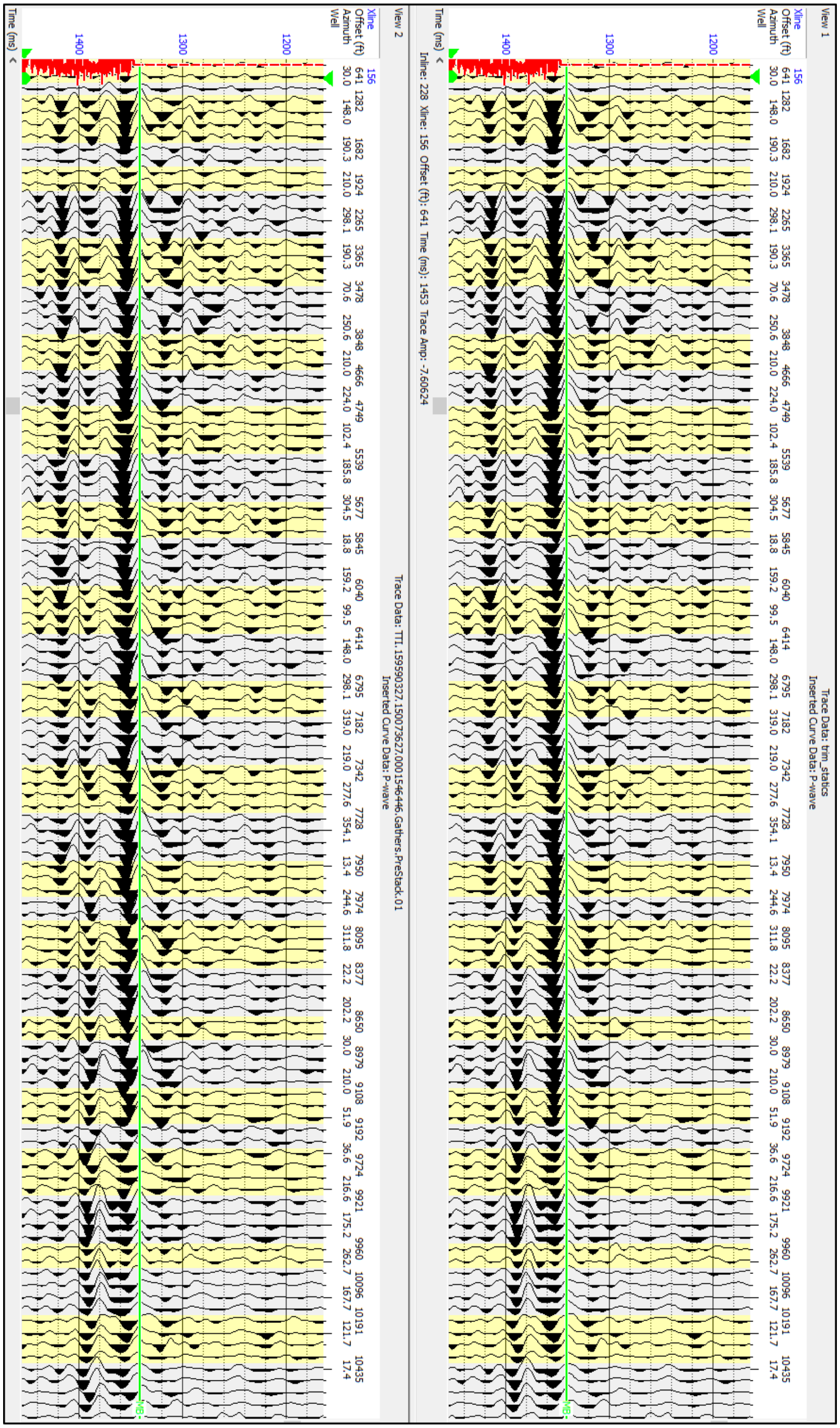

Figure 5.14 COV Gathers: Before (left) and after (right) applying azimuthal residuals.

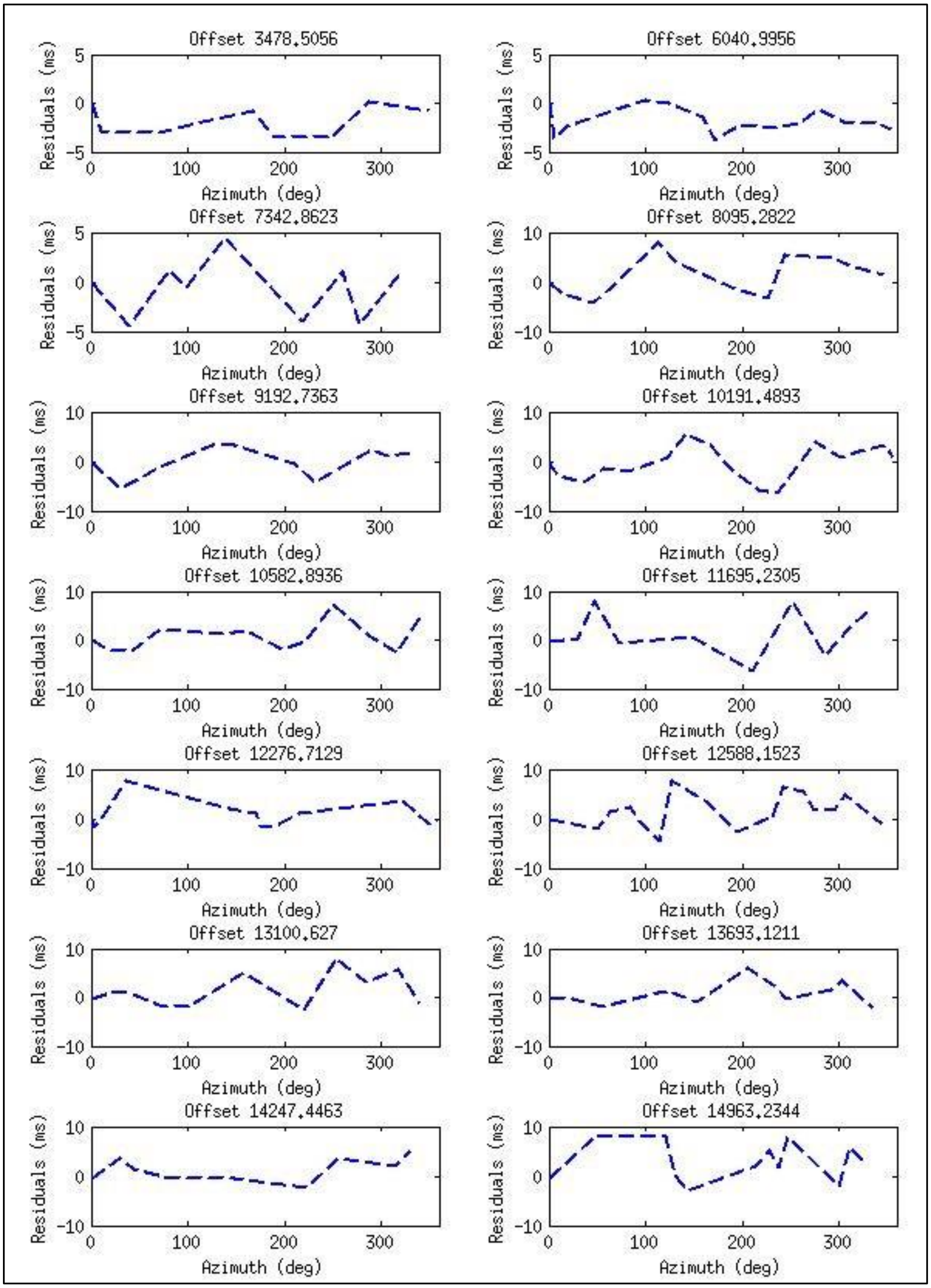

Figure 5.15 Travel time residuals for a COV gather as function of increasing azimuth.

Fast RMS velocity, slow RMS velocity, and their directions were calculated for all horizons. Input RMS velocities, along with inverted fast and slow RMS velocities for the top of Upper Green River, Mahogany Bench marker, top of Wasatch-180, and base of Wasatch-180 are shown respectively in Figure 5.16, Figure 5.17, Figure 5.18, and Figure 5.19. The V_{RMS}, fast V_{RMS} , and slow V_{RMS} are plotted to the same scale for each horizon, and the difference between the three velocities are not large, as can be seen as well in the next figures. From those inverted velocities, a velocity anisotropy percentage was calculated by dividing the difference between the fast and slow RMS velocities by the slow RMS velocity. Figure 5.20, Figure 5.21, Figure 5.22, and Figure 5.23 show respectively maps for the top of Upper Green River, Mahogany Bench marker, top of Wasatch-180, and base of Wasatch-180 V_{RMS} anisotropy percentage on the left and the fast V_{RMS} direction on the right. The V_{RMS} anisotropy percentage is not large because V_{RMS} includes the effect of overburden above the target horizons. The fast V_{RMS} direction is affected by the overburden, as well, and it's mainly oriented about 40^{o} from North for the top of Upper Green River and for the Mahogany Bench.

For the top and base of the oil target, Wasatch-180, there is a major trend for fast V_{RMS} direction at -40^{o} and a minor trend at 40^{o} clockwise from North, as can be seen by Figure 5.24 and Figure 5.25. In the following part of this chapter, the overburden will be removed using Dix (1955)-type interval VVAZ. In **Appendix** A, error analysis of this velocity inversion method is studied.

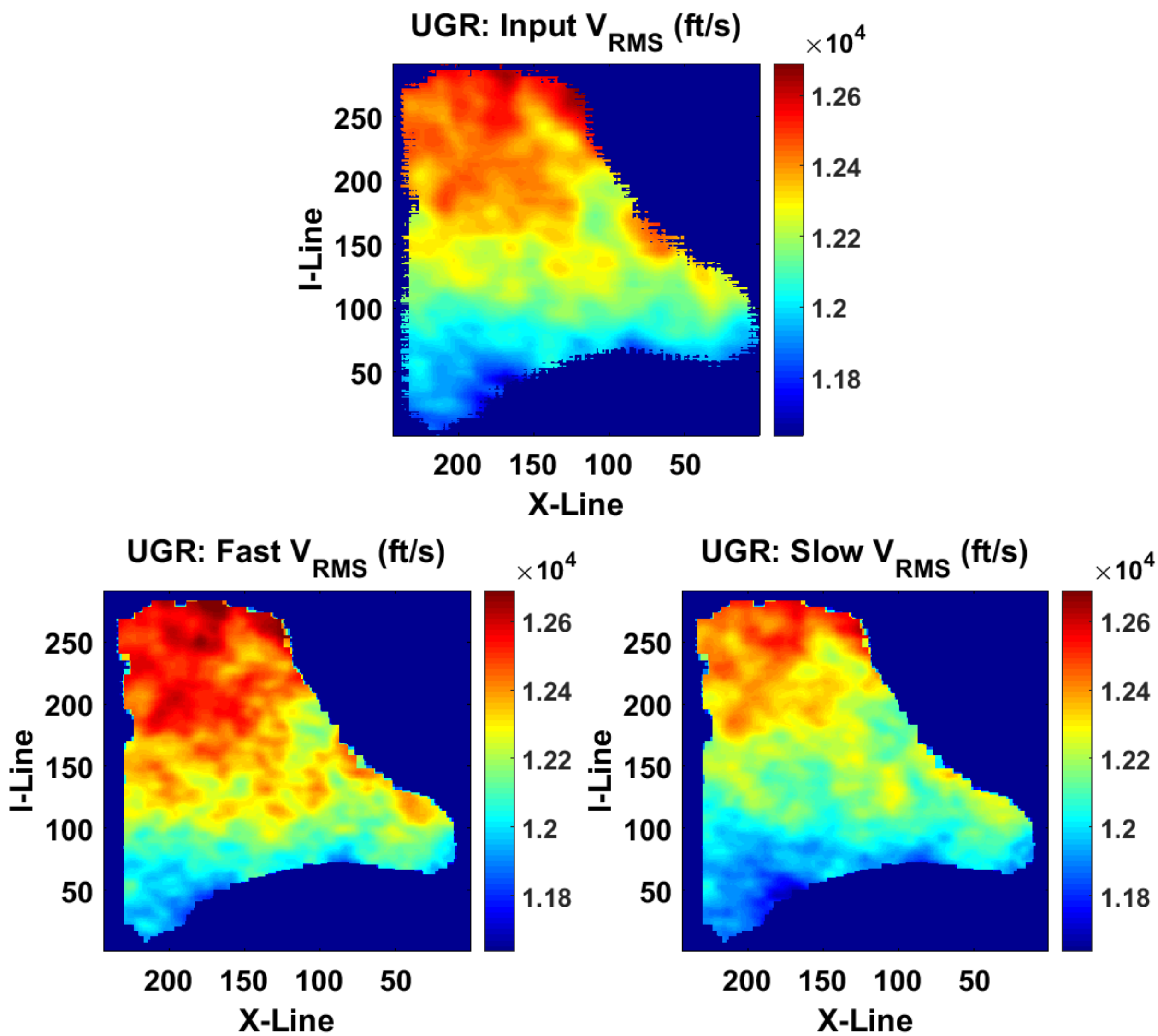

Figure 5.16 Input RMS velocities (top) vs inversion velocity results (bottom) for the top of Upper Green River. Fast velocities (right) and slow velocities (left) are plotted with same scale used for RMS velocities in feet/second.

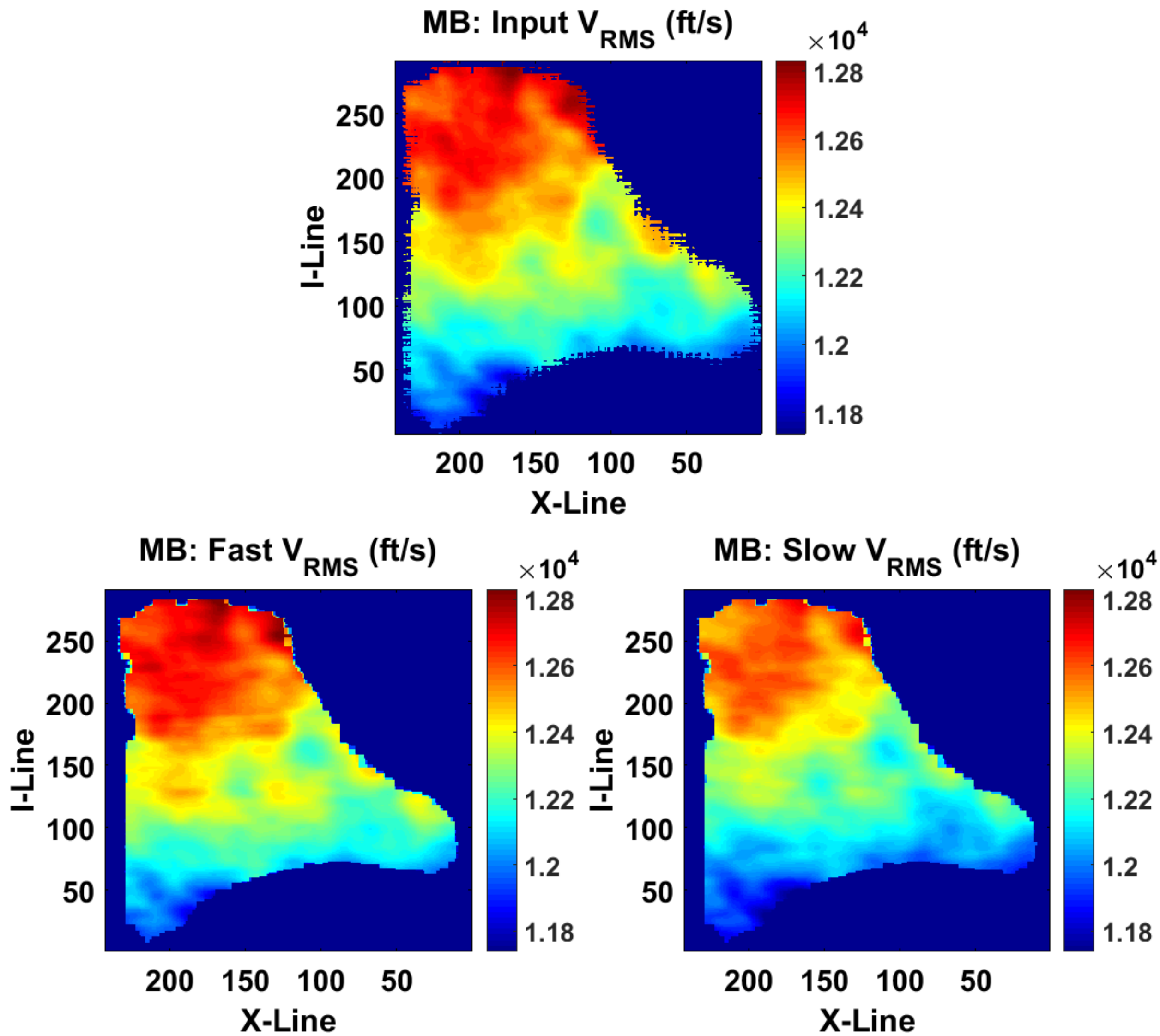

Figure 5.17 Input RMS velocities (top) vs inversion velocity results (bottom) for the Mahogany Bench marker or base of gas reservoir. Fast velocities (right) and slow velocities (left) are plotted with same scale used for RMS velocities in feet/second.

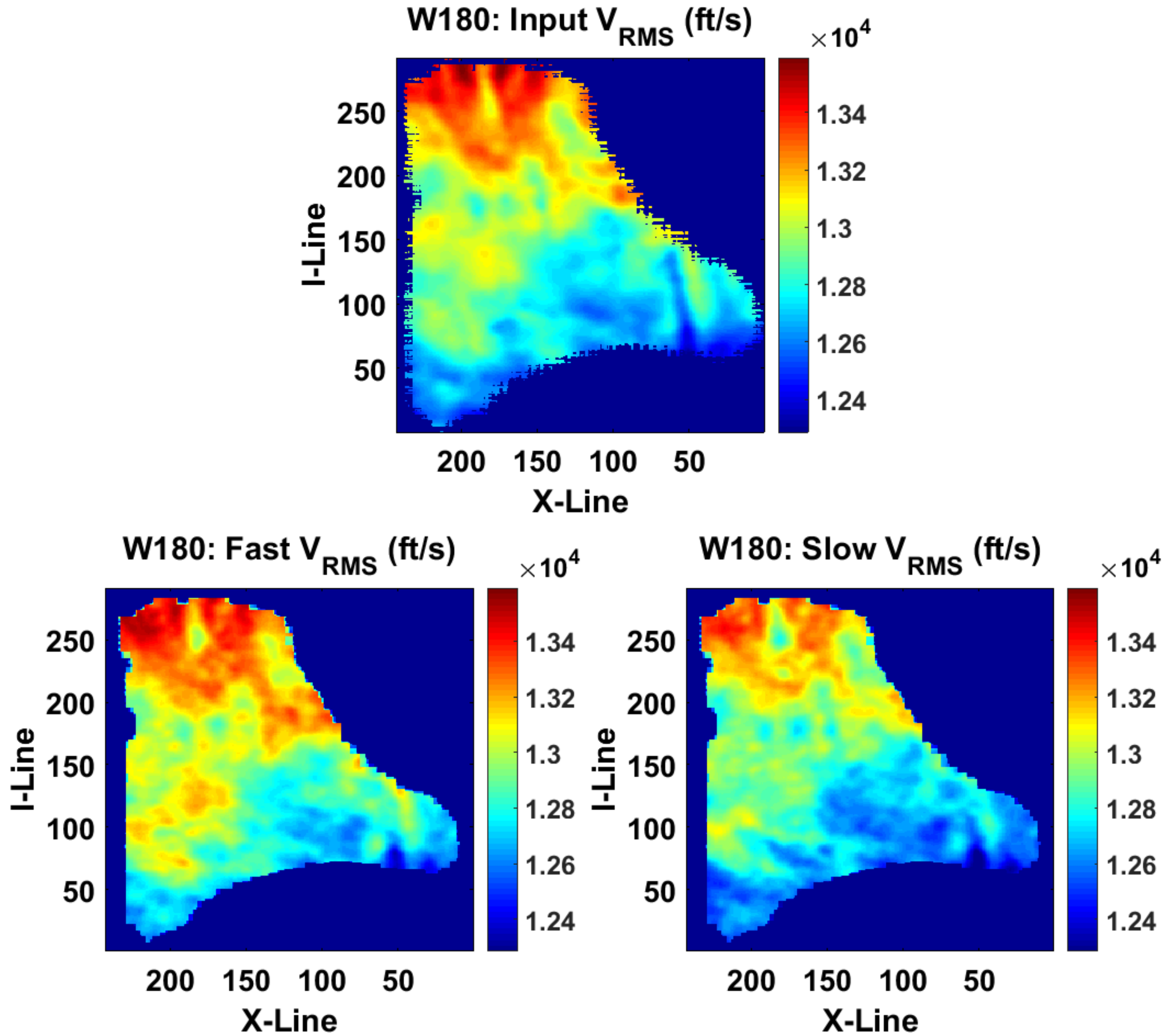

Figure 5.18 Input RMS velocities (top) vs inversion velocity results (bottom) for the top of Wasatch-180. Fast velocities (right) and slow velocities (left) are plotted with same scale used for RMS velocities in feet/second.

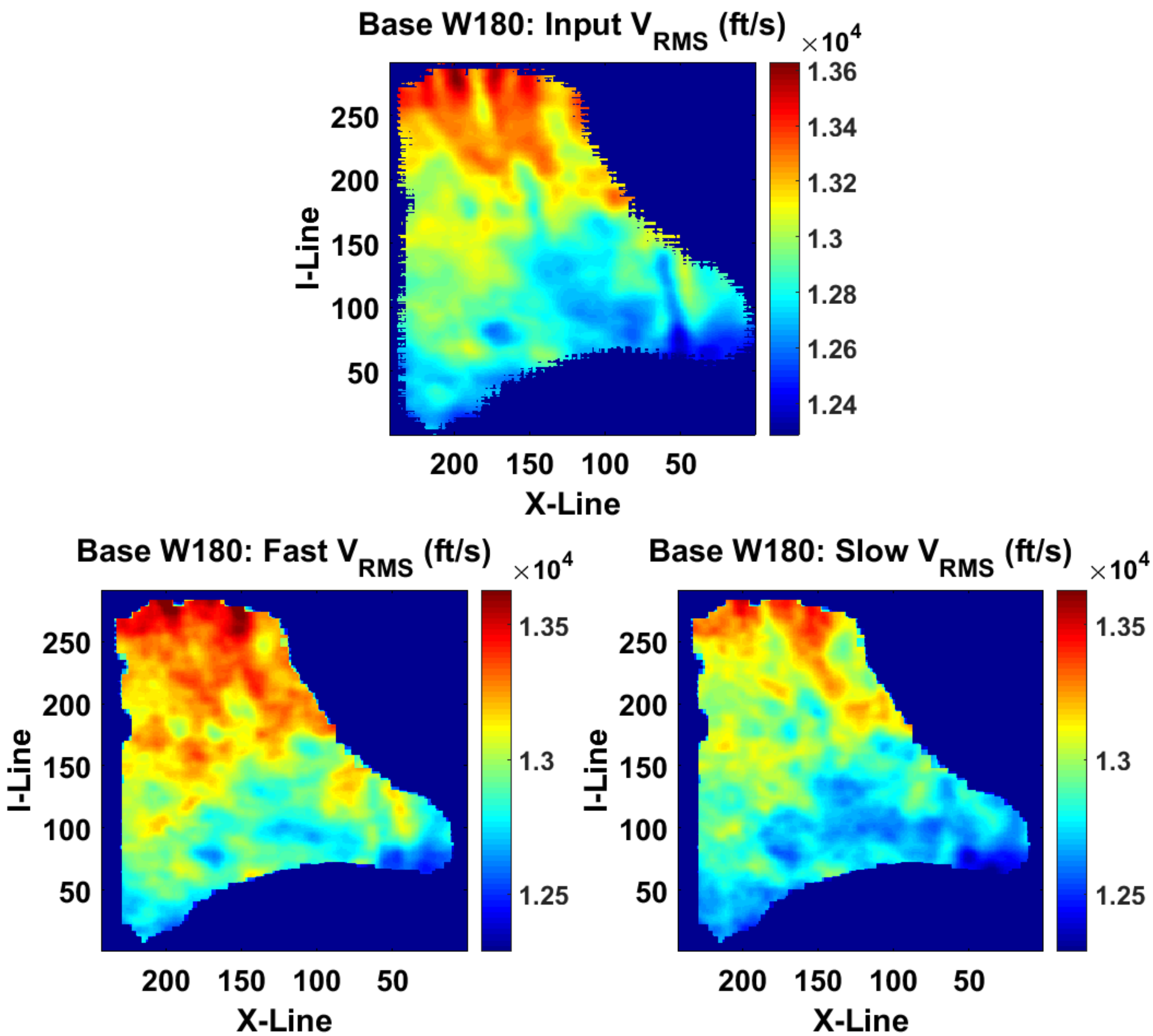

Figure 5.19 Input RMS velocities (top) vs inversion velocity results (bottom) for the base of Wasatch-180. Fast velocities (right) and slow velocities (left) are plotted with same scale used for RMS velocities in feet/second.

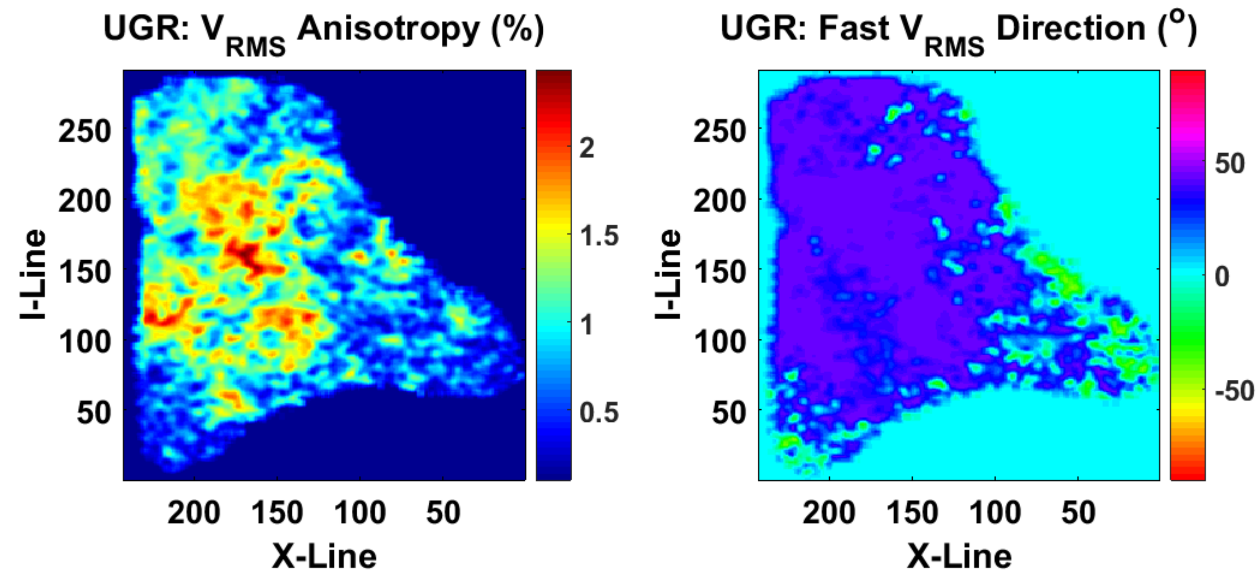

Figure 5.20 Inversion results for the top of Upper Green River: RMS velocity anisotropy percentage (left) and fast RMS velocity direction (right) in degrees clockwise from North. Those results can be interpreted for the overburden above the shallowest reservoir.

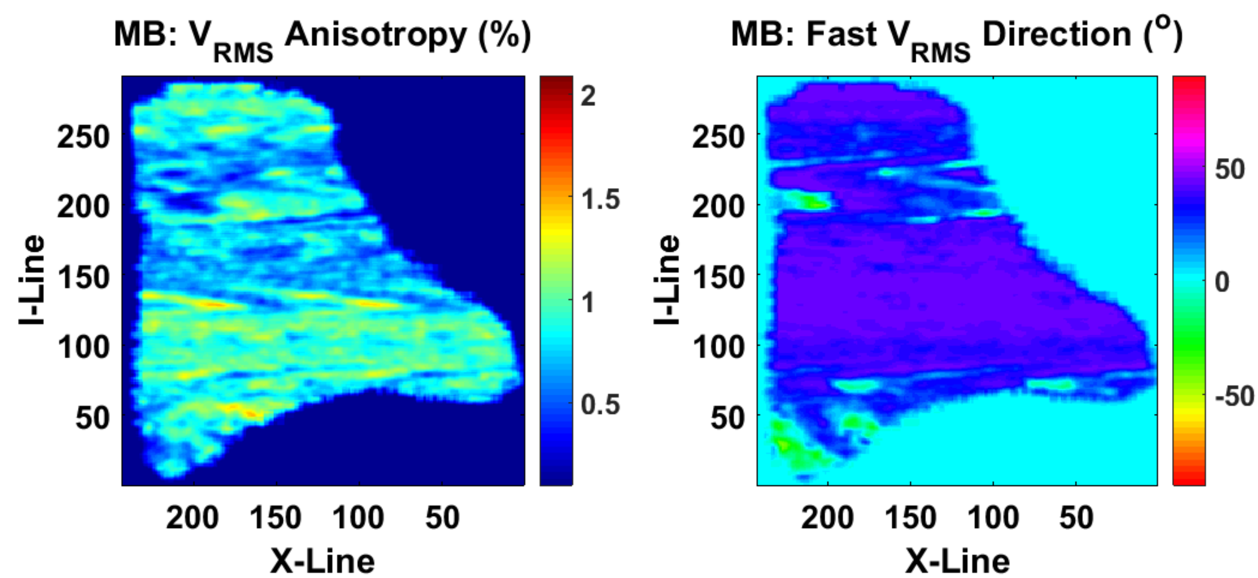

Figure 5.21 Inversion results for the Mahogany Bench marker: RMS velocity anisotropy percentage (left) and fast RMS velocity direction (right) in degrees clockwise from North. Those results can be interpreted for the Upper Green Reservoir with the inclusion of the overburden effects.

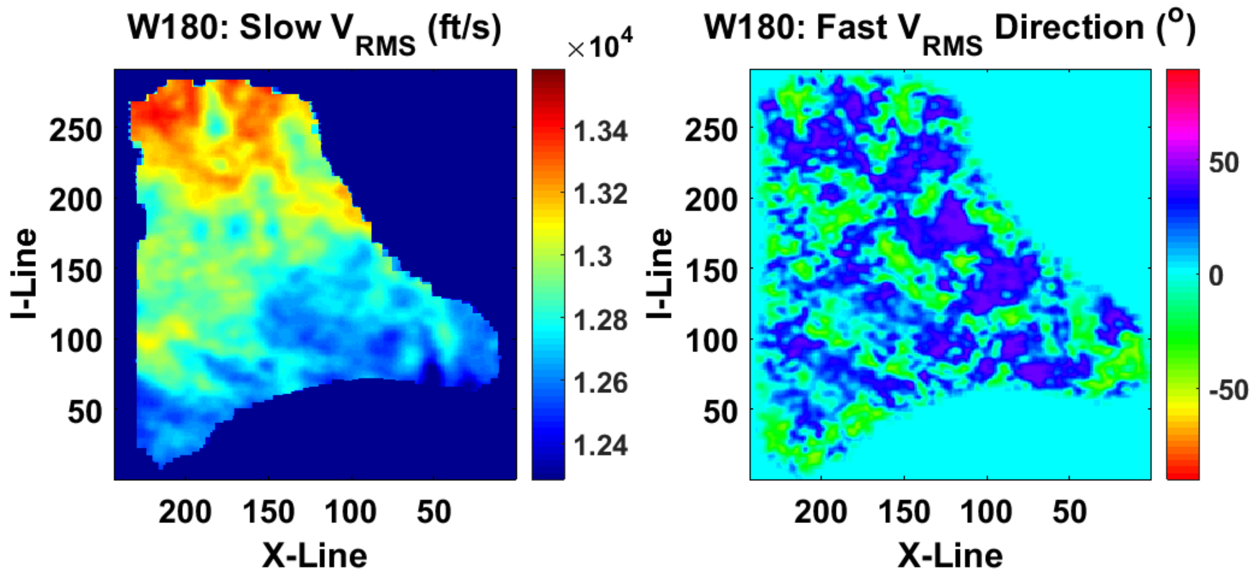

Figure 5.22 Inversion results for the top of Wasatch-180: RMS velocity anisotropy percentage (left) and fast RMS velocity direction (right) in degrees clockwise from North. Those results can be interpreted for the overburden above the shallowest reservoir.

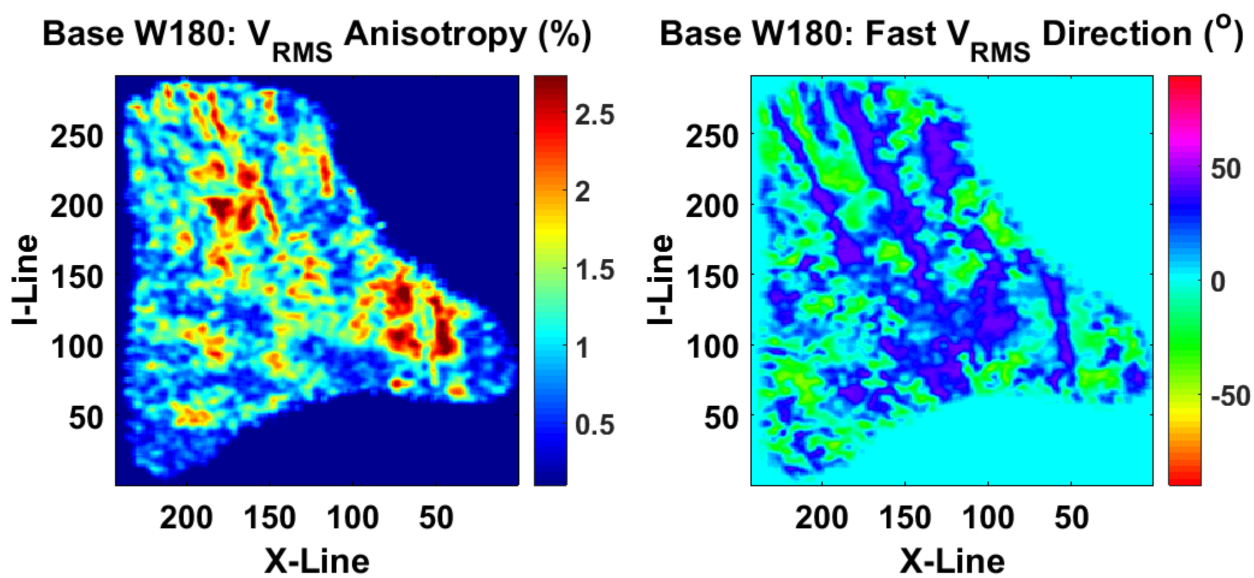

Figure 5.23 Inversion results for the base of Wasatch-180: RMS velocity anisotropy percentage (left) and fast RMS velocity direction (right) in degrees clockwise from North. Those results can be interpreted for the overburden above the shallowest reservoir.

5.4 Interval VVAZ of the Altamont-Bluebell 3D pre-stack data

For Dix (1955)-type interval ellipse coefficients, W_l, we use the Grechka et. al., 1999 relation:

$$W^{-1}{}_l = \frac{T_0(l)W^{-1}(l) - T_0(l-1)W^{-1}(l-1)}{T_0(l) - T_0(l-1)}, \tag{5.14}$$

where W_l is the interval ellipse coefficient, (*l-1*) is the top layer, and (*l*) is the bottom layer. This equation would simply be Dix equation if W was inverse squared of RMS velocity. However, W is more sophisticated because it is a vector and depends on direction. It is given, in terms of ellipse coefficients of Equation (5.3), as a symmetric matrix:

$$W = \begin{bmatrix} W_{11} & W_{12} \\ W_{12} & W_{22} \end{bmatrix} \tag{5.15}$$

Ellipse coefficients were inverted for top and base of each reservoir. From the two sets of ellipse coefficients, Dix (1955)-type interval coefficients were calculated. From those coefficients, fast, slow interval velocities, and their directions are calculated to estimate the interval velocity anisotropy orientation and percentage. Figure 5.24 shows the inversion results for the Upper Green River gas reservoir. The fast interval velocity is shown on top left while the slow interval velocities are shown on top right. The interval velocity anisotropy percentage (left) and direction (right) are shown on bottom. Unlike fast V_{RMS} direction maps of top and base (Mahogany Bench) of Upper Green River gas reservoir in Figure 5.20 and Figure 5.21, the interval velocity anisotropy of the same reservoir has a major trend at -35 and a minor trend at 40 clockwise from North as can been seen by Figure 5.24. This difference, along higher anisotropy percentages, are attributed to removing the overburden.

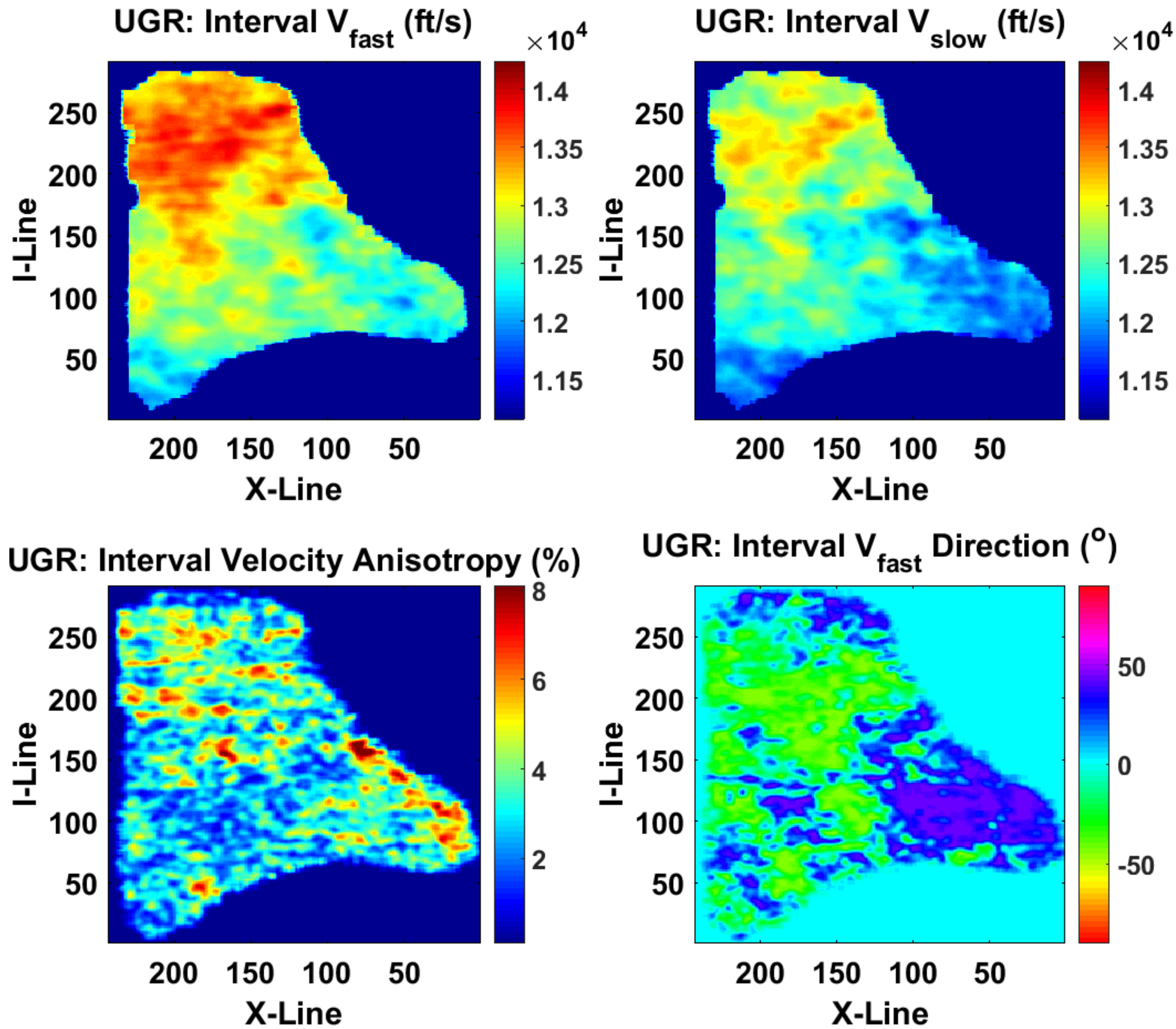

Figure 5.24 Inversion results for the Upper Green River gas reservoir: fast (left) and slow (right) interval velocities (top), percentage (left) and direction (right) of interval anisotropy (bottom).

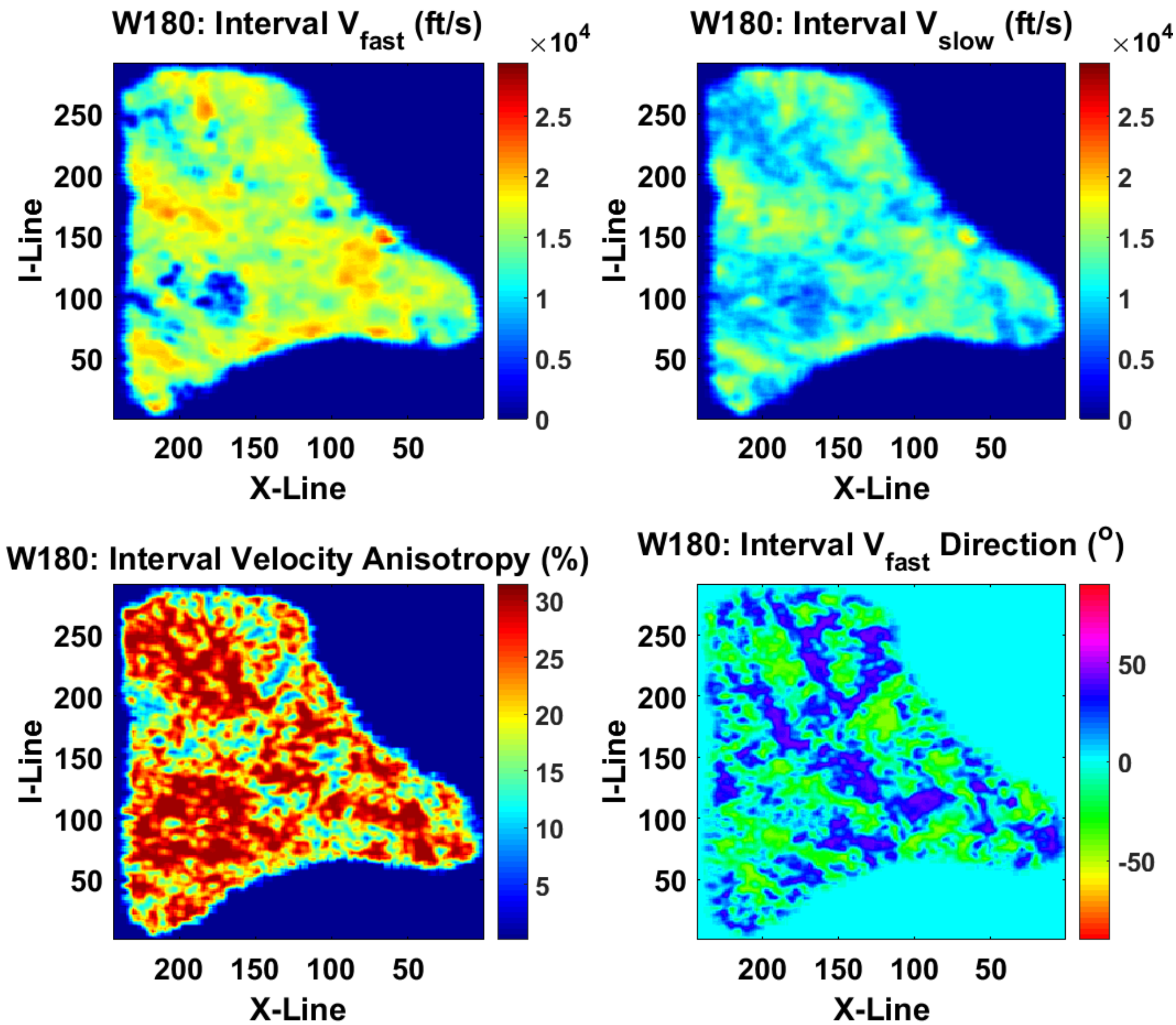

Figure 5.25 Inversion results for the Wasatch-180 oil reservoir: fast (left) and slow (right) interval velocities (top), percentage (left) and direction (right) of interval anisotropy (bottom)

For the oil reservoir, Wasatch-180, the interval velocity anisotropy percentages are higher. Focusing on much thinner fractured reservoir (less than fourth of Upper Green River) and using Dix (1955)-type interval properties has led to obtaining high anisotropy percentages in Figure 5.25. Recall that for the top and base of the oil target, Wasatch-180, there were a major trend for fast V_{RMS} direction at -40° and a minor trend at 40° from North clockwise as can be seen by Figure 5.22 and Figure 5.23. Looking at the higher interval velocity anisotropy zones, the -40° from North trend becomes dominant which implies that the Northeastern trend of fast V_{RMS} direction is related to overburden. In **Chapter 7**, the results of VVAZ here are compared to the AVAZ results of **Chapter 4**.

5.5 Summary

Physical modeling can be a valuable tool for testing and evaluating geophysical methods, especially for anisotropic media where numerical modeling becomes complicated and may require validation by experimental observations. For the study described in this chapter, a 3D pre-stack physical modeling dataset was acquired, processed, and used to evaluate a method for analyzing VVAZ. The most serious shortcoming in this study is that, because of inadequate spatial sampling during acquisition, there is not enough fold to overcome the fact that the reflection of the bottom of the phenolic layer is weak and contaminated by strong mode-converted PS waves generated by the top of the anisotropic layer. We devised an extra time-domain processing method to overcome this issue, and it was necessary to use it to advance the VVAZ analysis of the physically-modeled data. Results of the analysis proved to be very accurate.

A VVAZ workflow has been implemented for 3D pre-stack seismic data from the Altamont-Bluebell field. The method aligns reflection events using residual statics for azimuthal gathers to compute azimuthal travel times. Then, travel times are inverted using linear least squares fitting to obtain NMO ellipse coefficients. From those coefficients, slow and fast velocities as well as their orientation directions are estimated and used for velocity anisotropy orientation and intensity maps. The shortcoming of this method is that velocity anisotropy results include effects of the overburden. To overcome this shortcoming, Dix (1955)-type interval coefficients show an advantage over the use of coefficients obtained from RMS velocities for a single layer because they make VVAZ less sensitive to overburden properties. Therefore, we have applied a Dix (1955)-type interval technique to the thick gas reservoir and to the thin oil reservoir. After removing the effect of the overburden, the velocity anisotropy percentages have increased, while the orientation had a less dramatic change.

Chapter 6 VSP Analysis for Azimuthal Anisotropy: AVAZ, VVAZ & S-wave Splitting

Within the Altamont-Bluebell survey, multiple VSP datasets were acquired. The first dataset was a conventional zero-offset VSP. The objectives of the zero-offset VSP were a checkshot for sonic log calibration with seismic, a velocity model for processing other VSP datasets, and a Q model to aid with 3D processing of seismic data. The second dataset was 6 shots of offset VSPs. The objective of those shots was to estimate VTI Thomsen parameters to aid with 3D processing of seismic data, and also to create a HTI model for fracture characterization of the reservoirs. However, these offset VSPs were limited in terms of depth, offset, and azimuthal coverage, and walkaway VSPs would have been a better choice for such an objective, but certainly more expensive. The third dataset was a 4-component VSP. Its objective is S-wave splitting analysis for fracture characterization of the reservoirs.

In this part of the thesis, we began with the raw field data, applied processing, including some twists in order to use surface seismic methods of AVAZ and VVAZ on VSP data, which resulted in final products of azimuthal anisotropy intensity and orientation parameters. Offset VSPs were processed through the VSP-CDP transform, then AVAZ analysis was applied. A VVAZ workflow is developed here for offset, walkaround, or walkaway VSPs using a method for surface seismic. Interval anisotropy properties are calculated for between concetitivve receivers. For AVAZ and VVAZ, deeper levels including the deeper target of Wasatch-180 are more reliable because of better coverage. S-wave analysis is carried out using Alford (1986) 4-C rotation to separate fast and slow modes. This method assumes that the symmetry axis is vertically invariant. In order to overcome this assumption, a layer stripping technique was applied using Winterstien and Meadows (1991).

6.1 VSP DATA ACQUISTION

A zero-offset VSP (ZVSP) and 6 offset VSPs were acquired using a P-wave source on surface and a 2-level tool of 3-C geophones in the borehole. Another four-horizontal components VSP was acquired using an S-wave source and 3-C geophones with attached gyro to obtain tool orientation. Notice that although the number of components that are recorded is 6, it is called 4-C VSP because only the four horizontal components are used and provide additional information to zero-offset VSP. The natural frequency of the geophones is 15 Hz, and the vibroseis sweep is 4-96 Hz. The total depth (TD) is 14240′ referenced to Kelly Bushing (KB). The surface elevation of the borehole is 5254′ above mean sea level (MSL), while the Kelly Bushing elevation is 5288′ above MSL. Table 6.1 summarizes the geometry of all VSP datasets.

The two zero-offset VSPs were used to create a velocity model that has been used in different processing steps for the other VSPs. For AVAZ and VVAZ, shots 2 to 8 were used. The locations of the sources are shown in Figure 6.1. Figure 6.2 shows the acquired depths, offset, and azimuths for each shot. Depths from 8700′ to 14000′ are covered by 6 shots, and depths above 3400′ were covered by 4 shots. For all depths, one of the shots was a zero-offset VSP. The data quality was decent without noticeable casing or cementing effects.

Shot number	Shot-Borehole offset (ft)	Shot Azimuth (°)	Top receiver depth from KB (ft)	Bottom receiver depth from KB (ft)
1 (ZVSP)	408	156	480	3580
2 (ZVSP)	360	360	3400	14050
3	5755	170	8700	14050
4	3184	170	3300	8650
5	6332	108	3400	14050
6	2542	102	3300	14050
7	14954	95	8550	14000
8	10889	88	8550	14000
9	672	344	3300	14050
10	672	344	3300	14050

Table 6.1 Shot and receiver geometry.

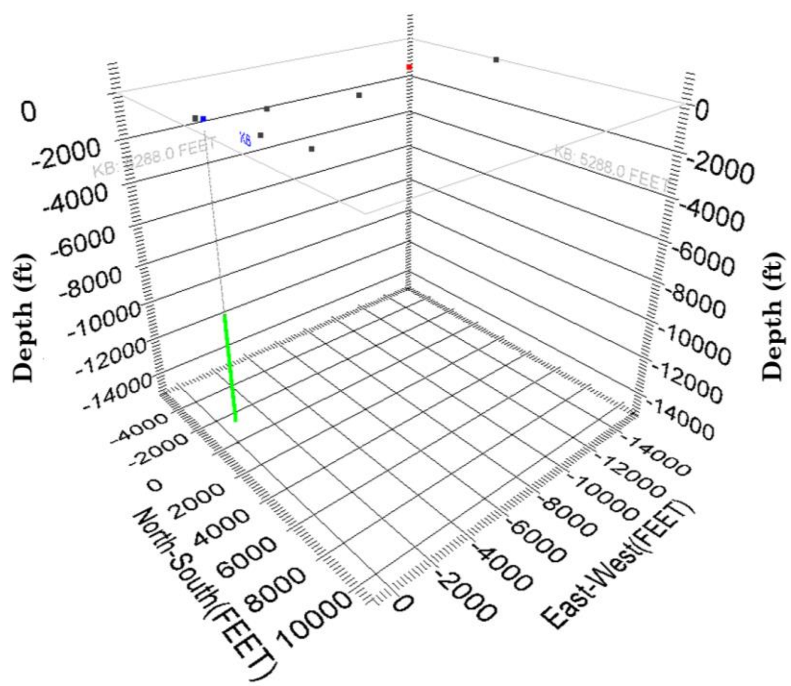

Figure 6.1 The geometry of the VSP survey. Shots are on surface indicated by small boxes. Live receivers for the red shot are in the borehole indicated by green dots.

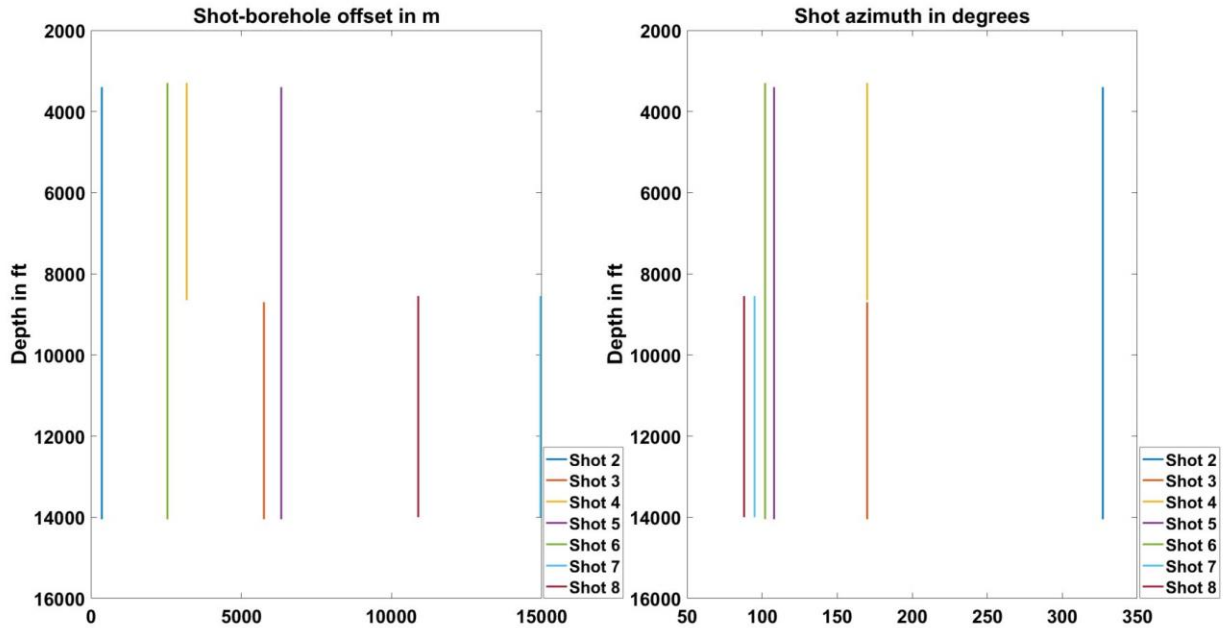

Figure 6.2 Acquired depths, offset, and azimuths for each shot.

The last dataset was a 4-component VSP and was acquired during two runs. Since there were no vertical shots, we have used shots from offset VSP to re-orient the tool into East-West and North-South directions as explained in the S-wave splitting section.

6.2 VSP Data processing

We processed the zero-offset VSP, offset VSPs and 4-C VSP for different purposes and therefore used different workflows. We began the processing with SEGY files. For zero-offset VSP, processing was straight-forward, with major processing steps being: geometry assignment, stacking, bandpass filtering, picking of P-wave first breaks, P and S wavefield separation, and deconvolution. Stacking here is different than surface seismic data processing. Basically in the field, each shot is repeated 3 to 5 times to reduce random noise. Noisy traces are deleted, and the rest of traces were stacked to form a single trace between shot and receiver. Bandpass filtering was applied to attenuate noise below 4 Hz and above 120 Hz. The first breaks were picked on the trough of the first arrival waveform, and those picks were used to create the P-wave velocity model used later for offset VSPs wavefield separation and for sonic log calibration. P-wave first breaks were used to calculate an amplitude decay function. Then, exponential gain was applied to account for amplitude decay as a function of time with f factor (f=2.0) as follows:

$$A(t) = A_0(t)t^f \tag{6.1}$$

For wavefield separation, time shifts and median filters were utilized. First, the downgoing P wave was aligned using P-wave first breaks. Then, a median filter was applied to remove the downgoing P wave from the vertical-component data. The filtered downgoing P wave was used for VSP deconvolution.

One of the advantages of VSP geometry over surface seismic geometry is that the source signature is known and can be used for deterministic deconvolution. After wavefield separation, a window is chosen around the first breaks on the downgoing P wave. The waveform inside that window can approximate the source signature. Figure 6.3 shows vertical-component data after P-wave first break picking with Automatic Gain Control (AGC) applied for display. Figure 6.4 and Figure 6.5 show the separated upgoing P-wave field after amplitude recovery and its amplitude spectrum respectively. This offset VSP shot and its amplitude spectrum after deconvolution are shown in Figure 6.6 and Figure 6.7 respectively.

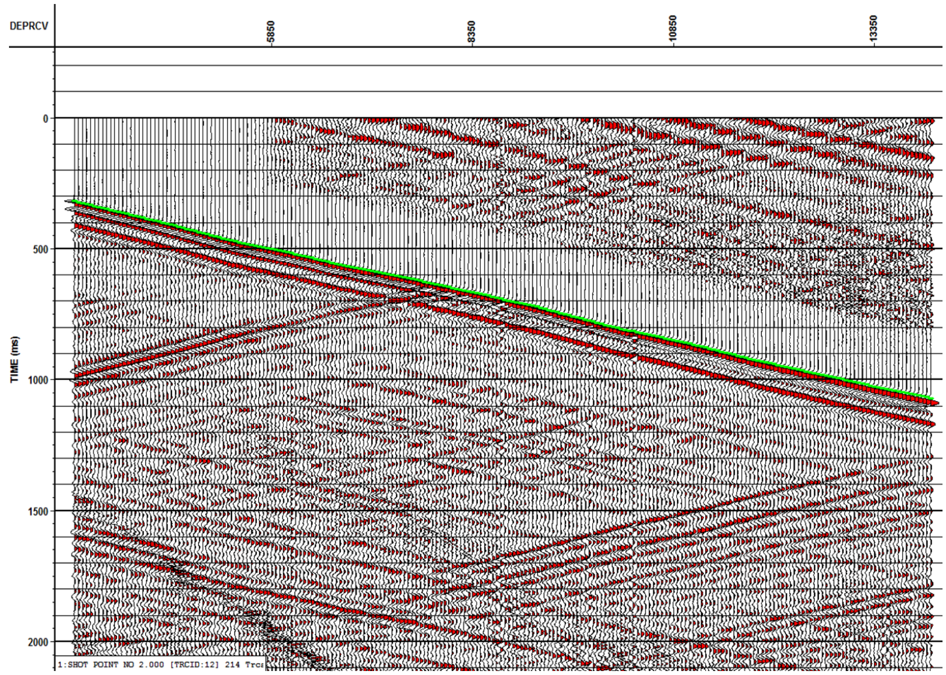

Figure 6.3 Vertical-component of a zero-offset VSP common-shot gather, with P-wave first arrival times indicated by green picks. AGC is applied for display.

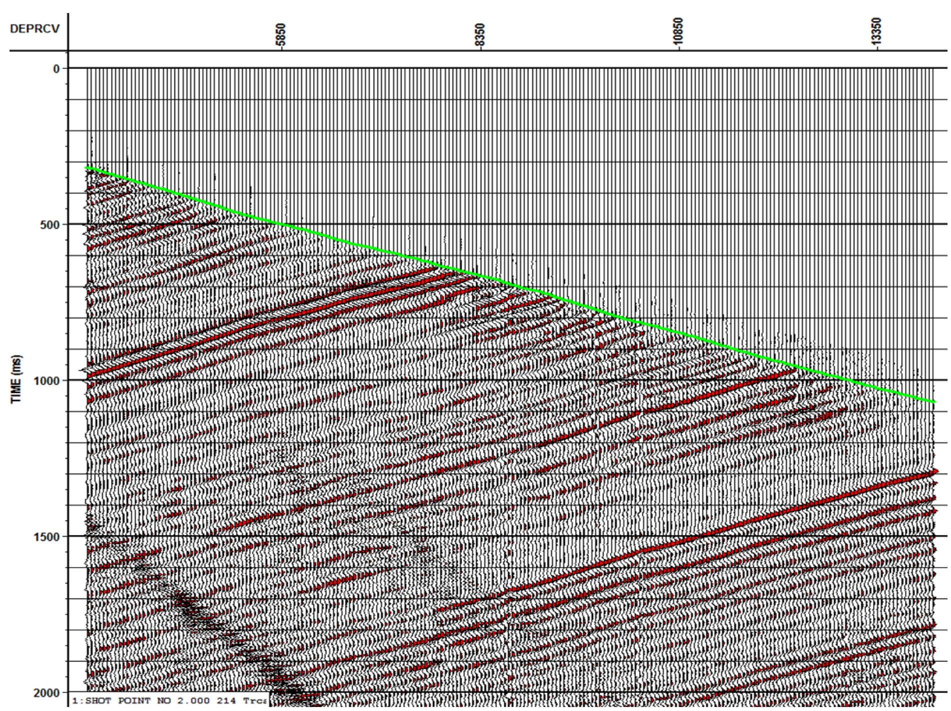

Figure 6.4 Upgoing P-wave of a zero-offset VSP common-shot gather after wavefield separation. P-wave arrival times indicated by green picks.

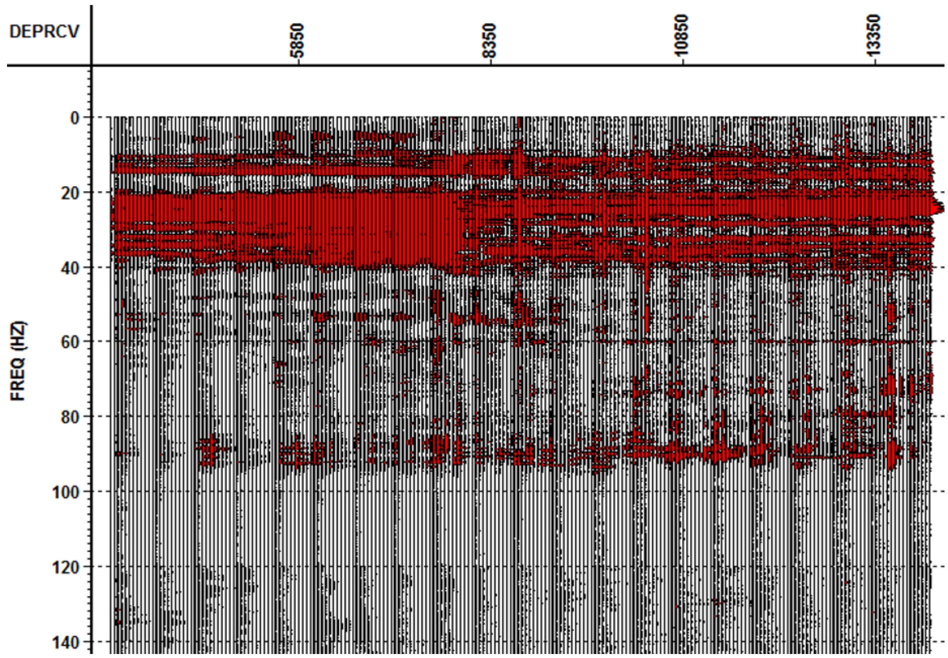

Figure 6.5 Amplitude spectra of the zero-offset VSP prior to deconvolution, displayed in Figure 6.4

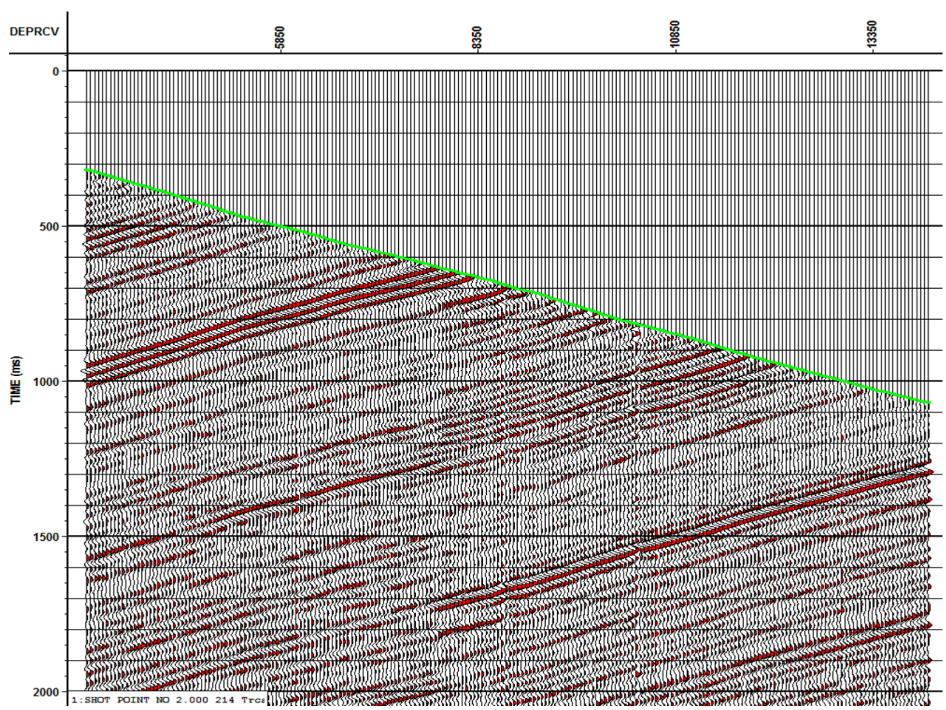

Figure 6.6 Upgoing P-wave of a zero-offset VSP common-shot gather after deterministic deconvolution. P-wave arrival times indicated by green picks.

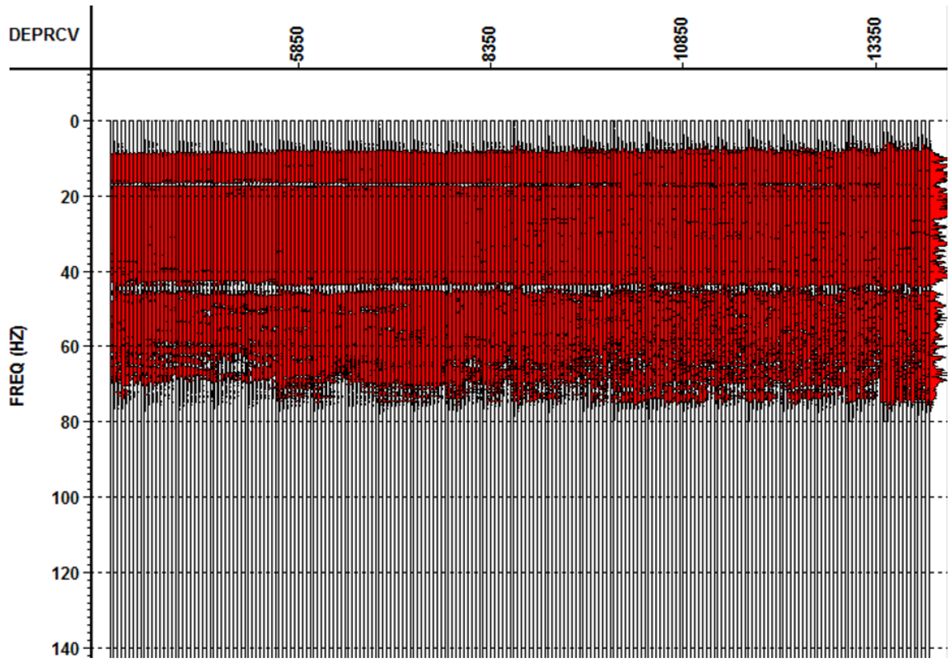

Figure 6.7 Amplitude spectra of the zero-offset VSP after deconvolution, displayed in Figure 6.6

Compared to zero-offset VSP processing, offset VSPs are harder to process. The main difficulty is that P-wave and S-wave modes are all captured by the three components, and therefore require an extra effort in separating different modes of body waves. A model-based wavefield separation processing workflow for offset VSPs was implemented and is summarized in Figure 6.8.

The first rotation applied to the 3-components is horizontal rotation to rotate the two horizontal components into a component within the propagation plane and a component transverse to the propagation plane, as explained by Figure 6.9. After horizontal rotation, the radial component will capture most of the data between the two rotated horizontal components, while the data is minimized for the transverse component. The other rotation was vertical rotation. After vertical orientation, the direct component is oriented towards the source and has most of the downgoing P-wave energy, as explained by Figure 6.10. The vertical (Z) and two horizontal (Y and X) components are shown respectively by Figure 6.11, Figure 6.12, and Figure 6.13 after applying bandpass filter, P-wave first breaks picking, and amplitude recovery. After horizontal rotation, the energy was maximized on the radial component as can be seen in Figure 6.14, and minimized on the transverse component as can be seen in Figure 6.15.

Vertical rotation is not the ideal way to separate upgoing P-wave and S-wave fields because the required rotation is temporally variant. However, it is applied to remove downgoing strong P-wave energy before time-variant rotation. After the vertical rotation, the direct component in Figure 6.16 is oriented toward the source, as can be seen by the maximized energy of P-wave first arrival times. The upgoing P-wave and S-wave fields are distributed between this component and the perpendicular component (the component orthogonal to the direct component) in Figure 6.17. Median and FK filters were used then to remove the downgoing P wavefield from direct and perpendicular components shown in Figure 6.18 and Figure 6.19 where the data are mostly upgoing P-wave and S-wave energy. Inverse vertical rotation is applied then to rotate the data back to vertical (Z’) and radial (X’) and shown respectively in Figure 6.20 and Figure 6.21.

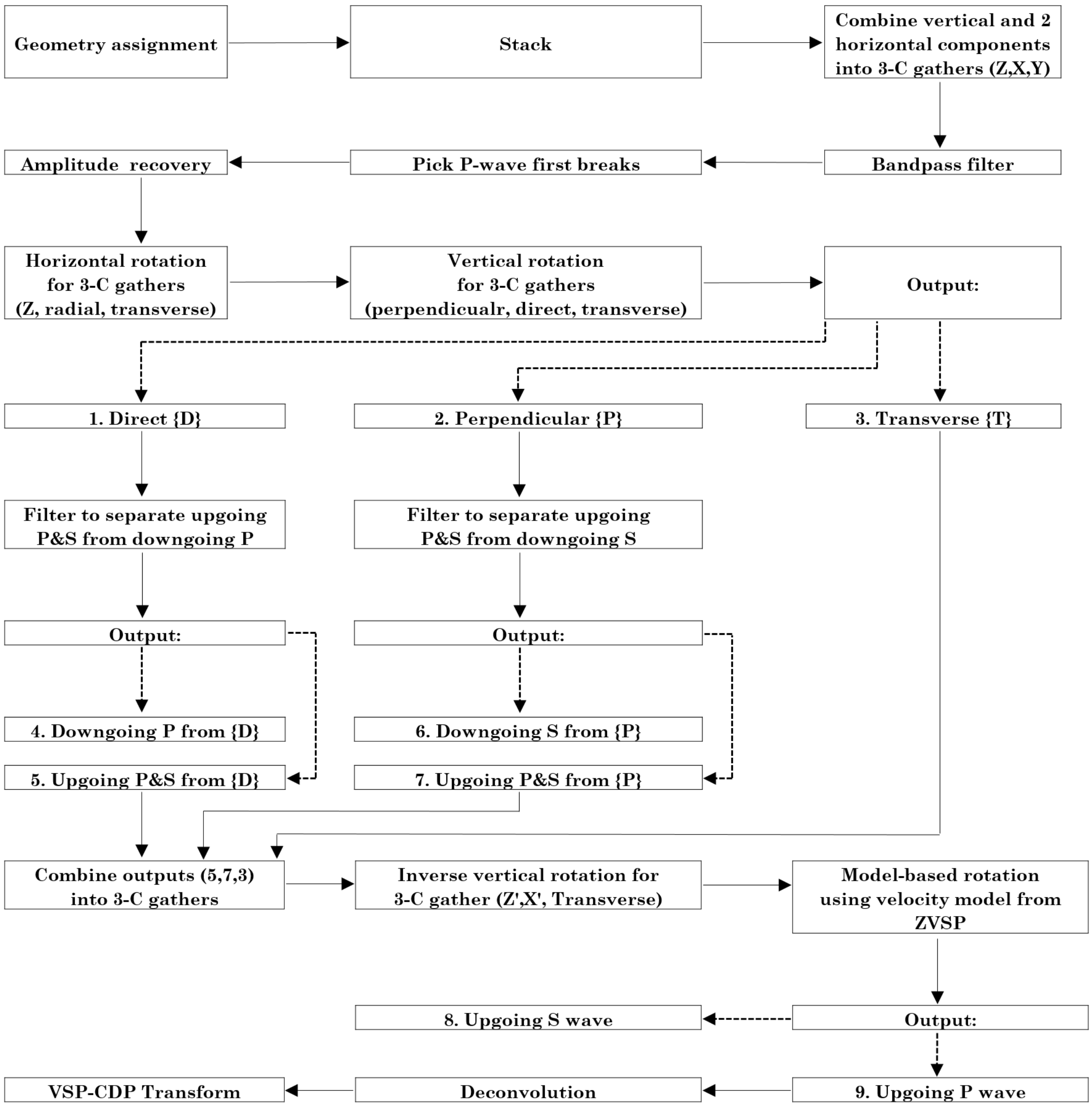

Figure 6.8 Model-based wavefield separation processing workflow for offset VSPs.

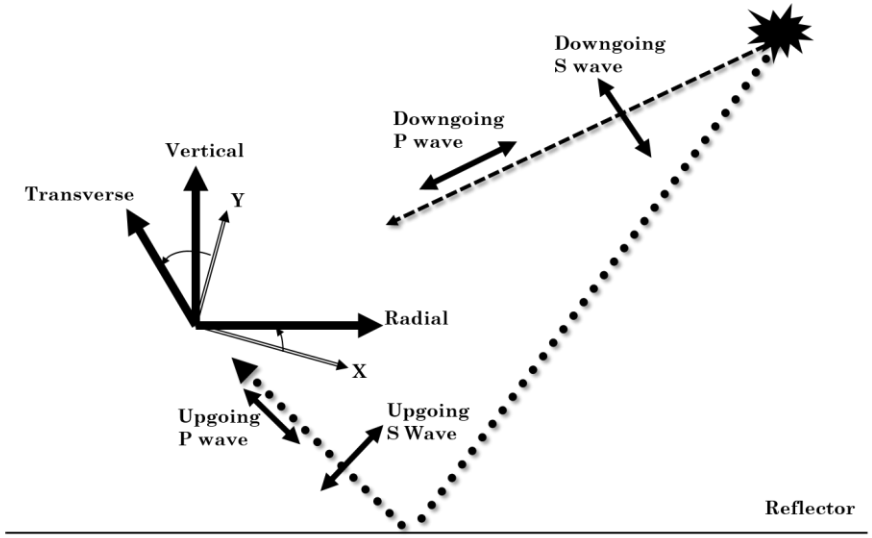

Figure 6.9 Horizontal rotation with different P and S wavefields illustrated by dashed line for downgoing raypath and dotted line for upgoing raypath. Original acquisition is along arbitrary X and Y orthogonal axes. After horizontal orientation, radial component is oriented at the propagation plane and contains most of the energy between horizontal components.

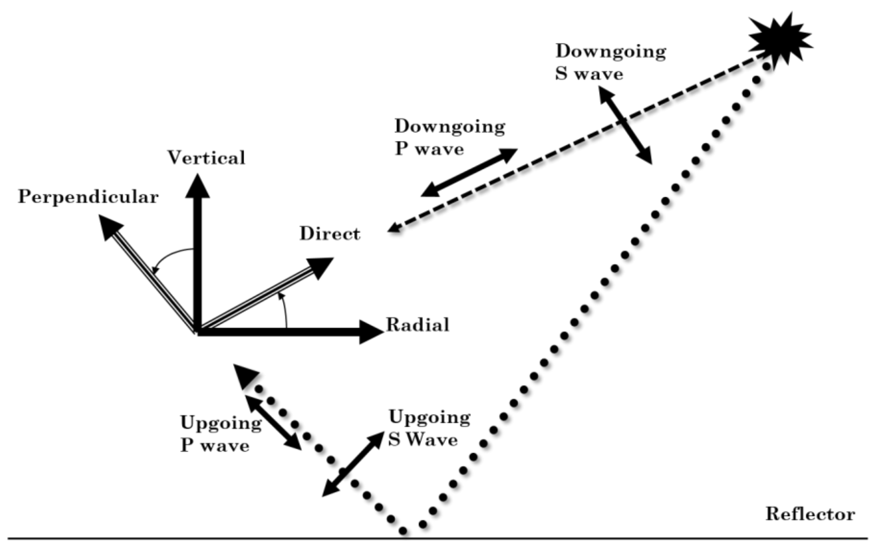

Figure 6.10 Vertical rotation with different P and S wavefields illustrated by dashed line for downgoing raypath and dotted line for upgoing raypath. After vertical orientation, direct component is oriented towards the source and contains most of the downgoing P-wave energy.

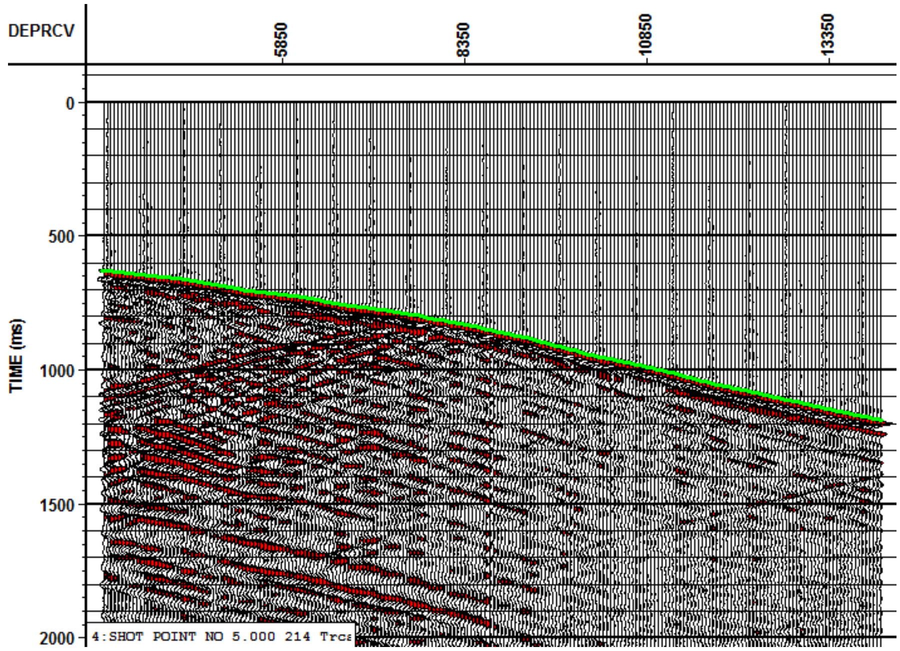

Figure 6.11 Vertical-component (Z) of an offset VSP common-shot gather after amplitude recovery and picking of P-wave first arrival times, indicated by green picks.

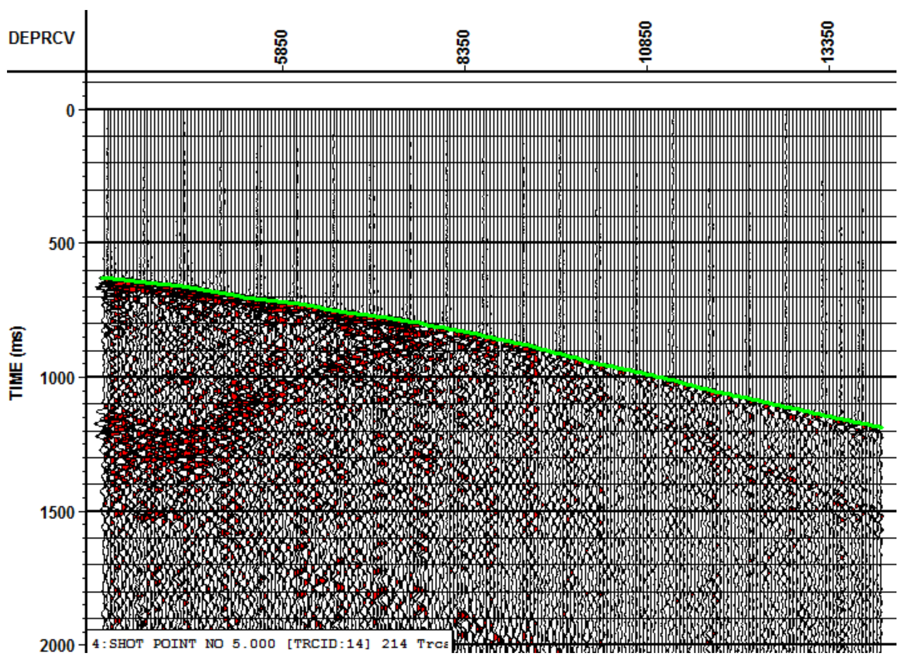

Figure 6.12 Horizontal-component (X) of an offset VSP common-shot gather after amplitude recovery and picking of P-wave first arrival times, indicated by green picks.

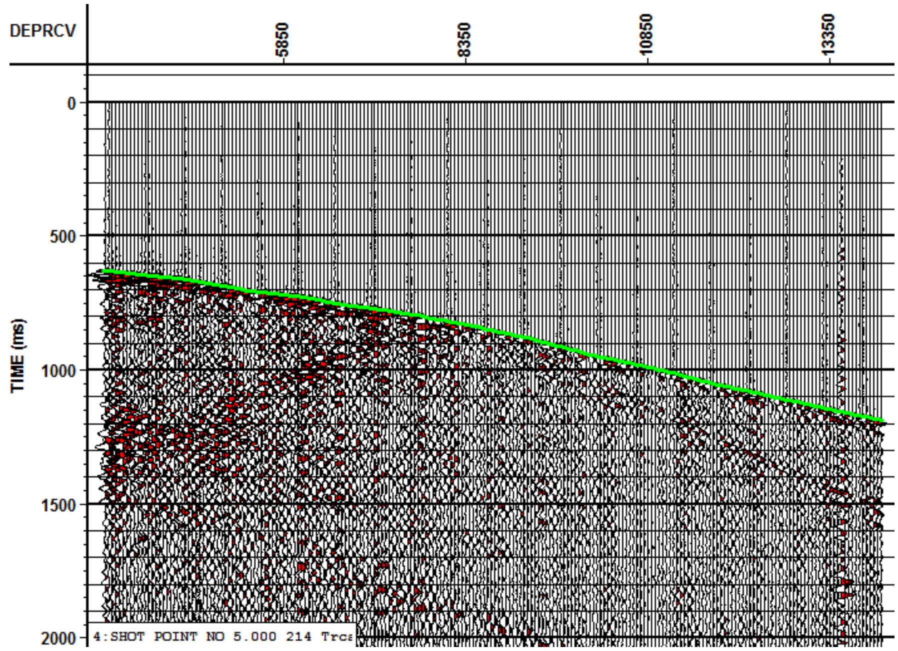

Figure 6.13 Horizontal-component (Y) of an offset VSP common-shot gather after amplitude recovery and picking of P-wave first arrival times, indicated by green picks.

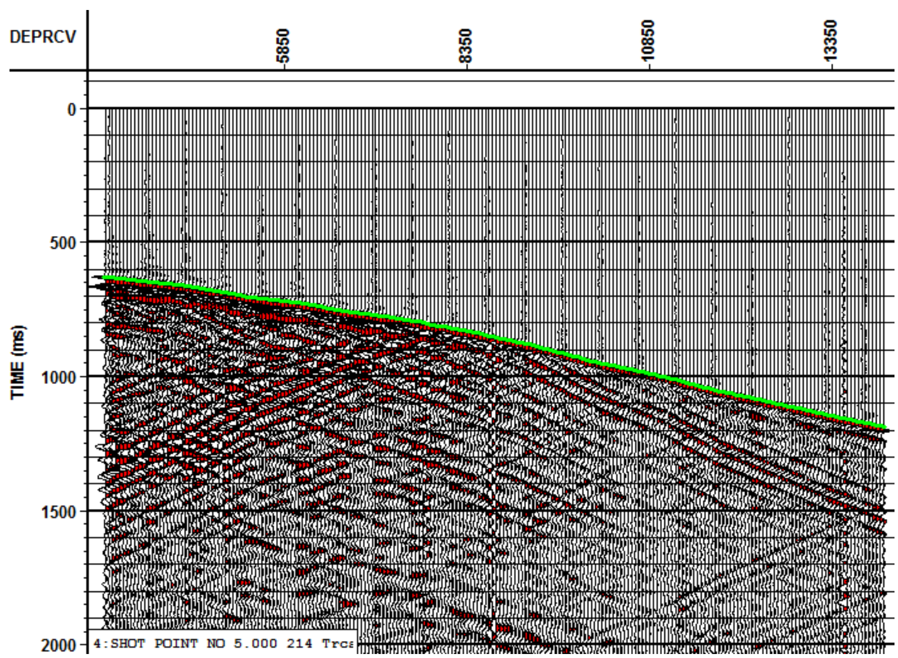

Figure 6.14 Radial-component (R) of an offset VSP common-shot gather after horizontal rotation.

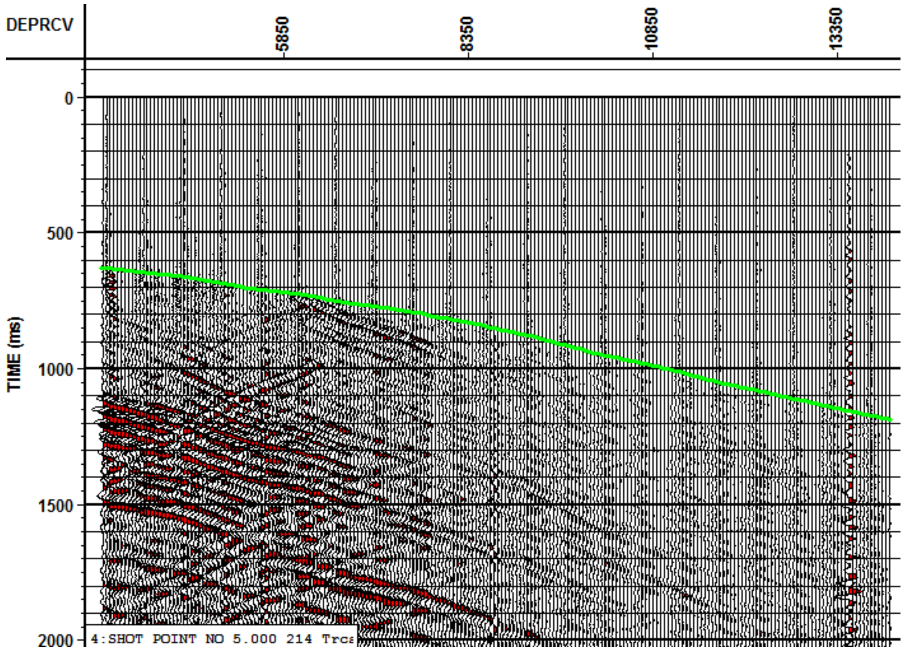

Figure 6.15 Transverse-component (T) of an offset VSP common-shot gather after horizontal rotation.

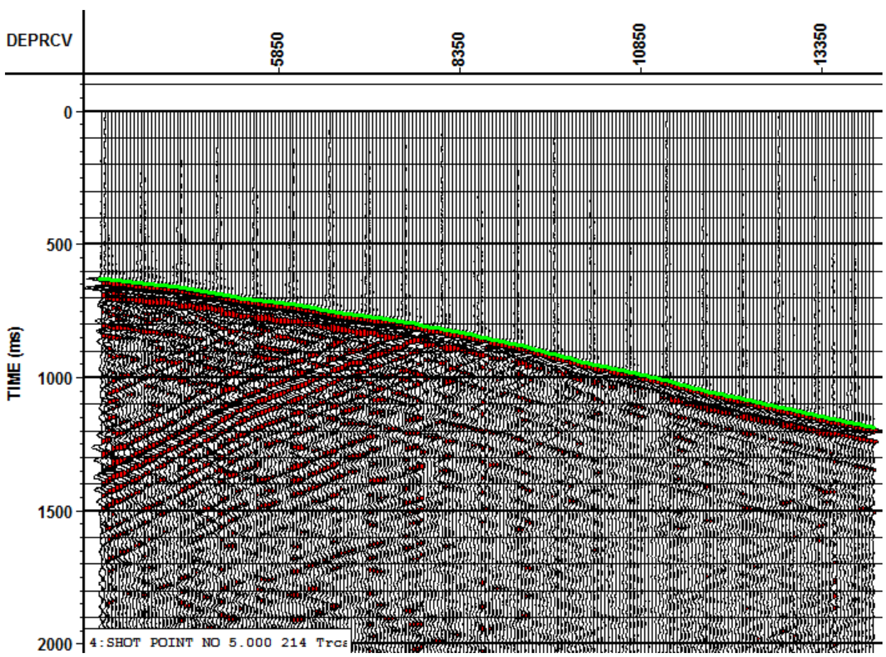

Figure 6.16 Direct-component (D) of an offset VSP common-shot gather after vertical rotation.

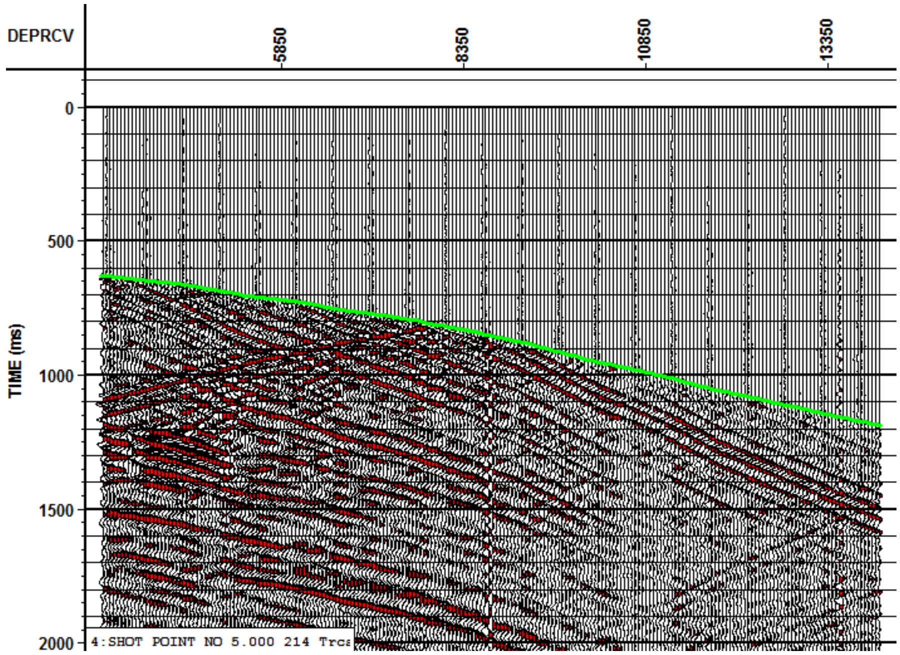

Figure 6.17 Perpendicular-component (P) of an offset VSP common-shot gather after vertical rotation.

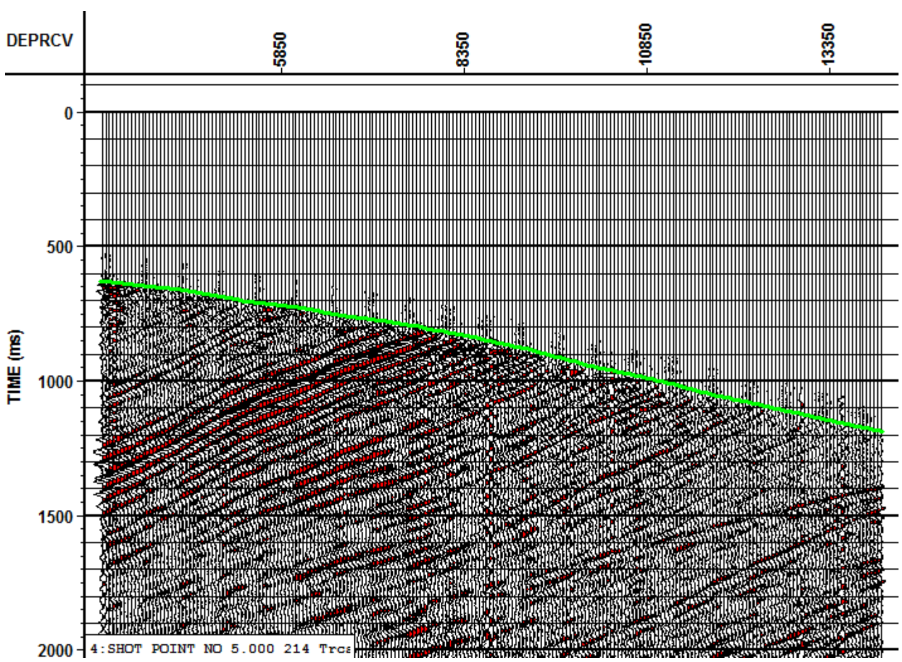

Figure 6.18 Upgoing P & S wavefields on direct-component (D) of an offset VSP common-shot gather after filtering out downgoing wavefields.

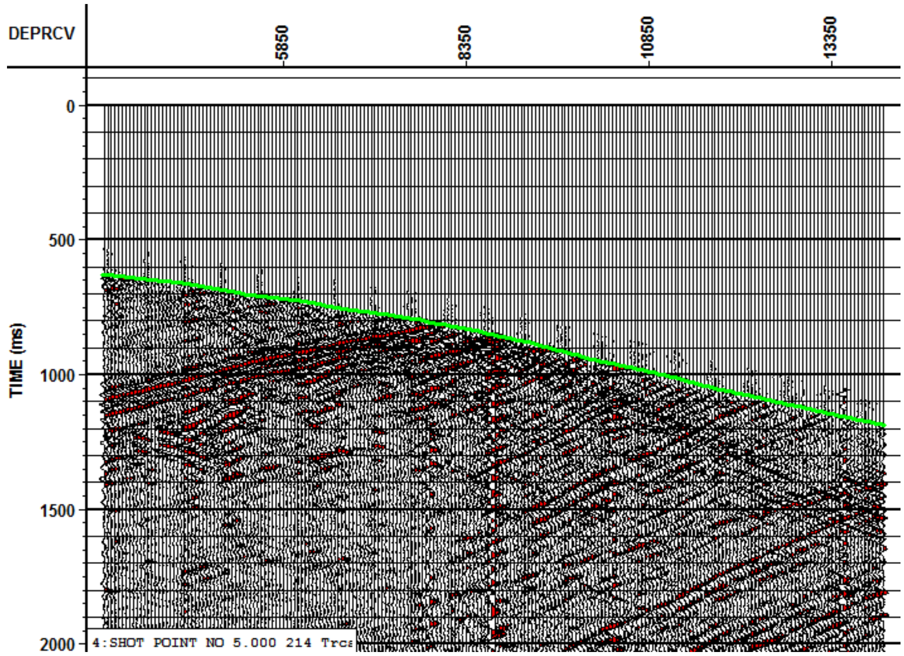

Figure 6.19 Upgoing P & S wavefields on perpendicular-component (P) of an offset VSP common-shot gather after filtering out downgoing wavefields.

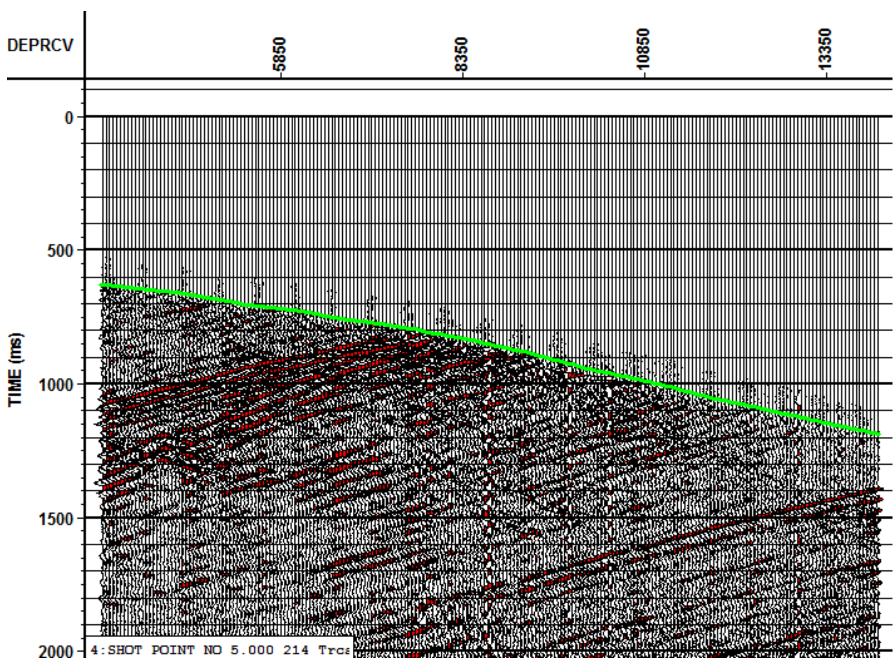

Figure 6.20 Vertical-component after inverse-vertical rotation.

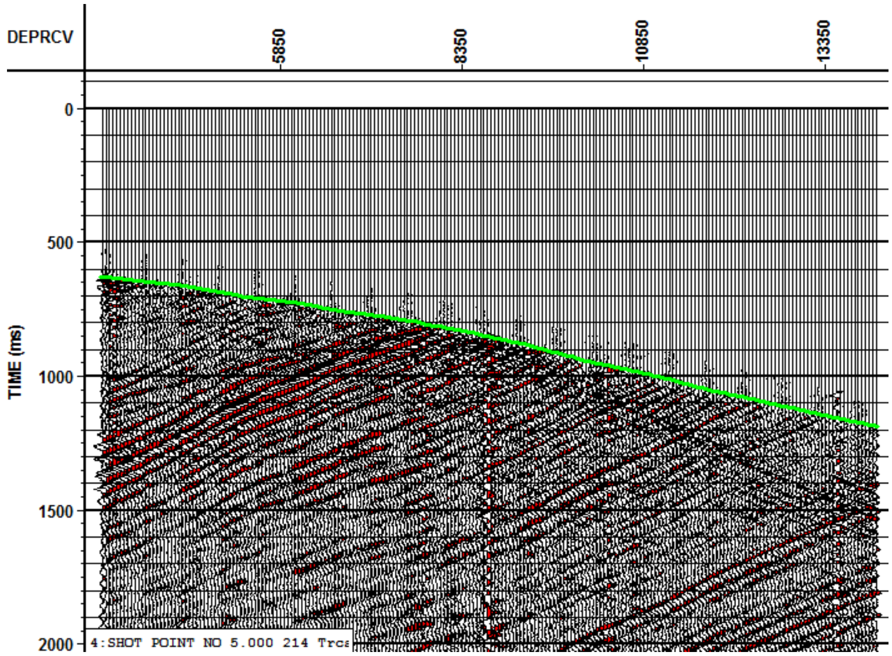

Figure 6.21 Radial-component after inverse-vertical rotation.

Next, a time-variant rotation was applied to separate upgoing P-wave energy shown in Figure 6.22 and upgoing S-wave energy shown Figure 6.23. Deconvolution and NMO correction were applied to the upgoing P wave. After NMO correction, events are supposed to match two-way-time of surface seismic events. 16` spacing was used for VSP-CDP transform. Figure 6.24 shows the VSP-CDP transform (left) and upgoing P-wave data (right) after deconvolution and NMO.

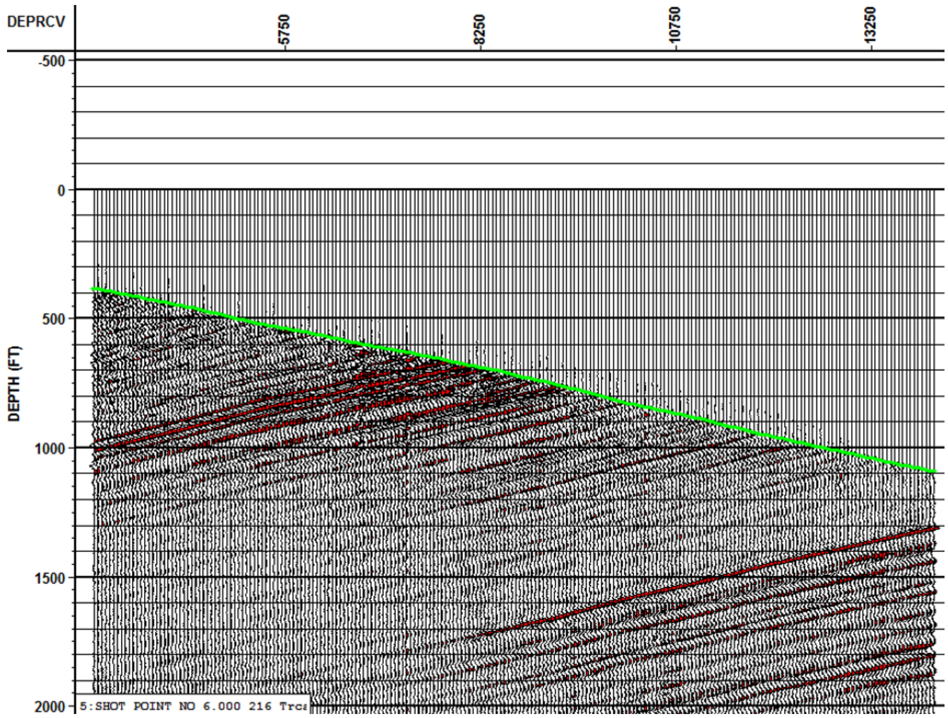

Figure 6.22 Upgoing P wavefield after model-based rotation.

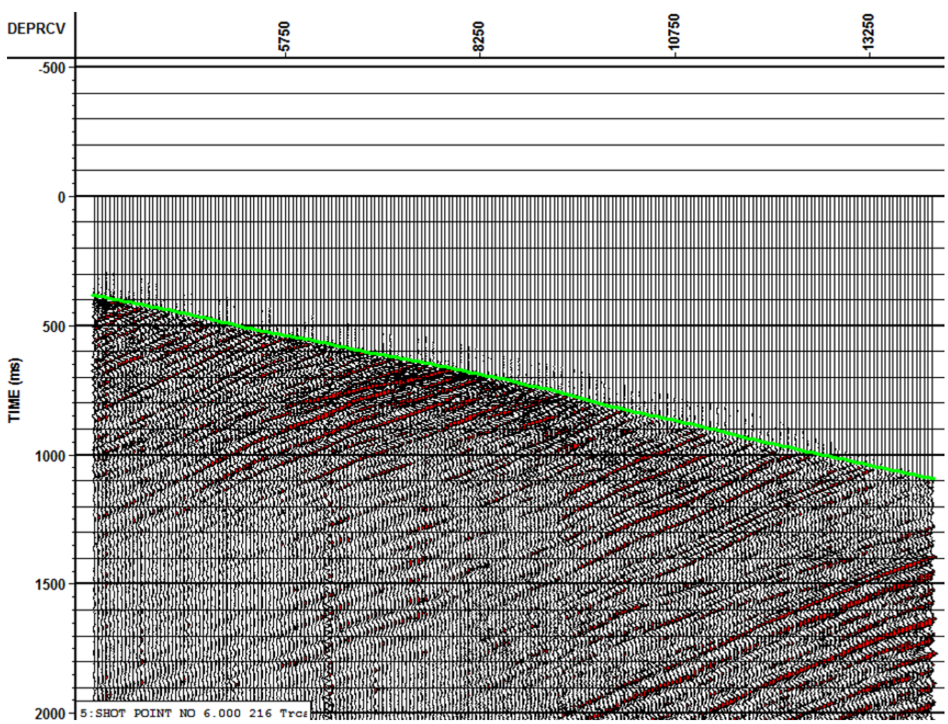

Figure 6.23 Upgoing S wavefield after model-based rotation.

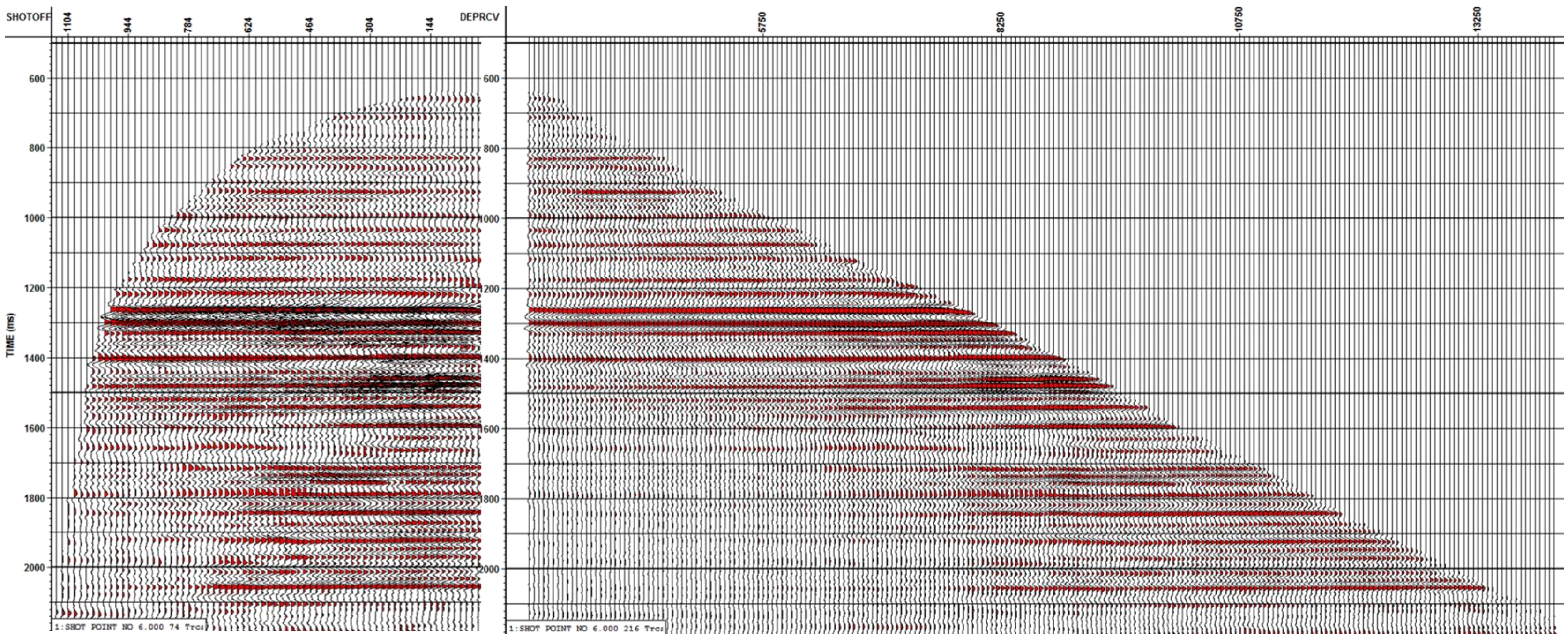

Figure 6.24 VSP-CDP transform (left) and NMO-corrected upgoing P wave.

6.3 AVAZ analysis for offset VSPs

From the VSP-CDP transform, the reflectivity-versus-offset amplitude curves of different VSP shots were extracted and are shown at the top of Figure 6.25. The angles of incidence were calculated using trigonometry:

$$\theta = \tan^{-1}\frac{z}{x_b}, \quad (6.2)$$

where z is the reflector depth, and x_b is the offset between the borehole and the VSP-CDP bin.

The reflectivity vs angle of incidence amplitude curves of different VSP shots are shown at the bottom Figure 6.25. AVAZ using linearized Rüger's inversion code, explained in **Chapter 4**, is implemented. It took 11 iterations to minimize the objective function. The inverted values for intercept, isotopic gradient, anisotropic gradient, and isotropy plane orientation were respectively -0.0125, 0.0612, 0.0168, and -89^{o} from North.

For the oil target, Wasatch-180, it took 36 iterations to minimize the difference between the measured data and theoretical reflectivity calculated by Rüger (1996). The values obtained for intercept, isotropic gradient, anisotropic gradient, and isotropy plane orientation were respectively -0.003, .001, 0.027, and -30^{0} clockwise from North. For the gas target, Upper Green River formation, there was much less data available at its depth of 5750′, as can be seen by Figure 6.2. The lack of data can affect the reliability of the results negatively.

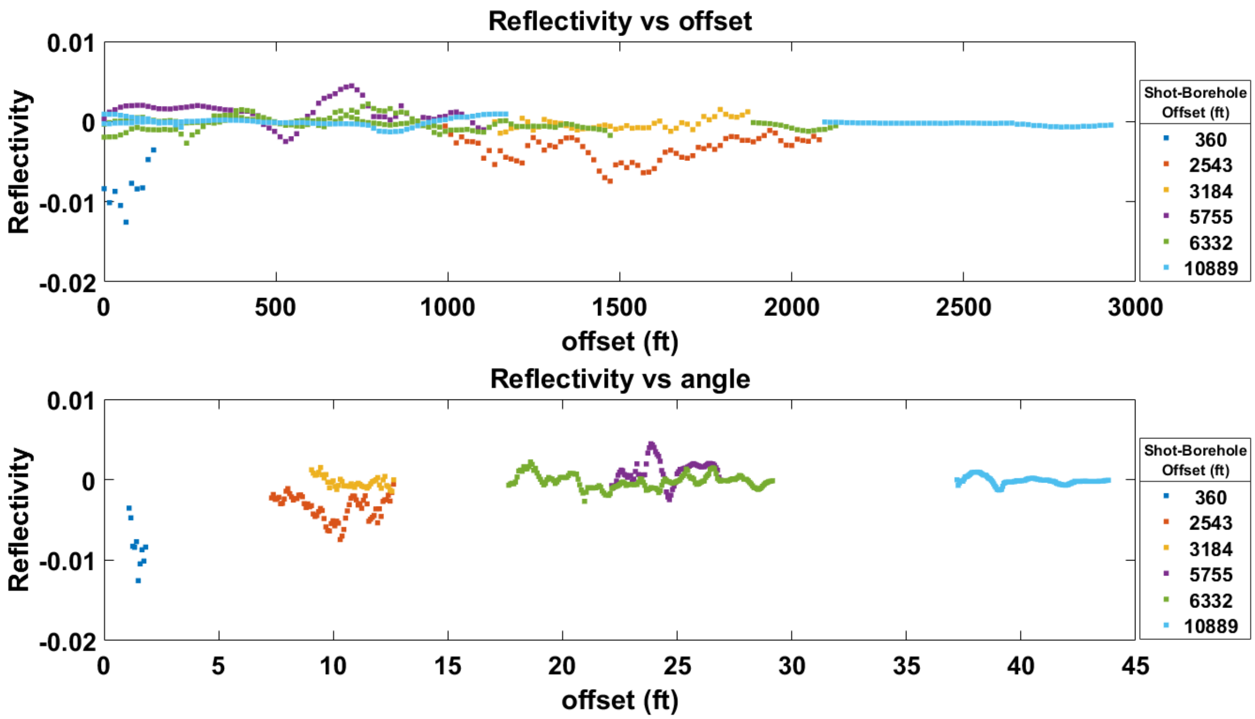

Figure 6.25 Reflectivity vs offset (top), and reflectivity vs angle of incidence (bottom).

6.4 VVAZ analysis for offset VSPs

Prior to VVAZ analysis, first arrival times were manipulated to reflect surface seismic RMS velocities and to account for the varying surface elevation. A schematic diagram showing the borehole and downgoing raypath from shot to geophone, indicated by black arrow are shown in Figure 6.26Figure 6.27. x is the borehole-shot offset. The vertical raypath from shot elevation is indicated by a red arrow. The blue arrow indicates the vertical raypath to the Seismic Reference Datum (SRD). The shot to geophone travel time is calculated from SRD and indicated by green arrow. And finally, the travel time from SRD is doubled, so the geophone can be treated as a CDP in surface seismic geometry. The equations were derived using geometry as below:

$$VT_{SE} = TT_{SE}.\cos(\tan^{-1}[\frac{x}{MD-KB+SE}]), \tag{6.3}$$

$$VT_{SRD} = VT - \frac{SE-B}{V_{avg}} + \frac{SRD-B}{V_r}, \tag{6.4}$$

and

$$TT_{SRD} = \frac{VT_{SRD}}{\cos(\tan^{-1}[\frac{x}{MD-KB+SE}])}, \tag{6.5}$$

where TT_{SE} is first arrival times indicated by the black arrow from shot directly to geophone on Figure 6.3. VT_{SE} is the vertical time from geophone to shot elevation, and is indicated by the red arrow. TT_{SRD} is the first arrival time from geophone to shot to SRD, and it is indicated by the green arrow. *MD* is the measured depth of geophone from *KB*. *SE* is the shot elevation. Finally, *B*, V_{avg}, and V_r are respectively base of weathering, average velocity, and replacement velocity.

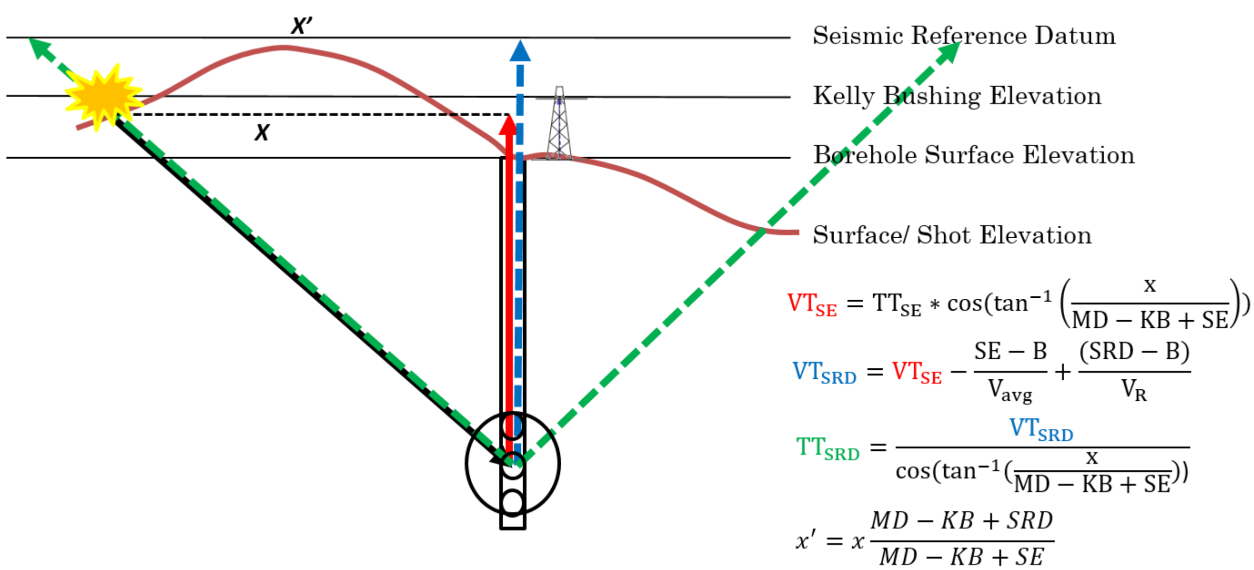

Figure 6.26 A schematic diagram showing borehole and downgoing raypath from shot to geophone, indicated by black arrow. X is the borehole-shot offset. Vertical raypath from shot elevation is indicated by red arrow. Blue arrow indicates vertical raypath to SRD. The shot to geophone traveltime is calculated from SDR and indicated by green arrow.

For all VSPs, each receiver represents a CDP of conventional surface seismic survey. The corrected arrival times or the double of TT_{SRD} (Equation 7.4) for all VSPs are used for the VVAZ inversion. Vertical arrival times were inverted and compared to VT_{SRD} in Equation (6.4) calculated for all VSPs. Inverted arrival times agreed closely with those of Shots 2, 4, and 6 and agreed somewhat less well with those of Shot 3, 5, 7 and 8, as can be seen in Figure 6.27. In **Appendix A**, error analysis of this VVAZ method are conducted.

Irregular topography and the near surface were not corrected for precisely enough. The effect of irregular topography is a shortcoming of using RMS velocities for VVAZ. A better solution would be to use an accurate interval algorithm. Inverted RMS velocities are shown in Figure 6.28 where the blue curve indicates the fast RMS velocity and the red curve indicates the slow RMS velocity. The orientation of the fast RMS velocity for all depths can be seen in the circular histogram in Figure 6.29. We have estimated Dix (1955)-type interval properties of anisotropy in Figure 6.30. The intervals used to calculate the ellipse coefficients involved every receiver (or 50′). On the left are the fast (blue) and slow (red) interval velocities. In the middle is the anisotropy intensity, and on the right is the interval anisotropy direction.

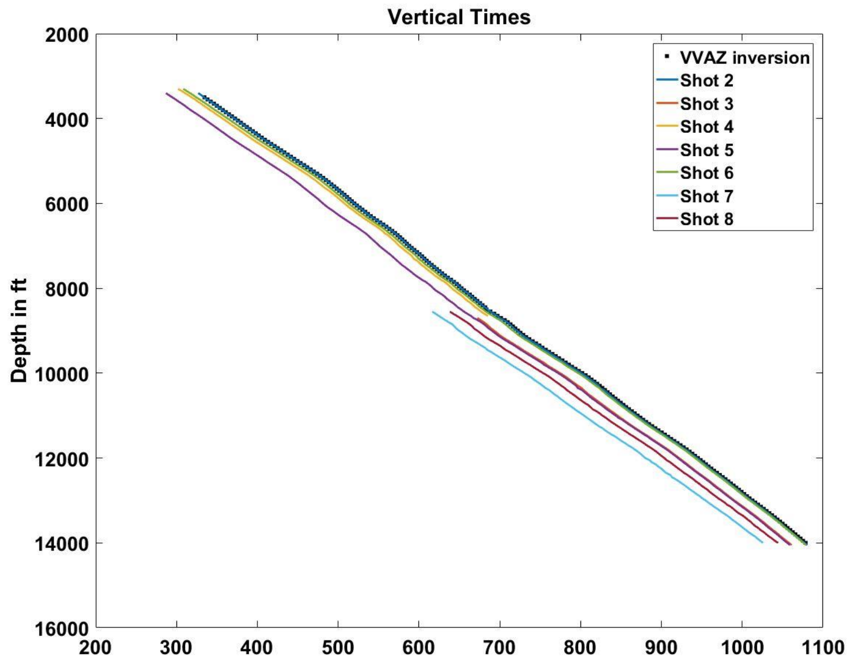

Figure 6.27 Vertical arrival times in ms of VVAZ inversion vs. calculated vertical traveltimes for each VSP shot.

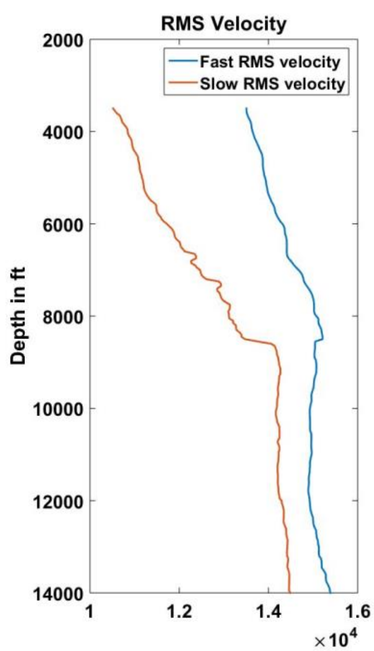

Figure 6.28 Inverted fast RMS velocity (blue) and slow RMS velocity (red).

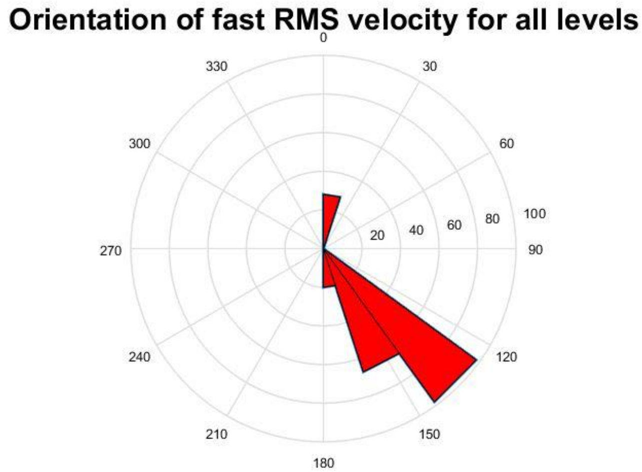

Figure 6.29 Circular histogram of fast RMS velocity direction for all receivers.

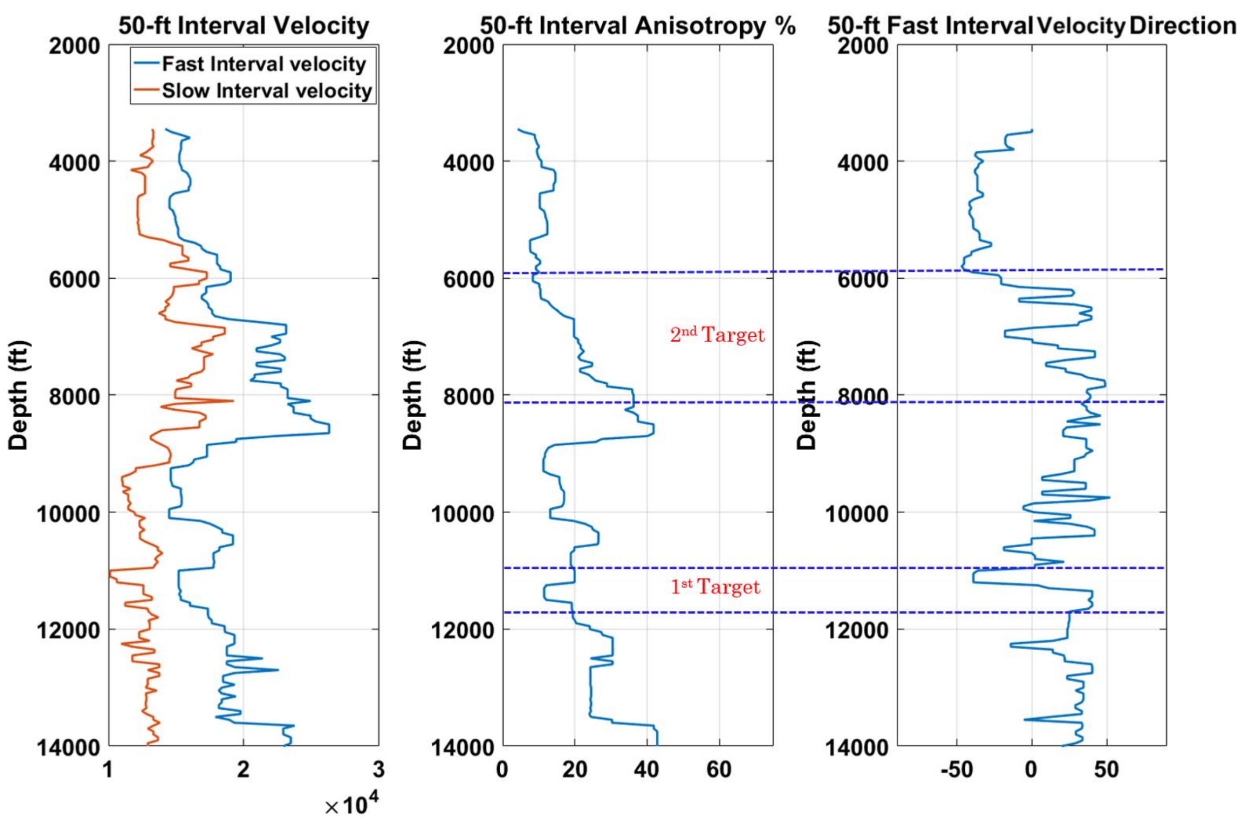

Figure 6.30 50′-interval anisotropy: slow and fast RMS velocity (left), anisotropy intensity (middle), and anisotropy direction (right).

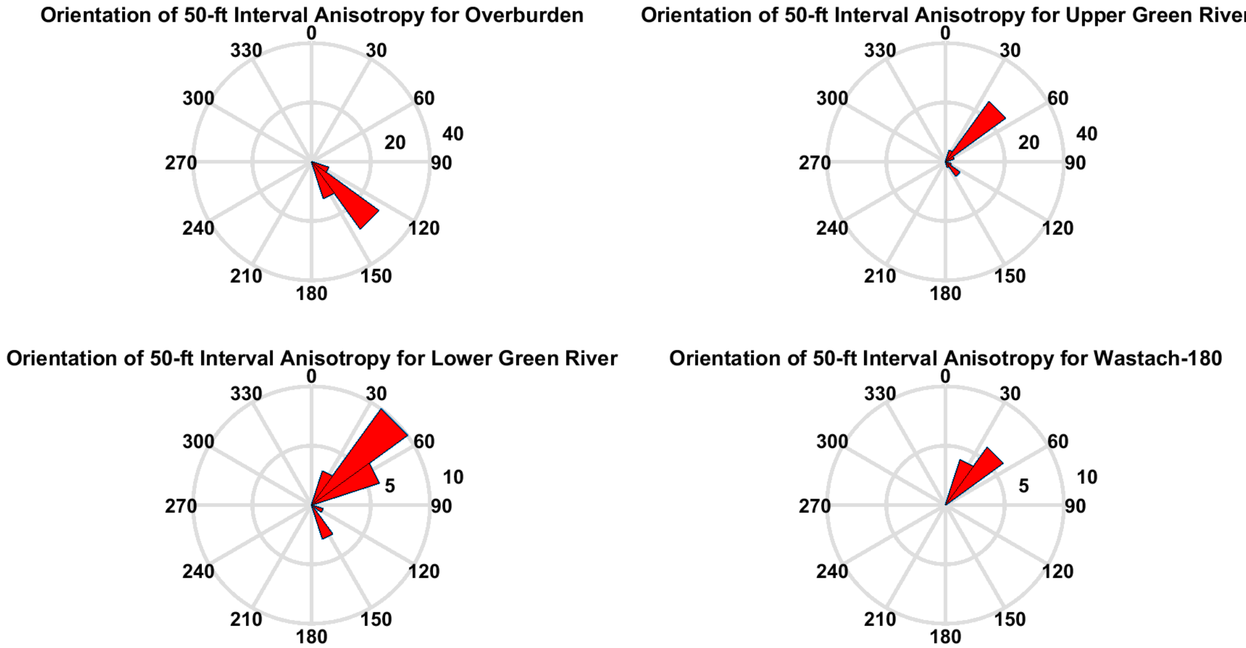

Figure 6.31 Circular histogram showing the orientation of 50′ interval anisotropy of: overburden, Upper Green River, Lower Green River, and Wasatch-180.

6.5 S-wave splitting for 4-C VSP

In HTI media, the P wave is fastest along the fracture planes, slowest perpendicular to fracture planes, and intermediate in other directions. On the other hand, the S wave splits into two phases; a phenomenon known as S-wave splitting, S-wave birefringence, or S-wave double-refraction. Polarizations of the two S waves are determined by the anisotropic axis of symmetry. The fast S is polarized along the fracture planes, and the slow S is perpendicular to the fracture planes. Beside the anisotropic axis of symmetry, the velocity of an S wave is controlled also by the angle of incidence and the azimuth of propagation. The two S waves travel at different velocities and hence are recorded at different times. The delay in time is proportionally related to the degree of S-wave anisotropy and the thickness of the anisotropic medium (Crampin, 1981).

The method is tested on a physical modeling dataset. It is applied to the common-receiver gathers from the second dataset illustrated in **Chapter 3**. For all common-receiver gathers, horizontal components of receivers and sources were aligned along either the x- or y-axis. In other words, they were aligned either parallel to the fracture plane or normal to the fracture plane. With this orientation, an S wave is fast along y-axis and slow along x-axis. In other directions, the S wave undergoes S-wave splitting and repolarizes along fast and slow directions. The fast S wave should mostly be recorded by V_{11} and the slow S wave by V_{22}. Energy on V_{12} and V_{21} should be minimal. This was not the case in our experiment! That suggests an error in the polarization direction of the horizontal transducers.

An Alford 4-component rotation (Alford, 1986) can be used to statistically rotate horizontal components (***V***) recorded in acquisition recorded system into anisotropy natural coordinate system (***U***) using rotation matrix ($\boldsymbol{R}(\theta)$):

$$V = \begin{bmatrix} v_{11} & v_{12} \\ v_{21} & v_{22} \end{bmatrix}, \tag{6.7}$$

$$U = \begin{bmatrix} u_{11} & u_{12} \\ u_{21} & u_{22} \end{bmatrix}, \tag{6.8}$$

and

$$R(\theta) = \begin{bmatrix} \cos\theta & sin\theta \\ -sin\theta & cos\theta \end{bmatrix} \tag{6.9}$$

The rotation matrix, $\boldsymbol{R}(\theta)$ is an orthogonal matrix that gives the identity matrix when multiplied by its transpose or its inverse. To find a new basis for the natural coordinate system, the counterclockwise rotation by angle (θ) is

$$U = R(\theta)\, V\, R^T(\theta). \tag{6.10}$$

Substituting equations (6.7), (6.8), and (6.9) into equation (6.10):

$$\begin{bmatrix} u_{11} & u_{12} \\ u_{21} & u_{22} \end{bmatrix} =$$
$$\begin{bmatrix} \cos^2\theta\, v_{11} + \sin^2\theta\, v_{22} + 0.5\sin 2\theta\,(v_{21} + v_{12}) & \cos^2\theta\, v_{12} - \sin^2\theta\, v_{21} + 0.5\sin 2\theta\,(v_{22} - v_{11}) \\ \cos^2\theta\, v_{21} - \sin^2\theta\, v_{12} + 0.5\sin 2\theta\,(v_{22} - v_{11}) & \cos^2\theta\, v_{22} + \sin^2\theta\, v_{11} - 0.5\sin 2\theta\,(v_{21} - v_{12}) \end{bmatrix}. \tag{6.11}$$

Equation (6.11) transforms $\boldsymbol{V}$, horizontal components in acquisition coordinate system into the natural coordinate system (Alford, 1986).

The rotation angle (θ) is found by scanning different angle values at angular interval of 1°, and selecting the angle that minimizes u_{12} and/or u_{21}. For each common-receive gather, angles were scanned within a time window to determine the rotation angle (θ) and Alford rotation was applied. Please refer to the 2nd dataset in **Chapter 3**. The two linear gathers with 0° and 90° azimuths respectively are shown by Figure 6.32 and Figure 6.33 before rotation in the left and after the rotation on the right. Alford rotation was applied to the second dataset. Figures 16, 18, and 20 show the unrotated data and the rotated data of the second dataset that was acquired over the Phenolic medium. The cross energy of the 90°-azimuth shot gather common-shot gather, is shown in **Error! Reference source not found.**.

Alford rotation behavior is just as anticipated. The rotation angles are very small because acquisition coordinate system is similar to the natural coordinate system. The small angles are caused by small errors in acquisition. The results of Alford rotation for the second dataset are quite satisfying. They provide confidence in S-wave acquisition tools.

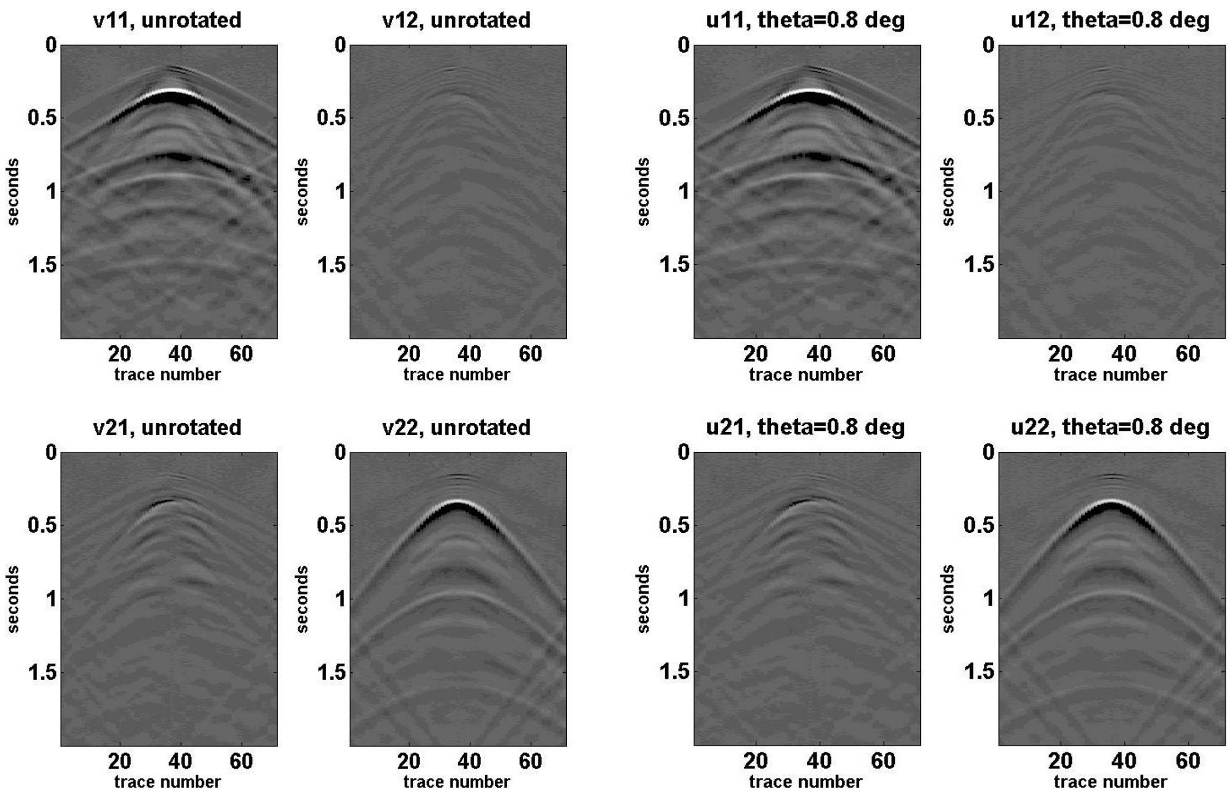

Figure 6.32 0^0-azimuth shot gather acquired over the phenolic layer: 4 Horizontal components before rotation (left) and after rotation (right).

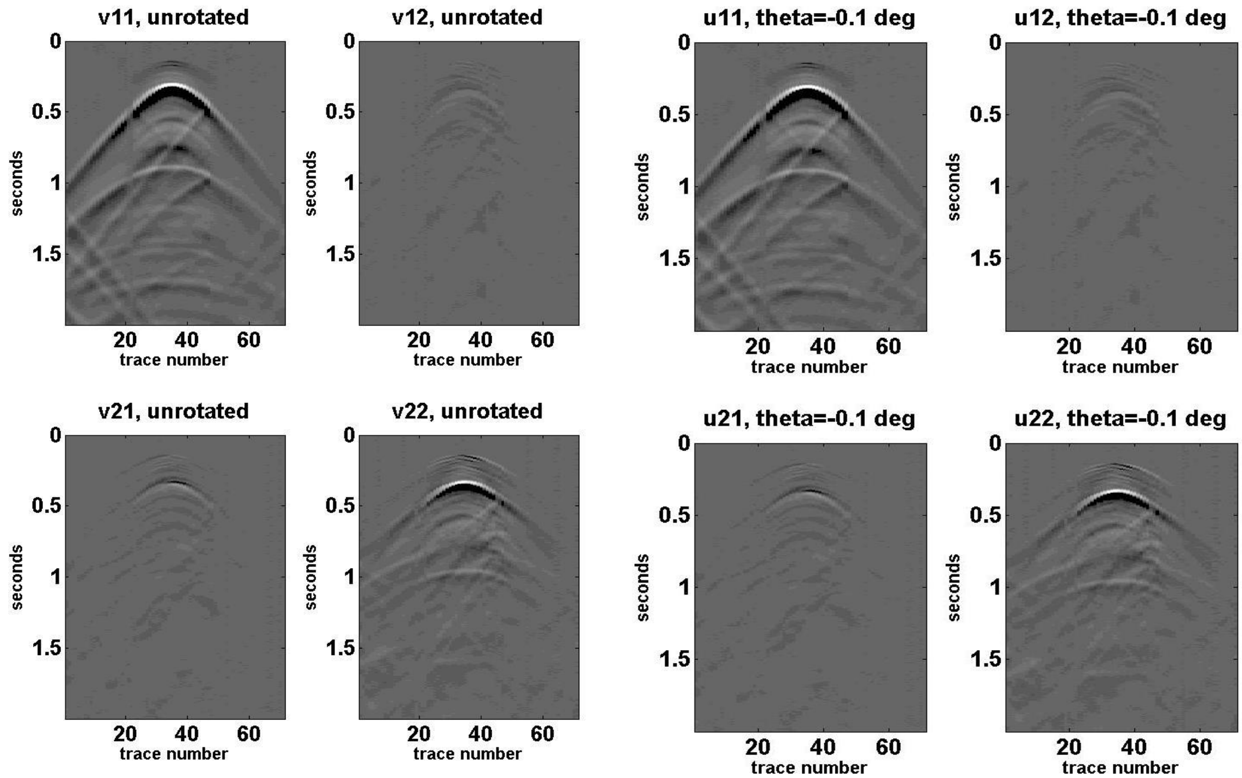

Figure 6.33 90°-azimuth shot gather acquired over the phenolic layer: 4 Horizontal components before rotation (left) and after rotation (right).

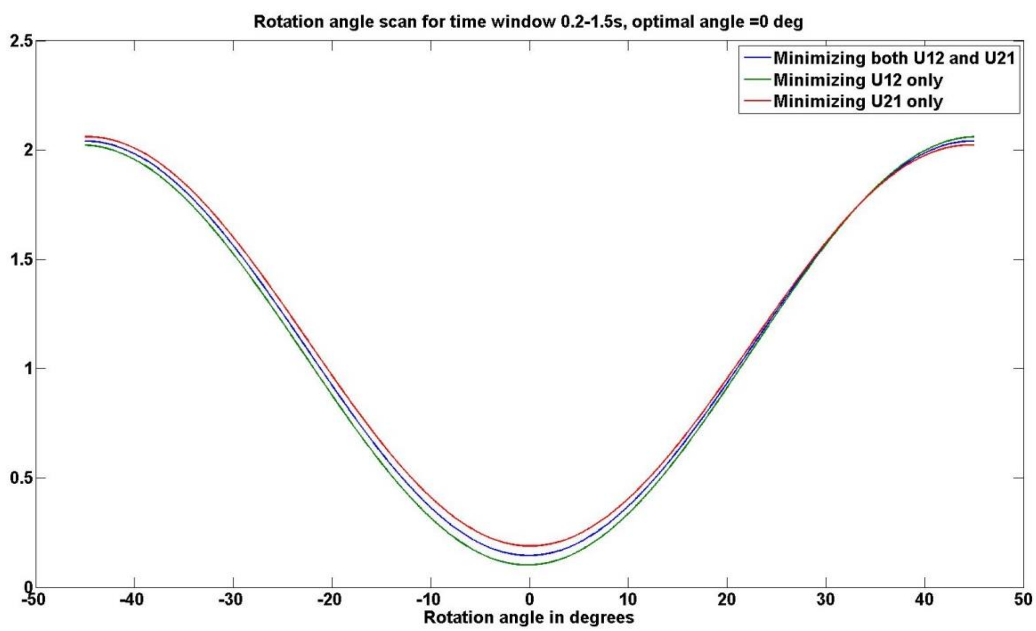

Figure 6.34. 90°-azimuth shot gather: cross energy vs. rotation angle.

The 4 components of the 4-C VSP, in the Altamont-Bluebell data are shown in Figure 6.35. Prior to applying 4-C rotation to the 4-components, the two horizontal components of the geophones are needed to be re-oriented into East-West and North-South directions. Luckily other VSP shots were acquired with the recording tool in place. Those shots were used to re-orient the tool by first using the P-wave first breaks from other shots to calculate the required angle to re-orient to that shot. And later, re-orient the tool into East-West and North-South directions. For Alford rotation, angles were scanned within a picked time window placed approximately centred on first S-wave arrival times to determine the rotation angle (θ). For layer stripping, all data below the depth at which S-wave polarization change is observed are rotated. Then, a static time shift is applied to remove the lag between fast and slow S waves at that depth. This technique simulates placing a source at the depth where S-wave polarization changes (Winterstien and Meadows, 1991). This layer-stripping method was applied to the 4 layers: overburden, Upper Green River Formation, Lower Green River Formation, and Wasatch Formation. For the last layer, which is the Wasatch-180 formation, Alford rotation was also applied. The four components of VSP data after rotation and layer stripping and the required rotation angle are shown in Figure 6.36 and Figure 6.37 respectively. Figure 6.38 shows an overlay of fast S-wave in blue traces and slow S-wave in red traces, while Figure 6.39 shows Fast S-wave first arrival times indicated by blue, and slow S-wave indicated by red.

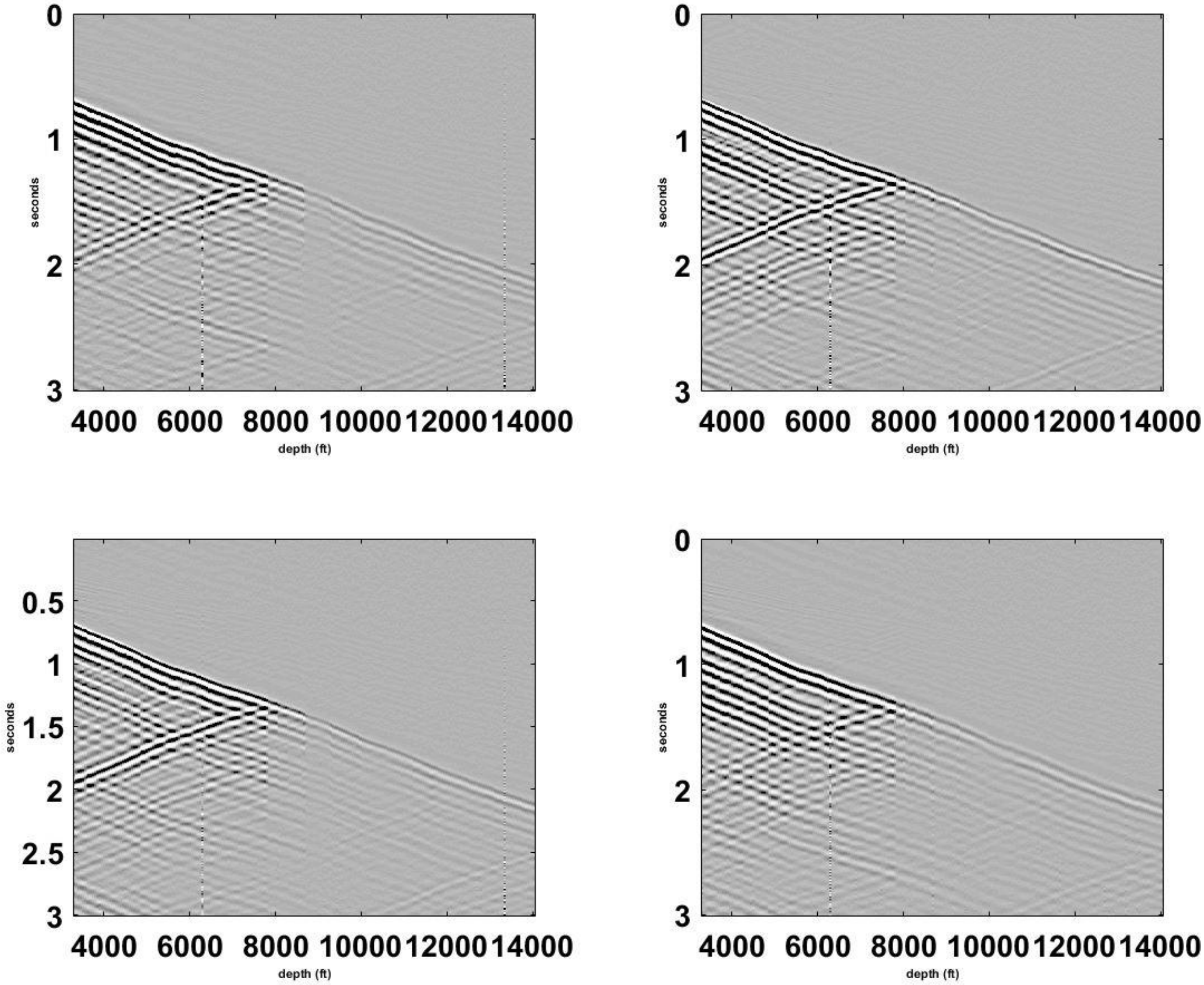

Figure 6.35 4-C VSP before rotation: N-S shot components (top), E-W shot components (bottom), N-S receiver components (left), and E-W receiver components (right).

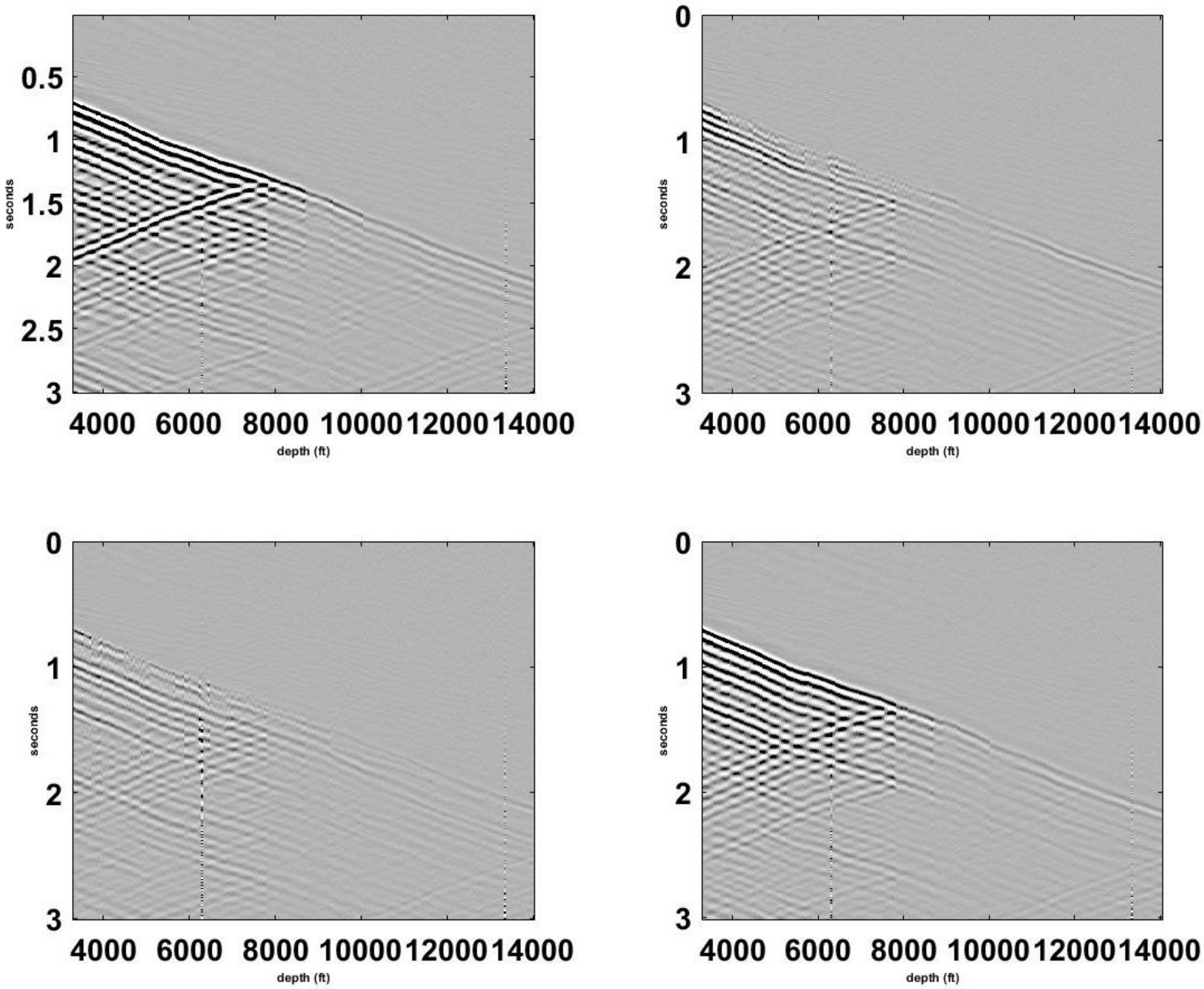

Figure 6.36 VSP after rotation and layer stripping: N-S shot components (top), E-W shot components (bottom), N-S receiver components (left), and E-W receiver components (bottom).

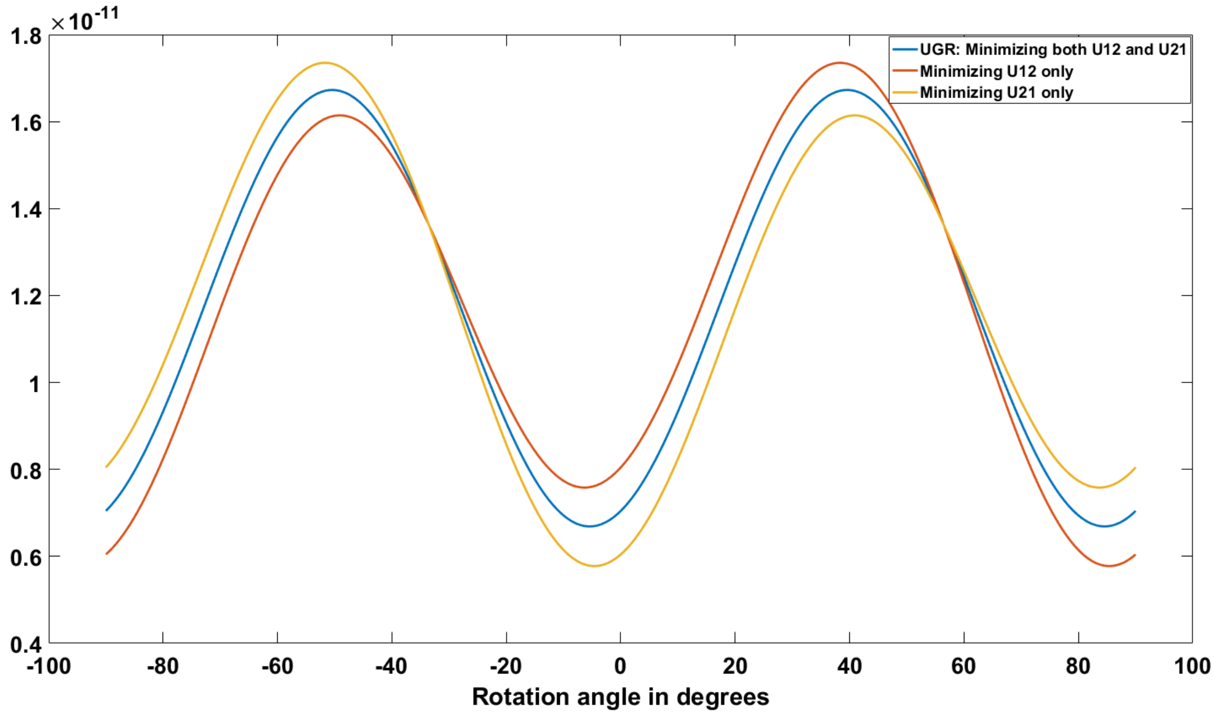

Figure 6.37 4-C VSP cross energy vs. rotation angle of: overburden, Upper Green River.

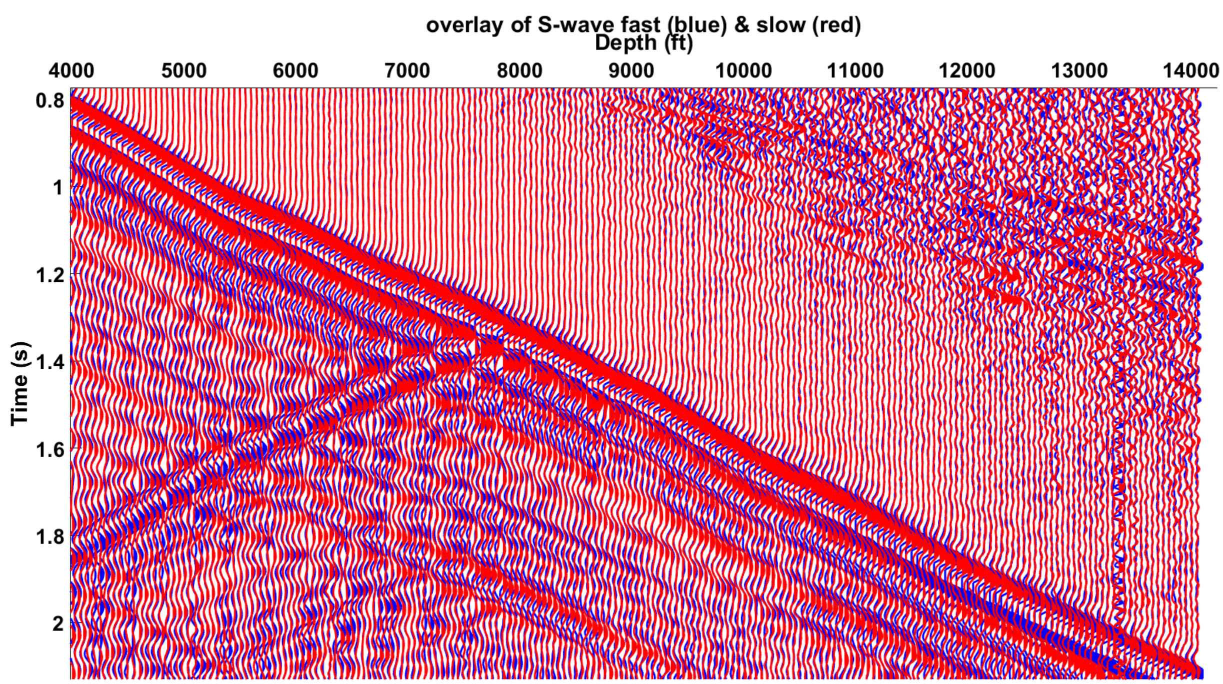

Figure 6.38 S-wave data after rotation and layer stripping of 4-C VSP. The S-wave fast is indicated by blue traces, while slow is indicated by red traces.

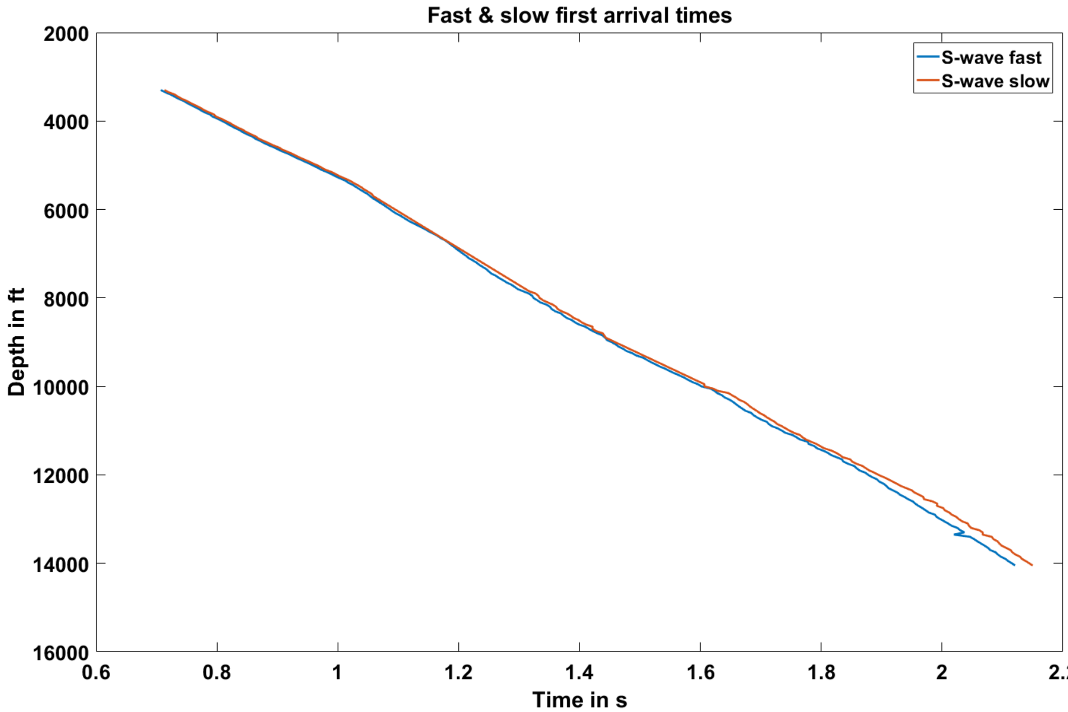

Figure 6.39 Fast S-wave first arrival times indicated by blue, and slow S-wave indicated by red.

The plot of cross energy against rotation angle is shown in Figure 6.40 for the 4 layers analyzed. The rotation angles of overburden, Upper Green River formation, Lower Green River formation, and Wasatch-180 formation were found to be as follows: The Upper and Lower green river formation have anisotropy orientation of Northwest-Southeast, while the overburden and Wasatch formation have anisotropy orientation of Northeast-Southwest. The fast S-wave and slow S-waves were picked on rotated data. The picks are shown in Figure 6.39 with blue picks being fast S-wave and red picks being slow S-waves. From, the lag between the two modes of S-wave, an anisotropy intensity log is calculated in the left side of Figure 6.40, while the anisotropy direction is shown on the right in the same figure. At the borehole location, the Wasatch formation has the most anisotropy intensity as can been seen by the anisotropy intensity log just below 10000 feet of depth. Wasatch-180, the oil target, which is within the Wasatch, has less anisotropy than the rest of the Wasatch but more than other formations.

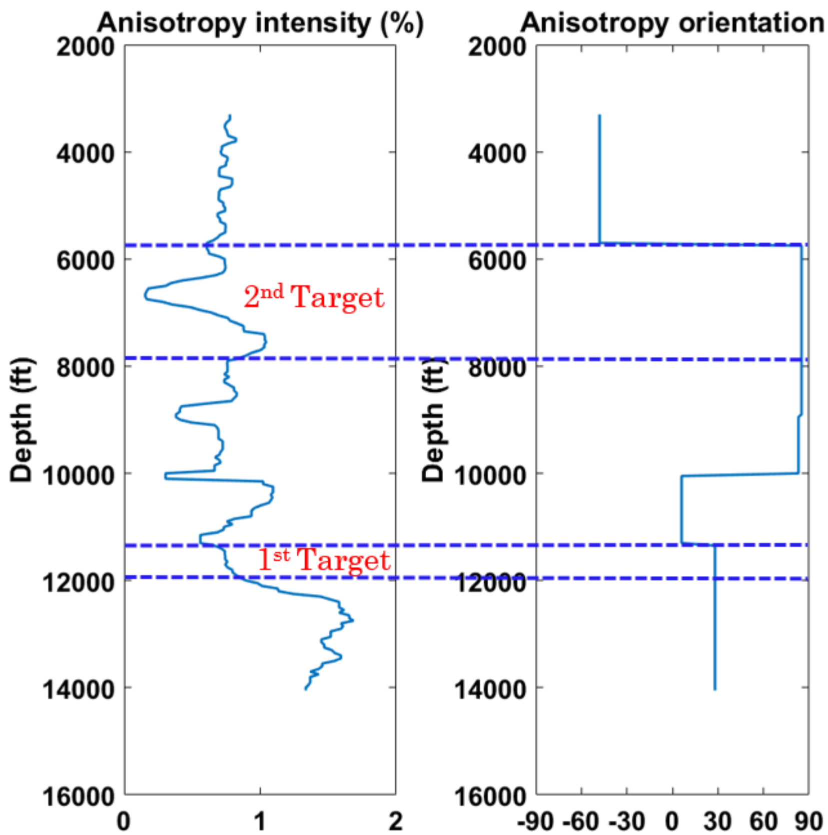

Figure 6.40 S-wave analysis: anisotropy intensity (left) and direction (right).

6.6 Summary

For the development of unconventional reservoirs, azimuthal variations of P-wave velocities can be a valuable tool for fracture information. In this paper, we have developed a VVAZ workflow for offset, workaround, or walkaway VSPs using a method for surface seismic. Vertical arrival times for all shots were not very similar at the beginning. Irregular topography and near surface effects were not corrected properly, which would affect the VVAZ method shown here, based on RMS velocity. Therefore, interval anisotropy properties were calculated, as well, to avoid the effects of overburden. The intervals used to calculate the ellipse coefficients involved every receiver (or 50′).

The three reservoirs were found to have anisotropy oriented along a Northeast-Southwest trend, while the overburden anisotropy was oriented Northwest-Southeast. The anisotropy intensity was found to be highest in the Wasatch formation and the lower part of the Upper Green River formation.

Chapter 7 Discussions & Conclusions

The last chapter wraps up this research by discussing the differences between travel time and amplitude methods for azimuthal anisotropy. Also it compares the results obtained by the two methods here, and summarizes key elements of the research.

7.1 AVAZ vs VVAZ

When comparing VVAZ to AVAZ, the following points need to be taken into consideration before making conclusions:

- The low-frequency part of the velocity structure controls the travel time and the high frequency part controls the reflectivity(Claerbout, 1985). He outlined the relation between accuracy and temporal frequency ($\frac{vk_z}{2\pi}$) in Figure 7.1, where k_z is the wavenumber. The low-frequency component of velocity structure controls travel times and has a high accuracy, whereas amplitude comes from reflectivity and is controlled by the higher resolution but lower accuracy component. That roughly implies the inversion of travel times will only get a smooth (but higher accuracy) velocity and the detail needs to come from amplitudes.
- Seismic data processing can lead to more errors in amplitudes than travel times. Both amplitudes and travel times need proper azimuthal sectoring or binning, as explained in **Chapter 2**. However, it is harder to avoid mistakes when dealing with amplitude. The data needs to be properly scaled. Also, any processing step needs to preserve amplitudes azimuthally, which can be questionably satisfied.

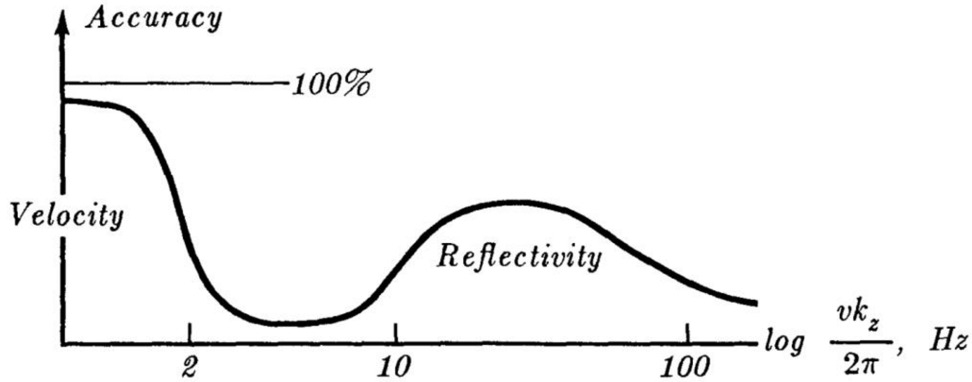

Figure 7.1 Accuracy vs. frequency of information obtained by surface seismic measurements (Claerbout, 1985).

- There is a 90° ambiguity associated with the estimate of axis of symmetry when using near-offset Rüger-style AVAZ, and priori information from well logs or VVAZ should be used as an external constraint.
- Do amplitude azimuthal variations techniques see what azimuthal travel time techniques see? The definite answer is no. AVAZ methods measure reflector properties. In other words, they measure the effect of having a contrast caused by an underlying anisotropic layer. If the top layer is anisotropic too, then it measures the effect caused by the contrast of the combination of the two layers. A more difficult scenario occurs when there is a considerable contrast in the axis of symmetries of the two layers where the AVAZ assumptions would be violated. Bakulin, et al. (2000a) showed the remarkable influence of background V_P/V_S ratio, as there will be no amplitude variations with azimuth even if the fracture intensity is high for a V_P/V_S

ratio of 1.75 in case of gas-filled cracks. On the other hand, azimuthal variations of travel times are influenced directly by traveling through anisotropic layers.

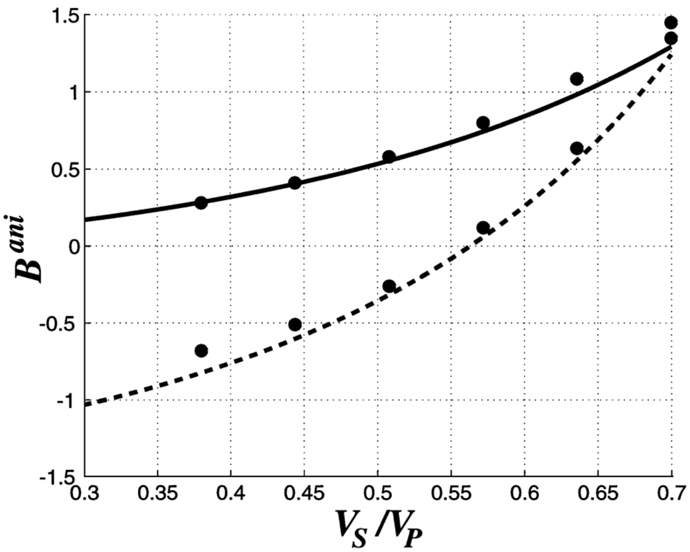

Figure 7.2 AVAZ gradient for P-wave reflection from the interface between isotropic and HTI media. The difference between two AVAZ gradients in the directions perpendicular and parallel to fractures was calculated for gas-filled cracks (dashed line) and liquid-filled cracks (solid line). There is no difference between the two gradients at V_S/V_P values around 0.57 for gas-filled cracks (After Bakulin, et al. (2000a)).

If the exploration goal is the regional stress field, then a low-resolution VVAZ method may be sufficient with an acceptable accuracy. For local anisotropy details, high-frequency AVAZ methods may be needed. However, considering all of the previous points and its unforgiving theoretical requirements, we believe that AVAZ complements VVAZ but should not be used alone. AVAZ can provide us with local fluctuations while VVAZ is providing us with more accurate, but lower resolution trends.

7.2 Summary and conclusions

For the development of unconventional reservoirs such as those of the Altamont-Bluebell field, azimuthal variations of P-wave velocities can be a valuable tool for fracture information. Here, we have developed a VVAZ workflow for offset, walkaround, or walkaway VSPs using a method adapted from surface seismic techniques. Azimuthal inversion of amplitude and travel time were applied to 3-D pre-stack surface seismic and offset VSPs. Also, S-wave splitting was analysed for four-component VSP data. The VVAZ method was validated using 3-D physical modeling datasets and the results for anisotropic planes of Phenolic were found to be adequate. The stiffness coefficients of Phenolic were measured too in this study and shown in Equation (3.17). Comparing the coefficients to Table (2.3) in Mahomoudian (2013), we can see the values measured here are smaller but relatively comparable and that is due to using different type of Phenolic.

Since both amplitude and travel time inversion for azimuthal anisotropy were performed for two reservoirs in the Altamont-Bluebell field, their results are compared here. A non-hyperbolic NMO equation for TI media derived by Grechka and Tsvankin (1998) was used for the azimuthal velocity inversion and the overburden effect was stripped by using Dix (1955) type interval properties. Those properties are compared to interface properties obtained by iterative nonlinear inversion of azimuthal amplitude variations based on Rüger (1996). Looking at anisotropy orientation from results obtained AVAZ (left) and VVAZ (right) for the Upper Green Reservoir in Figure 7.3, the difference in resolution can be spotted right away. AVAZ resolution is higher. Also, the major trend of anisotropy orientation is found to be similar in the Northwest-Southeast direction at about -40^{o} clockwise from North. However, on the southeastern corner of the survey VVAZ sees a Northwest-Southeast trend. The AVAZ and VVAZ anisotropy orientation maps for deeper oil target (Wasatch-180) are shown by Figure 7.4. Both VVAZ and AVAZ show a Northwest-Southeast major trend and Northeast-Southwest minor trend of anisotropy orientation. Those results are in agreement with geological and stress observations summarized in Table 2.1. The anisotropy intensity obtained by AVAZ and VVAZ can be compared, as well. Both AVAZ and VVAZ show higher anisotropy percentages for Wasatch-180 than Upper Green River.

Table 7.1 summarizes the results obtained at the VSP borehole location. Results were obtained for surface seismic data using azimuthal variations of amplitude and travel times for two reservoirs, and for VSP data using S-wave splitting, azimuthal variations of travel time, and amplitude. For anisotropy orientation, all results obtained by all methods using VSP and surface seismic data were consistent and show a Northeast-Southwest trend except for AVAZ using VSP data. For anisotropy intensity, the comparison should be relative. For example, Dix (1955)-type interval properties may give large value for small intervals like the ones used for VSP (50′ interval). All methods estimated anisotropy percentages below 3 except for interval VVAZ of both reservoirs and AVAZ of Wasatch-180.

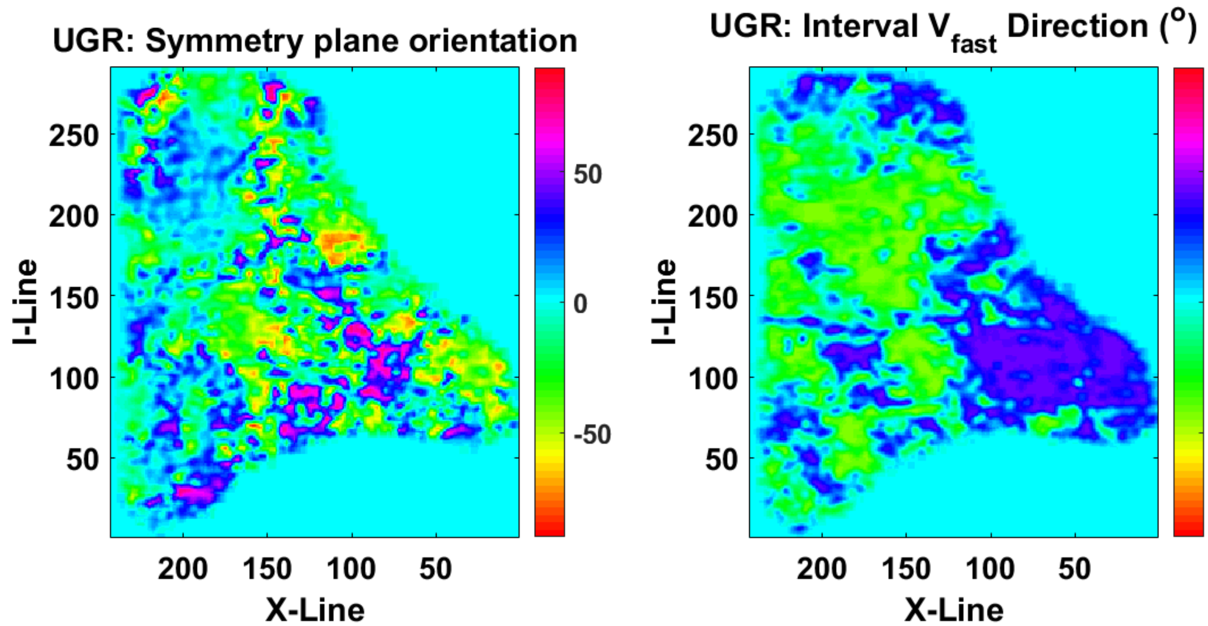

Figure 7.3 Anisotropy orientation for Upper Green Reservoir obtained by two different methods: AVAZ (left) and VVAZ (right).

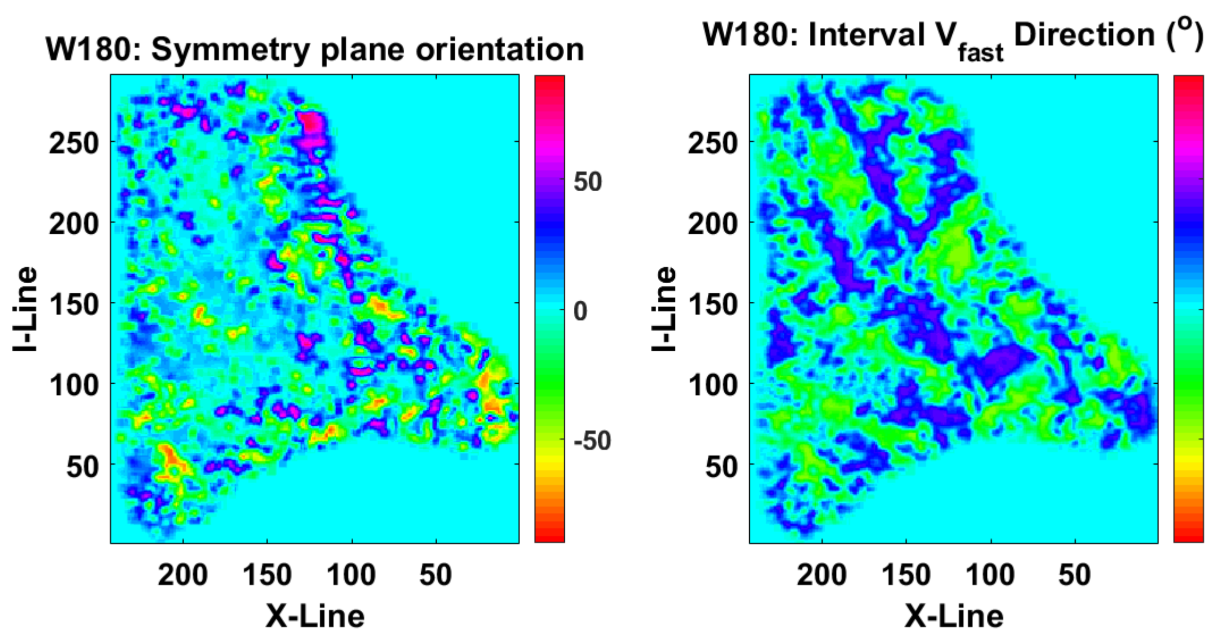

Figure 7.4 Anisotropy orientation for Wasatch-180 Reservoir obtained by two different methods: AVAZ (left) and VVAZ (right).

	Anisotropy Orientation (°)		Anisotropy Intensity (%)	
Reservoir :	**UGR**	**W180**	**UGR**	**W180**
VSP Data: S-wave Splitting	85	30	0.7	0.8
VSP Data: VVAZ	50	40	18	20
VSP Data: AVAZ	1	50	2	3
Surface Seismic Data: VVAZ	36	43	4	18
Surface Seismic Data: AVAZ	40	71	3	8

Table 7.1 The results obtained at the VSP borehole location. Results are obtained by VSP data and by surface seismic data using two azimuthal variations of amplitude and travel times for two reservoirs. For AVAZ, results are of the contrast not the reservoirs. Note: this specific location was found to differ from major trends across the survey by having a less anisotropy intensity and different orientation (Northwest-Southwest by most methods).

7.3 Forward-looking

Data processing plays an important role in azimuthal analysis of both amplitude and travel time, but even a bigger role in amplitude. The processing workflow should not be only AVA compliant but also AVAZ compliant. For example, a Radon filter should only be applied to azimuth sectors. In addition, the data needs to be sectored or COV binned. Downton et al. (2011) tested the influence of sectoring, sectoring followed by 5-D interpolation, and COV binning. They correlated azimuthal gradient to image log and concluded that regularized COV has best correlation at 0.71. Sectoring with 5-D interpolation came very close at 0.68, while sectoring without interpolation came behind at 0.49. Consequently, COV binning or sectoring followed by interpolation prior to migration is recommended here because migration assumes uniform sampling to prevent operator aliasing. Migration is required in the workflow of both VVAZ and AVAZ analysis because it collapses the Fresnel zone and diffractions (Mosher et al.,1996), and removes dip dependency from elliptical NMO velocity analysis. Pre-stack time migration

(PSTM) generally is enough land data, but depth migration would be required for areas of complex structures. To estimate parameters of azimuthal anisotropy, compensation for polar anisotropy, i.e. VTI migration, is recommended. Not accounting for VTI would retaliate with lower RMS velocities. Therefore, it is important for building a reliable background model for accurate estimation of azimuthal anisotropy parameters. For AVAZ, application of residual NMO is required for flat reflection events. It is not only that data processing plays an important role in azimuthal analysis, but the other way around can be right. The three parameters (V_{fast}, V_{slow}, and β_s) obtained, in **Chapter 5**, by VVAZ inversion and the VTI parameter (η) of Alkhalifa and Tsvankin (1995) can be used to compute travel time for PSTM. Jenner (2011) proposed a workflow for combining VTI and HTI anisotropy in PSTM, and it is suggested here for future work to improve seismic imaging of the Altamont-Bluebell 3-D seismic data.

AVAZ complements VVAZ but should not be used alone, as suggested earlier. AVAZ can provide us with local fluctuations while VVAZ is providing us with more accurate, but lower resolution trends. A joint model-based inversion of AVAZ and VVAZ (using the VVAZ model as the background, while using amplitude to converge toward local solutions) would be a suggested future work for the Altamont-Bluebell 3-D seismic data. This type of model-based inversion may get the advantages of AVAZ resolution, include a wavelet in the formulation of the problem, allow the symmetry axis to change as a function of layer, and constraint the ambiguity in the axis of symmetry. Integrating all available well information is vital too. Fractures can be created at different geological times under different conditions of stress, and more than one trend can exist.

Heterogeneities within subsurface can introduce difficulties of estimating fracture-induced seismic anisotropy. Therefore, integrating core data is important for such cases.

References

Adams, S., Shannon, D., Kucewicz, J., Latkiewicz, C., & Schuelke, J., 2015, Fractured Reservoir Characterization: Integrating Production and Seismic Data to Optimize Well Placement in Bluebell Field, Uinta Basin, NE Utah. In SEG Technical Program Expanded Abstracts 2015 (pp. 4893-4908). Society of Exploration Geophysicists.

Aki, K. and Richards, P.G., 1980, Quantitative Seismology: Theory and Methods, W.H.Freeman and Co., San Francisco, 932 pp.

Al Dulaijan, K., 2008, Near-surface characterization using seismic refraction and surface-wave methods. Masters thesis: University of Calgary.

Al Dulaijan, K., Owusu, J. C., & Weber, D. C., 2012, Azimuthal anisotropy analysis of walkaround vertical seismic profiling vertical seismic profiling: a case study from Saudi Arabia. Geophysical Prospecting, 60(6), 1082-1094.

Alford, R. M., 1986, Shear data in the presence of azimuthal anisotropy: Dilley Texas, SEG Expanded Abstracts, SEG Annual Convention.

Alkhalifah, T. and I. Tsvankin, 1995, Velocity analysis for transversely isotropic media: Geophysics, 60, no. 5, 1550–1566.

Auld, B., 1973, Acoustic fields and waves in solids: John Wiley & Sons.

Bakulin, A., Grechka, V., & Tsvankin, I., 2000a, Estimation of fracture parameters from reflection seismic data—Part I: HTI model due to a single fracture set. Geophysics, 65(6), 1788-1802.

Bakulin, A., Grechka, V., & Tsvankin, I., 2000b, Estimation of fracture parameters from reflection seismic data—Part II: Fractured models with orthorhombic symmetry. Geophysics, 65(6), 1803-1817.

Bakulin, A., V. Grechka, and I. Tsvankin, 2000, Estimation of fracture parameters from reflection seismic data—Part I: HTI model due to a single fracture set, Geophysics, 65, 1788.

Bates, C. R., Lynn, H. B., & Simon, M., 1999, The study of a naturally fractured gas reservoir using seismic techniques. AAPG bulletin, 83(9), 1392-1407.

Cary, P. W., 1999, Pre-stack imaging with 3-D common-offset-vector gathers. 11th Annual CREWES Report, 615-626.

Cary, P. W., & Lorentz, G. A., 1993, Four-component surface-consistent deconvolution. Geophysics, 58(3), 383-392.

CGGVeritas, 2014, GeoView: Hampson-Rusell Software Manual: Release 9.0. Calgary.

Cheadle, S. P., Brown, R. J., & Lawton, D. C., 1991, Orthorhombic anisotropy: A physical seismic modeling study. Geophysics, 56(10), 1603-1613.

Cheng, J., & Kang, W., 2013, Simulating propagation of separated wave modes in general anisotropic media, Part I: qP-wave propagators. Geophysics, 79(1), C1-C18.

Claerbout, J. F., 1985, Imaging the earth's interior: Blackwell Science Inc. Hoboken, New Jersey.

Crampin, S., 1981, A review of wave motion in anisotropic and cracked elastic-media. Wave motion, 3(4), 343-391.

Daley, P. F., and E. S. Krebes, 2006, Quasi-compressional group velocity approximation in a weakly anisotropic orthorhombic medium: Journal of Seismic Exploration, 14, 319–334.

Delbecq, F., Downton, J. E., & Letizia, M., 2013, A math-free look at azimuthal surface seismic techniques. CSEG Recorder, 38(1), 20e31.

Dix, C. H. , 1955, Seismic velocities from surface measurements. Geophysics, 20(1), 68-86.

Downton, J., 2016, GeoView (ProAz): Hampson-Rusell software manual & course note: Release 10.1. Calgary: CGGVeritas.

Downton, J., Hunt, L., Trad, D., Reynolds, S., & Hadley, S., 2011, 5D interpolation to improve AVO and AVAz: a quantitative case history. Canadian Journal of Exploration Geophysics, 37, 8-17.

Downton, J. E., & Roure, B., 2015, Interpreting azimuthal Fourier coefficients for anisotropic and fracture parameters. Interpretation, 3(3), ST9-ST27.

Fatti, J. L., Smith, G. C., Vail, P. J., Strauss, P. J., & Levitt, P. R., 1994, Detection of gas in sandstone reservoirs using AVO analysis: A 3-D seismic case history using the Geostack technique. Geophysics, 59(9), 1362-1376.

Fouch, T. D., Nuccio, V. F., Osmond, J. C., MacMillan, L., Cashion, W. B., & Wandrey, C. J., 1992, Oil and gas in uppermost Cretaceous and Tertiary rock, Uinta Basin, Utah.

Grechka, V., & Tsvankin, I., 1998, 3-D description of normal moveout in anisotropic inhomogeneous media. Geophysics, 63(3), 1079-1092.

Grechka, V., Tsvankin, I., & Cohen, J. K., 1999, Generalized Dix equation and analytic treatment of normal‐moveout velocity for anisotropic media. Geophysical Prospecting, 47(2), 117-148.

Gurevich, B., and Pervukhina, M., 2010, An analytical model for stress induced anisotropy of a cracked solid, SEG, Expanded Abstracts, 29, 2517-2521.

Hintze, L.F., 1988, Geologic history of Utah: Brigham Young University Geology Studies Special Publication 7, 202.

Hudson, J. A.,1988, Seismic wave propagation through material containing partially saturated cracks: Geophysical Journal International, 92, 33–37.

Jenner, E., 2001, Azimuthal anisotropy of 3-D compressional wave seismic data, Weyburn Field, Saskatchewan, Canada: Ph.D. thesis, Colorado School of Mines.

Jenner, E., 2011, Combining VTI and HTI anisotropy in pre-stack time migration: Workflow and data examples. The Leading Edge, 30(7), 732-739.

Lay. D. C., 1996, Linear algebra and its applications, 2nd ed, Addison-Wesley.

Li, X., 2008, An introduction to common offset vector trace gathering; CSEG Recorder, 33, no. 9, 28-34.

Lucas, P. T., & Drexler, J. M.,1976, Altamont-Bluebell--a major, naturally fractured stratigraphic trap, Uinta basin, Utah.

Lynn, H. B., Bates, R., Layman, M., & Jones, M. ,1995, Natural fracture characterization using P-wave reflection seismic data, VSP, borehole imaging logs, and the in-situ stress field determination. In Low Permeability Reservoirs Symposium. Society of Petroleum Engineers.

Lynn, H. B., Beckham, W. E., Simon, K. M., Bates, C. R., Layman, M., & Jones, M., 1999, P-wave and S-wave azimuthal anisotropy at a naturally fractured gas reservoir, Bluebell-Altamont field, Utah. Geophysics, 64(4), 1312-1328.

Mah, M., 1999, Experimental determination of the elastic coefficients of anisotropic materials with the slant-stack method: Ph.D thesis: University of Alberta.

Mahmoudian, F., 2013, Physical Modeling and Analysis of Seismic Data from a Simulated Fractured Medium: Ph.D. thesis, University of Calgary.

Mahmoudian, F., Margrave, G., Daley, P., Wong, J., and Henley, D., 2014, Estimation of elastic stiffness coefficients of an orthorhombic physical model using group velocity analysis on transmission data. Geophysics, 79, R27–R39.

Morgan, Craig D., J. Wallace Gwynn, M. Lee Allison, Richard Curtice, Milind D. Deo, Richard Jarrard, Thomas H. Morris, and Carol N. Tripp., 2003, Characterization of the Bluebell Oil Field, Uinta Basin, Duchesne and Uintah Counties, Utah (SS-106 Pt. 1).

Mosher, C. C., Keho, T. H., Weglein, A. B., & Foster, D. J., 1996, The impact of migration on AVO. Geophysics, 61(6), 1603-1615.

Musgrave, M. J. P., 1970. Crystal acoustics: Introduction to the study of elastic waves and vibrations in crystals. San Francisco: Holden-Day.

Rickman, R., Mullen, M., Petre, E., Grieser, B. and Kundert, D., 2008, A practical use of shale petrophysics for stimulation design optimization: all shale plays are not clones of the Barnett Shale. SPE 115258.

Roseink, J. & Anderson, J., 2013, Discovery thinking: AAPG Bulletin, 110167.

Rüger, A. 1996. Reflection coefficients and azimuthal AVO analysis in anisotropic media. Ph.D. thesis, Colorado School of Mines, Dept. of Geophysics, Golden, Colorado, USA.

Rüger, A. ,1997, P-wave reflection coefficients for transversely isotropic models with vertical and horizontal axis of symmetry. Geophysics, 62(3), 713-722.

Rüger, A., 1998, Variation of P-wave reflectivity with offset and azimuth in anisotropic media. Geophysics, 63(3), 935-947.

Rüger, A., 2001, Reflection coefficients and azimuthal AVO analysis in anisotropic media. Society of Exploration Geophysicists.

Rüger, A., 2002, Reflection coefficients and azimuthal AVO Analysis in anisotropic media: SEG Geophysical Monograph Series No. 10.

Rüger, A., and Tsvankin, I., 1997, Using AVO for fracture detection: Analytic basis and practical solutions: The Leading Edge, 10, 1429-1434.

Russell, B., & Hampson, D., 2006, The old and the new in seismic inversion. CSEG Recorder, 31(10), 5-11.

Schoenberg, M., 1980, Elastic wave behavior across linear slip interfaces: J. Acoust. Soc. Am., 68, 1516–1521.

Shuey, R. T., 1985, A simplification of the Zoeppritz equations. Geophysics, 50(4), 609-614.

Thomsen, L., 1986, Weak elastic anisotropy. Geophysics, 51, 1954–1966.

Thomsen, L., 1988, Reflection seismology over azimuthally anisotropic media. Geophysics, 53(3), 304-313.

Thomsen, L., 1995, Elastic anisotropy due to aligned cracks in porous rock. Geophysical Prospecting, 43(6), 805-829.

Tsvankin, I., 1997, Anisotropic parameters and P-wave velocity for orthorhombic media. Geophysics, 62(4), 1292-1309.

Vavryčuk, V., and I. Pšenčík, 1998, PP-wave reflection coefficients in weakly anisotropic elastic media: Geophysics, 63, 2129–2141.

Vestrum, R. W., 1994, Group- and phase-velocity inversions for the general anisotropic stiffness tensor: M.S. thesis, University of Calgary.

Winterstein, D. F., & Meadows, M. A., 1991, Shear-wave polarizations and subsurface stress directions at Lost Hills field. Geophysics, 56(9), 1331-1348.

Winterstein, D., 1992, How shear-wave properties relate to rock fractures: Simple cases. The Leading Edge, 11(9), 21-28.

Wong, J., F. Mahmoudian, and G. Margrave, 2011, Physical modeling III: Acquiring modeled data for VVAZ/AVAZ analysis: CREWES Research Report, 23, 1–17.

Zoback, M. L., and Zoback, M. D., 1990, Tectonic stress field of the continental United States, in Pakiser, L. C., and Mooney, W. D., Eds., Geophysical framework of the continental United States: CO, Geol. Soc. Am. Memoir 172, 523–539.

Zoeppritz, K., 1919,. On the reflection and propagation of seismic waves at discontinuities. Erdbebenwellen VII B, 66-84.

Appendix A. VVAZ Error Analysis

In this section, error analysis was preformed for the VVAZ method used in **Chapter 5** and **Chapter 6**. For a specific VSP receiver within Wasatch-180 (deep oil reservoir) and different shots at surface, noise was added to travel time (T) in Equation (5.19) in a random manner. The influence of noise was measured for various inverted parameters.

Figure A.1 shows a histogram of the right first arrival times (mean) of one trace and the travel times of same trace but with added random noise in seconds. Various random noise was added to all traces of a common-receiver gather prior to inversion. The standard deviation (σ) of travel times for one trace is 3.1 ms meaning 68% of travel times are within 6.2 ms. The data sample rate is 1 ms. Figure A.2, Figure A.3, and Figure 0.4 summarize respectively the influence of adding random noise to travel times on inverted fast RMS velocity, slow RMS velocity, and the direction of the fast RMS velocity. The histograms and standard deviations (σ) in those figures show that the influence on velocities and direction. Velocities estimate the anisotropy intensity and the influence of adding random noise was found to be very small. The standard deviations of fast and slow velocities respectively are 69 ft/s and 75 ft/s, meaning that adding noise of about 6.2 ms changes inversion results by 1-1.2%. However, the influence on the azimuth was found to larger. The standard deviation is 5^{o}, meaning that adding noise of about 6.2 ms changes inversion results by up to 5.6%.

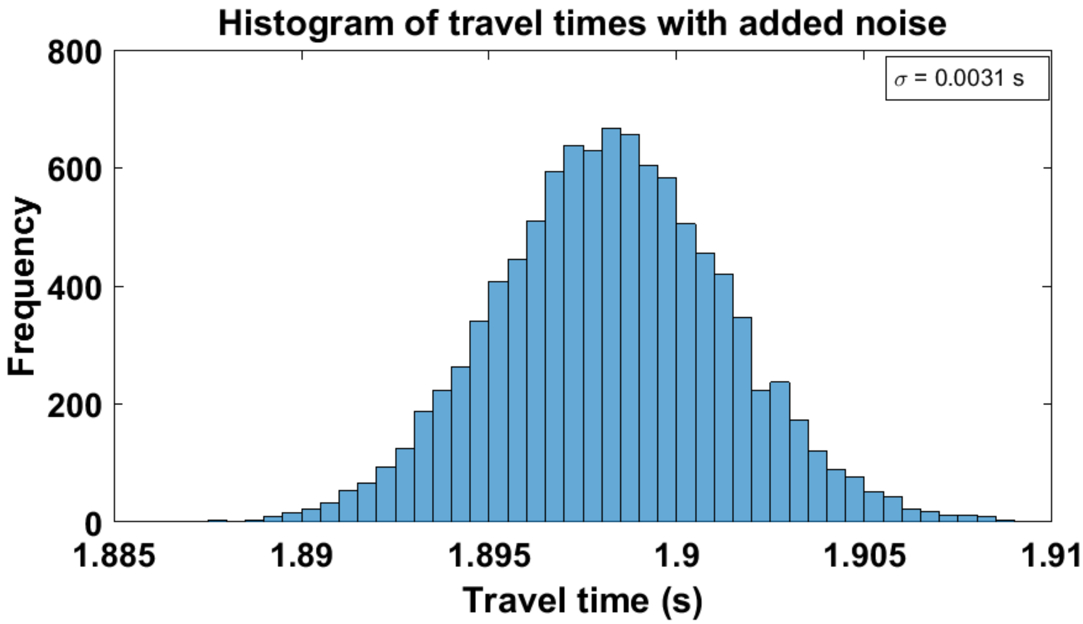

Figure A.1 A histogram of travel times in seconds for a specific VSP receiver within Wasatch-180 and one shot at surface with noise added in a random manner. The standard deviation is 3.1 s, meaning 68% of travel times are within 6.2 ms.

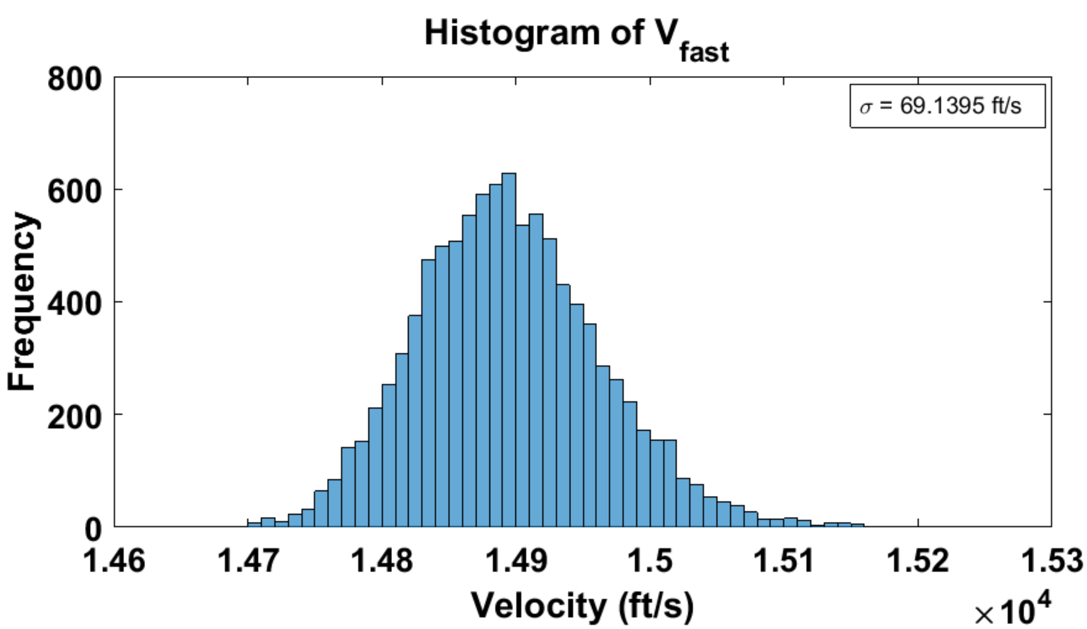

Figure A.2 A histogram of inverted V_{fast} in ft/s. The standard deviation is 69 ft/s, meaning that adding noise of about 6.2 ms changes inversion results by up to 1%.

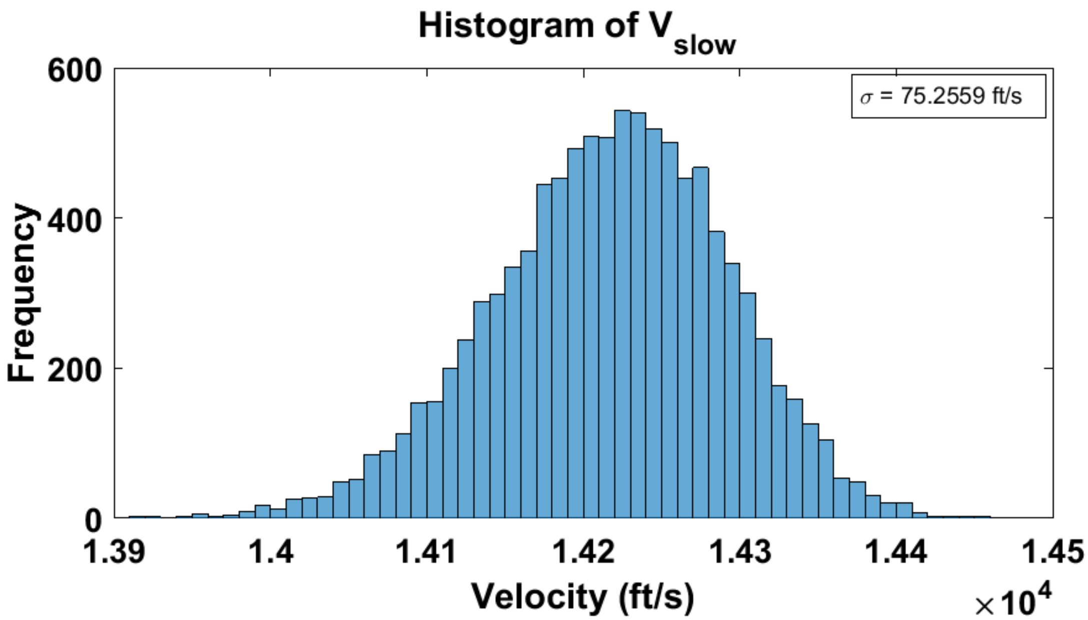

Figure A.3 A histogram of inverted V_{slow} in ft/s. The standard deviation is 75 ft/s, meaning that adding noise of about 6.2 ms changes inversion results by up to 1.2%.

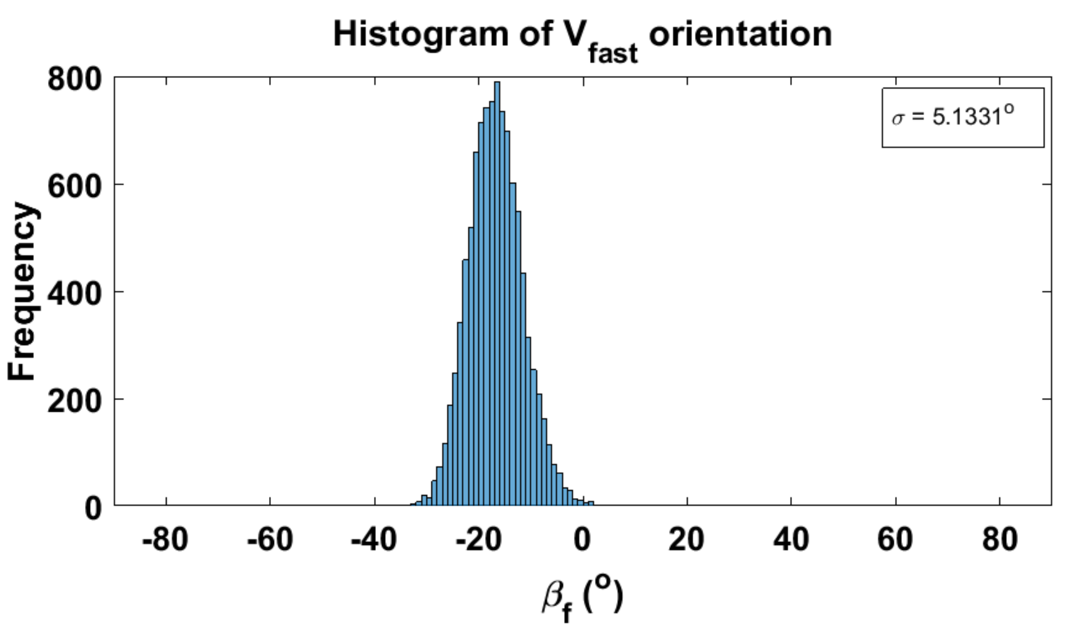

Figure 0.4 A histogram of inverted direction of V_{fast} in degrees. The standard deviation is 5^{o}, meaning that adding noise of about 6.2 ms changes inversion results by up to 5.6%.